Coupled optimization for shape, topology and material orientation of structures built by additive manufacturing

Abdelhak Touiti

Université Paris Cité

École doctorale Sciences Mathématiques de Paris Centre – ED386

Laboratoire Jacques-Louis Lions

Coupled optimization for shape, topology and material orientation of structures built by additive manufacturing

Par **Abdelhak TOUITI**

Thèse de doctorat de Mathématiques Appliquées

Dirigée par **François JOUVE**
et par **Grégoire ALLAIRE**

Présentée et soutenue publiquement

le 23/06/2023

Devant un jury composé de :

Olivier PANTZ, Professeur, Université Côte d'Azur, rapporteur
Francisco PERIAGO, Professeur, Universidad Politécnica de Cartagena, rapporteur
Grégoire ALLAIRE, Professeur, École Polytechnique, co-directeur de thèse
Samuel AMSTUTZ, Professeur, École Polytechnique, examinateur
Anne-Sophie BONNET-BEN DHIA, Directrice de Recherche, ENSTA Paris, examinatrice
Yves CAPDEBOSCQ, Professeur, Université Paris Cité, examinateur
François JOUVE, Professeur, Université Paris Cité, directeur de thèse
Chiara NARDONI, Ingénieure chercheuse, IRT systemX, examinatrice

This thesis has been partly done
at the Centre des Mathématiques Appliquées
of the École Polytechnique.

Titre :

Optimisation couplée pour la forme, la topologie et l'orientation des matériaux des structures construites par fabrication additive

Résumé :

Des recherches sur le processus de fabrication additive montrent que ce processus produit des matériaux ayant des comportements localement orthotropes anisotropes. De plus, les technologies de fabrication additive offrent la possibilité de contrôler l'orientation de l'anisotropie locale en variant la vitesse et la trajectoire de fabrication. En conséquence, l'optimisation de l'orientation de l'anisotropie locale en plus de la forme et de la topologie d'une pièce est devenue plus intéressante. À cette fin, nous avons développé plusieurs algorithmes d'optimisation de topologie et d'orientation couplés en 2D et 3D basés sur la méthode des lignes de niveau pour l'optimisation topologique. D'un autre côté, l'optimisation de l'orientation a été effectuée différemment selon la situation. Pour un simple problème de minimisation de compliance à chargement unitaire, nous utilisons une méthode explicite bien connue qui consiste à aligner l'axe du matériau le plus rigide avec la direction de la plus grande contrainte principale. Pour des problèmes plus industriels et complexes, tels qu'un problème d'optimisation à chargement multiple ou un problème d'optimisation non auto-adjoint (par exemple, un problème de déplacement cible...), nous utilisons une méthode de descente de gradient. Les aspects théoriques de chaque méthode ont été étudiés et expliqués, et leurs algorithmes ont été bien testés en 2D, et en 3D pour un matériaux isotrope transverse. Dans ce travail, nous avons traité divers exemples en 2D et 3D, principalement des exemples avec des problèmes auto-adjoints à chargement unitaire comme les exemples de poutre en porte-à-faux et de poutre en L, un exemple d'inverseur de déplacement avec un problème d'optimisation non auto-adjoint de déplacement cible, et un exemple de pont avec un problème d'optimisation à chargements multiples. Différentes stratégies d'optimisation couplées ont été comparées en 2D, telles que la mise à jour de l'orientation après chaque mise à jour de la forme, la réalisation d'un certain nombre d'itérations d'optimisation de l'orientation après un certain nombre de mises à jour sur la topologie ou la forme, et l'optimisation de l'orientation uniquement à la fin, après avoir complété l'optimisation de la forme. Pour les deux méthodes d'optimisation de l'orientation décrites, des schémas de régularisation de l'orientation dans la structure sont présentés. Finalement, nous avons également contribué au domaine de l'optimisation d'orientation en développant une méthode qui optimise l'orientation sous une contrainte d'inégalité à l'aide d'un Lagrangien augmenté pour les cas 2D et 3D, et en développant une méthode de descente de gradient basée sur l'approche de Ginzburg-Landau pour le cas 2D.

Mots clés :

Optimisation de forme, optimisation topologique, anisotropie, fabrication additive, optimisation de l'orientation des matériaux, optimisation de compliance, optimisation en multi-chargement, optimisation de déplacement cible, méthode des lignes de niveau, méthode de Lagrangien augmenté.

Title :

Coupled optimization for shape, topology and material orientation of structures built by additive manufacturing

Abstract :

Research on the additive manufacturing process showcases that this process produces materials that have locally orthotropic anisotropic behaviors. Additionally, additive manufacturing technologies offer the ability to control the local anisotropy orientation by varying the manufacturing speed and trajectory. As a result, optimizing the local anisotropy orientation in addition to a part shape and topology became more interesting. For this purpose, we developed several coupled topology and orientation optimization algorithms in 2D and 3D that are based on the level set method of topology optimization. On the other hand, the orientation optimization was proceeded differently depending on the situation. For a simple single load case minimal compliance problem, we use a well-known explicit method of aligning the stiffest material axis to the direction of greatest principal stress. For more industrial and complex problems, such as a multi-load optimization problem or a non self-adjoint optimization problem (e.g. target displacement problem...), we use a gradient descent method. The theoretical aspects of each method were studied and explained, and its algorithms were tested and were proved to work properly in 2D, and in 3D for transversely isotropic materials. In this work, we treated various 2D and 3D examples, which are mainly the single-loaded self-adjoint problems of cantilever and L beam, a target displacement problem of displacement inverter mechanism and a multi-loaded optimization problem of a bridge. Various strategies of coupled optimization were compared in 2D, such as updating the orientation after each update of the shape, performing a number of orientation optimization iterations after a certain number of updates on the shape, and optimizing the orientation only after performing a shape optimization loop. For both described orientation optimization methods, regularization schemes that smoothly vary the orientation across the structure are presented. Finally, we also contributed to the field of orientation optimization by developing a method that optimizes inequality-constrained orientations using an augmented Lagrangian for both 2D and 3D cases, and by developing a Ginzburg-Landau based gradient descent method that works for a case of 2D orientation optimization.

Keywords :

Shape optimization, topology optimization, anisotropy, additive manufacturing, orientation optimization, compliance optimization, multi-loaded optimization, target displacement optimization, level-set method, augmented Lagrangian

Remerciements

"Gratus animus est una virtus non solum maxima, sed etiam mater virtutum omnium reliquarum."
— *Marcus Tullius Cicero*

Je souhaite d'abord exprimer ma gratitude envers mon co-directeur de thèse, Grégoire Allaire, pour m'avoir offert cette opportunité de travailler avec lui. Je remercie Grégoire pour son accompagnement constant et rassurant, pour sa clairvoyance pertinente et son énorme maîtrise incontestable des mathématiques et de l'optimisation structurelle. En outre, je suis reconnaissant pour le temps qu'il a consacré à m'expliquer soigneusement les mathématiques, avec motivation et enthousiasme, sans jamais rechigner.

Je souhaite également remercier mon directeur principal, François Jouve, pour sa présence constante à mes côtés tout au long de la thèse, en particuler avec les problématiques numériques. Sa grande compétence et sa perception pratique des méthodes numériques en mathématiques et mécanique étaient tout aussi indispensables pour l'achèvement de ce travail. Je tiens également à remercier mes deux directeurs de m'avoir fourni d'excellentes conditions de travail.

Je remercie Olivier Pantz et Francisco Periago, pour avoir accepté de rapporter sur cette thèse. Je les remercie pour le temps qu'ils ont consacré à la relecture de ce manuscrit et pour leurs remarques pertinentes.

Je remercie Anne-Sophie Bonnet-Ben Dhia pour avoir dirigé ma soutenance de thèse, et Samuel Amstutz, Yves Capdeboscq, et Chiara Nardoni pour m'avoir fait l'honneur de faire partie de mon jury. Je remercie une autre fois Samuel Amstutz et Yves Capdeboscq pour avoir aussi accepté de participer aux comités de suivi de ma thèse.

Je tiens à remercier tous les contributeurs du projet Sofia, le projet qui a financé ce travail de thèse. J'exprime aussi ma gratitude envers tous les membres de l'équipe d'optimisation de formes du CMAP, à savoir Mathilde,

Jeet, Perle, Beniamin, Alex, Lalaina, Mathias, Alexis, Martin. Je remercie tout particulièrement Mathilde pour ses explications sur l'optimisation de forme et pour m'avoir intégré au groupe, Jeet pour son aide avec FreeFem++ et Petsc, Perle pour avoir partagé ses codes d'optimisation avec critère d'optimalité en 2D et de régularisation de l'orientation en 2D et 3D, Beniamin pour avoir partagé ses codes d'optimisation de forme en 2D et son aide dans la résolution de plusieurs problèmes liés à FreeFem++, et Alex pour ses explications de l'optimisation de l'orientation avec critère d'optimalité.

Je tiens également à remercier les anciens membres de mon bureau Poufsouffle, Ziad, Barbara, Marc et Clément, qui sont aussi mes premiers amis en France. Avec eux, je ne me suis jamais senti seul et j'ai partagé des moments merveilleux inoubliables. Je remercie également les nouveaux membres du bureau, Azar, Godfred, Dounia, Elanor, qui remplissent le bureau de dynamisme et d'enthousiasme. Je remercie aussi les autres membres de l'Université Paris Cité, en particulier Alessandro Zilio, Fabio, Sylvain, Yiyan, Sothea, Aaraona, Mohan, Junchao, Hiroshi, Raed et Elyès.

Je remercie aussi les doctorants du laboratoire Jacques-Louis Lions à Jussieu, en particulier Antoine et Eleanor.

Je tiens également à remercier mes anciens professeurs de master qui m'ont énormément aidé avec leurs conseils: Michel Jabbour, Paolo Vannucci, Mathis Plapp, Ziad Moumni de l'École Polytechnique et de l'ENSTA Paris. Je remercie aussi mon ancien superviseur de stage, Abderrahim Talha de l'Université de Lille, avec qui j'ai commencé à travailler sur l'optimisation de structures.

Je tiens aussi à remercier sincèrement Nathalie Bergame, Amina Hariti, Malika Larcher des services administratifs du laboratoire Jacques-Louis Lions et de l'Université Paris Cité, et Nasséra Naar, Alexandra Noiret, Sylvain Ferrand et Pierre Straebler du service administratif et informatique du Centre de Mathématiques Appliquées de l'École Polytechnique, pour leurs efficacité et réactivité tout au long des années de thèse.

Enfin, je tiens à remercier ma famille qui m'a soutenu et encouragé tout au long de la thèse, en particulier ma mère, mon père et ma chère tante, Lamia Touiti Bouebdellah, qui m'ont toujours encouragé dans mon parcours scientifique.

Summary

Introduction (en français) **1**

Introduction (in english) **9**

1 Shape optimization **19**

2 Mechanical problem and model **41**

3 2D orientation optimization **55**

4 3D orientation optimization **105**

5 Coupled optimization of topology and orientation **131**

Conclusion **193**

Bibliography **195**

Table of contents **206**

List of Figures

1 Composants fabriqués par fabrication additive pour l'aérospatiale, figures prises de [99, 59] 1
2 Fabrication additive utilisant la fusion sélective des métaux (une technologie de fusion de lit de poudre), figure de [110] (une version modifié de l'original qui est issue de [65]) 2
3 Rotation du repère matériel en utilisant les angles d'Euler, le repère $x'y'z'$ devient le repère $x_3y_3z_3 = xyz$ à la fin 5
4 Exemples d'orientations optimisées : tracé de la direction la plus rigide de l'anisotropie locale 6
5 Topologie et orientation d'anisotropie optimisées en couple en 2D pour un matériau orthotrope 7
6 Topologie et orientation d'anisotropie optimisées en couple en 3D pour un matériau isotrope transverse 8
7 Aerospace additive manufactured components, figures taken from [99, 59] 9
8 Additive manufacturing using selective metal melting (a powder bed fusion technology), figure from [110] (an updated version of the original which is from [65]) 10
9 Rotation of the material frame using Euler angles, $x_3y_3z_3$ is equivalent to $x'y'z'$ 12
10 Examples of optimized orientations: plot of the stiffest direction of the local anisotropy 13
11 Coupled optimized topology and anisotropy orientation in 2D for an orthotropic material 14
12 Coupled optimized topology and anisotropy orientation in 3D for a transverse isotropic material 15

1.1 Variation of the shape of an initial domain Ω_0 29
1.2 Level set function convection 32
1.3 A domain D composed by the material of the shape Ω and an ersatz material in $D\backslash\Omega$. 34

2.1 Powder bed fusion AM (figure from [24]) 42
2.2 Direct energy deposition AM (figure from [66]) 43
2.3 Layering and laser scanning in SLM (figure from [35]) 44
2.4 Columnar grains formation in SLM (figure from [87]) 44
2.5 Rotation of the material frame using Euler angles, $x_3y_3z_3$ is equivalent to $x'y'z'$ 50
2.6 Rotation of the transverse isotropic material frame using 2 Euler angles, $x_2y_2z_2$ is equivalent to $x'y'z'$ 52
2.7 Orientation angle α of the orthotropic material axes of a 2D structure 54

3.1 Boundaries of a shape Ω for a general objective function 61
3.2 Regularized optimal stiffest orientations of for an arch 67
3.3 Optimization of a cantilever 74
3.4 Optimization of a cantilever orientation using different initializations of the orientation 76
3.5 L-beam and arch optimal orientations with $\alpha_0 = 0$ 77
3.6 Cantilever orientation optimization with a gradient descent . . . 79
3.7 Displacement inverter orientation optimization 82
3.8 Multi-load bridge orientation optimization 84
3.9 Optimized stiffest direction orientation with the Ginzburg-Landau method for $\alpha_0 = 0$ 86
3.10 Objective function evolution with the Ginzburg-Landau method for $\alpha_0 = 0$ 86
3.11 Penalty function evolution with the Ginzburg-Landau method for $\alpha_0 = 0$ 87
3.12 Penalty parameter evolution with the Ginzburg-Landau method for $\alpha_0 = 0$ 87
3.13 Optimized stiffest direction orientation with the Ginzburg-Landau method for $\alpha_0 = \pi/2$ 88
3.14 Objective function evolution with the Ginzburg-Landau method for $\alpha_0 = \pi/2$ 88
3.15 Penalty function evolution with the Ginzburg-Landau method for $\alpha_0 = \pi/2$ 89
3.16 Penalty parameter evolution with the Ginzburg-Landau method for $\alpha_0 = \pi/2$ 89
3.17 Optimized stiffest direction orientation under a constraint on the angle geometrical gradient 91
3.18 Evolution of the constraint function $C(\alpha)$ in the orientation optimization under a constraint on the angle geometrical gradient 91

3.19 Evolution of the compliance in the orientation optimization under a constraint on the angle geometrical gradient 92
3.20 Evolution of the Lagrange multiplier in the orientation optimization under a constraint on the angle geometrical gradient 92
3.21 Optimized stiffest direction orientation under a constraint on the angle partial gradient with respect to y 93
3.22 Evolution of the constraint function $C(\alpha)$ in the orientation optimization under a constraint on the angle partial gradient with respect to y 94
3.23 Evolution of the compliance in the orientation optimization under a constraint on the angle partial gradient with respect to y 94
3.24 Evolution of the Lagrange multiplier in the orientation optimization under a constraint on the angle partial gradient with respect to y 95
3.25 Optimized stiffest direction orientation under a constraint of orientation angle difference to a fixed angle (Example 1) 96
3.26 Evolution of the constraint function $C(\alpha)$ in the orientation optimization under a constraint of orientation angle difference to a fixed angle (Example 1) 97
3.27 Evolution of the compliance in the orientation optimization under a constraint of orientation angle difference to a fixed angle (Example 1) 97
3.28 Evolution of the Lagrange multiplier in the orientation optimization a constraint of orientation angle difference to a fixed angle (Example 1) 98
3.29 Initial stiffest direction orientation for the optimization under a constraint of orientation angle difference to a fixed angle (Example 2) 99
3.30 Optimized stiffest direction orientation under a constraint of orientation angle difference to a fixed angle (Example 2) 100
3.31 Evolution of the constraint function $C(\alpha)$ in the orientation optimization under a constraint of orientation angle difference to a fixed angle (Example 2) 100
3.32 Evolution of the compliance in the orientation optimization under a constraint of orientation angle difference to a fixed angle (Example 2) 101
3.33 Evolution of the Lagrange multiplier in the orientation optimization a constraint of orientation angle difference to a fixed angle (Example 2) 101

3.34 Initial stiffest direction orientation for the optimization under a constraint of orientation angle difference to a fixed angle (Example 3) . . . 102
3.35 Optimized stiffest direction orientation under a constraint of orientation angle difference to a fixed angle (Example 3) 103
3.36 Evolution of the constraint function $C(\alpha)$ in the orientation optimization under a constraint of orientation angle difference to a fixed angle (Example 3) . . . 103
3.37 Evolution of the compliance in the orientation optimization under a constraint of orientation angle difference to a fixed angle (Example 3) . . . 104
3.38 Evolution of the Lagrange multiplier in the orientation optimization a constraint of orientation angle difference to a fixed angle (Example 3) . . . 104

4.1 Projection of e^{III} on xy . . . 112
4.2 Projection of e^{II} on zx_1 . . . 112
4.3 Rotation of the material frame using Euler angles, $x_3y_3z_3$ takes the orientation of $x'y'z'$ . . . 113
4.4 Projection of e^{I} on xy . . . 114
4.5 Frames of a 3D orientation projection for a transverse isotropic material . . . 119
4.6 Optimized orientation in 3D under a constraint on the angles vector geometrical gradient . . . 126
4.7 Evolution of the constraint function $C(\alpha)$ in the 3D orientation optimization under a constraint on the angles vector geometrical gradient . . . 126
4.8 Evolution of the compliance in the 3D orientation optimization under a constraint on the angles vector geometrical gradient . . . 127
4.9 Evolution of the Lagrange multiplier in the 3D orientation optimization under a constraint on the angles vector geometrical gradient . . . 127
4.10 Optimized orientation in 3D under a constraint on the angle partial gradient along y . . . 128
4.11 Evolution of the constraint function $C(\alpha)$ in the 3D orientation optimization under a constraint on the angle partial gradient along y . . . 129
4.12 Evolution of the compliance in the 3D orientation optimization under a constraint on the angle partial gradient along y . . . 129

4.13 Evolution of the Lagrange multiplier in the 3D orientation optimization under a constraint on the angle partial gradient along y 130

5.1 Initialization of the cantilever: plot of stiffest direction of the local anisotropy 136
5.2 Optimized cantilever: plot of stiffest direction of the local anisotropy 136
5.3 Initial shape of the cantilever 137
5.4 Optimized cantilever using strategy 1: simultaneous optimization of shape and orientation using the optimality criterion 139
5.5 Optimized cantilever using strategy 2: simultaneous optimization of shape and orientation using the optimality criterion for $n \geq 25$ 140
5.6 Optimized cantilever using strategy 3: optimization of orientation each 50 iterations of shape optimization using the optimality criterion 141
5.7 Optimized cantilever using strategy 4: optimization of shape then optimization of orientation using the optimality criterion . 142
5.8 Compliance evolution for each strategy of the coupled shape and orientation optimization using an optimality criterion for the 2D cantilever example 143
5.9 Lagrangian evolution for each strategy of the coupled shape and orientation optimization using an optimality criterion for the 2D cantilever example 144
5.10 Volume evolution for each strategy of the coupled shape and orientation optimization using an optimality criterion for the 2D cantilever example 145
5.11 2D L-beam load and boundary condition 146
5.12 Initialization of the L-beam: plot of stiffest direction of the local anisotropy 147
5.13 Optimized L-beam: plot of stiffest direction of the local anisotropy 147
5.14 Optimized cantilever using strategy 1: simultaneous optimization of shape and orientation using the gradient descent method . . . 152
5.15 Optimized cantilever using strategy 2: simultaneous optimization of shape and orientation using the gradient descent method for $n \geq 20$ 153
5.16 Optimized cantilever using strategy 3: simultaneous optimization of shape and orientation using the gradient descent method for $n \geq 50$ 154

5.17 Optimized cantilever using strategy 4: optimization of orientation the gradient descent method after each 20 iterations of shape optimization 155
5.18 Optimized cantilever using strategy 5: optimization of orientation using the gradient descent method after each 50 iterations of shape optimization 156
5.19 Optimized cantilever using strategy 6: optimization of shape then optimization of orientation using the gradient descent method 157
5.20 Compliance evolution for each strategy of the coupled shape and orientation optimization using the gradient descent method for the 2D cantilever example 158
5.21 Lagrangian evolution for each strategy of the coupled shape and orientation optimization using the gradient descent method for the 2D cantilever example 159
5.22 Volume evolution for each strategy of the coupled shape and orientation optimization using the gradient descent method for the 2D cantilever example 160
5.23 Displacement inverter optimization problem 163
5.24 Optimized displacement inverter: plot of stiffest direction of the local anisotropy 164
5.25 Obtained structures and objective functions for the two optimization strategies and the two initializations of the inverter example. Optimization 1: orientation optimized only in the end with $\alpha_0 = \pi/2$. Optimization 2: orientation optimized only in the end with $\alpha_0 = 0$. Optimization 3: concurrent optimization with $\alpha_0 = \pi/2$. Optimization 4: concurrent optimization with $\alpha_0 = 0$ 165
5.26 2D bridge loads and boundary conditions 167
5.27 Initial 2D bridge shape 168
5.28 Shape optimized anisotropic bridge with a fixed orientation . . . 169
5.29 Optimized bridge using horizontal orientations initialization and the strategy of optimizing the orientation using the gradient descent method after each 50 iterations of shape optimization . 170
5.30 Optimized bridge using vertical orientations initialization and the strategy of optimizing the orientation using the gradient descent method after each 50 iterations of shape optimization . 171
5.31 Compliance evolution for each optimization of the coupled shape and orientation optimization using the gradient descent method for the 2D bridge example 172

5.32 Lagrangian evolution for each optimization of the coupled shape and orientation optimization using the gradient descent method for the 2D bridge example 173
5.33 Volume evolution for each optimization of the coupled shape and orientation optimization using the gradient descent method for the 2D bridge example 174
5.34 3D displacement inverter problem model 183
5.35 Optimized displacement inverter 184
5.36 3D cantilever problem model 186
5.37 Optimized 3D cantilever structure for initialization using horizontal orientation case 187
5.38 Optimized 3D cantilever structure for initialization using vertical orientation case 188
5.39 3D bridge optimization problem model 190
5.40 Optimized 3D multi-loaded bridge structure 191

List of Tables

3.1 Initial and final compliances for the cantilever orientation optimization with different initialization of α 75
3.2 Initial and final data of the inverter target displacement optimization with different initialization of α 81
3.4 Material characteristics for 2D augmented Lagrangian orientation optimization for an inequality constraint 90

4.1 Material characteristics for 3D augmented Lagrangian orientation optimization for an inequality constraint 125

5.1 Material characteristics for the cantilever and the L-beam examples 135
5.2 Material characteristics for the cantilever 138
5.3 Material characteristics for the displacement inverter example . 162
5.4 The inverter example obtained displacement along e^x, in the midpoint of the subset Γ_0 of each optimization 166
5.5 Material characteristics for the 3D displacement inverter example 183

List of Algorithms

1 Constrained shape optimization augmented Lagrangian algorithm [18] 37
2 Topology optimization algorithm for elasticity 38

3 2D orientation optimization using an optimality criterion 60
4 2D orientation optimization using the gradient descent 63
5 2D orientation optimization using a Ginzburg-Landau approach . 65
6 2D orientation regularization algorithm 67

7 3D orientation optimization using the optimality criterion 115
8 3D orientation optimization using the gradient descent 117

9 2D topology optimization coupled with the optimality criterion method for orientation 134
10 2D topology optimization coupled with the gradient descent method for orientation 150
11 3D topology optimization coupled with the optimality criterion method for orientation 178
12 3D topology optimization coupled with the gradient descent method for orientation 181

Introduction (en français)

La fabrication additive [52] est devenue aujourd'hui une méthode courante de fabrication des pièces mécaniques grâce à ses nombreux avantages, tels que la réduction des déchets de production, la réduction du temps global de conception à la production, l'automatisation du processus de production, la capacité à produire des géométries très complexes et la capacité à manipuler les caractéristiques mécaniques des pièces produites (par exemple les métamatériaux, les composites...). Avec l'aide des technologies de conception assistée par ordinateur, des possibilités illimitées deviennent disponibles et les formes optimisées en topologie (contenant des formes libres (Free forms), des trous et des porosités) sont à la portée de chaque fabricant. La figure ci-dessous donne des exemples de pièces optimisées fabriquées additivement pour l'aérospatiale.

(a) Support d'aile pour Airbus A350 XWB

(b) Charnière de porte en titane

Figure 1: Composants fabriqués par fabrication additive pour l'aérospatiale, figures prises de [99, 59]

L'optimisation topologique des formes [1, 28] est la technique pour obtenir une conception structurelle optimale en variant la disposition des frontières et le nombre de trous et de porosités à l'intérieur du matériau pour améliorer certaines performances physiques.

En raison des limitations des méthodes de fabrication conventionnelles qui ne pouvaient pas construire des formes optimisées en topologie sans modifier leur formes résultantes, l'optimisation de la topologie a servi comme outil d'aide à la pré-conception qui inspire les concepteurs mécaniques à concevoir des formes relativement optimales. Depuis la fin des années 90, la méthode SIMP (ou Solid Isotropic Microstructure with Penalization for intermediate densities [26, 96]) a connu un grand succès en raison de son efficacité malgré ses problèmes pour pénaliser les densités intermédiaires dans certains cas et ainsi son incapacité à donner une description exacte de la forme optimale sur les limites de la structure.

Cependant, depuis le début des années 2000 et, en particulier, l'apparition des technologies de fabrication additive, il est plus judicieux de passer à une méthode d'optimisation de topologie capable de donner exactement la limite de la structure, comme la méthode des lignes de niveaux [19]. Ce type d'algorithme d'optimisation de topologie permet une automatisation complète de tout le processus de conception à la fabrication en utilisant la fabrication additive. De nombreuses technologies de fabrication additive existent aujourd'hui, telles que les technologies de fusion par lit de poudre et les technologies de dépôt d'énergie directe pour plusieurs types de matériaux (métaux, polymères, céramiques, ...). La figure 2 donne un exemple d'une technologie de fusion par lit de poudre.

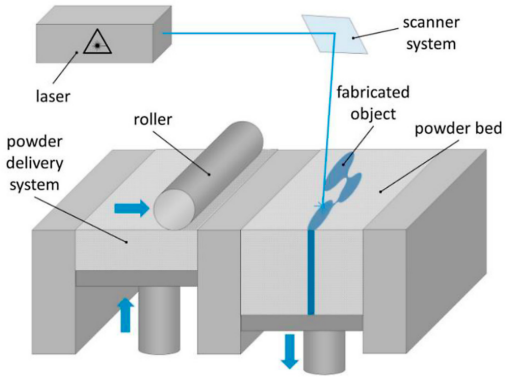

Figure 2: Fabrication additive utilisant la fusion sélective des métaux (une technologie de fusion de lit de poudre), figure de [110] (une version modifié de l'original qui est issue de [65])

Cette thèse fait partie du projet SoFIA ("SOlutions pour la Fabrication Industrielle Additive métallique"), un programme de recherche appliquée français sur la fabrication additive métallique regroupant les partenaires industriels AddUp, Aubert & Duval, ESI Group, FusiA, Michelin, Safran, Volume et Zodiac Aerospace, ainsi que les partenaires académiques représentés par le

CNRS (Centre National de la Recherche Scientifique). Le travail de cette thèse a été réalisé à la fois au Laboratoire Jacques-Louis Lions, avec l'Université Paris Cité, et au Centre des Mathématiques Appliquées de l'École Polytechnique.

La recherche expérimentale sur la fabrication additive montre que les pièces fabriquées avec cette méthode de production présentent un comportement physique localement anisotrope (mécanique, thermique...). Cette anisotropie est causée par plusieurs facteurs, tels que la direction de stratification, le chemin de balayage de laser et la formation de grains colonnaires causée par le gradient de chaleur à l'intérieur du matériau produit par le processus laser. L'anisotropie produite est considérée comme étant orthotrope. Pour la fabrication additive métallique, certains considèrent que l'utilisation d'un traitement HIP (Pression Isostatique à Chaud) annulera l'anisotropie du matériau, mais ce n'est pas une bonne idée si l'on souhaite atteindre une véritable automatisation complète du processus de conception à la fabrication, car dans ce cas, un opérateur devra intervenir pour exécuter le traitement HIP sur une autre machine différente de la machine de fabrication.

Une autre idée intéressante est d'optimiser l'orientation de l'anisotropie locale en plus de la forme ou de la topologie de la structure, ce qui fonctionnera pour tout type de matériau anisotrope obtenu par un processus de fabrication additive.

Le but principal et la nouveauté de cette thèse est le développement d'une méthode d'optimisation de la forme basée sur la méthode des lignes de niveaux couplée avec l'optimisation de l'orientation de l'anisotropie en élasticité orthotrope dans les cas 2D et 3D, à la fois pour une optimisation de l'orientation explicitement résoluble (dans le cas d'un problème de compliance en chargement unitaire) et pour des problèmes d'optimisation de l'orientation implicitement résolubles (avec un algorithme d'optimisation numérique pour tous les autres cas). Une autre nouveauté de ce travail est l'introduction de contraintes d'inégalité au problème d'optimisation de l'orientation de l'anisotropie.

D'autres travaux qui traitent le problème de l'optimisation topologique de forme couplée avec l'optimisation de l'orientation d'anisotropie que l'on peut trouver dans la littérature sont les suivants: [89] en utilisant une méthode SIMP pour l'optimisation de la topologie et le critère d'optimalité pour l'orientation, [91] en utilisant une méthode SIMP pour l'optimisation de la topologie et la descente de gradient pour l'orientation, et [27, 54, 8, 50] en utilisant une méthode d'homogénéisation pour l'optimisation de la topologie et le critère d'optimité pour l'orientation.

Le contenu de la présente thèse est le suivant. Dans le premier chapitre, nous

présentons les éléments principaux qui constituent un problème d'optimisation de forme et les différents types d'optimisation de forme avec leur cadre théorique pour les matériaux anisotropes. Dans ce chapitre, nous présentons l'optimisation de forme paramétrique, une partie essentielle dans l'optimisation d'orientation d'anisotropie, et nous expliquons comment calculer la dérivée de forme paramétrique à l'aide de la méthode de Lagrange. Puis, nous présentons l'optimisation de forme géométrique et ses composants principaux (variation de la frontière, dérivée de forme). Enfin, nous présentons l'optimisation de forme topologique à l'aide de la méthode des lignes de niveaux et ses ingrédients; advection de la fonction ligne de niveau, régularisation de la dérivée de forme et prise en compte d'une contrainte de volume. Cette méthode d'optimisation de forme topologique est résumée dans l'algorithme d'optimisation de topologie 2, que nous utilisons au chapitre 5.

Dans le deuxième chapitre, nous présentons le cadre physique de cette thèse en deux parties. Dans la première partie, nous discutons en détail la fabrication additive, son histoire et son développement, ainsi que ses différentes technologies et avantages par rapport aux méthodes de fabrication conventionnelles. Nous présentons également la technologie de fabrication SLM (Selective Laser Melting) et ses étapes pour construire une pièce métallique. Dans la seconde partie, nous présentons le formalisme d'anisotropie en élasticité en utilisant la notation de Kelvin en 2D et 3D pour un matériau anisotrope général et un cas particulier d'un matériau transversalement isotrope. Nous expliquons également le modèle de rotation de l'anisotropie en 2D en utilisant un angle géométrique et en 3D en utilisant les angles d'Euler (voir la figure 3). Cette seconde partie sert de colonne vertébrale pour le modèle de matériau localement anisotrope utilisé dans tous les chapitres suivants.

Dans le troisième chapitre, nous présentons plusieurs méthodes utilisées pour l'optimisation de l'orientation anisotrope locale en 2D. La première méthode est un résultat de critère d'optimalité classique établi par Pauli Pedersen [82, 83], consistant à aligner l'orientation la plus rigide avec la direction de plus grande valeur absolue des contraintes principales. Cette méthode est limitée aux problèmes d'optimisation auto-adjoints à chargement unitaire, qui sont des problèmes explicitement résolvables, tels que la minimisation de la compliance. Une seconde méthode est une méthode de descente de gradient classique qui utilise l'approche théorique d'optimisation de forme paramétrique du chapitre 1 pour optimiser l'angle d'orientation. Enfin, une troisième méthode est une méthode de descente de gradient basée sur une approche de Ginzburg-Landau consistant à optimiser le cosinus et le sinus de l'angle d'orientation, en éliminant ainsi la contrainte sur la norme unitaire du vecteur d'orientation. Les deux dernières méthodes peuvent optimiser n'importe quel problème d'optimisation

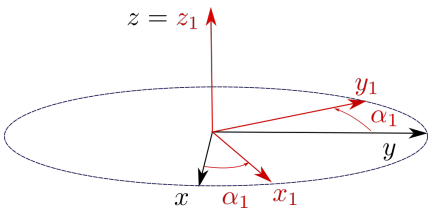

(a) Rotation avec le premier angle d'Euler par rapport à z'

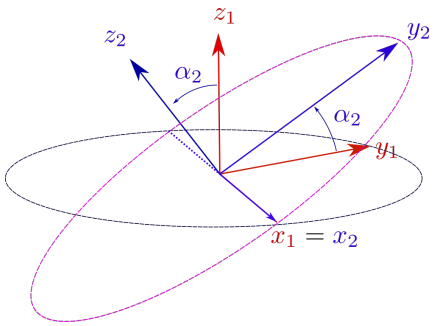

(b) Rotation avec le deuxième angle d'Euler angle par rapport à x_1

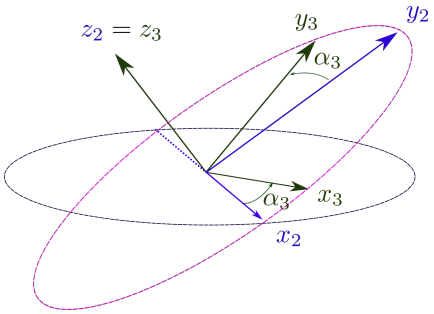

(c) Rotation avec le deuxième angle d'Euler angle par rapport à z_2

Figure 3: Rotation du repère matériel en utilisant les angles d'Euler, le repère $x'y'z'$ devient le repère $x_3y_3z_3 = xyz$ à la fin

d'orientation, y compris des problèmes non auto-adjoints, tels qu'un déplacement cible ou une minimisation de contraintes, et des problèmes contraints. Des algorithmes pour chaque méthode d'optimisation décrite sont présentés et expliqués. Nous donnons également deux méthodes de régularisation d'orientation, l'une qui fonctionne en régularisant le gradient pendant l'exécution d'un algorithme d'optimisation, et l'autre qui a été développée à l'origine par Perle Geoffroy-Donders [8, 50] et qui consiste à régulariser l'orientation séparément du problème d'optimisation. Enfin, ce chapitre présente également les méthodes de Lagrangien augmenté et de descente de gradient projeté pour prendre en compte les contraintes d'inégalité dans l'optimisation de l'orientation locale. Dans ce chapitre, plusieurs exemples ont été étudiés, tels qu'une poutre en porte-à-faux, une poutre en L, un pont et un inverseur de déplacement (la figure 4 donne quelques résultats obtenus par la méthode de descente de gradient).

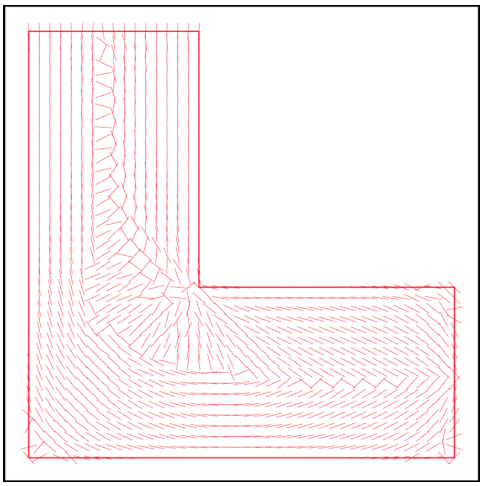

(a) Orientation optimisée d'une poutre en L

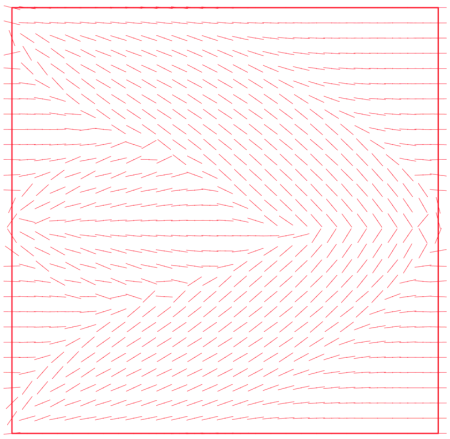

(b) Orientation optimisée d'un inverseur de déplacement

Figure 4: Exemples d'orientations optimisées : tracé de la direction la plus rigide de l'anisotropie locale

Dans le quatrième chapitre, nous traitons l'optimisation de l'orientation en 3D pour un matériau isotrope transverse et un matériau orthotrope général. Tout d'abord, nous utilisons la méthode du critère d'optimalité de Pauli Pedersen qui donne les formules exactes des valeurs d'angles d'Euler optimaux qui sont déterminées géométriquement à partir des directions des contraintes principales (dans les deux cas de matériau). Deuxièmement, nous présentons la méthode d'optimisation de l'orientation basée sur un algorithme de descente de gradient. Dans ce chapitre, nous présentons également la méthode de régularisation de l'orientation en 3D et le traitement des contraintes d'inégalité en

utilisant un Lagrangien augmenté. Les algorithmes de critère d'optimalité et d'optimisation de l'orientation par descente de gradient développés dans ce chapitre sont une partie essentielle des résultats en 3D du cinquième chapitre. Finalement, nous donnons des résultats numériques uniquement pour les algorithmes d'optimisation par descente de gradient soumis à des contraintes d'inégalité pour un matériau isotrope transverse.

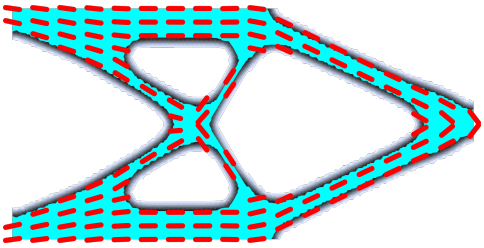

(a) Topologie et orientation optimisées d'un porte-à-faux 2D: tracé de la direction la plus rigide de l'anisotropie locale

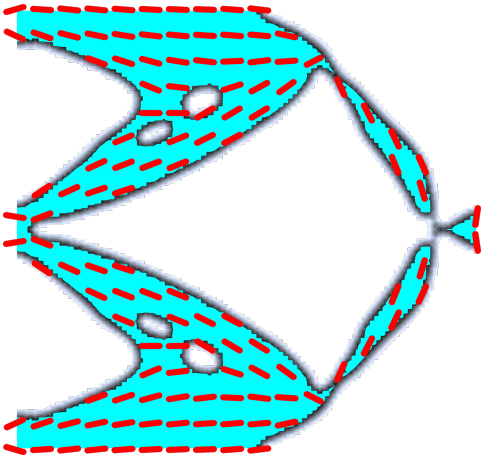

(b) Topologie et orientation optimisées d'un inverseur de déplacement 2D: tracé de la direction la plus rigide de l'anisotropie locale

Figure 5: Topologie et orientation d'anisotropie optimisées en couple en 2D pour un matériau orthotrope

Dans le cinquième chapitre, nous présentons les méthodes d'optimisation couplée de la forme avec l'orientation que nous avons établies. Ces algorithmes sont mis en oeuvre en combinant l'algorithme d'optimisation de la forme avec les algorithmes d'optimisation de l'orientation. Premièrement, pour la méthode d'optimisation de l'orientation basée sur le critère d'optimalité, et deuxièmement, pour la méthode d'optimisation de l'orientation basée sur la descente de gradient. Ce chapitre est divisé en deux parties. Dans la première partie, nous présentons et traitons le problème d'optimisation couplé en 2D et nous comparons diverses stratégies d'optimisation couplée. Dans la seconde partie, nous traitons l'optimisation en 3D pour un matériau orthotrope général et un matériau isotrope transverse. Mais, nous ne donnons que des résultats numériques pour un matériau isotrope transverse. Dans les deux parties de ce chapitre, nous étudions plusieurs exemples tels qu'une poutre en porte-à-faux et une poutre en L pour l'optimisation de compliance en chargement unique, un inverseur de déplacement pour le problème de déplacement cible, et un pont

pour l'optimisation de compliance en chargement multiple (les figures 5 et 6 donnent certains exemples traités).

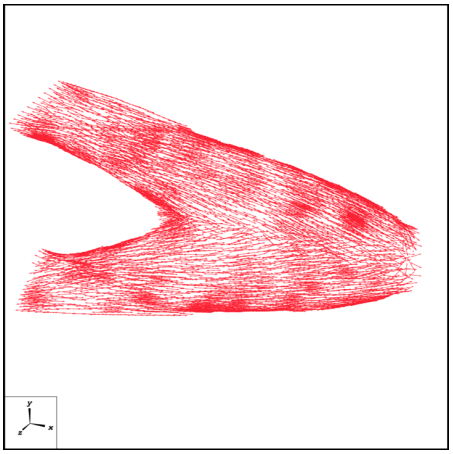

(a) Topologie et orientation optimisées d'un porte-à-faux 3D: tracé de la direction la plus rigide de l'anisotropie locale

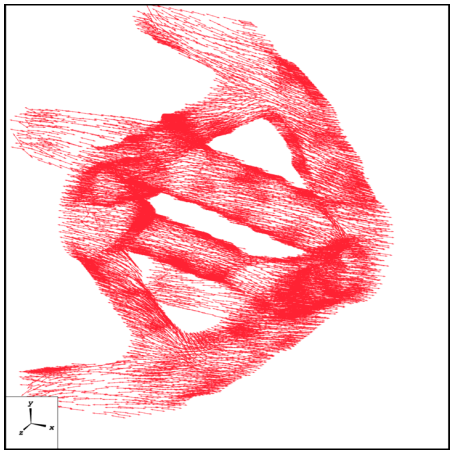

(b) Topologie et orientation optimisées d'un inverseur de déplacement 3D: tracé de la direction la plus raide de l'anisotropie locale

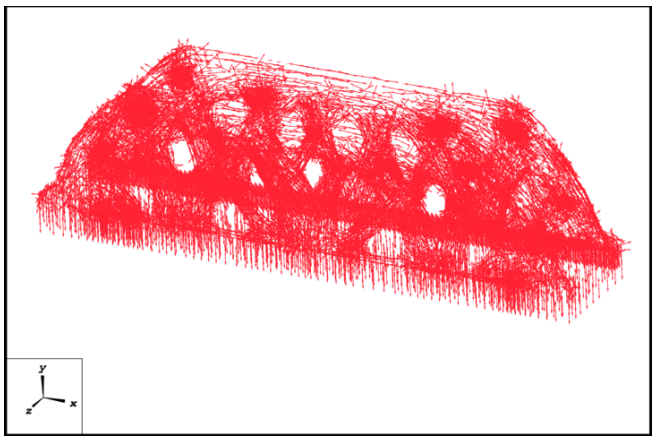

(c) Topologie et orientation optimisées d'un pont 3D: tracé de la direction la plus rigide de l'anisotropie locale

Figure 6: Topologie et orientation d'anisotropie optimisées en couple en 3D pour un matériau isotrope transverse

Introduction (in english)

Additive manufacturing [52], or AM, has become today a mainstream method of mechanical parts manufacturing thanks to its many advantages, reducing manufacturing wastes, reducing the overall design-to-manufacturing time, automation of the manufacturing process, the ability to produce very complex geometries, the ability to manipulate the mechanical characteristics of the produced parts (e.g. meta-materials, composites..). With the help of computer-aided design technologies, unlimited possibilities become available, and topology-optimized shapes (containing free forms, holes and porosities) are within reach of every manufacturer. The figure below gives examples of additive manufactured optimized parts for aerospace.

(a) Airbus A350 XWB jet wing bracket

(b) Titanium door hinge

Figure 7: Aerospace additive manufactured components, figures taken from [99, 59]

Topology optimization of shapes [1, 28] is the technique for obtaining an optimal structural design by varying the boundaries layout and the number of holes and porosities inside the material to improve some physical performances.

Because of the limitations of conventional manufacturing methods that could not build topology-optimized shapes without modifying their resulting layout,

topology optimization served as a predesign-aiding tool that inspires mechanical designers to design shapes that are relatively optimal. Since the late 90s, the SIMP method (or Solid Isotropic Microstructure with Penalization for intermediate densities [26, 96]) was successful thanks to its efficiency despite its problems for penalizing intermediate densities in some cases and thus its inability to give the exact optimal shape description on the structure boundaries.

However, since the early 2000s and, in particular, the appearance of additive manufacturing technologies, it makes more sense to switch to a topology optimization method that is capable of exactly giving the structure boundary, such as the level set method [19]. This type of topology optimization algorithm makes it possible to fully automate all the design-to-manufacturing process using additive manufacturing. Multiple technologies of additive manufacturing exist nowadays such as the powder bed fusion technologies and direct energy deposition technologies for multiple material types (metals, polymers, ceramics...). Figure 8 gives an example of a powder bed fusion technology.

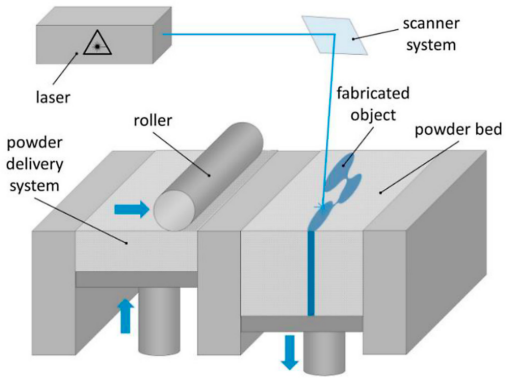

Figure 8: Additive manufacturing using selective metal melting (a powder bed fusion technology), figure from [110] (an updated version of the original which is from [65])

This thesis is part of the SoFIA project ("SOlutions pour la Fabrication Industrielle Additive métallique" - Solutions for Industrial Metal Additive Manufacturing), which is a French applied research program for metal additive manufacturing that is put together by the following industrial partners, AddUp, Aubert & Duval, ESI Group, FusiA, Michelin, Safran, Volume and Zodiac Aerospace, as well as academic partners represented by the CNRS (Centre National de la Recherche Scientifique). The work of this thesis was carried out both at the Laboratoire Jacques-Louis Lions, with the Université Paris Cité, and at the Centre des Mathématiques Appliquées of the École Polytechnique.

Experimental research of additive manufacturing showcases that the parts

that are built with this manufacturing method are observed to have a locally anisotropic physical behavior [61, 33, 85, 95, 56, 97] (mechanical, thermal...). This anisotropy is caused by multiple factors; the layering direction, the laser scanning path, and the columnar grains formations that is caused by the heat gradient inside the material that is produced by the laser process. The anisotropy that is produced is observed to be orthotropic. For metal AM, some would argue that using HIP (Hot Isostatic Pressing) treatment will cancel the material anisotropy, but this is not a good idea if one wants to achieve a truly full automation of the whole design-to-manufacturing process, because in that case an operator should interfere to execute the HIP treatment in another machine that is different from the manufacturing machine.

One more interesting idea is to optimize the local anisotropy orientation in addition to the structure shape or topology, which will work for any type of anisotropic material that is obtained by an additive manufacturing process.

The main goal and novelty of this thesis is the development of a level set-based shape optimization method that is coupled with the optimization of anisotropy orientation in orthotropic elasticity in both 2D and 3D cases, for both explicitly solvable orientation optimization (in a case of a single load compliance problem) and implicitly solvable orientation optimization problems (with a numerical optimization algorithm for all other cases). Another novelty of this work is the introduction of inequality constraints to the anisotropy orientation optimization problem.

Other works that treat the problem of coupled topological shape and anisotropy orientation optimization that one can find in the literature are the following: [89] using a SIMP method for topology optimization and the optimality criterion for the orientation, [91] using a SIMP method for topology optimization and the gradient descent for the orientation, and [27, 54, 8, 50] using a homogenization method for topology optimization and the optimality criterion for the orientation.

The content of the present thesis is the following. In the first chapter, we present the main elements that constitute a shape optimization problem and the different types of shape optimization with their theoretical framework for anisotropic materials. In this chapter, we present parametric shape optimization, an essential part of anisotropy orientation optimization, and we explain how to compute the parametric shape derivative using the Lagrangian method. Then, we present geometrical shape optimization and its main components (boundary variation, shape derivative). Lastly, we present topological shape optimization using the level set method and its ingredients; advection of the level set function, regularization of the shape derivative, and taking into account

a volume constraint. This topological shape optimization method is summarized in the topology optimization algorithm 2, that we use in chapter 5.

In the second chapter, we present the physical framework of this thesis in two parts. In the first part, we discuss additive manufacturing in more detail, its history and development, and its various technologies and advantages over conventional manufacturing methods. We also present the SLM (Selective Laser Melting) manufacturing technology and its steps for building a metallic part. In the second part, we present the pointwise anisotropy formalism in elasticity using the Kelvin notation in 2D and 3D for a general anisotropic material and a particular case of a transversely isotropic material. We also explain the rotation model of anisotropy in 2D using a geometrical angle and in 3D using the Euler angles (see figure 9). This second part serves as the backbone of the locally anisotropic material model used in all the following chapters.

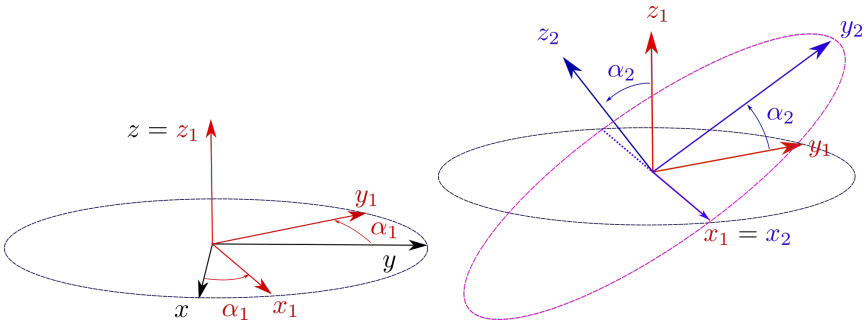

(a) Rotation by the first Euler angle about z'

(b) Rotation by the second Euler angle about x_1

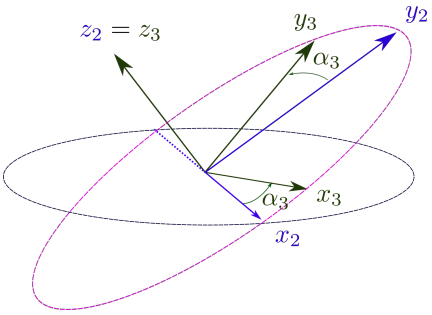

(c) Rotation by the third Euler angle about z_2

Figure 9: Rotation of the material frame using Euler angles, $x_3y_3z_3$ is equivalent to $x'y'z'$

In the third chapter, we present several methods that we use for the local anisotropy orientation optimization in 2D. The first method is a classical optimality criterion result established by Pauli Pedersen [82, 83], and it consists

of aligning the stiffest orientation with the major absolute principal stress direction. This method is limited to single-load self-adjoint optimization problems, which are explicitly solvable problems, such as the minimization of compliance. A second method is a classical gradient descent method that uses the parametric shape optimization theoretical approach of chapter 1 to optimize the orientation angle. Finally, a third method is a gradient descent method which is based on a Ginzburg Landau approach that consists of optimizing the cosine and the sine of the orientation angle, thus removing the constraint of the orientation vector being a unit vector. The latter two methods can optimize whatever orientation optimization problem including non self-adjoint problems, such as a target displacement or a stress minimization problem, and constrained problems. Algorithms for each stated optimization method are presented and explained. We also give two orientation regularization methods, one that works by regularization of the gradient during an optimization algorithm execution, and the other which was originally developed by Perle Geoffroy-Donders [8, 50] and that consists in regularizing the orientation separately from the optimization problem. Finally, this chapter also presents the augmented Lagrangian and the projected gradient descent methods to take account of inequality constraints in orientation optimization. In this chapter, several examples were studied such as a cantilever, an L-beam, a bridge and a force inverter (figure 10 gives some results obtained by the gradient descent method).

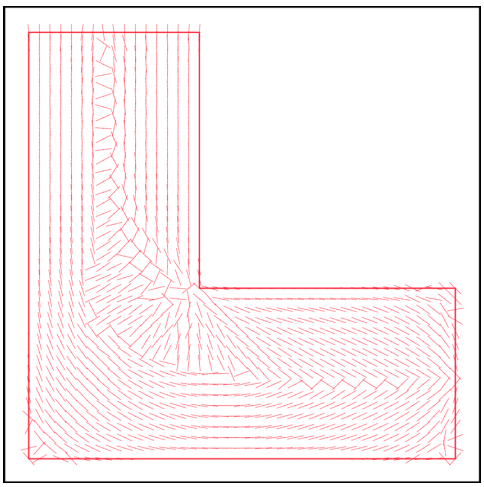

(a) Optimized orientation of an L-beam

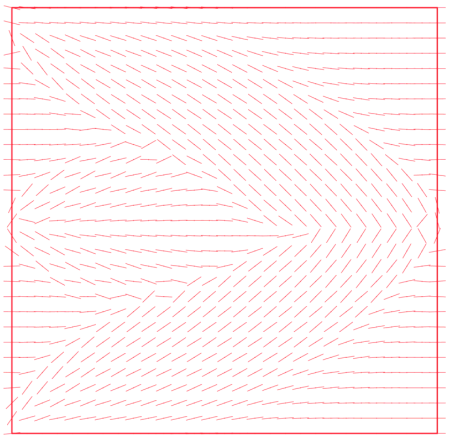

(b) Optimized orientation of a displacement inverter

Figure 10: Examples of optimized orientations: plot of the stiffest direction of the local anisotropy

In the fourth chapter, we treat the orientation optimization in 3D for a trans-

versely isotropic material and a general orthotropic material. First, we use the optimality criterion method of Pauli Pedersen which gives the exact formulas for the optimal Euler angles values that are geometrically determined from the directions of optimal stress (in both material cases). Second, we present the orientation optimization method, based on a gradient descent algorithm. In this chapter, we also present the 3D orientation regularization method and the treatment of inequality constraints using an augmented Lagrangian. The algorithms of optimality criterion and gradient descent orientation optimization that were developed in this chapter are an essential part for the 3D results of the fifth chapter. Finally, we give numerical results only for the inequality constrained gradient descent optimization algorithms for a transversely isotropic material.

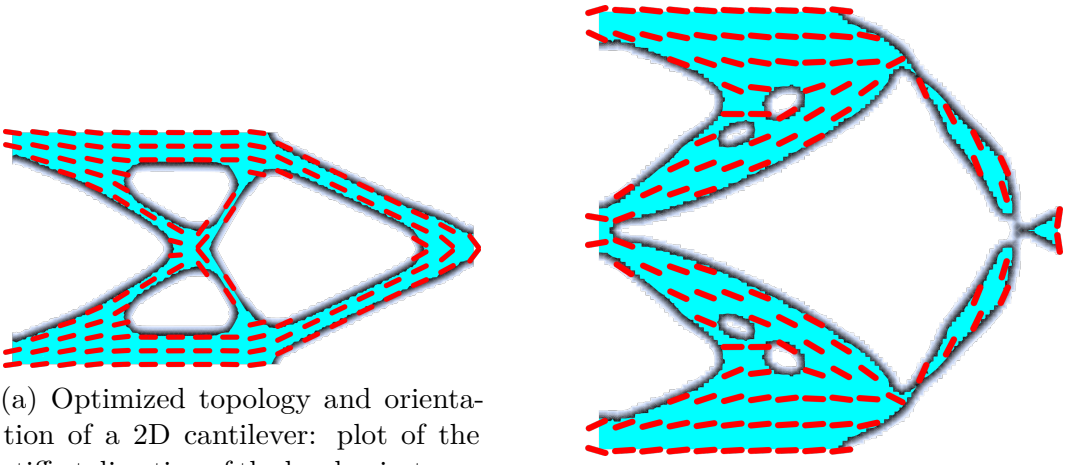

(a) Optimized topology and orientation of a 2D cantilever: plot of the stiffest direction of the local anisotropy

(b) Optimized topology and orientation of a 2D displacement inverter: plot of the stiffest direction of the local anisotropy

Figure 11: Coupled optimized topology and anisotropy orientation in 2D for an orthotropic material

In the fifth chapter, we present the coupled shape and orientation optimization methods that we have established, which are algorithms that have been implemented by combining the algorithm of shape optimization with the algorithms of orientation optimization. First, for the optimality criterion orientation optimization method and second, for the gradient descent orientation optimization method. This chapter is divided into two parts. In the first part, we present and treat the coupled optimization problem in 2D, and we compare various coupled optimization strategies. In the second part, we treat the optimization in 3D for a general orthotropic material and a transversally isotropic material,

but we give numerical results only for a transversally isotropic material. In both parts of this chapter, we study multiple examples such as a cantilever, an L-beam, a displacement inverter and a multi-loaded bridge (figures 11 and 12 give some treated examples).

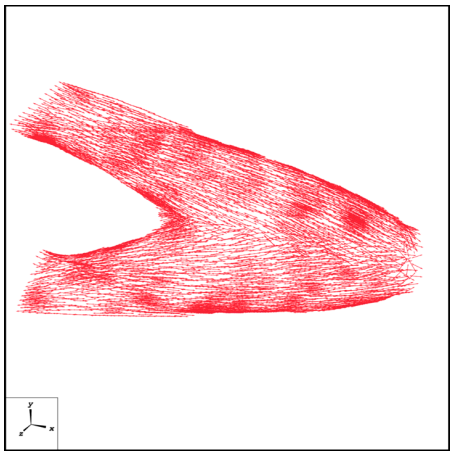

(a) Optimized topology and orientation of a 3D cantilever: plot of the stiffest direction of the local anisotropy

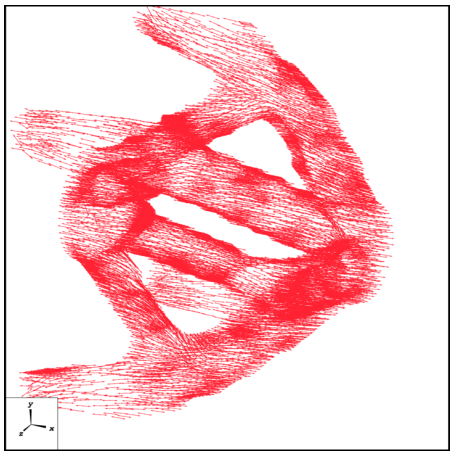

(b) Optimized topology and orientation of a 3D displacement inverter: plot of the stiffest direction of the local anisotropy

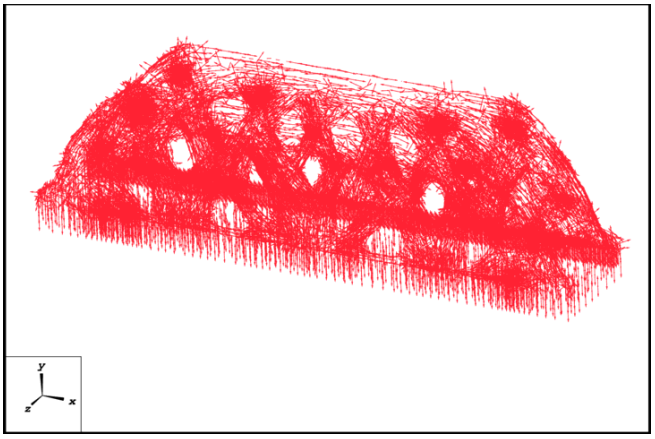

(c) Optimized topology and orientation of a 3D bridge: plot of stiffest direction of the local anisotropy

Figure 12: Coupled optimized topology and anisotropy orientation in 3D for a transverse isotropic material

é

List of mathematical symbols

D	design domain (page 27)
Ω	shape of geometrical structure
f	body force (page 20)
g	surface force (page 20)
$e(u)$	strain tensor (page 20)
x	coordinate vector
σ	stress tensor
u	displacement vector
A	Hooke's law tensor (page 21)
A^*	Hooke's law tensor (page 55 in 2D and page 105 in 3D)
n	boundary normal vector
$\partial\Omega$	boundary of the shape Ω
Γ	free boundary of the shape Ω (page 21)
Γ_D	Dirichlet boundary
Γ_N	Neumman boundary
U_{ad}	space of admissible designs
J	objective function
j	body specific objective function (page 22)
l	surface specific objective function (page 22)
Γ_l	boundary part where the surface specific objective function is defined (page 22)
α	in Chapter 1: an ordinary parameter to optimize in Chapters 2, 3 and 5: the 2D orientation angle (page 53)
q	Lagrange multiplier of the elasticity equation (page 23)
p	adjoint state (page 162)
$\mathcal{L}$	Lagrangian function (page 23)
u_0	target displacement
V_T	target volume
Ω_θ	deformation of shape (page 28)
θ	shape variation mapping (page 28)
λ	Lagrange multiplier
ϕ	level set function (page 32)

$\mathcal{V}$	velocity vector of the level set function convection (page 32)
j'_r	regularized gradient (page 33)
r	regularization parameter (page 33)
$\mathcal{L}_c$	Lagrangian of the volume constraint (page 35)
$C(\Omega)$	constraint function (page 35)
$\mathcal{L}_{al}$	augmented Lagrangian (page 36)
b	augmented Lagrangian penalization parameter (page 36)
$\{\sigma\}$	vector that models the stress tensor in Kelvin formalism (page 45)
$\{e\}$	vector that models the strain tensor in Kelvin formalism
$\hat{A}$	matrix that models the Hooke's law tensor in Kelvin formalism: stiffness constitutive matrix (page 45)
$\hat{S}$	compliance constitutive matrix
α_1, α_2 and α_3	Euler angles for an orthotropic material orientation (page 49)
E_1, E_2 and E_3	Young moduli for an orthotropic material (page 46)
$\nu_{21}, \nu_{31}, \nu_{31}, \nu_{23}, \nu_{31}$ and ν_{12}	Poisson's rations for an orthotropic material (page 46)
G_{12}, G_{13} and G_{23}	shear moduli for an orthotropic material (page 46)
E_1 and E_p	Young moduli for a transverse isotropic material (page 47)
ν_{1p}, ν_{p1} and ν_p	Poisson's rations for a transverse isotropic material (page 47)
G_{1p}	shear modulus for a transverse isotropic material (page 47)
$x'y'z'$	material frame (page 49)
xyz	fixed Galilean frame (page 49)
$e^{x'}$,$e^{y'}$ and $e^{z'}$	material frame base vectors (page 46)
$x_1y_1z_1$, $x_2y_2z_2$ and $x_3y_3z_3$	frames obtained by the Euler elementary rotations (page 50)
$\hat{A}^*$	constitutive stiffness matrix for the rotated material (page 51)
R	Kelvin formalism rotation matrix (page 51)
Q	conventional rotation matrix
Q_1, Q_2 and Q_3	elementary rotations rotation matrices

σ_I and σ_{II}	principal stresses in 2D
$\sigma_{\max}$	major absolute principal stress (page 58)
$e_{\sigma_{\max}}$	major absolute principal stress direction vector
α_{opt}	optimal 2D orientation angle obtained by the optimality criterion (page 59)
$\mathfrak{c}$	cosine of the orientation angle (page 63)
$\mathfrak{s}$	sine of the orientation angle (page 63)
J_p	Ginzburg-Landau objective function (page 64)
ε_p	Ginzburg-Landau penalty parameter (page 64)
η	regularization parameter (page 66)
$\mathfrak{b}$	regularization vector (page 66)
c	constant scalar bound of an inequality condition (page 68)
j'_{r_α}	regularized gradient with respect to the orientation (page 68)
r_α	regularization parameter with respect to the orientation (page 68)
$\bar{\alpha}_n$	projected orientation angle (page 68)
ξ	slack variable of the augmented Lagrangian (page 70)
α_f	fixed orientation angle (page 73)
$\boldsymbol{\alpha}$	Euler angles vector (page 124)
e^I,e^{II} and e^{III}	principal stresses directions
$e^{x_1}e^{y_1}e^{z_1}$, $e^{x_2}e^{y_2}e^{z_2}$ and $e^{x_3}e^{y_3}e^{z_3}$	vector basis of the three Euler elementary rotations frames. (page 109)
α_a^{opt},α_2^{opt} and α_3^{opt}	optimal 3D orientation angles obtained by the optimality criterion (page 110)
$\boldsymbol{\alpha}^{opt}$	optimal 3D orientation angles vector obtained by the optimality criterion
$\mathcal{R}_r$	fixed frame of reference (page 119)
β_1 and β_2	orientation angles of the transverse isotropic material with respect of the frame of reference (page 119)
$\mathcal{R}_G$	fixed Galilean frame (page 119)
$\mathcal{U}_{ad}^{\Omega}$	set of admissible shapes (page 176)
$\mathcal{U}_{ad}^{\alpha}$	set of admissible orientation angles (page 176)
$\mathcal{U}_{ad}^{\boldsymbol{\alpha}}$	set of admissible orientation angles vector (page 176)
n_{per}	period of orientation updates (page 149)
n_{or}	starting iteration number of orientation updates (page 149)

Chapter 1

Shape optimization

In structural design [2, 28] a shape optimization problem is defined by three essential inputs:

1. a **model**, which is usually written as a partial derivative equation, that evaluates the physical behavior of a structure.
2. an **objective function**; it is the cost function or the physical criterion that is to be minimized or maximized. It can be for example the structure compliance, volume or its maximal stress.
3. a **set of admissible optimization variables** (also called design variables) that model the structure's shape and that take into account the potential constraints that are imposed on the structure.

What distinguishes shape optimization from structural optimization is that shape optimization is also applied in multiple other fields than structural mechanics such as fluid mechanics [44] and magnetostatics [20].

Shape optimization problems fall into three main categories:

1. **Parametric optimization**: where the shape is parameterized by a number of design variables such as thickness, truss configuration, radius, geometric angles or dimensions. Examples of parametric optimization can be found in [2, 28].
2. **Geometrical shape optimization**: where the boundaries of the structure are changed while the topology is fixed. Examples of geometric optimization can be found in [64, 84, 75].
3. **Topology optimization**: where the boundaries and topology of the structure are changed by the optimization. We say that the topology of the structure has changed when the number of holes in 2D and 3D or the

number of handles in 3D has changed. Examples of topology optimization can be found in [1, 3, 28, 96].

1.1 Parametric shape optimization

1.1.1 Setting of the problem

In this work, we mainly study the physical problem of linear elasticity, which is a model that describes the displacements (or the deformations) and the stresses that occur inside a solid material under some loading conditions and the assumption of infinitesimal strains. The model of elasticity is a system of partial differential equations.

Let Ω be an open subset of $\mathbb{R}^N$ (with $N = 2$ or 3). The subset Ω is also called domain, shape or structure and it models the volume that is occupied by a solid material when there is no loading applied. It models a structure free of any deformation.

The forces that are applied on the structure Ω can be either body forces or surface forces. We denote by f a body force that is applied to Ω and by g a surface force that is applied on Γ_N, which is a part of the boundary of the domain Ω. After the deformation, every point x of Ω is displaced to $x + u(x)$. We denote by u the elastic displacement vector, which is the output of solving the elasticity problem. We suppose that $f, g \in H^1(\Omega)$ and $u \in (H^1(\Omega))^N$, where $H^1(\Omega)$ is given by Definition 1.

Definition 1 *The Sobolev space $H^1(\Omega)$ is defined by*

$$H^1(\Omega) = \left\{ v \in L^2(\Omega) \ s.t. \ , \forall i \in \{1, \dots, N\}, \frac{\partial v}{\partial x_i} \in L^2(\Omega) \right\},$$

where $\frac{\partial v}{\partial x_i}$ is the partial derivative of v in a weak sense or in the sense of distributions.

Using the displacement vector u, we can determine the strain tensor $e(u)$, which models the relative displacements within the deformed material.

$$e(u) = \frac{1}{2}\left(\nabla u + (\nabla u)^t\right) = \frac{1}{2}\left(\frac{\partial u_i}{\partial x_j} + \frac{\partial u_j}{\partial x_i}\right)_{1 \le i,j \le N}.$$

The stress tensor σ, which gives the state of stress at a point x when the material is deformed, is mapped linearly to e through the Hooke's law:

$$\sigma = Ae(u),$$

where A is a fourth-order tensor that is called the elasticity tensor or the stiffness tensor. A is an input to the elasticity model as it describes the material characteristics, it contains the elastic moduli that are defined by the type of used material (see chapter 2 for more details).

As a result, the entries of σ are written as:

$$\sigma_{ij} = \sum_{k=1}^{N} \sum_{l=1}^{N} A_{ijkl} e_{kl},$$

the tensors e and σ are functions with values in the set of symmetric matrices. The balance of forces in the solid and on its charged boundaries gives:

$$\begin{cases} -\operatorname{div} \sigma = f & \text{in } \Omega \\ \sigma n = g & \text{on } \Gamma_N. \end{cases}$$

By adding a Dirichlet condition on the border Γ_D to model a fixed surface of the structure Ω and by expressing the balance of forces using the displacement u, the elasticity problem is summarized as a boundary value problem: find u from Ω into $\mathbb{R}^N$ such that

$$\begin{cases} -\operatorname{div}(Ae(u)) = f & \text{in } \Omega \\ u = 0 & \text{on } \Gamma_D \\ Ae(u)n = g & \text{on } \Gamma_N \\ Ae(u)n = 0 & \text{on } \Gamma. \end{cases} \tag{1.1}$$

Note that the boundary of Ω is defined by

$$\partial\Omega = \Gamma_D \cup \Gamma_N \cup \Gamma,$$

with disjoints subsets Γ_D, Γ_N and Γ. Note also that Γ is called the free boundary since it is where the shape can move without restriction. The variational formulation (or weak form) of the partial derivative problem (1.1) is written:

find $u \in V$ such that, for any $v \in V$,

$$\int_\Omega Ae(u) \cdot e(v)\mathrm{dx} = \int_\Omega fv\mathrm{dx} + \int_{\Gamma_N} gv\mathrm{d}s. \tag{1.2}$$

where V is a real Hilbert space of test functions that is defined by :

$$V = \{v \in (H^1(\Omega))^N \text{ s.t. } v = 0 \text{ on } \Gamma_D\}, \tag{1.3}$$

1.1.2 Existence and uniqueness of solution of the elasticity problem

The linear form and the bilinear form of the variational formulation (1.2) are both continuous. Additionally, for both isotropic and most anisotropic materials the bilinear form is known to be coercive (or elliptic) [23, 109]. Using those two pieces of information, the Lax-Milgram lemma ensures the existence and uniqueness of the solution u.

1.1.3 Objective function and the Lagrangian

This section is devoted to parametric optimization. Therefore, the shape Ω is fixed and not subject to optimization. However, this shape is assumed to be filled with an non homogeneous material, parametrized by a scalar function α defined in the shape Ω. For example it can be a thickness or an angle that orients a laminated composite. The elastic linear tensor of the elasticity problem is now explicitly dependent of the parameter α and we denote it by $A(\alpha)$. Note that u is also implicitly dependent of α as it is the solution of the elasticity problem with Hooke's law $A(\alpha)$. The set of admissible optimization variables is then defined by

$$U_{ad} = \{\alpha \in L^\infty(\Omega)\}. \tag{1.4}$$

As we have stated in this chapter's introduction, in a shape optimization problem, we need to define an objective function. This function is usually an integral of a specific integrand j, a function of the displacement u inside the domain Ω, and/or of another integrand l, function of the displacement u on a border $\Gamma_l \subset \partial\Omega$. In full generality, we have a cost function J that is the sum of the two types of cost functions, i.e. written:

$$J(\alpha) = \int_\Omega j(u)\mathrm{d}x + \int_{\Gamma_l} l(u)\mathrm{d}s, \tag{1.5}$$

We consider an optimization problem, which is a minimization of $J(\alpha)$ over the set U_{ad}:

$$\inf_{\alpha \in U_{ad}} J(\alpha). \tag{1.6}$$

The existence of an optimal design α is dependent on the choice of the admissible set $\mathcal{U}_{ad}$. Shape optimization problems are known to be generally non convex and non compact problems with some exceptions (for example adding some well chosen smoothness constraints to the admissible set could help). Basically, the question of existence of optimal parameter is theoretically involved and we shall not dwell into it (see section 5.2 of [2] for more details). In practice, we are satisfied by determining local minima using numerical methods and by improving the objective function to a certain degree that could respond to a design engineer specifications.

The Lagrangian of problem (1.6) under the constraint of elasticity equation is defined by

$$\mathcal{L}(\alpha, u, q) = \int_\Omega j(u)\mathrm{d}x + \int_{\Gamma_l} l(u)\mathrm{d}s - \int_\Omega (A(\alpha)e(u)\cdot e(q) - fq)\mathrm{d}x + \int_{\Gamma_N} gq\mathrm{d}s, \tag{1.7}$$

where q is the Lagrange multiplier. Note that the constraint is written in a variational form. To find the definition of the adjoint problem, we need to differentiate the Lagrangian with respect to u. Then, the adjoint state p is defined as the solution of the following variational formulation, for any test function or direction of derivation $\beta \in V$ (where V is defined by (1.3)):

$$\left\langle \frac{\partial \mathcal{L}(\alpha, u, p)}{\partial u}, \beta \right\rangle = 0,$$

This gives the following variational formulation: find $p \in V$ such that, $\forall \beta \in V$:

$$\int_\Omega \left(-A(\alpha)e(\beta)\cdot e(p) + \frac{\mathrm{d}j(u)}{\mathrm{d}u}\beta \right) \mathrm{d}x + \int_{\Gamma_l} \frac{\mathrm{d}l(u)}{\mathrm{d}u}\beta \mathrm{d}s = 0. \tag{1.8}$$

The solution p of (1.8) is called the adjoint displacement. Alternatively, the

adjoint problem can be also written as a partial differential equation:

$$\begin{cases} -\operatorname{div}(Ae(p)) = \dfrac{\mathrm{d}j(u)}{\mathrm{d}u} & \text{in } \Omega \\ p = 0 & \text{on } \Gamma_D \\ Ae(p)n = \dfrac{\mathrm{d}l(u)}{\mathrm{d}u} & \text{on } \Gamma_l \\ Ae(p)n = 0 & \text{on } \partial\Omega \setminus (\Gamma_D \cup \Gamma_l). \end{cases} \tag{1.9}$$

1.1.4 Derivation with respect to the optimization parameters

To find local minima for a parametric shape optimization minimization, we usually use the gradient descent method. For this reason, we have to compute the gradient of the objective function $J(\alpha)$, which is done using the following theorem:

Theorem 1.1.1 *The gradient of the cost function $J(\alpha)$ is*

$$J'(\alpha) = -A'(\alpha)e(u) \cdot e(p).$$

If $\alpha \in \mathcal{U}_{ad}$ is a local minimum of J on $\mathcal{U}_{ad}$, then α satisfies the optimality condition,

$$J'(\alpha) = 0.$$

Proof of Theorem 1.1.1

Recall that the set of optimal designs $\mathcal{U}_{ad}$ is unconstrained. To compute the derivative of the objective function $J(\alpha)$, we use the Lagrangian method which resolves on taking the variational formulation of the elasticity problem as a constraint on the optimization problem. The Lagrangian was given by (1.7). In this definition the three variables α, u, q are independent, which makes it easy to compute partial derivatives of the Lagrangian. We assume that $u \equiv u(\alpha)$ is the solution of the elasticity system but $q \in V$ is independent of α. The chain rule for the derivative of the cost function in the direction $\beta \in V$ gives:

$$\begin{aligned}\left\langle \frac{\mathrm{d}J}{\mathrm{d}\alpha}, \beta \right\rangle = \left\langle \frac{\mathrm{d}\mathcal{L}(\alpha, u, q)}{\mathrm{d}\alpha}, \beta \right\rangle &= \left\langle \frac{\partial \mathcal{L}}{\partial \alpha}, \beta \right\rangle + \left\langle \frac{\partial \mathcal{L}}{\partial u} \frac{\mathrm{d}u}{\mathrm{d}\alpha}, \beta \right\rangle \\ &= \left\langle \frac{\partial \mathcal{L}}{\partial \alpha}, \beta \right\rangle + \left\langle \frac{\partial \mathcal{L}}{\partial u}, \frac{\mathrm{d}u}{\mathrm{d}\alpha} \beta \right\rangle .\end{aligned} \tag{1.10}$$

To avoid calculating the derivative of u with respect to the parameter α we need to find q such that $\langle \frac{\partial \mathcal{L}(\alpha,u,q)}{\partial u}, \frac{\mathrm{d}u}{\mathrm{d}\alpha}\beta \rangle = 0$. Thefore we choose $q = p$, where p is the solution of the adjoint problem (1.9). Finally, the partial derivative $\frac{\partial \mathcal{L}}{\partial \alpha}$ is easily computed and is equal to $-A'(\alpha)e(u) \cdot e(p)$, which yields the result.

1.1.4.1 Example: compliance

Let us take the example of compliance minimization. The compliance is the deformation energy of the structure and it is equal to the work of the applied forces. Thus, the specific functions of $J(\Omega)$ becomes written as $j(u) = fu$ and $l(u) = gu$. The surface type border Γ_l is then replaced by Γ_N. The objective function is written:

$$J(\alpha) = \int_\Omega fu\mathrm{dx} + \int_{\Gamma_N} gu\mathrm{d}s, \tag{1.11}$$

and the adjoint problem is written: find $p \in (H^1(\Omega))^N$ such that

$$\begin{cases} -\operatorname{div}(Ae(p)) = f & \text{in } \Omega \\ p = 0 & \text{on } \Gamma_D \\ Ae(p)n = g & \text{on } \Gamma_N \\ Ae(p)n = 0 & \text{on } \Gamma. \end{cases} \tag{1.12}$$

Notice that problem (1.12) is the same problem as the problem of elasticity (1.1). The solution of (1.12) is then:

$$p = u, \tag{1.13}$$

we say that the compliance minimization problem is a self adjoint problem.

1.1.4.2 Example: Target displacement field

A more involved example is the problem of target displacement optimization, where one want the displacement u to be close to a target displacement u_0 on some region of the shape Ω. We suppose the region of the target displacement

to be Γ_N. In this case, we have $j(u) = 0$, and $l(u) = \frac{1}{2}|u - u_0|^2$ on $\Gamma_l = \Gamma_N$. The objective function for this target displacement problem then is written,

$$J(\alpha) = \int_{\Gamma_N} \frac{1}{2}|u - u_0|^2 \mathrm{d}s. \tag{1.14}$$

and the adjoint problem (1.9) becomes: find $p \in (H^1(\Omega))^N$ such that

$$\begin{cases} -\operatorname{div}(Ae(p)) = 0 & \text{in } \Omega \\ p = 0 & \text{on } \Gamma_D \\ Ae(p)n = u - u_0 & \text{on } \Gamma_N \\ Ae(p)n = 0 & \text{on } \Gamma. \end{cases} \tag{1.15}$$

The optimization problem now is a non self-adjoint problem because u is not solution of the problem (1.15). The adjoint problem in this case is written in the following variational form:

Find $p \in V$, such that $\forall v \in V$ (where V is defined by (1.3))

$$\int_\Omega Ae(p) \cdot e(v)\mathrm{dx} = \int_{\Gamma_N} (u - u_0)v\mathrm{d}s, \tag{1.16}$$

which has to be solved numerically whenever one wants to compute $J'(\alpha)$.

1.2 Geometric shape optimization

In this section, we introduce the fundamental elements of geometrical shape optimization. We note that the work of this thesis do not focus on this type of shape optimization. Nevertheless, the theoretical components of this section are essential to understand the last chapter of the thesis.

1.2.1 Model problem

The main idea of geometrical shape optimization is to change the boundary of the initial domain or structure Ω without changing its topology. We study the same problem of elasticity (1.1) for an arbitrary Hooke's law A and under the same boundary conditions. Recall that the solution of elasticity is the displacement vector $u \in (H^1(\Omega))^N$. We suppose that the boundary $\partial\Omega$ of Ω is

partitioned into three disjoints borders

$$\partial\Omega = \Gamma \cup \Gamma_N \cup \Gamma_D,$$

where Γ is the variable part of the boundary, Γ_D is a fixed part of the design boundary on which the displacement is fixed to zero (homogeneous Dirichlet boundary condition), and Γ_N is also a fixed part of the design boundary on which the forces g are applied (Neumann boundary condition). It is assumed that the variable part Γ of the border is free of any effort (homogeneous Neumann boundary condition).

The objective function in this case also becomes a function of Ω and we generally write it as:

$$J(\Omega) = \int_\Omega j(u)\mathrm{dx} + \int_{\Gamma_l} l(u)\mathrm{d}s, \tag{1.17}$$

where $j(u)$ is a body specific objective function and $l(u)$ is a surface specific objective function. The problem of geometrical shape optimization is written as:

$$\inf_{\Omega \in U_{ad}} J(\Omega). \tag{1.18}$$

The material domain Ω is defined inside a fixed set $D \subset \mathbb{R}^N$, with $N = 2$ or 3, which models the design domain. The design domain is represented numerically by a fixed mesh. In geometrical shape optimization, we suppose that we optimize the material domain shape under a target volume constraint $\int_\Omega dx = V_T$, where V_T is a given volume.

The set of admissible shapes is then:

$$\mathcal{U}_{ad} = \left\{ \Omega \subset D \text{ s.t. } \int_\Omega dx = V_T \right\}, \tag{1.19}$$

We note that the set of admissible shapes could be user defined and include other constraints, which can be geometrical or physical. For the compliance minimization problem case, it is mandatory to include the target volume constraint. Without it, the stiffest design would be $\Omega = D$. The existence of an optimal shape is subject to the choice of $\mathcal{U}_{ad}$. For example, if we add a perimeter constraint to the problem (1.18), we can show the existence of a global minimum. But generally speaking, existence of optimal solution for

most of the applications of shape optimization cannot be proved (see section 5.3 of [2]). That is why we content ourself with local optima obtained using a gradient method.

1.2.2 Derivation with respect to the shape

Numerical algorithms of geometrical shape optimization use gradient methods such as the gradient descent method and the Newton method to obtain a local minimum for a certain cost function. For this purpose, one has to compute a shape derivative which is a derivative with respect to the domain. If $\Omega_0 \subset \mathbb{R}^N$ is an given bounded, Lipschitz open domain, we define its deformation by a field θ as

$$\Omega_\theta = (Id + \theta)(\Omega_0),$$

where Id is the identity mapping and $\theta \in W^{1,\infty}\left(\mathbb{R}^N, \mathbb{R}^N\right)$ the variation mapping, where the Sobolev space $W^{1,\infty}\left(\mathbb{R}^N, \mathbb{R}^N\right)$ is defined by

$$W^{1,\infty}\left(\mathbb{R}^N, \mathbb{R}^N\right) = \left\{\theta \in L^\infty\left(\mathbb{R}^N\right)^N, \quad \nabla\theta \in L^\infty\left(\mathbb{R}^N\right)^{N\times N}\right\}.$$

We note that when $\|\theta\|_{W^{1,\infty}(\mathbb{R}^N,\mathbb{R}^N)}$ is sufficiently small, the mapping $Id + \theta$ is a diffeomorphism in $\mathbb{R}^N$. We can now introduce the definition of the shape derivative of a function $J(\Omega)$.

Definition 2 *The shape derivative of $J(\Omega)$ at Ω is defined as the Fréchet derivative in $W^{1,\infty}\left(\mathbb{R}^N, \mathbb{R}^N\right)$ evaluated at 0 for the mapping $\theta \mapsto J((Id + \theta)(\Omega))$ i.e.,*

$$J((Id + \theta)(\Omega)) = J(\Omega) + J'(\Omega)(\theta) + o(\theta) \quad \text{with} \quad \lim_{\theta\to 0} \frac{o(\theta)}{\|\theta\|_{W^{1,\infty}}} = 0,$$

where $J'(\Omega)$ is a continuous linear form on $W^{1,\infty}\left(\mathbb{R}^N, \mathbb{R}^N\right)$.

The expression of the shape derivative for the different possible cases of the integral in a cost function $J(\Omega)$ is obtained by the following lemma.

Lemma 1 *Let Ω be a smooth bounded open set and $j, l, l_F \in W^{2,1}(\mathbb{R}^N)$. Define*

$J_1(\Omega), J_2(\Omega)$ and $J_3(\Omega)$ by:

$$J_1(\Omega) = \int_\Omega j(x)dx, \quad J_2(\Omega) = \int_\Gamma l(x)ds,$$
$$J_2(\Omega) = \int_{\Gamma_F} l_F(x)ds, \quad \text{s.t.} \quad \Gamma \text{ is varying and } \Gamma_F \text{ is fixed,}$$

then the functions $J_1(\Omega), J_2(\Omega)$ and $J_3(\Omega)$ are differentiable at Ω in the direction $\theta \in W^{1,\infty}\left(\mathbb{R}^N, \mathbb{R}^N\right)$ with the derivative

$$J_1'(\Omega)(\theta) = \int_\Gamma \theta n j ds, \quad J_2'(\Omega)(\theta) = \int_\Gamma \theta n \left(\frac{\partial l}{\partial n} + Hl\right) ds, \quad J_3'(\Omega)(\theta) = 0,$$

where H is the mean curvature of $\partial\Omega$ (assumed to be smooth).

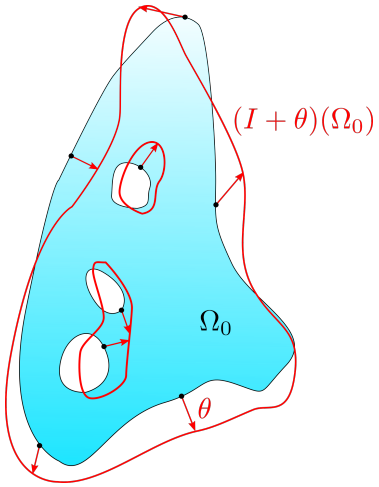

Figure 1.1: Variation of the shape of an initial domain Ω_0

In this thesis, we always do not allow Γ_l of (1.17) to move during the optimization. Thus, the expression of the shape derivative of (1.17) will always be expressed as

$$J'(\Omega)(\theta) = \int_{\partial\Omega} j(\Omega)\theta n dx,$$

which means that, for a shape variation $Id + \theta$, $J(\Omega)$ is only sensitive to the perturbations that are normal to the shape boundary. Note also that when we set the direction of variation θ to $-tj(\Omega)n$, where $t \in \mathbb{R}^+$ is a variation step. We have

$$J((Id+\theta)(\Omega)) = J(\Omega) - t\int_{\partial\Omega} j(\Omega)^2 ds + \mathcal{O}\left(t^2\right),$$

where it is clear that, for a small step t, we have $J((Id+\theta)(\Omega)) \leq J(\Omega)$. Consequently, we chose $\theta = -tj(\Omega)n$ as a descent direction and we update the

shape Ω iteratively with a gradient descent approach until the convergence to a local minimum of the cost function .

1.2.3 Shape gradient in linear elasticity

To obtain the shape gradient with the linear elasticity model (1.1), we use the same approach that we used for parametric optimization. We write the Lagrangian equation of problem (1.6) under the constraint of elasticity, which is the sum of objective function and variational form of the elasticity equations multiplied by a Lagrange multiplier q. In the context of geometrical shape optimization, this approach is known as the Céa's method. The Lagrangian in this case is written:

$$\mathcal{L}(\Omega, u, q) = \int_\Omega j(u)\mathrm{dx} + \int_{\Gamma_l} l(u)\mathrm{d}s - \int_\Omega (A_\Omega e(u)\cdot e(q) - fq)\mathrm{d}x + \int_{\Gamma_N} gq\mathrm{d}s. \quad (1.20)$$

As usual, the adjoint solution p is defined as the precise value of the function q which cancels the partial derivative with respect to the state u of the Lagrangian. This means that $p \in (H^1(\Omega))^N$ satisfies the following optimality condition:

$$\left\langle \frac{\partial \mathcal{L}(\Omega, u, p)}{\partial u}, \beta \right\rangle = 0,$$

for any test function or direction of derivation $\beta \in V$ (where V is defined by (1.3)). In other words, p satisfies the following adjoint problem:

$$\begin{cases} -\operatorname{div}(Ae(p)) = \dfrac{\mathrm{d}j(u)}{\mathrm{d}u} & \text{in } \Omega \\ p = 0 & \text{on } \Gamma_D \\ Ae(p)n = \dfrac{\mathrm{d}l(u)}{\mathrm{d}u} & \text{on } \Gamma_l \\ Ae(p)n = 0 & \text{on } \partial\Omega \setminus (\Gamma_D \cup \Gamma_l). \end{cases}$$

Finally, the shape gradient is given by the following theorem.

Theorem 1.2.1 *Let $\Omega \subset \mathbb{R}^N$ be a smooth bounded open set. Let $f \in \left(H^1\left(\mathbb{R}^N\right)\right)^N, g \in \left(H^2\left(\mathbb{R}^N\right)\right)^N$ and $u(\Omega) \in V$ be the solution to*

(1.1) *Then the shape derivative of* $J(\Omega)$ *along* $\theta \in W^{1,\infty}\left(\mathbb{R}^N, \mathbb{R}^N\right)$ *is given by:*

$$J'(\Omega)(\theta) = \int_\Gamma \theta n \left(j(u) - Ae(u) \cdot e(p) + fp\right) ds,$$

where $p(\Omega) \in V$ *is the solution to the adjoint problem.*

Proof of Theorem 1.2.1
The Lagrangian of $J(\Omega)$ is given in (1.20) where q is an arbitrary function of V, which makes it independent of Ω. The chain rule derivative of the cost function in a direction θ writes

$$J'(\Omega)(\theta) = \mathcal{L}'(\Omega)(\theta) = \frac{\partial \mathcal{L}}{\partial \Omega}(\theta) + \left\langle \frac{\partial \mathcal{L}}{\partial u}, u'(\Omega)(\theta) \right\rangle,$$

where $\dfrac{\partial \mathcal{L}}{\partial \Omega}(\theta)$ denotes the partial shape derivative of the Lagrangian that we obtain by deriving $\mathcal{L}$ with respect to Ω while supposing that all the other variables are fixed. To avoid calculating the derivative of u with respect to the shape, we need to find q such that $\langle \frac{\partial \mathcal{L}(\Omega,u,q)}{\partial u}, u'(\Omega)(\theta)\rangle = 0$. We choose $q = p$, which naturally satisfies the later optimality condition.

In the same spirit, when a volume constraint of the type $\lambda\left(\int_\Omega dx - V_T\right)$ is added to the Lagrangian, its the shape derivative becomes:

$$\mathcal{L}'(\Omega)(\theta) = \int_\Gamma \theta n(j(u) - Ae(u) \cdot e(p) + fp + \lambda)\mathrm{ds}. \tag{1.21}$$

1.3 Topology optimization with the level set method

Now that we have set the theoretical framework of geometrical shape optimization, we introduce the level set topology optimization method [12, 13, 7, 15, 11, 6] and we present its essential numerical elements.

The level set function

The level-set representation, introduced by Osher and Sethian [90, 79, 74, 80, 81, 78, 111, 94, 93, 92, 25, 60], consists of defining a continuous function $\phi : D \to \mathbb{R}$ that takes the zero value on the boundary $\partial\Omega$ of a shape Ω, negative

values inside Ω, and positive outside. We define the level set function for shape and topology optimization by:

$$\begin{cases} \phi(x) < 0 \text{ if } x \in \Omega \\ \phi(x) = 0 \text{ if } x \in \partial\Omega \\ \phi(x) > 0 \text{ if } x \in D \backslash \bar{\Omega}. \end{cases}$$

The level set function purpose is to map Ω with a function that is numerically easy to manipulate. The advantage of having the negative values of ϕ inside the material is that the geometrical gradient of ϕ on $\partial\Omega$ directly gives the direction of the normal vector n which is needed in the computation of the shape derivative.

Transport of a level set function

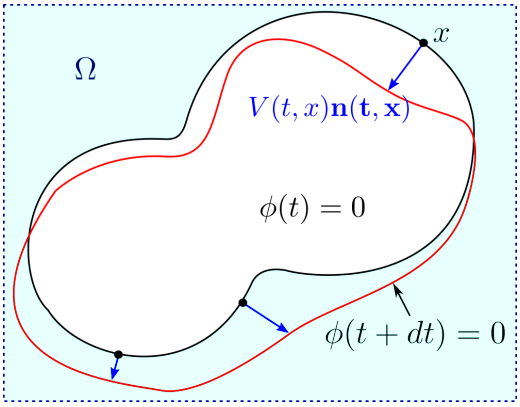

Figure 1.2: Level set function convection

To vary the boundary of the shape, we convect the level set function using the following transport equation:

$$\begin{cases} \dfrac{\partial \phi}{\partial t}(t,x) + \mathcal{V}(x)\nabla\phi(t,x) = 0 & \text{on } (0,T) \times D, \\ \phi(0,x) = \phi_0(x) & \text{on } D. \end{cases} \tag{1.22}$$

where ϕ_0 is the level set associated to the initial shape Ω_0, $\mathcal{V}$ the local velocity vector of the convection of the level set, which is normal to the level set outer surface, and $t \in \mathbb{R}$ is the instant where the level set become $\phi(t)$. When $t = T \in \mathbb{R}$ we obtain the final shape.

When the velocity vector is parallel to the normal, meaning

$$\mathcal{V} = \mathcal{V}_{\mathcal{N}} n,$$

with a scalar normal velocity $\mathcal{V}_{\mathcal{N}}$, the transport equation (1.22) becomes a Hamilton Jacobi equation

$$\begin{cases} \dfrac{\partial \phi}{\partial t}(t,x) + \mathcal{V}_{\mathcal{N}}(x)|\nabla \phi(t,x)| = 0 & \text{on } (0,T)\times D, \\ \phi(0,x) = \phi_0(x) & \text{on } D, \end{cases}$$

Finally, we choose $\mathcal{V}_{\mathcal{N}} = -(j(u) - A_\Omega e(u)\cdot e(p) + fp + \lambda)$ to convect the shape in the direction of the gradient descent.

1.3.1 Regularization of the shape derivative

Regularizing the shape derivative is important to avoid abrupt variations on the shape boundary and topology that could lead to numerical instabilities. This procedure is assured by projecting the shape gradient from the space $L^2(\Gamma)$ with the inner product $\int_\Gamma uv \, \mathrm{d}x$, into the space $H^1(\Omega)$ with the inner product $a(u,v) = \int_\Omega \nabla u \nabla v \, \mathrm{d}s + \int_\Omega uv \, \mathrm{d}s$. This is achieved by solving the following variational formulation: find $j'_r \in H^1(\Omega)$ such that

$$\int_\Omega \left(r^2 \nabla j'_r(\Omega) \nabla \varphi + j'_r(\Omega)\varphi \right) dx = \int_\Gamma j'(\Omega)\varphi ds \quad \forall \varphi \in H^1(\Omega), \tag{1.23}$$

where j'_r is the new regularized gradient. The regularization parameter r is homogeneous to a length-scale that indicates how far from the boundary $\partial\Omega$ the regularized gradient is acting. [39]

Signed distance function

From a practical standpoint, we want ϕ to be not too steep to avoid inaccuracies in the location of ϕ, but also not too flat to avoid instabilities that results because of the division by zero in the evaluation of the normal vector. A good method is to periodically restore ϕ to the signed distance function d_Ω, which is defined as:

$$\forall x \in \mathbb{R}^N, d_\Omega(x) = \begin{cases} -d(x,\partial\Omega) & \text{if } x \in \Omega, \\ 0 & \text{if } x \in \partial\Omega, \\ d(x,\partial\Omega) & \text{if } x \in \mathbb{R}^d \backslash \bar{\Omega}. \end{cases}$$

where $d(x, \partial\Omega) = \min_{p\in\partial\Omega} |x - p|$ is the Euclidean distance from a point $x \in D$ to the shape boundary $\partial\Omega$. Notice that when we apply the signed distance function, ϕ satisfies $|\nabla\phi(x)| = 1$ on the boundary $\partial\Omega$.

Ersatz material approximation

The ersatz material approximation consists of modeling the void in the design domain D by a very soft material. This is obtained by multiplying the stiffness tensor in the void $D\backslash\Omega$ by a small parameter ε:

$$\forall x \in D, A_\Omega(x) = \begin{cases} A & \text{if } x \in \Omega \\ \varepsilon A & \text{if } x \in D\backslash\Omega. \end{cases}$$

Note that the displacement u will depend on ε in this case. The value of ε is typically chosen to be around 10^{-3}.

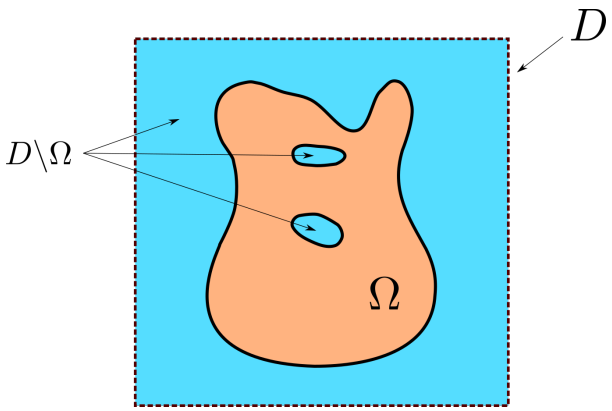

Figure 1.3: A domain D composed by the material of the shape Ω and an ersatz material in $D\backslash\Omega$.

1.3.2 Adding a constraint to topology optimization

In most cases of topology optimization problems and as with the case of geometrical shape optimization, we optimize the structure Ω under a volume constraint $\int_\Omega dx = V_T$, where the constant input value V_T represents the target volume. The optimization problem is then also (1.18) with the same set of admissible shapes (1.19). In the following, we explain the methods that generally one could use to take into account the volume constraint, which are the method of optimality criterion and the method of augmented Lagrangian. Note that these methods can be used to take into account constraints on any

other variables than the volume.

Classic Lagrangian method for the shape constraint

The constrained optimization using a classic Lagrangian method [16, 18] consists of defining a Lagrangian function $\mathcal{L}_c(\Omega, \lambda)$ as the sum of the objective function $J(\Omega)$ and the constraint function $C(\Omega) = \int_\Omega dx - V_T$ multiplied by a Lagrange multiplier $\lambda > 0$:

$$\mathcal{L}_c(\Omega, \lambda) = J(\Omega) + \lambda C(\Omega).$$

When λ is zero, the Lagrangian do not contain the constraint $C(\Omega)$. To make sure that is $C(\Omega)$ is taken into account we have to find λ that maximizes $\mathcal{L}_c(\Omega, \lambda)$. The minimization problem (1.18) is then replaced by the following min-max or saddle point problem:

$$\min_{\Omega \in \mathcal{U}_{\text{ad}_0}} \max_{\lambda \in \mathbb{R}} \mathcal{L}_c(\Omega, \lambda),$$

where:

$$\mathcal{U}_{ad_0} = \{\Omega \subset D\}.$$

Practically, we update the value of λ^n at each iteration $n \in \mathbb{N}$ in the direction that maximizes the Lagrangian $\mathcal{L}_c(\Omega, \lambda)$ using:

$$\lambda^{n+1} = \lambda^n + t_\lambda C(\Omega),$$

where $t_\lambda > 0$ is a gradient ascending step of the update of λ^n. Note that the Lagrange multiplier is increased if the current volume of the structure is greater than the targeted volume and is decreased otherwise. Regardless of this, this could lead to oscillations of the volume. Thus, we relax it with the value of the Lagrange multiplier computed by assuming that the optimality condition $\frac{\partial \mathcal{L}_c(\Omega,\lambda)}{\partial \Omega} = 0$ is satisfied, the optimality condition is written as:

$$J'(\Omega) + \lambda C'(\Omega) = 0,$$

which gives that:

$$\lambda = -\frac{\int_{\partial\Omega} j(\Omega) ds}{\int_{\partial\Omega} ds}.$$

Finally, the Lagrange multiplier is updated at each iteration by

$$\lambda^{n+1} = (\lambda^n + \lambda)/2 + t_\lambda C(\Omega) \tag{1.24}$$

This simple method of optimization of constraints works correctly. However, it shows a rather slow and oscillatory convergence of the Lagrange multiplier λ (equivalently the satisfaction of the constraints). This make this method limited to examples that are featuring only one or a few constraints.

Augmented Lagrangian method

The idea of the augmented Lagrangian consists of adding a quadratic penalty term on $C(\Omega)$ to the Lagrangian $\mathcal{L}_c(\Omega, \lambda)$. This changes the constrained problem into a sequence of unconstrained problems featuring two parameters $\lambda \in \mathbb{R}$ and $b \geq 0$:

$$\min_{\Omega \in \mathcal{U}_{\text{ad}}} \mathcal{L}_{al}(\Omega, \lambda^n, b^n), \text{ where } \mathcal{L}_{al}(\Omega, \lambda, b) := J(\Omega) + \lambda C(\Omega) + \frac{b}{2} C(\Omega)^2. \tag{1.25}$$

The augmented Lagrangian algorithm proceeds by alternating the resolution of (1.25) for fixed values of the parameters λ^n and b^n, and the update of the latter according to the rule, for some $\alpha_{al} > 1$:

$$\lambda^{n+1} = \lambda^n + b^n C(\Omega^n), \text{ and } b^{n+1} = \begin{cases} \alpha_{al} b^n & \text{if } b^n < b_{\text{target}}, \\ b^n & \text{otherwise} \end{cases} \tag{1.26}$$

The value of λ^n is updated at each iteration $n \in \mathbb{N}$ in the direction that maximizes the Lagrangian $\mathcal{L}_{al}(\Omega, \lambda, b)$ while the constraint is gradually enforced, more and more strictly by increasing the value of b^n, until b^n reaches a target value b_{target}. We stop increasing the value of b^n when b_{target} is reached to get a smooth convergence of λ^n at the end.

The advantage of the augmented Lagrangian is that it is faster than the optimality classic Lagrangian method which make it a better option to handle

multiple industrial constraints. Another advantage is that it can be modified easily to handle inequality constraints ([18, 76] also see section 4.4). The main drawbacks of the augmented Lagrangian is that it is difficult to tune correctly its parameters (λ^0, b^0 and α_{al}^0), which are very case-dependent. The objective and constraint functions usually have a lot of oscillations before convergence to their final values. The augmented Lagrangian constrained shape optimization algorithm is described in the following algorithm:

Algorithm 1: Constrained shape optimization augmented Lagrangian algorithm [18]

1 Initialization: Initialize shape Ω^0 and the values of the parameters λ^0, b^0.
2 **for** $n = 1, ...,$ *until convergence* **do**
3 | Find a descent direction θ^n for $\Omega \mapsto \mathcal{L}(\Omega, \lambda^n, b^n)$.
4 | Obtain the new shape $\Omega^{n+1} := (\mathrm{Id} + t^n\theta^n)$, where $t^n > 0$ is chosen sufficiently small so that $\mathcal{L}(\Omega^{n+1}, \lambda^n, b^n) < \mathcal{L}(\Omega^n, \lambda^n, b^n)$.
5 | Compute the new parameters λ^{n+1}, b^{n+1} using (1.26).
6 **end**

1.3.3 Topology optimization algorithm

Eventually, the algorithm of topology optimization with the level set method is summarized in the algorithm 2. We start by fixing an initial shape Ω_0 and initializing a level set function for Ω_0. A value for the target volume is chosen. Recall that the initial shape needs to have some holes in it if one is considering optimizing the topology (holes or porosities in a case of a 3D problem). We then perform the optimization loop (from step 3 to 14) until the convergence of the objective function. The result of the algorithm is a structure Ω that has an optimal shape or topology. In general, and from a practical point of view, the holes of the initialized shape are preferred to be small as this allows the initial shape to converge to a broader range of topology options but not too small to avoid falling into intermediate minima. As with a bigger number of holes, the number of intermediate minima is multiplied. Also, the initial volume value of the shape Ω should not be very distant from the target volume V_t to avoid aggressive descent of the Lagrangian function, as this could lead to the volume of the shape converging further from the targeted volume. Another thing that one can do during the optimization from time to time to speed up the optimization process is to eliminate the regions that are disconnected entirely from the shape, as those regions can lead to significant errors in the structure shape volume during the optimization. The topology optimization

algorithms that we use in this work are written in `FreeFem++` [17] for its high computational speed but it is also possible to use any other partial differential equations solving language as `Matlab` or `FEniCSx`. The convection of the level set function is executed using the library `advect` [31], a library that solves the linear transport equation (1.22) by the unconditionally stable method of characteristics. Note that the level-set has to be a $\mathbb{P}^1$ function to use `advect`. In the other hand, The redistancing of level set function is preformed using the library `mshdist` [38].

Algorithm 2: Topology optimization algorithm for elasticity

Initialization: Initialize the level set function ϕ_0 and deduce the shape Ω_0.
for $n = 0, ...,$ *until convergence* **do**
  Compute the displacement u_n by solving the elasticity problem and the adjoint displacement p_n (if needed) using the adjoint problem, for the shape Ω_n
  Compute the shape derivative $\theta \mapsto J'(\Omega_n)(\theta)$.
  Deduce a descent direction $\mathcal{V}_{\Omega_n}$ for J from Ω_n, i.e. a vector field $\mathcal{V}_{\Omega_n} : \mathbb{R}^d \to \mathbb{R}^d$ such that $J'(\Omega_n)(\mathcal{V}_{\Omega_n}) < 0$.
  Regularize the descent direction $\mathcal{V}_{\Omega_n}$ by solving the regularization problem (1.23).
  Advect the level set function with the velocity $\mathcal{V}_{\mathcal{N},\Omega_n} t_n$ to obtain ϕ_{n+1} using the Hamilton-Jacobi equation, where $t^n > 0$ is a small descent step.
  Redistance the level set function ϕ_{n+1}.
  Deduce the updated shape Ω_{n+1} from ϕ_{n+1}
  if $J(\Omega_{n+1}) < J(\Omega_n)$ **then**
    continue to the next iteration
  else
    reduce the step t_n then get back to step 3.
  end
end

1.3.4 Industrial applications with the level set topology optimization method

Apart from compliance shape optimization of elastic materials, the level-set method has a broad range of applications [73] that are important for industrial

purposes, such as the optimization of shape and topology for material damage and fracture [14, 41], plasticity [42], constraints of mechanical linkages [86], multi-material domains [103, 104, 5], structures with random uncertainties [4], compliant mechanisms [68, 58], electric motors [47], stress minimization [10, 21, 22], vibration and multiple loads structural optimization [9], architectural designs [37], robust designs [40], additive manufacturing technologies (topology and trajectory of laser, topology of design and coupled with the building supports [30]).
The level-set method also provides a wide range of physical applications, such as fluid mechanics [34, 112, 44], thermic [44], thermoelasticity [30], magnetostatics [20], flexoelectricity [51], and multiphysics [45, 44].

Chapter 2

Mechanical problem and model

2.1 Additive manufacturing

Additive manufacturing [52, 46, 106, 55, 57, 43] (or AM) is a contemporary method of manufacturing that allows obtaining industrial parts by adding material layer by layer and/or fiber by fiber. This manufacturing method is an essential part of what is known as the industrial revolution 4.0 and it made possible to manufacture a geometric part directly from a computer-aided design (a virtual design obtained through the use of a computing machine, abbreviated CAD) in an automated process without caring about the manufacturing limitations as the different positioning and the setups for the manufactured part for the machining operations and the subtractive manufacturing tools positions. This is different from classical subtractive manufacturing methods such as milling and turning (or machining), where one removes material from a raw material block to obtain the desired geometry.
The AM method was first used for prototyping, which is why it is also called rapid prototyping, as it could not produce quality material and geometrical characteristics. Nevertheless, AM technologies have evolved nowadays. Moreover, the materials, accuracy, and overall output quality have improved. AM became capable of producing high-edge industrial designs and gained popularity by the name of 3D printing. AM includes a wide range of materials such as polymers, metals, ceramic, concrete and glass. The advantages of AM over conventional manufacturing are numerous. It allows to build rather complex geometries that were not possible in conventional manufacturing. Undercuts and draft angles are not limited by the dimensions of the tools. Freeform surfaces became possible. Lattice structures and porous regions

of the part also became possible to manufacture. Multipart mechanisms could be built in the same time. The overall design-to-manufacturing time and number of steps are reduced because of the elimination of the process planning where one has to make a detailed analysis to determine the classical conventional manufacturing operations, their operations orders, tools, and fixtures, particularly when the parts have more complex geometries. Other advantages of AM are that the process is fully automatic and that it gives the ability to make changes to the design without changing the manufacturing time. Finally, and very importantly, AM is a better ecological alternative because it reduces conventional manufacturing wastes (chips, molds...). In contrast, the disadvantages of AM are porosities that are formed within the material and during the process and the generated anisotropic characteristics. Those minor defects can be eliminated by applying a hip treatment in the case of metallic design.

AM technologies for metals and polymers

For metallic design, technologies of additive manufacturing include powder bed fusion (electron beam melting, selective laser melting...), direct energy deposition and material jetting. For polymers design, fused material deposition and vat polymerization.

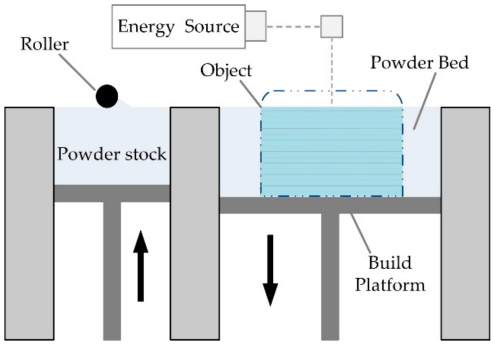

Figure 2.1: Powder bed fusion AM (figure from [24])

SLM additive manufacturing

Selective laser melting [108, 107, 101, 62, 98] (also called SLM) is an additive manufacturing powder bed fusion technology that consists of selectively melting and fusing metal powders using a high-power-density laser as a heat energy source to build a metallic part layer by layer. This technology started developing in the late 1990s. Today, it is capable of producing net-shape parts up to 99.9% relative density and of processing a wide range of metallic materials, such as copper, aluminum, and tungsten, thanks to the recent

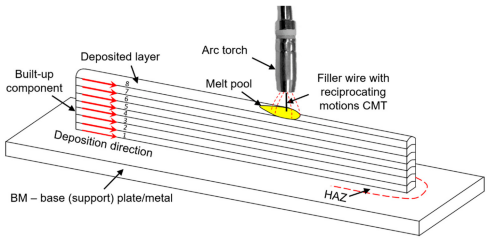

Figure 2.2: Direct energy deposition AM (figure from [66])

developments of fiber optics and high-power lasers. The steps of building a metallic geometry from a CAD file using SLM are seamless and automatic. First, a STEP file (a file format that represents the part and that is obtained from a CAD software) is converted to an STL file (STereoLithography), this STL file is processed by a commercial software or an optimization algorithm to create support structures for any overhanging regions and to prepare slice layouts for all the layers and the laser scanning paths of each layer. Then, the building process is conducted inside a machine building chamber that is filled with an inert gas (nitrogen or argon) to protect the heated metal against oxidation. The AM machine lays a thin layer of metal powder on a substrate plate. Then a high energy density laser start scanning the powder to form the first solid layer of the part by melting and fusing selected areas according to the processed layer data. Once the laser scanning is completed, the building platform is lowered and another metallic layer is built on top by repeating the previous layer steps. This whole process of laying powder, laser scanning and platform lowering is repeated successively until the wanted part is completely built. Once the metallic part is built, the loose powders that are inside the machine chamber are removed, and the built part is separated from the substrate plate and from the supporting structures.

Anisotropy in AM

Parts that are built with an additive manufacturing technology, without the addition of post-processing treatment, are observed to have a locally anisotropic physical behavior (mechanical, thermal...), precisely an orthotropic type of anisotropy. The resulted orthotropic anisotropy of the parts is usually a sum of various orthotropic anisotropy. First, an orthotropic elastic and resistance to fatigue anisotropy that is caused by the layering (see figure 2.3) direction (in plane behavior different to normal to plan behavior) and by the laser scanning path (parallel to fibers behavior is different to transversal to fibers behavior). This anisotropy type is stronger in the case of polymer materials AM. And second, a transverse isotropic elastic and plastic anisotropy

that is caused by the columnar grains formations caused by the heat gradient (see figure 2.4). This anisotropy type is stronger in metallic materials.

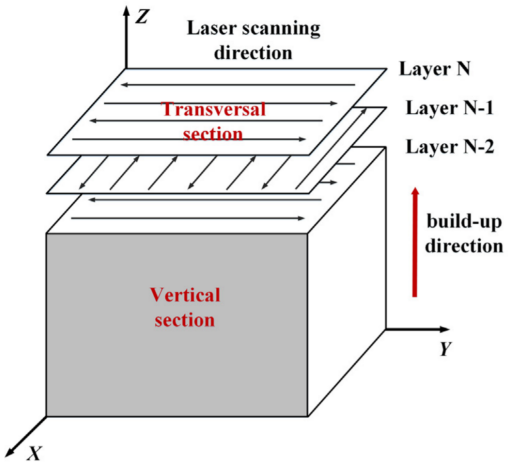

Figure 2.3: Layering and laser scanning in SLM (figure from [35])

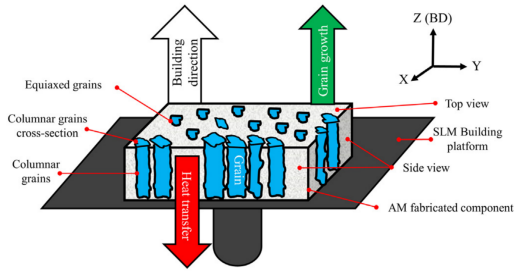

Figure 2.4: Columnar grains formation in SLM (figure from [87])

2.2 Elastic anisotropy

2.2.1 Hooke's law for anisotropic bodies

Consider a structure Ω composed by a linearly elastic anisotropic material [100] with the Hooke's tensor A; the model that we study is the same as the model (1.1) with the same general boundary conditions.

The Kelvin formalism [63, 69] consist of writing the stress and strain tensors as vectors, in 3D they are written as:

$$\{\sigma\} = \left\{ \begin{array}{l} \sigma_1 = \sigma_{11} \\ \sigma_2 = \sigma_{22} \\ \sigma_3 = \sigma_{33} \\ \sigma_4 = \sqrt{2}\sigma_{23} \\ \sigma_5 = \sqrt{2}\sigma_{31} \\ \sigma_5 = \sqrt{2}\sigma_{12} \end{array} \right\}, \quad \{e\} = \left\{ \begin{array}{l} e_1 = e_{11} \\ e_2 = e_{22} \\ e_3 = e_{33} \\ e_4 = \sqrt{2}e_{23} \\ e_5 = \sqrt{2}e_{31} \\ e_6 = \sqrt{2}e_{12} \end{array} \right\}.$$

Where the index notation of i in σ_i and e_i is well known as the Voigt notation [102] ($11 \to 1, 22 \to 2, 33 \to 3, 23 \to 4, 31 \to 5, 12 \to 6$). Which results in a simpler and a rather efficient manipulation of the elasticity tensor. Note that we add the cases $\{\cdot\}$ to differentiate the Kelvin vectorial notation of the stress and strain from their tensorial notations. The Hooke's law of elasticity is expressed then with Kelvin formalism as follows:

$$\left\{ \begin{array}{c} \sigma_1 \\ \sigma_2 \\ \sigma_3 \\ \sigma_4 \\ \sigma_5 \\ \sigma_6 \end{array} \right\} = \left[\begin{array}{cccccc} A_{11} & A_{12} & A_{13} & \sqrt{2}A_{14} & \sqrt{2}A_{15} & \sqrt{2}A_{16} \\ A_{12} & A_{22} & A_{23} & \sqrt{2}A_{24} & \sqrt{2}A_{25} & \sqrt{2}A_{26} \\ A_{13} & A_{23} & A_{33} & \sqrt{2}A_{34} & \sqrt{2}A_{35} & \sqrt{2}A_{36} \\ \sqrt{2}A_{14} & \sqrt{2}A_{24} & \sqrt{2}A_{34} & 2A_{44} & 2A_{45} & 2A_{46} \\ \sqrt{2}A_{15} & \sqrt{2}A_{25} & \sqrt{2}A_{35} & 2A_{45} & 2A_{55} & 2A_{56} \\ \sqrt{2}A_{15} & \sqrt{2}A_{26} & \sqrt{2}A_{35} & 2A_{46} & 2A_{56} & 2A_{66} \end{array} \right] \left\{ \begin{array}{c} e_1 \\ e_2 \\ e_3 \\ e_4 \\ e_5 \\ e_6 \end{array} \right\},$$

where A_{ij} are written using Voigt notations; for example A_{16} is the same as A_{1112}.

The Hooke's law is then written:

$$\{\sigma\} = \hat{A}\{e\}.$$

$\hat{A}$ is known as the stiffness constitutive matrix. Kelvin formalism switches the algebra of the elasticity tensor from that of a fourth order tensor to that of a 6×6 square symmetric matrix. The inverse of $\hat{A}$ denoted $\hat{S}$ is known as the compliance constitutive matrix. $\hat{A}$ and $\hat{S}$ are two symmetric definite positive matrices.

in 2D the Kelvin formalism is:

$$\{\sigma\} = \left\{ \begin{array}{l} \sigma_1 = \sigma_{11} \\ \sigma_2 = \sigma_{22} \\ \sigma_6 = \sqrt{2}\sigma_{12} \end{array} \right\}, \quad \{e\} = \left\{ \begin{array}{l} e_1 = e_{11} \\ e_2 = e_{22} \\ e_6 = \sqrt{2}e_{12} \end{array} \right\}.$$

Notice that we have the indexes 1, 2 and 6 as a result of Voigt notation. Hooke's law is then:

$$\begin{Bmatrix} \sigma_1 \\ \sigma_2 \\ \sigma_6 \end{Bmatrix} = \begin{bmatrix} A_{11} & A_{12} & \sqrt{2}A_{16} \\ A_{12} & A_{22} & \sqrt{2}A_{26} \\ \sqrt{2}A_{16} & \sqrt{2}A_{26} & 2A_{66} \end{bmatrix} \begin{Bmatrix} e_1 \\ e_2 \\ e_6 \end{Bmatrix}.$$

2.2.2 Examples of constitutive matrices

2.2.2.1 Orthotropy

A 3D orthotropic material [100] is defined by an orthogonal base, that we denote $e^{x'}e^{y'}e^{z'}$, and by nine constants; three Young's moduli E_1, E_2 and E_3 associated respectively to each direction of the material frame, it have six Poisson's ratios $\nu_{21}, \nu_{31}, \nu_{31}, \nu_{23}, \nu_{31}$ and ν_{12} but is defined by only three considering the relations between the Poission ratios:

$$\frac{\nu_{23}}{E_2} = \frac{\nu_{32}}{E_3}, \quad \frac{\nu_{31}}{E_3} = \frac{\nu_{13}}{E_1} \quad \text{and } \frac{\nu_{12}}{E_1} = \frac{\nu_{21}}{E_2}. \tag{2.1}$$

The material also is defined by three shear moduli G_{12}, G_{13} and G_{23}.

The 3D orthotropic material compliance constitutive matrix [100] is symmetric defined by 9 independent elastic components, it is written in the material base as:

$$\hat{S} = \begin{bmatrix} \frac{1}{E_1} & -\frac{\nu_{21}}{E_2} & -\frac{\nu_{31}}{E_3} & 0 & 0 & 0 \\ -\frac{\nu_{12}}{E_1} & \frac{1}{E_2} & -\frac{\nu_{32}}{E_3} & 0 & 0 & 0 \\ -\frac{\nu_{13}}{E_1} & -\frac{\nu_{23}}{E_2} & \frac{1}{E_3} & 0 & 0 & 0 \\ 0 & 0 & 0 & \frac{1}{2G_{23}} & 0 & 0 \\ 0 & 0 & 0 & 0 & \frac{1}{2G_{31}} & 0 \\ 0 & 0 & 0 & 0 & 0 & \frac{1}{2G_{12}} \end{bmatrix}. \tag{2.2}$$

The stiffness constitutive matrix which is the inverse of $\hat{S}$ is written:

$$\hat{A} = \begin{bmatrix} \frac{1-\nu_{23}\nu_{32}}{E_2E_3\Delta} & \frac{\nu_{21}+\nu_{31}\nu_{23}}{E_2E_3\Delta} & \frac{\nu_{31}+\nu_{21}\nu_{32}}{E_2E_3\Delta} & 0 & 0 & 0 \\ \frac{\nu_{12}+\nu_{13}\nu_{32}}{E_3E_1\Delta} & \frac{1-\nu_{31}\nu_{13}}{E_3E_1\Delta} & \frac{\nu_{32}+\nu_{31}\nu_{12}}{E_3E_1\Delta} & 0 & 0 & 0 \\ \frac{\nu_{13}+\nu_{12}\nu_{23}}{E_1E_2\Delta} & \frac{\nu_{23}+\nu_{13}\nu_{21}}{E_1E_2\Delta} & \frac{1-\nu_{12}\nu_{21}}{E_1E_2\Delta} & 0 & 0 & 0 \\ 0 & 0 & 0 & 2G_{23} & 0 & 0 \\ 0 & 0 & 0 & 0 & 2G_{31} & 0 \\ 0 & 0 & 0 & 0 & 0 & 2G_{12} \end{bmatrix}, \tag{2.3}$$

where

$$\Delta = \frac{1 - \nu_{12}\nu_{21} - \nu_{23}\nu_{32} - \nu_{31}\nu_{13} - 2\nu_{12}\nu_{23}\nu_{31}}{E_1E_2E_3}.$$

2.2.2.2 Transverse isotropy

A transverse isotropic material is a special case of an orthotropic 3D material where two of its base vectors $e^{x'}e^{y'}e^{z'}$ form a plane of isotropy; a plane where the material behavior is the same in all directions that are in the plane, we chose the plane of isotropy $e^{y'}e^{z'}$. The material behaves symmetrically about the base vector $e^{x'}$ which is orthogonal to the plane of isotropy.

A transverse isotropic material is defined by 5 independent constants; two Young's moduli E_1 and E_p, and three Poisson's ratios ν_{1p}, ν_{p1} and ν_p but defined by only two considering the relation between the Poisson's ratios ν_{1p} and ν_{p1}:

$$\frac{\nu_{p1}}{E_p} = \frac{\nu_{1p}}{E_1}. \tag{2.4}$$

The material also is defined by one shear modulus G_{1p}. The transverse isotropic material compliance constitutive matrix then is symmetric defined by 5 independent elastic components, it is written in the material base as:

$$\hat{S} = \begin{bmatrix} \frac{1}{E_1} & -\frac{\nu_{p1}}{E_p} & -\frac{\nu_{p1}}{E_p} & 0 & 0 & 0 \\ -\frac{\nu_{1p}}{E_1} & \frac{1}{E_p} & -\frac{\nu_p}{E_p} & 0 & 0 & 0 \\ -\frac{\nu_{1p}}{E_1} & -\frac{\nu_p}{E_p} & \frac{1}{E_p} & 0 & 0 & 0 \\ 0 & 0 & 0 & \frac{1+\nu_p}{E_p} & 0 & 0 \\ 0 & 0 & 0 & 0 & \frac{1}{2G_{1p}} & 0 \\ 0 & 0 & 0 & 0 & 0 & \frac{1}{2G_{1p}} \end{bmatrix}. \tag{2.5}$$

$\hat{S}$ is obtained from (2.2) by replacing the indexes of the elastic moduli and

ratios 2 and 3 by p due to the fact that E_2 became equivalent to E_3. ν_{23} then became equal to ν_{32} (2.1), which we denote by a single symbol ν_p that plays the role of an isotropic Poisson's ratio in the plane of E_2 and E_3. Finaly, G_{23} is replaced by the isotropic shear modulus $\frac{E_2}{2(1+\upsilon_2)}$ [53].

The stiffness constitutive matrix which is the inverse of $\hat{S}$ is written:

$$\hat{A} = \begin{bmatrix} \frac{1-\nu_p\nu_p}{E_p^2\Delta} & \frac{\nu_{p1}+\nu_{p1}\nu_p}{E_p^2\Delta} & \frac{\nu_{p1}+\nu_{p1}\nu_p}{E_p^2\Delta} & 0 & 0 & 0 \\ \frac{\nu_{1p}+\nu_{1p}\nu_p}{E_pE_1\Delta} & \frac{1-\nu_{p1}\nu_{1p}}{E_pE_1\Delta} & \frac{\nu_p+\nu_{1p}\nu_{1p}}{E_pE_1\Delta} & 0 & 0 & 0 \\ \frac{\nu_{1p}+\nu_{1p}\nu_p}{E_1E_p\Delta} & \frac{\nu_p+\nu_{1p}\nu_{p1}}{E_1E_p\Delta} & \frac{1-\nu_{1p}\nu_{p1}}{E_1E_p\Delta} & 0 & 0 & 0 \\ 0 & 0 & 0 & \frac{E_p}{1+\nu_p} & 0 & 0 \\ 0 & 0 & 0 & 0 & 2G_{1p} & 0 \\ 0 & 0 & 0 & 0 & 0 & 2G_{1p} \end{bmatrix}, \tag{2.6}$$

where

$$\Delta = \frac{(1+\nu_p)(1-\nu_p-2\nu_{p1}\nu_{1p})}{E_p^2E_1}.$$

2.2.2.3 Isotropy

The isotropic material compliance constitutive matrix is symmetric defined by 2 independent elastic components:

$$\hat{S} = \begin{bmatrix} \frac{1}{E} & -\frac{\nu}{E} & -\frac{\nu}{E} & 0 & 0 & 0 \\ & \frac{1}{E} & -\frac{\nu}{E} & 0 & 0 & 0 \\ & & \frac{1}{E} & 0 & 0 & 0 \\ & & & \frac{1+\nu}{E} & 0 & 0 \\ & sym & & & \frac{1+\nu}{E} & 0 \\ & & & & & \frac{1+\nu}{E} \end{bmatrix}.$$

Note that $\hat{S}$ can be obtained from the orthotropic compliance matrix by replacing all the Young's moduli by one Young's modulus E, all the Poisson's ratios by only one Poisson's ratio ν, and the G_{ij} by the isotropic shear modulus $\frac{E}{2(1+\upsilon)}$ [53].

The stiffness constitutive matrix which is the inverse of $\hat{S}$ is written:

$$\hat{A} = \begin{bmatrix} \frac{(1-\nu)E}{(1-2\nu)(1+\nu)} & \frac{\nu E}{(1-2\nu)(1+\nu)} & \frac{\nu E}{(1-2\nu)(1+\nu)} & 0 & 0 & 0 \\ & \frac{(1-\nu)E}{(1-2\nu)(1+\nu)} & \frac{\nu E}{(1-2\nu)(1+\nu)} & 0 & 0 & 0 \\ & & \frac{(1-\nu)E}{(1-2\nu)(1+\nu)} & 0 & 0 & 0 \\ & & & \frac{E}{1+\nu} & 0 & 0 \\ & & & & \frac{E}{1+\nu} & 0 \\ & sym & & & & \frac{E}{1+\nu} \end{bmatrix}.$$

2.2.2.4 2D orthotropy

A 2D orthotropic material is defined by two Young's moduli; E_1 in the axis of A_{11} and E_{22} in the axis of A_{22}. It has two Poisson's ratios ν_{12} and ν_{21} but is defined by only one considering the relations between the Poisson's ratios:

$$\frac{\nu_{12}}{E_1} = \frac{\nu_{21}}{E_2}.$$

The material also is defined by one shear modulus G_{12}.

A 2D orthotropic material constitutive tensor is symmetric defined by 4 independent elastic constants:

$$\hat{A} = \begin{bmatrix} \frac{E_1}{1-\nu_{12}\nu_{21}} & \frac{\nu_{21}E_1}{1-\nu_{12}\nu_{21}} & 0 \\ \frac{\nu_{12}E_2}{1-\nu_{12}\nu_{21}} & \frac{E_2}{1-\nu_{12}\nu_{21}} & 0 \\ 0 & 0 & 2G_{12} \end{bmatrix} \tag{2.7}$$

2.2.3 Orientation of an anisotropic material model in elasticity

2.2.3.1 Orientation of elastic orthotropy

Euler angles

The local orientation of an orthotropic material in Ω can be described as the orientation of a relative orthogonal right-handed frame $x'y'z'$ with respect to a fixed system of frame xyz. The relative frame $x'y'z'$ is the frame where the anisotropic constitutive matrix $\hat{A}$ is defined. We chose x' to be in the direction of E_1, y' to be in the direction of E_2 and z' consequently in the direction

of E_3. The orientation of material in this case is obtained using consecutive elementary rotations of $x'y'z'$ by three angles α_1, α_2 and α_3 along the axes of the material frame, note that every rotation axis should be different than the one before. Those angles are called the Euler angles, and they are very important in this work as they give the exact orientation of the anisotropic material. We introduce three intermediate frames $x_1y_1z_1$ $x_2y_2z_2$ $x_3y_3z_3$. In our case, we chose to rotate with α_1 about the axis z', leading to the new frame $x_1y_1z_1$, then with α_2 about x_1, leading to the new frame $x_2y_2z_2$ and then with α_3 about z_2 leading to the new frame $x_3y_3z_3$ which is exactly xyz (see figure 4.3). In material science this is called a zxz Euler type rotation.

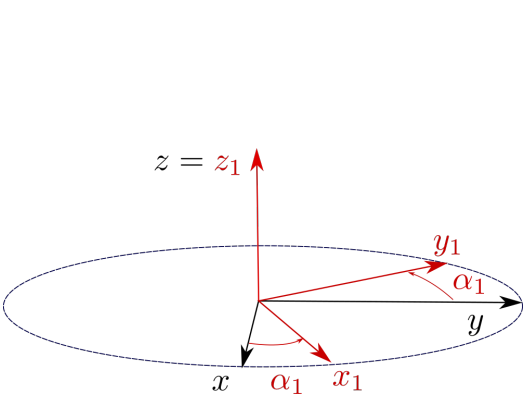

(a) Rotation by the first Euler angle about z'

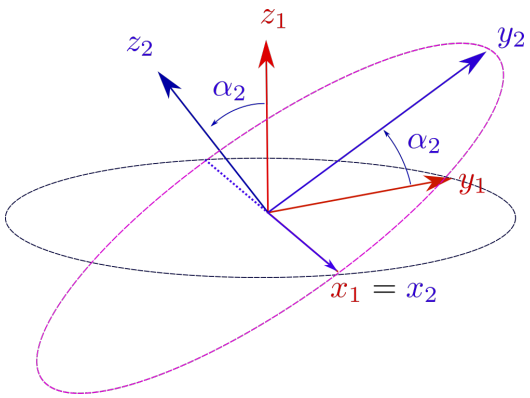

(b) Rotation by the second Euler angle about x_1

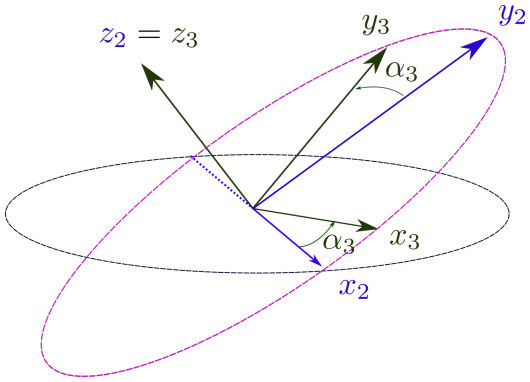

(c) Rotation by the third Euler angle about z_2

Figure 2.5: Rotation of the material frame using Euler angles, $x_3y_3z_3$ is equivalent to $x'y'z'$

Kelvin rotation matrix

We denote with $\hat{A}^*(\alpha_1, \alpha_2, \alpha_3)$ the constitutive stiffness matrix for the rotated anisotropic material (A^* for the associated rotated Hooke's tensor). $\hat{A}^*(\alpha_1, \alpha_2, \alpha_3)$ is expressed in terms of $\hat{A}$ and the three Euler angles by:

$$\hat{A}^*(\alpha_1, \alpha_2, \alpha_3) = R(\alpha_1, \alpha_2, \alpha_3)\hat{A}R^t(\alpha_1, \alpha_2, \alpha_3). \tag{2.8}$$

R is an orthogonal matrix that behaves as a global rotation 6×6 matrix for the Kelvin formalism algebra (see [100] section 2.2.2 page 30). The orthogonality of R is a big advantage of using the Kelvin formalism. R is expressed using the components of the 3D rotation matrix Q as follows [71]:

$$R = \begin{bmatrix} Q_{11}^2 & Q_{12}^2 & Q_{13}^2 & \sqrt{2}Q_{12}Q_{13} & \sqrt{2}Q_{13}Q_{11} & \sqrt{2}Q_{11}Q_{12} \\ Q_{21}^2 & Q_{22}^2 & Q_{23}^2 & \sqrt{2}Q_{22}Q_{23} & \sqrt{2}Q_{23}Q_{21} & \sqrt{2}Q_{21}Q_{22} \\ Q_{31}^2 & Q_{32}^2 & Q_{33}^2 & \sqrt{2}Q_{32}Q_{33} & \sqrt{2}Q_{33}Q_{31} & \sqrt{2}Q_{31}Q_{32} \\ \sqrt{2}Q_{21}Q_{31} & \sqrt{2}Q_{22}Q_{32} & \sqrt{2}Q_{23}Q_{33} & Q_{23}Q_{32} + Q_{22}Q_{33} & Q_{33}Q_{21} + Q_{31}Q_{23} & Q_{31}Q_{22} + Q_{32}Q_{21} \\ \sqrt{2}Q_{31}Q_{11} & \sqrt{2}Q_{32}Q_{12} & \sqrt{2}Q_{33}Q_{13} & Q_{32}Q_{13} + Q_{33}Q_{12} & Q_{31}Q_{13} + Q_{33}Q_{11} & Q_{31}Q_{12} + Q_{32}Q_{11} \\ \sqrt{2}Q_{11}Q_{21} & \sqrt{2}Q_{12}Q_{22} & \sqrt{2}Q_{13}Q_{23} & Q_{12}Q_{23} + Q_{13}Q_{22} & Q_{11}Q_{23} + Q_{13}Q_{21} & Q_{11}Q_{22} + Q_{12}Q_{21} \end{bmatrix}, \tag{2.9}$$

where Q is expressed in terms of the 3 elemental rotations matrices Q_1, Q_2 and Q_3, associated respectively to the angles α_1, α_2 and α_3:

$$Q(\alpha_1, \alpha_2, \alpha_3) = Q_1(\alpha_1)Q_2(\alpha_2)Q_3(\alpha_3).$$

Q_1,Q_2 and Q_3 are given by:

$$Q_1(\alpha_1) = \begin{bmatrix} \cos(\alpha_1) & -\sin(\alpha_1) & 0 \\ \sin(\alpha_1) & \cos(\alpha_1) & 0 \\ 0 & 0 & 1 \end{bmatrix}, \tag{2.10}$$

$$Q_2(\alpha_2) = \begin{bmatrix} 1 & 0 & 0 \\ 0 & \cos(\alpha_2) & -\sin(\alpha_2) \\ 0 & \sin(\alpha_2) & \cos(\alpha_2) \end{bmatrix}, \tag{2.11}$$

$$Q_3(\alpha_3) = \begin{bmatrix} \cos(\alpha_3) & -\sin(\alpha_3) & 0 \\ \sin(\alpha_3) & \cos(\alpha_3) & 0 \\ 0 & 0 & 1 \end{bmatrix}. \tag{2.12}$$

2.2.3.2 Orientation of elastic transverse isotropy

Euler angles

As with the case of orthotropic materials, the local orientation of a transversely isotropic material in Ω can also be described as the orientation of a relative orthogonal right-handed frame $x'y'z'$ with respect to a fixed system of frame of reference xyz. The relative frame $x'y'z'$ is the frame where the anisotropic constitutive matrix $\hat{\mathrm{A}}$ is defined by (2.6). This means, from a mechanical experimental point of view, that if we measure Young's modulus in the direction of x', the value of E_1 is obtained, and if we measure Young's modulus in all the directions that are perpendicular to x' (especially y' and z'), the value of E_p is then obtained. In this case the material orientation is defined using only two Euler angles α_1 and α_2. As a result, we have two intermediate frames $x_1y_1z_1$ and $x_2y_2z_2$. We choose to rotate with α_1 about the axis z', leading to the new frame $x_1y_1z_1$, then with α_2 about y_1, leading to the new frame $x_2y_2z_2$ which is exactly xyz (see figure 2.6). In material science, this is called a zy Euler type rotation.

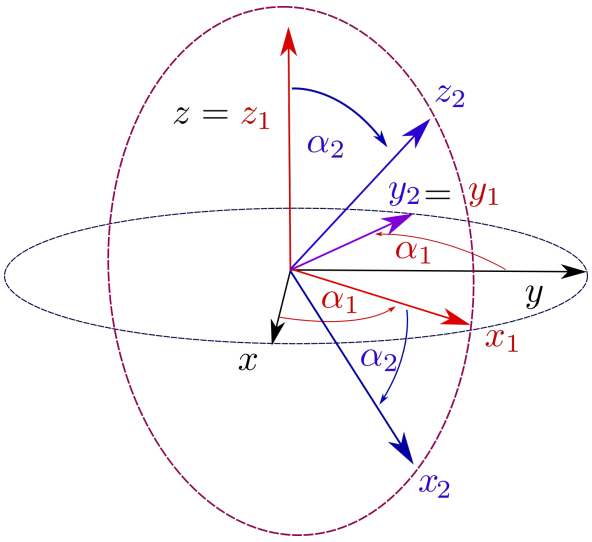

Figure 2.6: Rotation of the transverse isotropic material frame using 2 Euler angles, $x_2y_2z_2$ is equivalent to $x'y'z'$

Kelvin rotation matrix

We denote with $\hat{A}^*(\alpha_1, \alpha_2)$ the constitutive stiffness matrix for the rotated transverse isotropic material (A^* for the associated rotated Hooke's tensor).

$\hat{A}^*(\alpha_1, \alpha_2)$ is expressed in terms of $\hat{A}$ and the two Euler angles by:

$$\hat{A}^*(\alpha_1, \alpha_2) = R(\alpha_1, \alpha_2)\hat{A}R^t(\alpha_1, \alpha_2), \tag{2.13}$$

where R is the Kelvin rotation matrix written as (2.9). Where Q now is expressed in terms of the 2 elementary rotations matrices Q_1 and Q_2, associated respectively to the angles α_1 and α_2:

$$Q(\alpha_1, \alpha_2) = Q_1(\alpha_1)Q_2(\alpha_2),$$

the matrix Q_1 is given by (2.10) and Q_2 by:

$$Q_2(\alpha_2) = \begin{bmatrix} \cos(\alpha_2) & 0 & \sin(\alpha_2) \\ 0 & 1 & 0 \\ -\sin(\alpha_2) & 0 & \cos(\alpha_2) \end{bmatrix}. \tag{2.14}$$

Note that we have an expression of the matrix Q_2 different than the expression in (2.11) because of the fact that we are rotating about a different axis .

2.2.3.3 Orientation of 2D elastic orthotropy

In the case of a 2D orthotropic material, the material orientation is defined by a single angle α (see figure 2.7). The constitutive stiffness matrix that is obtained from the rotated material that is expressed on the frame xyz is denoted $\hat{A}^*(\alpha)$, and written:

$$\hat{A}^*(\alpha) = R(\alpha)\hat{A}R^t(\alpha), \tag{2.15}$$

where R is the Kelvin 2D rotation matrix that is written as in (2.9) (without the use the third, fourth and fifth row and line). While the matrix Q is given by:

$$Q(\alpha) = \begin{bmatrix} \cos(\alpha) & -\sin(\alpha) \\ \sin(\alpha) & \cos(\alpha) \end{bmatrix} \tag{2.16}$$

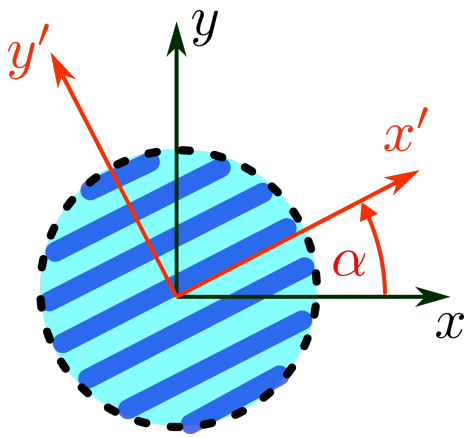

Figure 2.7: Orientation angle α of the orthotropic material axes of a 2D structure

Chapter 3

2D orientation optimization

3.1 Optimal direction using an optimality criterion

We consider a structure in a 2D problem (hypothesis of plane stress or plane strain) with a fixed shape Ω composed by a linearly elastic orthotropic material with the Hooke's law fourth order elasticity tensor $A^*(\alpha)$. Where $\alpha \in \mathbb{R}$ is the angle from an initial frame of reference to a material fixed frame where the orthotropic elasticity Hooke's law is known, fixed and denoted A. A is defined by the following elasticity moduli; two Young's moduli E_1 and E_2, one Poisson's ratio ν_{12} and one shear moduli G_{12}. The relation between A in Kelvin formalism and the elasticity moduli is given by (2.7) We suppose that $E_1 > E_2$. α is defined from the x-axis to the direction where E_1 is physically measured (which is equivalent to the component $\hat{A}_{11}$ of the stiffness constitutive tensor).

The model that we study is the same as (1.1). We want to find the material local anisotropy orientation everywhere in the domain Ω that minimizes the compliance of this structure. The compliance objective function is then written as:

$$J(\alpha) = \int_\Omega f u \,\mathrm{dx} + \int_{\Gamma_N} g u \,\mathrm{ds} = \int_\Omega A^*(\alpha) e(u) \cdot e(u) \,\mathrm{dx}\,.$$

The orientation is modeled by the angle α. Consequently, the set of admissible designs is defined by:

$$\mathcal{U}_{ad} = \left\{ \alpha \in L^2(\Omega) \right\}. \tag{3.1}$$

The problem of optimization is then written as:

$$\inf_{\alpha \in \mathcal{U}_{ad}} J(\alpha) \tag{3.2}$$

Using the theorem of complementary energy (see section 2.22 in [2]) that gives:

$$\begin{aligned} \int_\Omega fu \,\mathrm{dx} + \int_{\Gamma_N} gu \,\mathrm{ds} = \quad & \min_{\sigma \in L^2(\Omega; \mathcal{M}_s)} \int_\Omega (A^*(\alpha))^{-1}\sigma \cdot \sigma \,\mathrm{dx}, \\ & \begin{cases} -\operatorname{div} \sigma = f \text{ in } \Omega \\ \sigma n = g \text{ on } \Gamma_N \\ \sigma n = 0 \text{ on } \partial\Omega \setminus (\Gamma_D \cup \Gamma_N) \end{cases} \end{aligned} \tag{3.3}$$

where σ is a statically admissible stress tensor and $\mathcal{M}_s$ is the space of symmetric matrices. We can rewrite the optimization problem (3.2) as a double minimization

$$\begin{aligned} \inf_{\alpha \in \mathcal{U}_{ad}} \quad & \min_{\sigma \in L^2(\Omega; \mathcal{M}_s)} \int_\Omega (A^*(\alpha))^{-1}\sigma \cdot \sigma \,\mathrm{dx}, \\ & \begin{cases} -\operatorname{div} \sigma = f \text{ in } \Omega \\ \sigma n = g \text{ on } \Gamma_N \\ \sigma n = 0 \text{ on } \partial\Omega \setminus (\Gamma_D \cup \Gamma_N) \end{cases} \end{aligned} \tag{3.4}$$

The order of the two minimizations is unimportant: they can be exchanged or combined in a single minimization on the pair (α, σ) . We write (3.4) in the form:

$$\inf_{\alpha \in \mathcal{U}_{ad}} \min_{\sigma \in H} \int_\Omega (A^*(\alpha))^{-1}\sigma \cdot \sigma \,\mathrm{dx}, \tag{3.5}$$

where H is given by:

$$H = \left\{ \sigma \in L^2(\Omega; \mathcal{M}_s), -\operatorname{div} \sigma = f \text{ in } \Omega, \sigma n = g \text{ on } \Gamma_N, \sigma n = 0 \text{ on } \partial\Omega \setminus (\Gamma_D \cup \Gamma_N) \right\} \tag{3.6}$$

We note that $\mathcal{U}_{ad} \times H$ is a non-empty convex closed set. The interest of (3.5)

is to exchange the two minimizations, which does not change the problem, and to optimize one and then the other.

Remark 1 *Unfortunately, there is no information about the existence of solution of* (3.5)*. However, if we want the existence of a solution, we can choose the set of admissible designs as [2] (see theorem 5.12, page 88):*

$$\mathcal{U}_{ad}^{R} = \left\{ \alpha \in L^2(\Omega),\ s.t.\ ||\alpha||_{H^1(\Omega)} < R \right\}$$

The primary idea of the optimality condition is to exchange the two minimizations in (3.5) to obtain

$$\inf_{\sigma \in H} \quad \min_{\alpha \in \mathcal{U}_{ad}} \quad \int_{\Omega} (A^*(\alpha))^{-1} \sigma \cdot \sigma \, \mathrm{dx}, \tag{3.7}$$

It turns out that at fixed σ, it is easy to perform the minimization in α in $\mathcal{U}_{ad}$.

Consequently, we have found optimality conditions for the optimization problem (3.2) which are:

1. if we know the optimal σ, then an optimal α is given by solving:

$$\min_{\alpha \in \mathcal{U}_{ad}} \quad \int_{\Omega} (A^*(\alpha))^{-1} \sigma \cdot \sigma \, \mathrm{dx} \tag{3.8}$$

   Optimizing the integral of (3.8) is equivalent to optimizing $(A^*(\alpha))^{-1}\sigma \cdot \sigma$ at every point $x \in \Omega$.

2. if we fix α, then the optimal σ is the unique point of minimum of (3.3) (obtained by solving a simple partial differential equation).

3.1.1 Pointwise optimality criterion approach

The approach of a pointwise optimality criterion consist of reducing the global minimization problem (3.8) to a local pointwise mechanical one (at the scale of a node or a finite element). What makes such an approach possible is that we suppose that the stress field σ is constant. The problem of compliance minimization then becomes:

$$\min_{\alpha} j(\alpha) = \left(A^*(\alpha)\right)^{-1} \sigma \cdot \sigma,$$

which admits the following optimality condition

$$\frac{\partial j(\alpha)}{\partial \alpha} = 0.$$

We then search for the values of α that nullify $\frac{\partial j(\alpha)}{\partial \alpha}$ and satisfy $\frac{\partial^2 j(\alpha)}{\partial \alpha^2} > 0$. Note that $\frac{\partial j(\alpha)}{\partial \alpha}$ and $\frac{\partial^2 j(\alpha)}{\partial \alpha^2}$ are obtained directly:

$$\frac{\partial j(\alpha)}{\partial \alpha} = ((A^*(\alpha))^{-1})'\sigma \cdot \sigma \quad \text{and} \quad \frac{\partial^2 j(\alpha)}{\partial \alpha^2} = ((A^*(\alpha))^{-1})''\sigma \cdot \sigma.$$

The result of this analysis is established by Pedersen in [82, 83] where it was found that that the optimal direction of an orthotropic material is when the stiffest material direction takes the direction of the major principal stress, under the condition of:

$$\begin{aligned} A_{1111} + A_{2222} - 2A_{1122} - A_{1212} \geq 0, \qquad & \text{or} \\ (A_{1111} + A_{2222} - 2A_{1122} - A_{1212})^2 \left[(\sigma_{11} - \sigma_{22})^2 + 4\sigma_{12}^2\right] \leq (A_{1111} - A_{2222})^2 (\sigma_{11} + \sigma_{22})^2 . & \end{aligned} \tag{3.9}$$

The otherwise case was reinvestigated by Gea and Luo in [48] were they proved the existence of multiple global minima. Other works that explains the optimality criterion approach are in [36, 67]. In this work, we only studies examples that fall into the first case, which represent materials with relatively low shear stiffness and some materials with relatively high shear stiffness.

3.1.2 Optimal orientation

We determine the principal stresses σ_I and σ_{II} by computing the eigenvalues of the stress tensor:

$$\sigma_I = \frac{\sigma_{11} + \sigma_{22}}{2} + \sqrt{\left(\frac{\sigma_{11} - \sigma_{22}}{2}\right)^2 + \sigma_{12}^2},$$

$$\sigma_{II} = \frac{\sigma_{11} + \sigma_{22}}{2} - \sqrt{\left(\frac{\sigma_{11} - \sigma_{22}}{2}\right)^2 + \sigma_{12}^2}.$$

We then choose the major absolute principal stress σ_{max} as:

$$\sigma_{\max} = \begin{cases} \sigma_I & \text{if } |\sigma_I| > |\sigma_{II}|\,, \\ \sigma_{II} & \text{otherwise.} \end{cases}$$

The major absolute principal stress direction is the eigenvector $e_{\sigma_{\max}} = (\sigma_{\max} - \sigma_{22}, \sigma_{12})$ associated to $\sigma_{\max}$, it is obtained by solving $(\sigma - \sigma_{\max} I)\, e_{\sigma_{\max}} = 0$.

Finally, the expression of the angle α_{opt}, the angle that gives the direction of the vector $e_{\sigma_{max}}$, is obtained through geometric trigonometry:

$$\alpha_{opt} = \begin{cases} \begin{cases} \arccos\left(\frac{\sigma_{\max}-\sigma_{22}}{\sqrt{(\sigma_{\max}-\sigma_{22})^2+\sigma_{12}^2}}\right) & \text{if } \sigma_{12} \geq 0 \\ -\arccos\left(\frac{\sigma_{\max}-\sigma_{22}}{\sqrt{(\sigma_{\max}-\sigma_{22})^2+\sigma_{12}^2}}\right) & \text{if } \sigma_{12} < 0 \end{cases} & \text{if } \sigma_{max} \neq \sigma_{22} \\ \frac{\pi}{2} & \text{if } \sigma_{max} = \sigma_{22} \\ \alpha_{old} & \text{if } \sigma_{max} = 0. \end{cases} \tag{3.10}$$

The orientation is defined as a modulo π function; thus α_{opt} obtained by the equations of (3.10) is continuous on $\mathbb{Z}/\pi\mathbb{Z}$ with $\pi/2$ being the same as $-\pi/2$. Note also that when $\sigma_{max} = \sigma_{22}$, σ_{12} becomes zero since the tensor σ becomes diagonal. The orientation takes, in this case, the same direction as the y-axis. Lastly, when σ_{max} is zero, there is no stress applied on the material point x. As a result, there is no need to choose the anisotropy direction angle α_{opt} different from its original value α_{old} for this do not have any effect on the objective function.

3.1.3 Numerical algorithm

We deduce a minimization algorithm for (3.7), called alternate directions algorithm, which consists in minimizing successively and alternately in α and in σ. The angle α is updated using a principal stress-based method. The alternate directions algorithm is described by the algorithm 3.

Note that minimizing (3.11) is equivalent to solving the elasticity equation

Algorithm 3: 2D orientation optimization using an optimality criterion

1 Initialization of the angle $\alpha_0 \in \mathcal{U}_{ad}$.
2 **for** $n = 0, ..,$ *until convergence* **do**
3 Calculation of the state σ_n, unique solution of:

$$\min_{\sigma \in H} \quad \int_\Omega (A^*(\alpha_n))^{-1}\sigma \cdot \sigma \, \mathrm{dx}, \tag{3.11}$$

4 Update the angle α_n to α_{n+1}; the angle corresponding to the major principal stress obtained using the optimality formula (3.10).
5 **end**

(1.1), to get the displacement u_n, and to determining σ_n by

$$\sigma_n = A^*(\alpha_n)e(u_n)$$

This algorithm is interpreted as an alternate minimization in σ then in α of the function (3.5). In particular, we deduce that the objective function always decreases during the iterations

$$\begin{aligned} J(\alpha_{n+1}) &= \int_\Omega A^*(\alpha_{n+1})^{-1}\sigma_{n+1} \cdot \sigma_{n+1} dx \\ &\leq \int_\Omega A^*(\alpha_{n+1})^{-1}\sigma_n \cdot \sigma_n dx \\ &\leq \int_\Omega A^*(\alpha_n)^{-1}\sigma_n \cdot \sigma_n dx = J(\alpha_n) \end{aligned}$$

3.2 Optimal direction using a gradient descent method

The application of orientation optimization using the optimality criterion is limited to the problem of a single load compliance optimization. Wistfully, industrial applications are unrestricted to this problem; e.g. multi-load objective function, target displacement problem, stress optimization... That is why we need to optimize the orientation with a numerical method such as the gradient descent.

In this section, we will introduce the anisotropy orientation optimization with a gradient descent method. We will consider the problem of compliance to

compare this method with the optimality criterion method, then we will apply the method to the optimization of the problem of target displacement and of a multi-load compliance problem.

In these optimization problems, we study the same model of linear elasticity (1.1) with the same set of admissible designs (3.1). We suppose a general objective function $J(\alpha)$ that is the sum of a the integral of the function j defined on Ω and of the integral of the function l defined on Γ_J, where Γ_J does not intersect the Dirichlet boundary Γ_D (see figure 3.1).

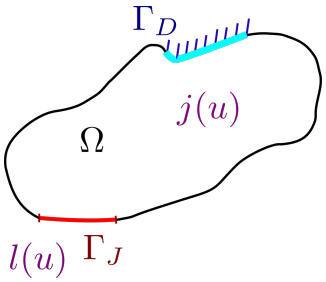

Figure 3.1: Boundaries of a shape Ω for a general objective function

$$J(\alpha) = \int_\Omega j(u)\mathrm{dx} + \int_{\Gamma_J} l(u)\mathrm{d}s. \tag{3.12}$$

The orientation optimization problem is then written as:

$$\inf_{\alpha \in \mathcal{U}_{ad}} J(\alpha). \tag{3.13}$$

Notice that the orientation optimization problem is expressed exactly in the same way as a parametric shape optimization problem. Consequently, we use theorem 1.1.1 to get the expression of the gradient of the objective function, which gives:

$$J'(\alpha) = -\left(A^*(\alpha)\right)' e(u) \cdot e(p), \tag{3.14}$$

where p is the adjoint displacement obtained by solving the adjoint problem (1.9). Note that in the considered setting, the angle of anisotropy does not have any relation to the shape of the structure, but rather to the intrinsic properties of the elastic material.

Objective function gradient alternative expression

In this part, we use the Kelvin notation, the derivative of $\hat{A^*}$ (i.e. A^* in Kelvin notation) with respect to the angle α is written as:

$$\Big(\hat{A^*}(\alpha)\Big)' = \Big(R(\alpha)\Big)'\hat{A^*}R^t(\alpha) + R(\alpha)\hat{A^*}\Big(R^t(\alpha)\Big)'. \tag{3.15}$$

Mehrabadi & Al.[72] gives the expression of $\Big(R(\alpha)\Big)'$ in terms of $R(\alpha)$:

$$\Big(R(\alpha)\Big)' = PR(\alpha), \tag{3.16}$$

where P is a constant matrix defined as:

$$P_{ij} = -\xi_{ijk}m_k,$$

where ξ_{ijk} is Levi-Civita symbol defined by:

$$\xi_{ijk} = \begin{cases} +1 \text{ if } (i,j,k) \text{ is } (1,2,3),(2,3,1), \text{ or } (3,1,2), \\ -1 \text{ if } (i,j,k) \text{ is } (3,2,1),(1,3,2), \text{ or } (2,1,3), \\ \ \ 0 \text{ if } i=j, \text{ or } j=k, \text{ or } k=i. \end{cases}$$

and m is the unit vector of the axis of rotation by α (which is equal to the base vector e^z in the 2D case).

Using (3.16) and (2.8) in (3.15) we obtain the expression of $\Big(\hat{A^*}(\alpha)\Big)'$ in terms of $\hat{A^*}(\alpha)$:

$$\Big(\hat{A^*}(\alpha)\Big)' = P\hat{A^*}(\alpha) + \hat{A^*}(\alpha)P^t. \tag{3.17}$$

By writing (3.14) in the Kelvin formalism, then by replacing the derivative $(A^*(\alpha))'$ with the expression of (3.17), we obtain:

$$J'(\alpha) = -\Big\{e(u)\Big\}\Big(P\hat{A^*}(\alpha) + \hat{A^*}(\alpha)P^t\Big)\Big\{e(p)\Big\}, \tag{3.18}$$

where $\Big\{e(u)\Big\}$ and $\Big\{e(p)\Big\}$ are respectively the two Kelvin notation strain

vectors for the displacement strain tensor $e(u)$, and the adjoint displacement strain tensor $e(p) = \frac{1}{2}(\nabla p + (\nabla p)^t)$.

Numerical algorithm

The numerical algorithm of the orientation optimization using the gradient descent method is presented in algorithm 4

Algorithm 4: 2D orientation optimization using the gradient descent

```
1  Initialize the angles α_0.
2  Compute the displacement u_0 by solving the elasticity problem.
3  Compute the objective function J(α_0).
4  for n = 1, .., until convergence do
5  |  Compute the gradient J'(α_n) using (3.18).
6  |  α_n = α_{n-1} − t_n J'(α_n), where t_n > 0 is a small descent step.
7  |  Compute u_n.
8  |  Compute the objective function J(α_n).
9  |  if J(α_n) < J(α_{n-1}) then
10 |  |  t_{n+1} = 1.2 t_n and continue to the next iteration.
11 |  else
12 |  |  t_{n+1} = t_n/2 and return to step 5.
13 |  end
14 end
```

3.3 Optimal direction using a Ginzburg-Landau based gradient descent method

Consider the linear elasticity model (1.1) defined on the structure Ω with the same boundary conditions as in figure 3.1, where j is a function that is defined in Ω and l is a function defined on Γ_J, a boundary of Ω that does not intersect the Dirichlet boundary Γ_D. Another variation of the gradient descent method, is to optimize the vector $(\mathfrak{c}, \mathfrak{s}) = (\cos\alpha, \sin\alpha) \in (L(\Omega)^2)^2$ instead of the angle α. This is possible because A^* is written as a function of the rotation matrix Q which is expressed using $\cos\alpha$ and $\sin\alpha$ in (2.16). The objective function $J(\alpha)$ in (3.12) is also a function of $\mathfrak{c}$ and $\mathfrak{s}$, thus the optimization problem (3.13) becomes:

$$\inf_{(\mathfrak{c},\mathfrak{s})\in\mathcal{U}_{ad}} J(\mathfrak{c},\mathfrak{s}), \tag{3.19}$$

where the set of the admissible designs $\mathcal{U}_{ad}$ is given by:

$$\mathcal{U}_{ad} = \{(\mathfrak{c},\mathfrak{s}) \in L(\Omega)^2 \quad \text{s.t.} \quad \mathfrak{c}^2 + \mathfrak{s}^2 = 1\}. \tag{3.20}$$

Note that $\mathfrak{c}$ and $\mathfrak{s}$ are assured to be a cosine and a sine function by means of the constraint $\mathfrak{c}^2 + \mathfrak{s}^2 = 1$. To impose this constraint, we add a penalty term to the objective function, and we obtain a new objective function:

$$J_p(\mathfrak{c},\mathfrak{s}) = \frac{J(\mathfrak{c},\mathfrak{s})}{J(\mathfrak{c}_0,\mathfrak{s}_0)} + \frac{1}{\varepsilon_p}\int_\Omega \left(\mathfrak{c}^2 + \mathfrak{s}^2 - 1\right)^2 dx,$$

where ε_p is a small positive penalty parameter. Note that we divide the objective function $J(\mathfrak{c},\mathfrak{s})$ by its initial value $J(\mathfrak{c}_0,\mathfrak{s}_0)$, which is different to zero by nature of the orientation optimization problems, to harmonize the new objective function terms ($\mathfrak{c}_0$ and $\mathfrak{s}_0$ are the initial values of $\mathfrak{c}$ and $\mathfrak{s}$). This approach of optimizing the cosine and sine of the angle α under a penalty function that ensures the constraint in (3.20) is called a Ginzburg-Landau approach [29]. The optimization problem (3.19) becomes:

$$\inf_{\mathfrak{c},\mathfrak{s}\in L^2(\Omega)} J_p(\mathfrak{c},\mathfrak{s}).$$

The gradients of $J_p(\mathfrak{c},\mathfrak{s})$ with respect to its parameters is obtained using the theorem 1.1.1, which gives:

$$\frac{\partial J_p(\mathfrak{c},\mathfrak{s})}{\partial \mathfrak{c}} = -\frac{\partial A^*(\mathfrak{c},\mathfrak{s})}{\partial \mathfrak{c}} e(u)\cdot e(p) + \frac{4}{\varepsilon_p}\mathfrak{c}\left(\mathfrak{c}^2 + \mathfrak{s}^2 - 1\right), \tag{3.21}$$

and:

$$\frac{\partial J_p(\mathfrak{c},\mathfrak{s})}{\partial \mathfrak{s}} = -\frac{\partial A^*(\mathfrak{c},\mathfrak{s})}{\partial \mathfrak{s}} e(u)\cdot e(p) + \frac{4}{\varepsilon_p}\mathfrak{s}\left(\mathfrak{c}^2 + \mathfrak{s}^2 - 1\right), \tag{3.22}$$

where p is the adjoint displacement obtained by solving the adjoint problem (1.9).

Algorithm

We start with a big value of the penalization parameter ε_p, for example $\varepsilon_p = 1000$, and we decrease it linearly during the optimization. The orientation optimization algorithm which relies on this Ginzburg-Landau approach is written as algorithm 5:

Algorithm 5: 2D orientation optimization using a Ginzburg-Landau approach

Initialize the values of $\mathfrak{c}_0$, $\mathfrak{s}_0$ and ε_p^0.
compute the gradients $\frac{\partial J_p(\mathfrak{c}_n,\mathfrak{s}_n)}{\partial \mathfrak{c}_n}$ and $\frac{\partial J_p(\mathfrak{c}_n,s_n)}{\partial s_n}$ using (3.21) and (3.22).
compute the displacement u_0 by solving the elasticity problem, then compute the objective function $J_p(\mathfrak{c}_0, \mathfrak{s}_0)$.
for $n = 1, ..,$ *until convergence* **do**
    compute $\mathfrak{c}_n = \mathfrak{c}_{n-1} - t_n \frac{\partial J_p(\mathfrak{c}_n,\mathfrak{s}_n)}{\partial \mathfrak{c}_n}$, where t_n is a small descent step.
    compute $\mathfrak{s}_n = \mathfrak{s}_{n-1} - t_n \frac{\partial J_p(\mathfrak{c}_n,\mathfrak{s}_n)}{\partial \mathfrak{s}_n}$.
    compute u_n.
    compute the objective function $J_p(\mathfrak{c}_n, \mathfrak{s}_n)$.
    if $J_p(\mathfrak{c}_n, \mathfrak{s}_n) < J_p(\mathfrak{c}_{n-1}, \mathfrak{s}_{n-1})$ **then**
        $t_{n+1} = 1.2t_n$, $\varepsilon_p^{n+1} = \beta\varepsilon_p^n$, where $0 < \beta < 1$, and then continue to the next iteration.
    else
        $t_{n+1} = t_n/2$ and return to step 5.
    end
end

3.4 Regularization of orientation

The results of orientation optimization are not usually continuous or smooth. However, in additive manufacturing, it is better to have smoothly continuous orientations. As the discontinuity means interruption of the laser scanning process, which is a more time consuming step. But also leads to structures that have inferior fatigue resistance. For this purpose, we have implemented two orientation regularization methods. The first one consist of regularizing a given orientation [8, 49] and it only works for the compliance minimization problem. Although this method was developed for regularizing the orientation of laminated composites, it is also a method that works for any type of orthotropic material. The second method is to regularize the orientation by regularization

of the gradient field, this method works for any cost function but only with a gradient based method.

3.4.1 Regularization of a given orientation field

We describe this regularization method without going into details (for more details see section 4.5.3 of [49]), to regularize the orientation for the compliance minimization problem, we make a small change on the cost function, we express the compliance on function of the stress tensor σ and we add a small regularization term:

$$\int_\Omega \left(A(\alpha)^{*-1}\sigma \cdot \sigma + \frac{1}{4}\eta^2 |\nabla \alpha|^2 \right) \mathrm{dx}.$$

We define a vector $\mathfrak{b}$ as:

$$\mathfrak{b} = (\cos(2\alpha), \sin(2\alpha))^t.$$

The rotation matrix $R(\alpha)$ can be expressed with the parameter $\mathfrak{b}$ instead of α; $R(\alpha) = \tilde{R}(\mathfrak{b})$. The advantage of using this new expression is that $\mathfrak{b} \to \tilde{R(\mathfrak{b})}$ is a linear function, which makes the calculations of its derivative simple. We then regularize $\beta = 2\alpha$ instead of α. The cost function becomes:

$$\int_\Omega \left(A^{*-1}\tilde{R}(\mathfrak{b})\sigma \cdot \tilde{R}(\mathfrak{b})\sigma + \eta^2 |\nabla \beta|^2 \right) \mathrm{dx}.$$

To solve this minimization problem we search for the $\delta\mathfrak{b}$ and $\delta\beta$ that minimizes:

$$\int_D A^{*-1}\tilde{R}\left(\mathfrak{b} + \delta\mathfrak{b}\right)\sigma \cdot \tilde{R}\left(\mathfrak{b} + \delta\mathfrak{b}\right)\sigma \mathrm{dx} + \eta^2 \int_D \left|\nabla\left(\beta + \delta\beta\right)\right|^2 \mathrm{dx}.$$

Note that the vector $\mathfrak{b}$ verify:

$$\nabla\beta = \mathfrak{b} \wedge \nabla\mathfrak{b}.$$

Therefore, we can write the optimality condition of the minimization problem as the variational problem:

find $\delta\mathfrak{b}$ such that $\forall \delta c \in H^1\left(D; \mathbb{R}^2\right)$:

$$2\int_D A^{*-1}\tilde{R}(\mathfrak{b}+\delta\mathfrak{b})\sigma\cdot\tilde{R}'(\delta c)\sigma\mathrm{dx}+2\eta^2\int_D(\mathfrak{b}\wedge\nabla(\mathfrak{b}+\delta\mathfrak{b}))(\mathfrak{b}\wedge\nabla\delta c)\mathrm{dx}=0. \quad (3.23)$$

In the end, we update the vector $\mathfrak{b}$ to the new value of $\frac{\mathfrak{b}_{n-1}+\delta\mathfrak{b}_n}{|\mathfrak{b}_{n-1}+\delta\mathfrak{b}_n|}$ and we deduce from it the new regular angle α.

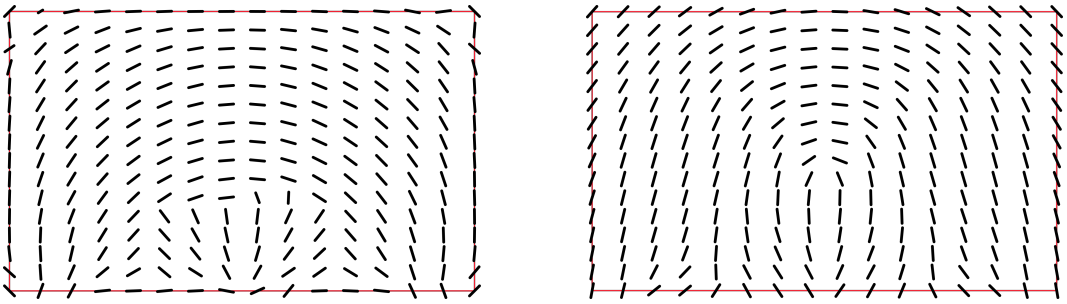

(a) Orientations before the regularization

(b) Orientations after the regularization

Figure 3.2: Regularized optimal stiffest orientations of for an arch

The algorithm 6 resumes all the steps of this method of regularization. The figure 3.2 gives an example of the orientations, before and after using this algorithm.

Algorithm 6: 2D orientation regularization algorithm

Initialize the orientation α_0 and compute vector $\mathfrak{b}_0$.
Iterate until convergence, for $n \geq 0$:
for $n = 1, ..,$ *until convergence* **do**
    Compute the strain tensor $e(u_n)$ through the problem of linear elasticity.
    Compute the increment $\delta\mathfrak{b}_n$ by solving the variational problem (3.23).
    Compute and normalize the vector $\mathfrak{b}_n$ by $\mathfrak{b}_n \leftarrow \frac{\mathfrak{b}_{n-1}+\delta\mathfrak{b}_n}{|\mathfrak{b}_{n-1}+\delta\mathfrak{b}_n|}$.
    Deduce α_n.
end

3.4.2 Regularization while optimizing the orientation

This method resembles the regularization of the shape procedure in section 1.3.1. The regularization of the orientation angle is performed by the regularization

of the gradient, which is done by projecting the gradient $j'(\alpha)$ from the space $L^2(\Omega)$ with the inner product $\int_\Omega uv \, \mathrm{d}x$, into the space $H^1(\Omega)$ with the inner product

$$a(u,v) = \int_\Omega \nabla u \cdot \nabla v \, \mathrm{d}x + \int_\Omega uv \, \mathrm{d}x. \tag{3.24}$$

This is achieved by solving the following variational formulation:

find $j'_{r_\alpha}(\alpha) \in L^2(\Omega)$ such that

$$\int_\Omega \left(r_\alpha^2 \nabla j'_{r_\alpha}(\alpha) \cdot \nabla \varphi + j'_{r_\alpha}(\alpha)\varphi \right) dx = \int_\Omega j'(\alpha)\varphi dx \quad \forall \varphi \in H^1(\Omega),$$

where $j'_{r_\alpha}(\alpha)$ is the new regularized gradient that is now in $H^1(\Omega)$. The regularization parameter r_α is a regularization length-scale that indicates how much distance from the point x the regularized gradient is covering.

3.5 Constrained orientation optimization

3.5.1 Projected gradient descent

The goal is to project the new orientation angle α_{n+1}, obtained by updating α along the descent direction, into $\bar{\alpha}_{n+1}$ which belongs to a chosen interval $[\alpha_{\min}, \alpha_{\max}]$. This is simply done by:

$$\bar{\alpha}_n = \max(\min(\alpha_n, \alpha_{\max}), \alpha_{\min}).$$

Remark 2 *The projection of the angle in a projected gradient method should not be applied to an optimality criterion method such as the method of directions of principal strains, because the projection do not give necessarily an optimal angle. The projection should be coupled with a gradient descent loop that ensures that the algorithm will converge to an optimal solution at the end.*

3.5.2 Augmented Lagrangian for inequality constraints

In industrial problems, we may have to add some inequality constraints to the orientation. Suppose that we have one inequality constraint of the form $C(\alpha) \leq c$, where $c \in \mathbb{R}$ is a given limit value. The optimization problem is

then written:

$$\inf_{\alpha \in \mathcal{U}_{ad}} J(\alpha), \tag{3.25}$$

with the set of admissible space:

$$\mathcal{U}_{ad} = \left\{ \alpha \in L^2(\Omega), \quad C(\alpha) \leq c \right\}.$$

There are multiple ways to use the augmented Lagrangian method for an inequality constraint. One way [76] is to define a new objective function where we add a term that depends on the previous iteration to the standard Lagrangian $\mathcal{L}_c(\alpha, \lambda) = J(\alpha) - \lambda(c - C(\alpha))$, where $\lambda \in \mathbb{R}^+$ is the Lagrange multiplier. For instance, for the iteration $n \in \mathbb{N}$, for $b > 0$ the new augmented Lagrangian is written:

$$\mathcal{L}_{al}(\alpha, \lambda) = J(\alpha) - \lambda(c - C(\alpha)) - \frac{b}{2}(\lambda - \lambda_{n-1})^2. \tag{3.26}$$

Note that a quadratic penalty term on the constraint is not added since it can generate instabilities (see [32] section 5.2.1). On the other hand, a quadratic penalty is applied to any move of λ away from the previous estimate λ_{n-1} , which encourages λ to stay close to the previous estimate λ_{n-1} [76], and $b \in \mathbb{R}_+^*$ is the penalty parameter. Thus, the constrained problem (3.25) changes into the following unconstrained problem:

$$\min_{\alpha \in L^2(\Omega)} \max_{\lambda \in \mathbb{R}_+} \mathcal{L}_{al}(\alpha, \lambda) \tag{3.27}$$

For an iteration $n \in \mathbb{N}$, the augmented Lagrangian algorithm proceeds by alternating the resolution of (3.27) for fixed values of the parameters λ_n and b_n, and the update of the latter according to:

$$\lambda_{n+1} = \begin{cases} \lambda_n - \frac{1}{b_n}(c - C(\alpha_n)) & \text{if} \quad \lambda_n - \frac{1}{b_n}(c - C(\alpha_n)) \geq 0 \\ 0 & \text{otherwise,} \end{cases} \tag{3.28}$$

and:

$$b_{n+1} = \begin{cases} \alpha_{al} b_n & \text{if } b_n < b_{\text{limit}} \\ b_n & \text{otherwise,} \end{cases}$$

for $\alpha_{al} > 1$. Note that it is unnecessary to make b tend to infinity to satisfy

the Lagrange multiplier move constraint. Thus we gradually increase the value of b until it reaches a limit value that is initially defined.

The idea of the update of the Lagrange multiplier λ_{n+1} using $\lambda_n - \frac{1}{b_n}(c - C(\alpha_n))$ in (3.28) is that when $C(\alpha_n) > c$, the value of λ is increased to impose the equality constraint of $C(\alpha) = c$, which will reduce the value of $C(\alpha)$. The value of λ keeps increasing until $C(\alpha)$ reaches a value equal to or lower than the limit c. When $C(\alpha_n) < c$, the value of λ is decreased to alleviate the equality constraint of $C(\alpha) = c$ from the augmented Lagrangian objective function. Finally, because λ_{n+1} has to be always positive, it is assigned to a null value whenever $\lambda_n - \frac{1}{b_n}(c - C(\alpha_n))$ gives a negative value.

Another method of augmented Lagrangian is to use a "gap variable" (also called a "slack variable") $\xi \in \mathbb{R}^+$ by replacing the problem (3.25) by the multivariable optimization problem:

$$\min_{\substack{\alpha \in L^2(\Omega), \\ \xi \in \mathbb{R}_+}} J(\alpha) \text{ s.t. } C(\alpha) + \xi = c.$$

The obtained problem is solved by using an equality augmented lagrangian objective function:

$$\mathcal{L}_{al}(\alpha, \lambda, \xi) = J(\alpha) - \lambda(C(\alpha) + \xi - c) + \frac{1}{2b}(C(\alpha) + \xi - c)^2,$$

which gives the problem

$$\min_{\substack{\alpha \in L^2(\Omega), \\ \xi \in \mathbb{R}_+}} \max_{\lambda \in \mathbb{R}_+} \mathcal{L}_{al}(\alpha, \lambda, \xi).$$

By replacing ξ by its optimal expression, the above problem becomes:

$$\min_{\alpha \in \mathbb{R}_+} \mathcal{L}_{al_2}(\alpha, \lambda) = J(\alpha) - \lambda \max(b\lambda, c - C(\alpha)) + \frac{1}{2b}(\max(b\lambda, c - C(\alpha)))^2,$$

In this work, we prefer to use the first augmented Lagrangian formulation, using (3.26) as the latter gives another variable ξ that has to be optimized. Another thing that is preferred to do, is to work with the angle α defined in the space $H^1(\Omega)$ instead of $L^2(\Omega)$, the inner product $\int_\Omega uv \, \mathrm{d}x$, is then replaced by the inner product:

$$a(u, v) = \int_\Omega \nabla u \nabla v \, \mathrm{d}x + \int_\Omega uv \, \mathrm{d}x,$$

which is helpful for obtaining smooth variations of the angle α. Hence (3.27) becomes:

$$\min_{\alpha \in H^1(\Omega)} \max_{\lambda \in \mathbb{R}_+} \mathcal{L}_{al}\left(\alpha, \lambda\right),$$

for $n \in \mathbb{N}$.

The inequality constraint augmented Lagrangian gradient descent algorithm works by replacing the Lagrangian gradient $\frac{\partial \mathcal{L}(\alpha,p)}{\partial \alpha}$ in algorithm 4 by:

$$\frac{\partial \mathcal{L}(\alpha, p, \lambda)}{\partial \alpha} = -\left(A^*(\alpha)\right)' e(u) \cdot e(p) + \lambda C'(\alpha), \tag{3.29}$$

which is obtained using theorem 1.1.1, where p is the adjoint displacement that is obtained by solving some adjoint problem.

3.5.3 Examples using an augmented Lagrangian for inequality constraint

In this section, we give some examples of constraints that we have applied to the angle during the optimization using the inequality constraint augmented Lagrangian.

3.5.3.1 Constrained angle's geometrical gradient

This example consists of optimizing the orientation angle α under a constraint $C(\alpha) \leq c$, where $C(\alpha)$ is given by the L^2-norm of the geometrical gradient of the angle:

$$C(\alpha) = \int_\Omega |\nabla \alpha|^2 \mathrm{dx}.$$

The optimization problem is then equivalent to (3.25) but with the set of admissible designs:

$$\mathcal{U}_{ad} = \left\{\alpha \in H^1(\Omega), \quad C(\alpha) \leq c\right\}.$$

The augmented gradient objective function is then defined as:

$$\mathcal{L}_{al}(\alpha, \lambda) = J(\alpha) - \lambda(c - \int_\Omega |\nabla \alpha|^2 \mathrm{dx}) - \frac{1}{2b}(\lambda - \lambda_{n-1})^2.$$

To obtain the dual function gradient (3.29) we need to calculate $C'(\alpha)$, which can be obtained using a directional derivative. Thus, $\forall \beta \in H^1(\Omega)$:

$$< C'(\alpha), \beta >= \int_\Omega \nabla C'(\alpha)\nabla\beta + C'(\alpha)\beta \text{ dx} = 2\int_\Omega \nabla\alpha\nabla\beta \text{ dx} \tag{3.30}$$

Consequently, $C'(\alpha)$ is obtained by solving the variational problem: find $C'(\alpha) \in H^1(\Omega)$, such that $\forall \beta \in H^1(\Omega)$,

$$\int_\Omega \nabla C'(\alpha)\nabla\beta + C'(\alpha)\beta \text{ dx} = 2\int_\Omega \nabla\alpha\nabla\beta \text{ dx}.$$

Remark 3 *If we had worked with the angle α defined in the space $L^2(\Omega)$ instead of $H^1(\Omega)$, we would have $\int_\Omega C'(\alpha)\beta \ dx = 2\int_\Omega \nabla\alpha\nabla\beta \ dx$, which is not well defined for α in $L^2(\Omega)$.*

3.5.3.2 Constrained angle's geometrical partial gradient

In this example, we add an inequality constraint of the type $C(\alpha) \leq c$ on the L^2-norm of the geometrical partial gradient of the angle α with respect to a chosen coordinate, let's say, for example, the coordinate of y. Where the value $c \in \mathbb{R}$ is a fixed upper bound and $C(\alpha)$ is given in this case by:

$$C(\alpha) = \int_\Omega |\frac{\partial\alpha}{\partial y}|^2 \text{dx}.$$

For $\alpha \in H^1(\Omega)$, using the method described in Section 3.5.3.1, we obtain the gradient of $C(\alpha)$ by solving the following variational problem:

find $C'(\alpha) \in H^1(\Omega)$, such that $\forall \beta \in H^1(\Omega)$,

$$\int_\Omega \nabla C'(\alpha)\nabla\beta + C'(\alpha)\beta \text{ dx} = 2\int_\Omega \frac{\partial\alpha}{\partial y}\frac{\partial\beta}{\partial y} \text{ dx}.$$

Remark 4 *If we had worked with the angle α defined in the space $L^2(\Omega)$ instead of $H^1(\Omega)$, we would have $\int_\Omega C'(\alpha)\beta \ dx = 2\int_\Omega \frac{\partial\alpha}{\partial y}\frac{\partial\beta}{\partial y} \ dx$, which is not well defined for α in $L^2(\Omega)$.*

3.5.3.3 Constraint on the angle difference to a fixed value

In this example, we add an inequality constraint of the type $C(\alpha) \leq c$ on the L^2-norm of the difference of the angle α with respect to a chosen fixed value of the angle α_f. The value $c \in \mathbb{R}$ is a fixed upper bound and $C(\alpha)$ is given in this case by:

$$C(\alpha) = \int_\Omega |\alpha - \alpha_f|^2 \mathrm{dx}.$$

For $\alpha \in H^1(\Omega)$, following Section 3.5.3.1, the gradient of $C(\alpha)$ is obtained by solving the following variational problem:

find $C'(\alpha) \in H^1(\Omega)$, such that $\forall \beta \in H^1(\Omega)$,

$$\int_\Omega \nabla C'(\alpha) \nabla \beta + C'(\alpha)\beta \ \mathrm{dx} = \int_\Omega 2(\alpha - \alpha_f)\beta.$$

Note that in the case of $\alpha \in L^2(\Omega)$, we will obtain $C'(\alpha) = 2(\alpha - \alpha_f)$.

3.6 Numerical Results

3.6.1 2D orientation optimization using the optimality criterion

We give the example of the optimization of the orientation of a cantilever (figure 3.3) using the optimality criterion optimization algorithm to minimize compliance. The elastic moduli of the material are set to $E_1 = 10$, $E_2 = 1$, $\nu_{12} = 0.3$ and $G_{12} = 1$ (the moduli satisfy $A_{1111} + A_{2222} - 2A_{1122} - A_{1212} > 0$). The boundary conditions are represented in the figure 3.3a. And we initialized with a horizontal direction of the material stiffest direction, which means that $\alpha_0 = 0$ (the stiffest material direction is the direction along which the Young modulus E_1 is measured).

The convergence of the compliance with the optimality criterion (figure 3.3c) is incredibly fast (~7 iterations). The compliance decrease significantly after the first update of orientation, then continue a very smaller decrease at every iteration. This is due to the stress field that is also converging to an appropriate configuration according to the change on the anisotropy orientation. The compliance converges when the stress field stabilizes.

We observe that we obtained a globally symmetric orientation field, that converges geometrically to the point where the force g is applied.

Note that the orientation is not symmetric on the right corners because the stress field is infinitesimal on those regions. And the principal stress field is unstable on those region. Note also that in regions where the stress field is hydrostatic, the orientation gets a random direction.

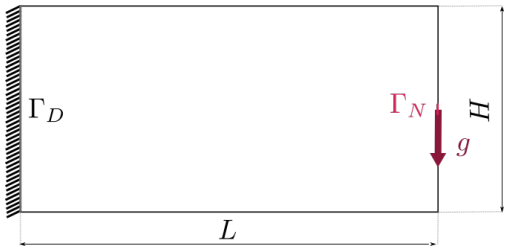

(a) Cantilever boundary condition

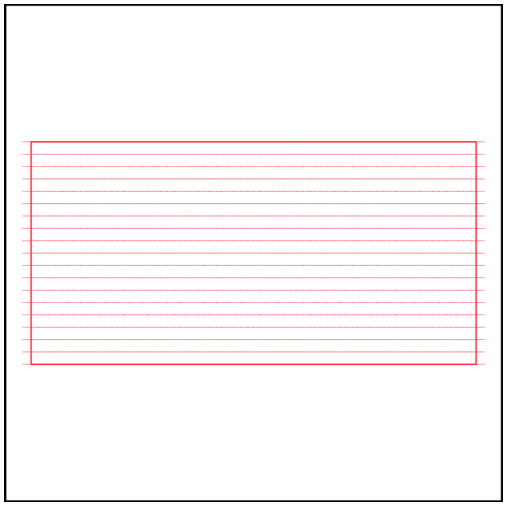

(b) Initial stiffest direction

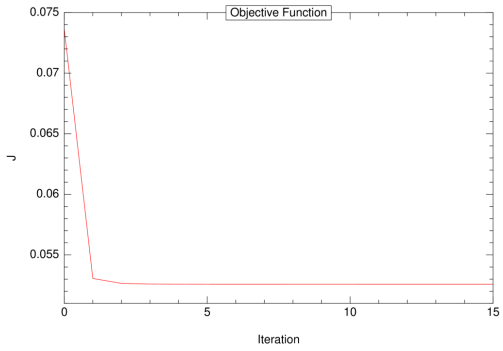

(c) Evolution of the compliance

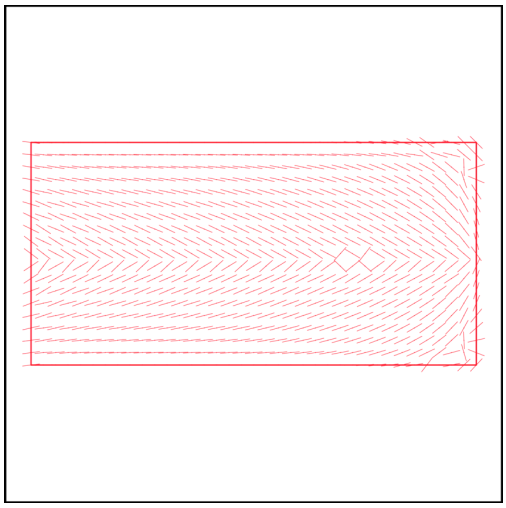

(d) Optimized stiffest direction

Figure 3.3: Optimization of a cantilever

The approach of optimality criterion supposed that the stress σ is constant during the optimization, which is not the case practically because the stress field σ is updated in each iteration, and it changes each time the orientation is updated. Although the stress converges and stabilizes at the end of the optimization loop, it's possible for the stress field to converge to a slightly different state according to the initialization of the stress field (that comes from the initial orientation). This explains why we obtain a different orientation field when we start with a different position of the orientation (figure 3.4). We observed a small loss of the symmetry of the optimized orientation when we started with a non symmetric initialization. (figures 3.4b and 3.4d)

Table 3.1: Initial and final compliances for the cantilever orientation optimization with different initialization of α

α_0	0	$\pi/2$	$\pi/4$	Random
Initial compliance	0.0736	0.4196	0.2099	0.1317
Final compliance	0.0526	0.0527	0.0527	0.0561

In the figure 3.5, We present the orientations that are obtained by the optimality criterion for an L-beam and arch examples with their boundary conditions. The elastic moduli that were used are the same as in the cantilever case, and the initial orientation of the stiffest material direction is horizontal for both examples.

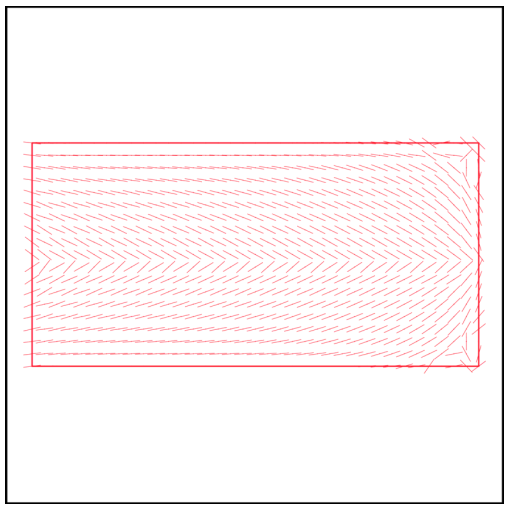

(a) Optimized stiffest direction for $\alpha_0 = \pi/2$

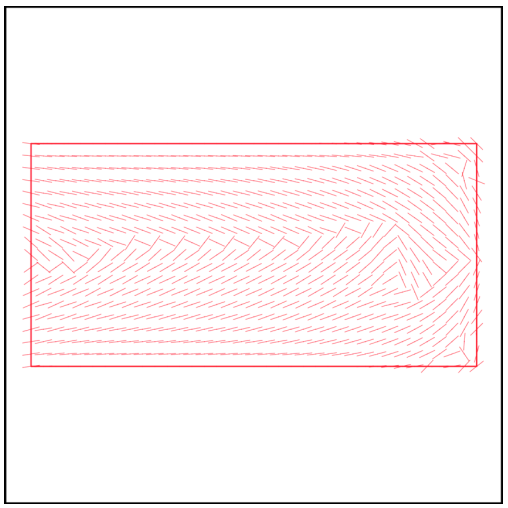

(b) Optimized stiffest direction for $\alpha_0 = \pi/4$

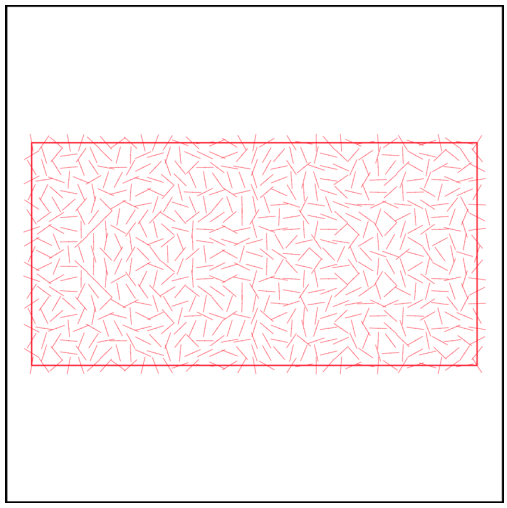

(c) Initial stiffest direction with random α_0

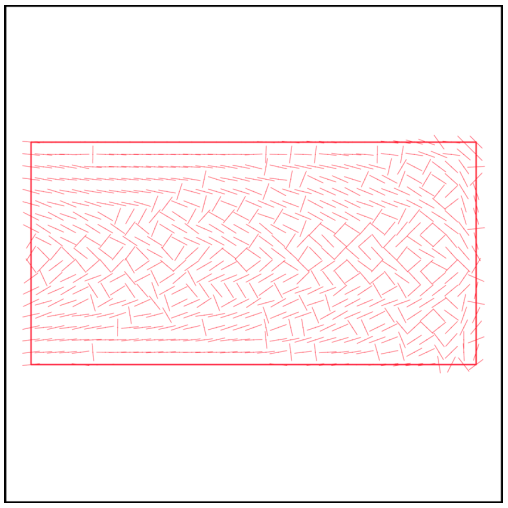

(d) Optimized stiffest direction with random α_0

Figure 3.4: Optimization of a cantilever orientation using different initializations of the orientation

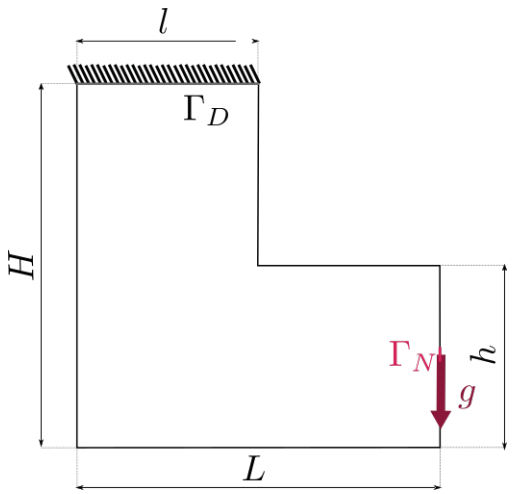

(a) L-beam boundary conditions

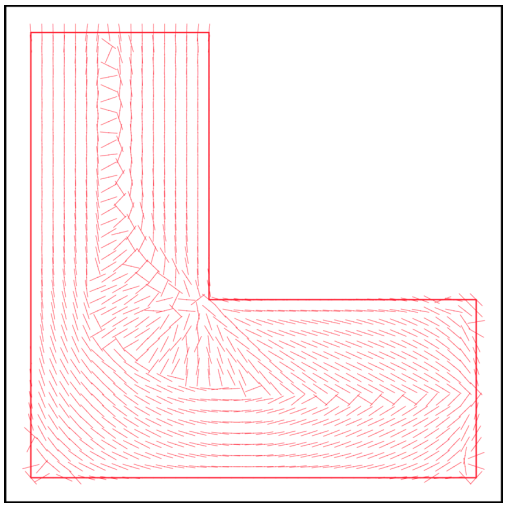

(b) Optimized stiffest direction of an L-beam

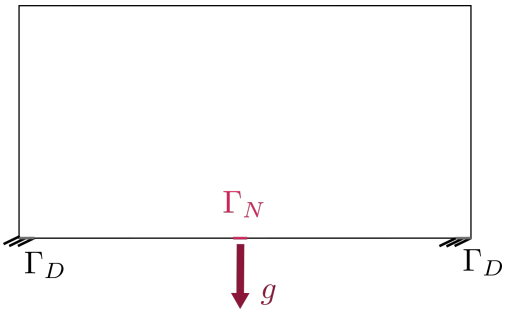

(c) Arch boundary conditions

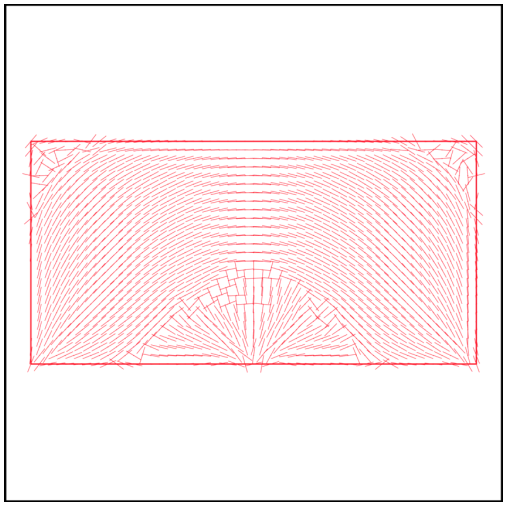

(d) Optimized stiffest direction of an arch

Figure 3.5: L-beam and arch optimal orientations with $\alpha_0 = 0$

3.6.2 2D orientation optimization using the gradient descent method

3.6.2.1 Gradient descent method for single-load compliance

The mechanical compliance is equal to the work of the forces that are applied to the structure Ω. Suppose that we apply a single surface force on Γ_N. Then, the compliance is

$$J(\alpha) = \int_{\Gamma_N} gu\text{ds}.$$

Notice that this is a special case of (1.5) with $l(u) = gu$ and $\Gamma_l = \Gamma_N$. As we have said in section 1.1.4.1 the compliance problem is self adjoint. The derivative of $J(\alpha)$ is then written as:

$$J'(\alpha) = -\left(A^*(\alpha)\right)' e(u) \cdot e(u).$$

We study the example of cantilever of figure 3.3a with the elastic moduli set to $E_1 = 10$, $E_2 = 1$, $\nu_{12} = 0.3$ and $G_{12} = 1$. We set the applied force to $ge_x = 1$.

In figure 3.6, we present the results of the orientation optimization for three different initializations of the orientation. Horizontal, vertical and a random orientation.

We observe that the optimizations converge to different local minima (different final orientations of the material) with different final values of compliance, according to the orientation initialization. The convergence of the compliance is smooth for the three optimizations. The smallest value of compliance is obtained when we started with a horizontal orientation. We also observe that, the smaller is the final compliance, the faster is the convergence. Another thing that we observe, which is obvious, is the number of iterations for the convergence of the descent gradient method, which is much larger than the iteration number with optimality criterion method (80 iterations for $\alpha_0 = 0$ while only 7 iterations with the optimality criterion optimization).

We also observe that the final orientations have a very close configuration to the orientations that were obtained by the optimality criterion in figure 3.4, especially when we started with horizontal orientations.

The initialization with horizontal direction of the stiffest material direction gave a globally symmetric and regular result. The final orientations resemble the orientations that are obtained by the optimality criterion in figure 3.3. The final objective function is slightly better (0.0524) than the one that is obtained

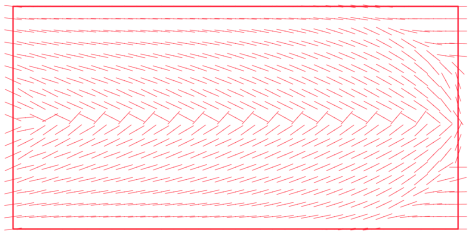

(a) Optimized stiffest direction for $\alpha_0 = 0$

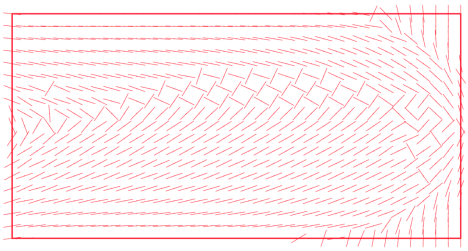

(b) Optimized stiffest direction for $\alpha_0 = \pi/2$

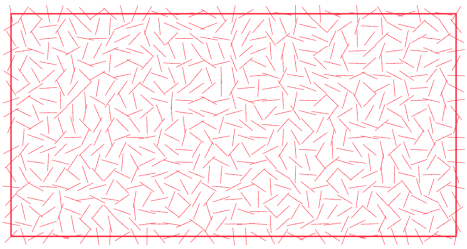

(c) Initial stiffest direction for random α_0

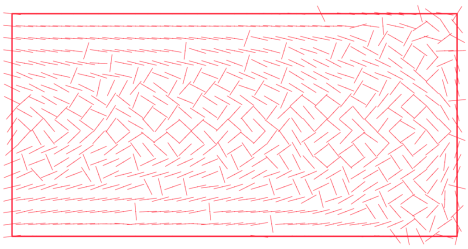

(d) Optimized stiffest direction for random α_0

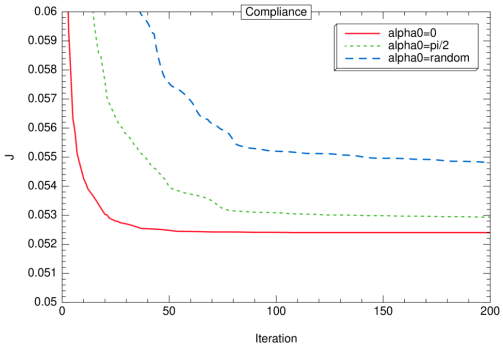

(e) Objective function evolution

Figure 3.6: Cantilever orientation optimization with a gradient descent

with the optimality criterion (0.0526).

The initialization with vertical orientations gave an unsymmetrical less regular result that globally resembles the result of the optimality criterion. The final objective function is larger (0.0529) than the one that is obtained with the optimality criterion (0.0527). Note that there exist some regions that have a symmetry about the longitudinal middle axis of the beam and some larger regions that are smoother.

Lastly, the random initialization of the rigid orientation gave an upper smooth orientation region that has a symmetry about the longitudinal middle axis on the bottom of the beam. The rest of the regions is irregular, non smooth and less symmetrical.

The final objective function is better (0.0548) than the one that is obtained with the optimality criterion (0.0561).

We observe that using a gradient method, one can obtain results that are very close to the optimality criterion optimization and sometimes better (example of horizontal and random orientation). We also observe that the initialization with horizontal orientation gave the better optimized orientations. And that the final orientation tend to be more regular when the initialization is regular. We also observe that the final orientation field is smoother and more defined in the regions where the deviatoric stress field is strong. This is because the optimal orientations take the orientations of the absolute major principal stress which is well defined on those regions. Finally, we observe that the regions that are irregular are closer to the longitudinal midline of the beam and that this irregular region becomes very big when we started with random iterations.

3.6.2.2 Gradient descent method for a target displacement

A target displacement optimization problem consists of minimizing a mean squared error of the displacement to a target value on a chosen region or surface.

We chose the example of a displacement inverter: the idea behind this mechanism is that when we pull the left surface Γ_N of the mesh D with its lower and upper parts fixed (see figure 3.7a), we want the opposite surface Γ_0 to move in the opposite direction, which is not possible with an isotropic material.

The objective function is written in this case as:

$$J(\alpha) = \int_{\Gamma_0} \frac{1}{2}|u - u_0|^2 \text{ ds}.$$

We also do not want the left surface of the mesh to move dramatically when we pull it: thus we add a null target displacement condition on the surface Γ_N.

The objective function becomes:

$$J(\alpha) = \int_{\Gamma_0} \frac{1}{2}|u - u_0|^2 \, \mathrm{ds} + \int_{\Gamma_N} \frac{1}{2}|u|^2 \, \mathrm{ds}.$$

In this case, the gradient of the objective function is written:

$$J'(\alpha) = -\left(A^*(\alpha)\right)' e(u) \cdot e(p),$$

where p is the adjoint displacement, solution of the elasticity adjoint problem of the inverter example:

find $p \in H^1(\Omega)^2$, such that $\forall v \in H^1(\Omega)^2$:

$$\begin{cases} -\operatorname{div}(A^* e(p)) = 0 & \text{in } \Omega \\ p = 0 & \text{on } \Gamma_D \\ A^* e(p) n = u & \text{on } \Gamma_0 \cup \Gamma_N. \end{cases}$$

We chose $E_1 = 10$, $E_2 = 1$, $\nu_{12} = 0.3$ and $G_{12} = 1$. We set the applied force to $g = -e_x$ and the target displacement to $u_0 = e_x$.

Table 3.2: Initial and final data of the inverter target displacement optimization with different initialization of α

α_0	0	$\pi/2$	$\pi/4$
Initial cost function	0.0385	0.0416	0.0403
Final cost function	0.0366	0.0367	0.0367
Initial u_x in the middle of Γ_0	-0.0335	-0.0691	-0.0536
Final u_x in the middle of Γ_0	-0.0120	-0.0118	-0.0119

For the three different initializations, the objective function converges smoothly to its final value. The horizontal initialization of the cantilever gave the least value of the objective function.

The obtained orientations are regular and symmetric when we initialized with symmetric orientation using a constant α_0 (figure 3.7b and figure 3.7c). We also observe that the optimal orientations are orientated in a way that when we pull the left surface, the structure compress its upper and lower surfaces to

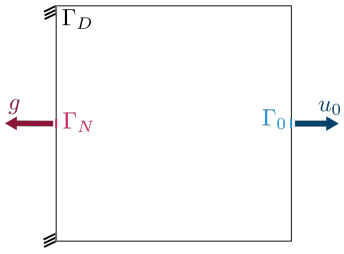

(a) Inverter boundary conditions

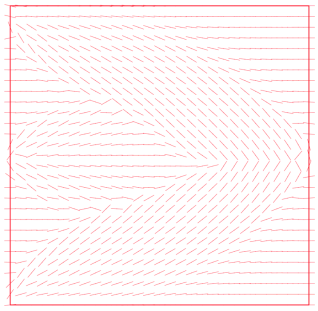

(b) Optimized stiffest direction for $\alpha_0 = 0$

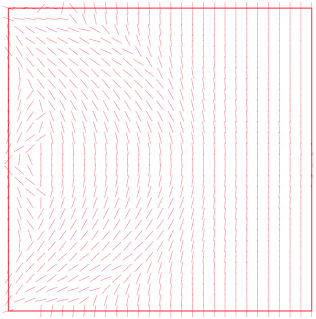

(c) Optimized stiffest direction for $\alpha_0 = \pi/2$

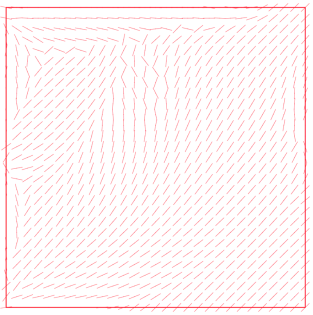

(d) Optimized stiffest direction for $\alpha_0 = \pi/4$

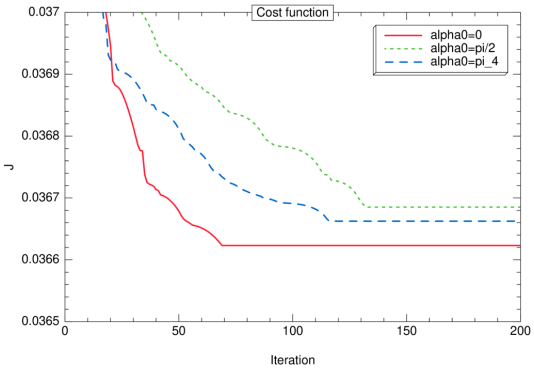

(e) Objective function evolution

Figure 3.7: Displacement inverter orientation optimization

push the surface Γ_0 to the opposite direction.

While we could not move the surface Γ_0 in the wanted direction, we were able to reduce the movement of the surface Γ_0 in the unwanted direction (Table 3.2). The initialization with vertical orientations gave the best target displacement. It can be explained by the fact that the opening that is created by the obtained orientations close to the applied force is wider than the one that is in figure 3.7b, which will result in a greater compression of the structure and thus to a more reach for the displacement of the surface Γ_0.

We also observe that the regions that did not play a role in the compression mechanism created by the optimal orientation conserved their initial orientations (central region of the compressing area and the right corners regions of the mesh).

Finally, we observe that we have lost the symmetry of the optimal orientation when we started with a non symmetric orientations (figure 3.7d).

3.6.2.3 Gradient descent method for multi-load compliance

We study the example of a bridge under three vertical loading cases g_1, g_2 and g_3 (see figure 3.8). Each loading case i generates a displacement field u_i. The applied forces can be interpreted as a car that crosses the bridge and that changes its position, to a position i associated to the load case i.

The mesh D is fixed on the tip of its right bottom corner. We fix the movement of the tip of its left bottom corner on the y-axis while we let it move freely on the direction of the x-axis.

The objective function which is the total compliance is then written as the sum of the compliance of each case

$$J(\alpha) = \sum_{i=1}^{3} \int_{\Omega} u_i g_i \mathrm{dx}.$$

The gradient of the objective function is the sum of the gradients of each case:

$$J'(\alpha) = -\sum_{i=1}^{3} \left(A^*(\alpha)\right)' e(u_i) \cdot e(u_i).$$

We choose equal values of the applied loadings; $g_1 e_y = g_2 e_y = g_3 e_y = -1$ (e_y is the unit vector of the vertical axis).

We initialize with a horizontal and a vertical orientation and we launch the optimization loop.

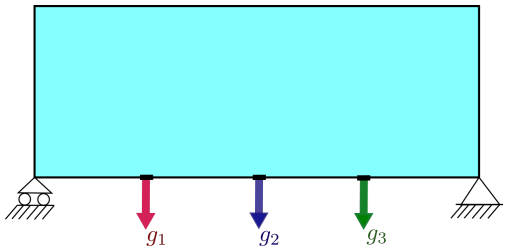

(a) Bridge applied forces and boundary conditions

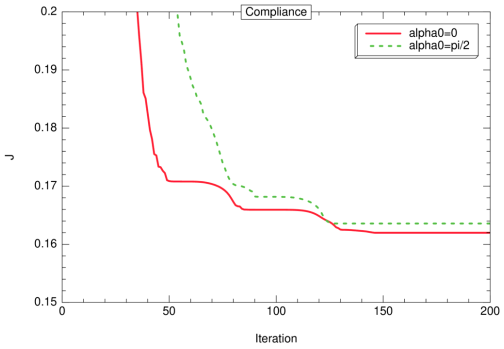

(b) Objective function evolution

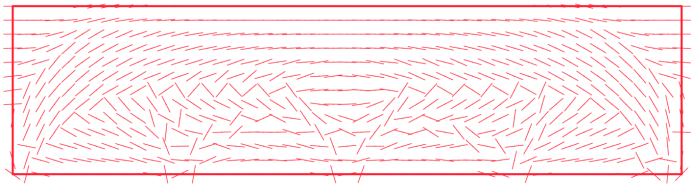

(c) Optimized stiffest direction for $\alpha_0 = 0$

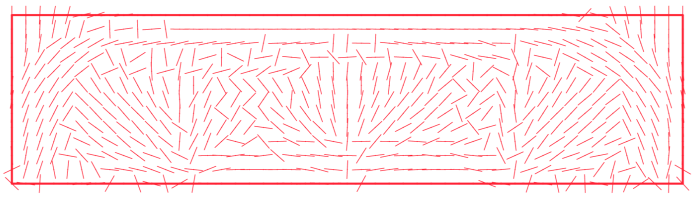

(d) Optimized stiffest direction for $\alpha_0 = \pi/2$

Figure 3.8: Multi-load bridge orientation optimization

We observe that the compliance converge smoothly for the two initialization and that the two final values of the compliance are very close to each other.

The obtained orientations are globally symmetric. The regularity of both examples is not typical especially for the initialization with $\alpha_0 = \pi/2$ on the zones where orientation that diverge from the points of applied forces meet with the perpendicular orientation of the superior area.

The optimal orientation gives a sketch of a suspension bridge where the rigid orientations create a suspension network that connect to the points of applied forces and that hangs the bottom surface of the bridge to the upper arch that

is supporting the bridge.

3.6.3 2D orientation optimization using the Ginzburg-Landau approach

Suppose the case of a single-load compliance optimization problem for the 2D cantilever of figure 3.3a with the same anisotropic material and the same mesh as in section 3.6.2.1. Using the Ginzburg-Landau approach, the new objective function becomes, for both applied force g and initial displacement u_0 non-nulls on Γ_N:

$$J_p(\mathfrak{c},\mathfrak{s}) = \frac{\int_{\Gamma_N} gu\,\mathrm{ds}}{\int_{\Gamma_N} gu_0\,\mathrm{ds}} + \frac{1}{\varepsilon_p}\int_\Omega \left(\mathfrak{c}^2+\mathfrak{s}^2-1\right)^2 dx.$$

Starting with a horizontal orientation ($\alpha_0 = 0$), $\varepsilon_p = 1000$ and $\alpha_{GL} = 0,917$. We apply the Ginzburg-Landau orientation optimization algorithm 5, which converges in 130 iterations. In the end, we obtain the figure of 3.9. The evolution of the compliance, the Ginzburg-Landau penalty function $\int_\Omega \left(\mathfrak{c}^2+\mathfrak{s}^2-1\right)^2 dx$ and the penalization parameter ε_p are presented in the figures 3.10, 3.11 and 3.12.

We also solve the same optimization problem starting with a vertical orientation ($\alpha_0 = \pi/2$), it also converges in 130 iterations, and we obtain the orientation of the figure 3.13. The evolution of the compliance, the Ginzburg-Landau penalty function and the penalization parameter ε_p of the vertically initialized orientation are presented in the figures 3.14, 3.15 and 3.16. The obtained orientations for both initialization are close to the ones that are obtained using the classical gradient descent method of section 3.6.2.1. The final objective functions are respectively 0,0573 and 0,0524.

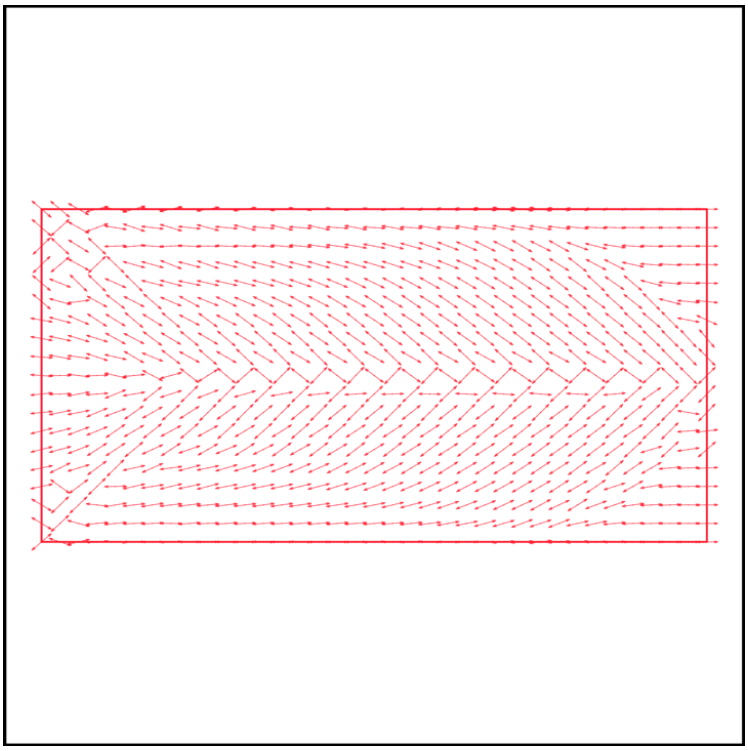

Figure 3.9: Optimized stiffest direction orientation with the Ginzburg-Landau method for $\alpha_0 = 0$

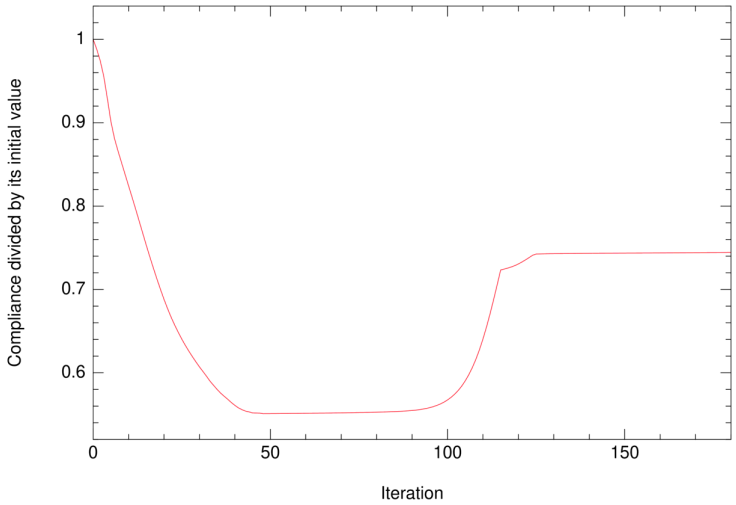

Figure 3.10: Objective function evolution with the Ginzburg-Landau method for $\alpha_0 = 0$

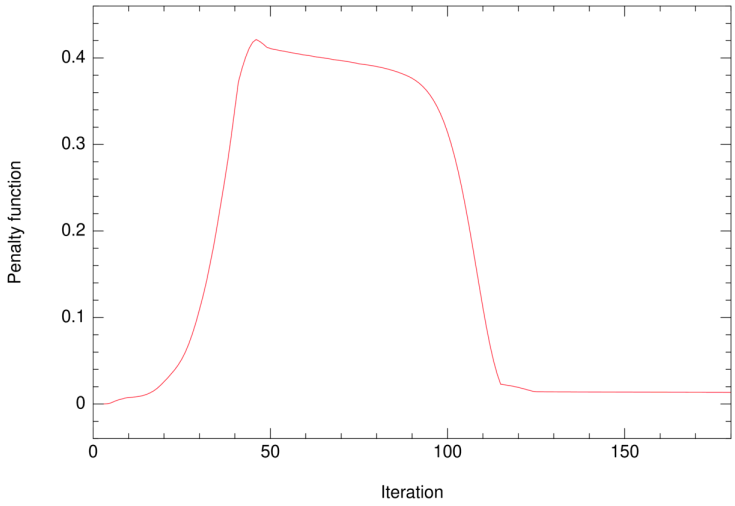

Figure 3.11: Penalty function evolution with the Ginzburg-Landau method for $\alpha_0 = 0$

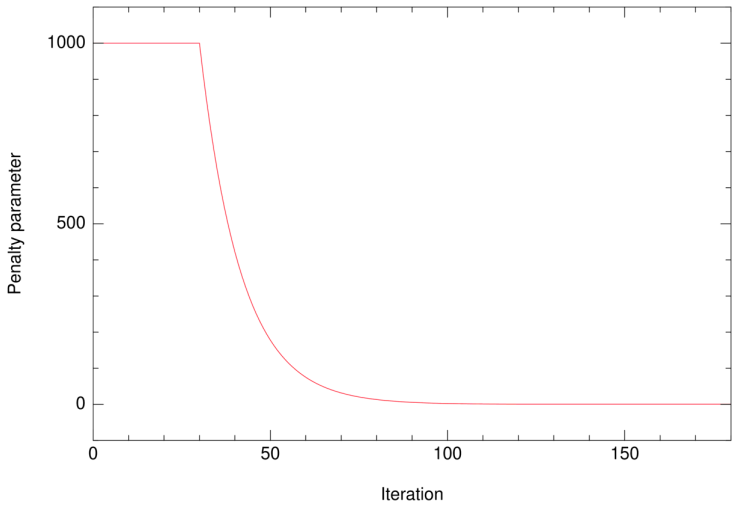

Figure 3.12: Penalty parameter evolution with the Ginzburg-Landau method for $\alpha_0 = 0$

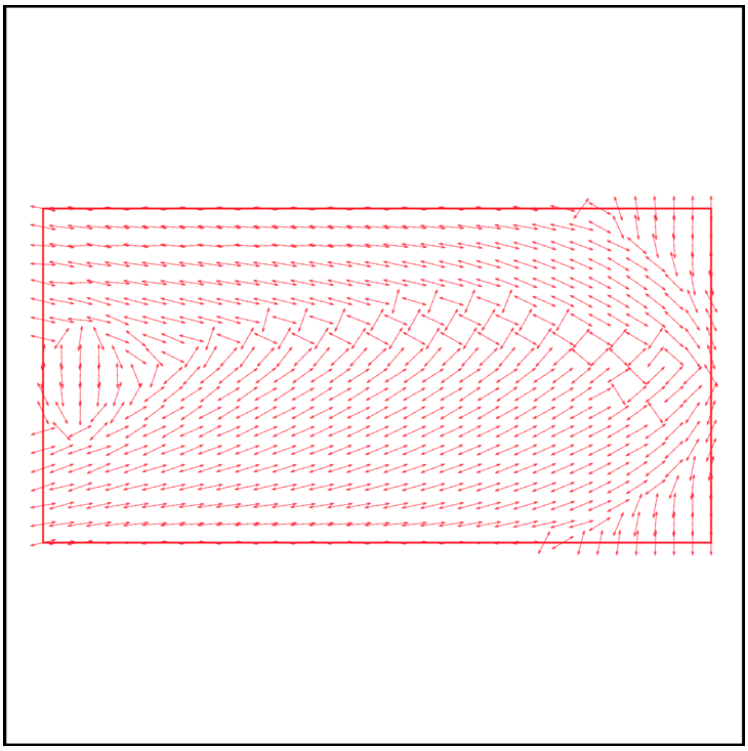

Figure 3.13: Optimized stiffest direction orientation with the Ginzburg-Landau method for $\alpha_0 = \pi/2$

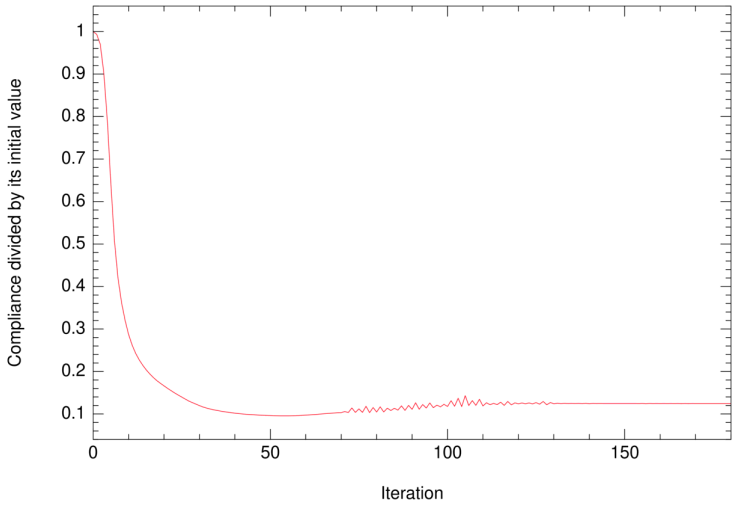

Figure 3.14: Objective function evolution with the Ginzburg-Landau method for $\alpha_0 = \pi/2$

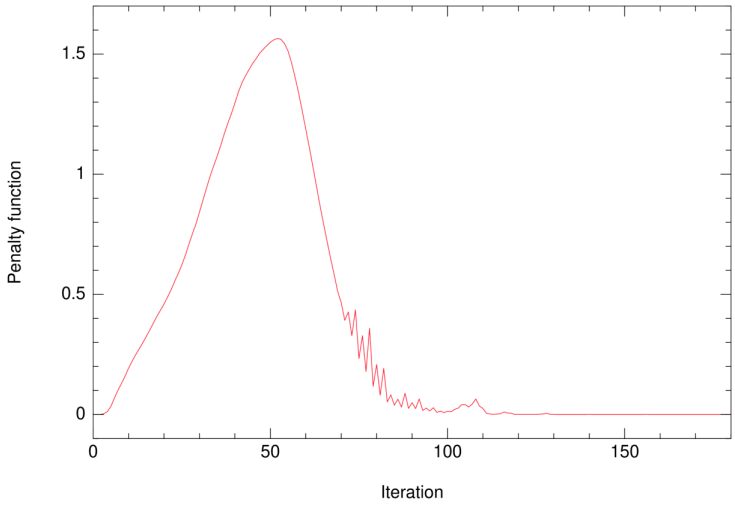

Figure 3.15: Penalty function evolution with the Ginzburg-Landau method for $\alpha_0 = \pi/2$

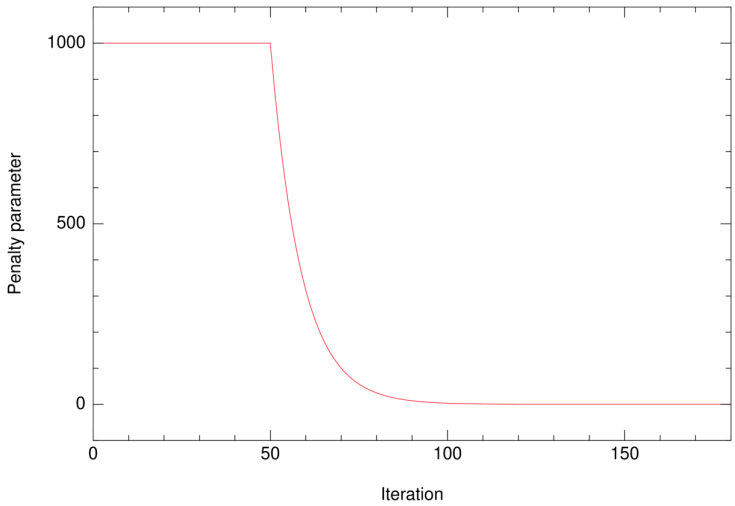

Figure 3.16: Penalty parameter evolution with the Ginzburg-Landau method for $\alpha_0 = \pi/2$

E_{11}	E_{22}	G_{12}	ν_{12}	α_0
10	1	1	0.3	0

Table 3.4: Material characteristics for 2D augmented Lagrangian orientation optimization for an inequality constraint

3.6.4 2D constrained orientation optimization

In all the examples of this section, we study a 2D cantilever of dimensions 2×1 that have the same applied load and boundary conditions as the cantilever of 3.6.1. The used mesh is a triangular mesh of 1891 nodes. The cantilever structure is filled with an orthotropic material characterized by the mechanical moduli given in table 3.3 (the Poisson's ratio ν_{21} is given by $\nu_{21} = \nu_{12}\frac{E_2}{E_1}$). Recall that the material orientation is parameterized by one orientation angle α. We apply the gradient descent orientation optimization algorithm 4 under a generalized constraint that is written $C(\alpha) \leq c$, where $C(\alpha)$ is the constraint function and c is a real constant that we fix before the optimization (see section 3.5.2 for details on the inequality constraint method).

3.6.4.1 Constrained angle's geometrical gradient

In this example, we apply a constraint on the L^2-norm of the geometrical gradient of the type $C(\alpha) = \int_\Omega |\nabla\alpha|^2 \mathrm{d}x \leq c$, for $c = 30$ (see section 3.5.3.1 for more details on the approach). The initial orientation is set horizontally ($\alpha_0 = 0$). We initialize b to 10^5, b_{limit} to 10^7, α_{al} to 1.1 and λ_0 to 0. The algorithm converges in 55 iterations. The obtained orientation is given in figure 3.17. We observe that the constraint $C(\alpha) \leq 30$ is verified by the final orientation (see figure 3.18). Accordingly, we also observe that the final orientation is well regularized in the domain Ω.

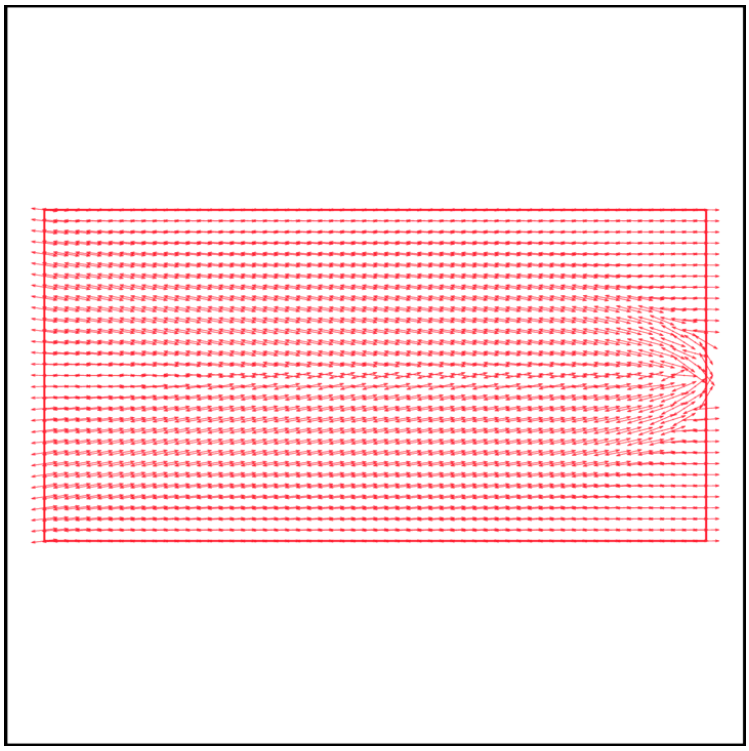

Figure 3.17: Optimized stiffest direction orientation under a constraint on the angle geometrical gradient

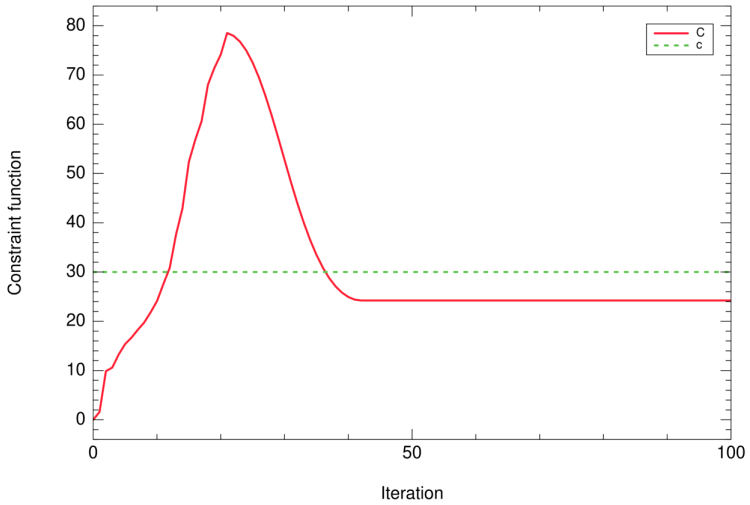

Figure 3.18: Evolution of the constraint function $C(\alpha)$ in the orientation optimization under a constraint on the angle geometrical gradient

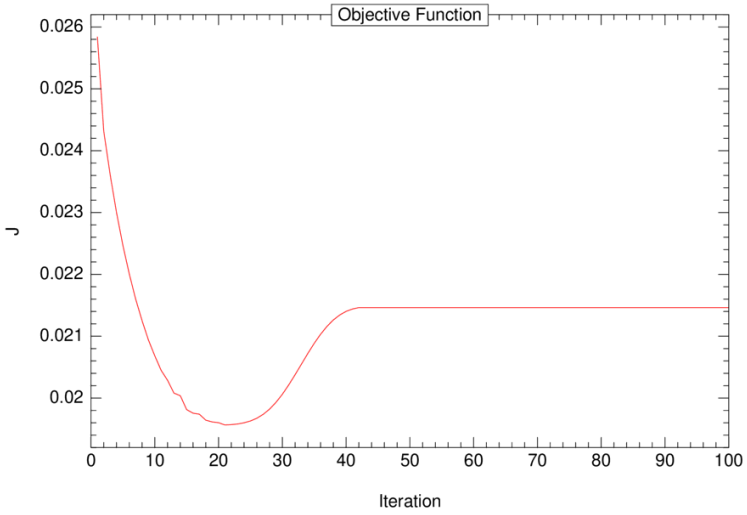

Figure 3.19: Evolution of the compliance in the orientation optimization under a constraint on the angle geometrical gradient

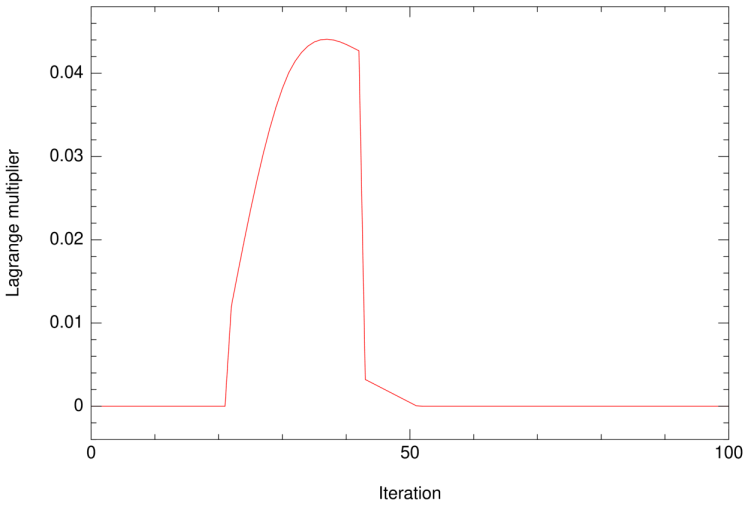

Figure 3.20: Evolution of the Lagrange multiplier in the orientation optimization under a constraint on the angle geometrical gradient

3.6.4.2 Constraint on the orientation angle difference to a fixed angle

In this example, we apply constraint on the L^2-norm of the geometrical partial gradient of the type $C(\alpha) = \int_\Omega |\frac{\partial \alpha}{\partial y}|^2 \mathrm{dx} \leq 15$, for $c = 15$ (see section 3.5.3.2 for more details on the approach). The initial orientation is set horizontally ($\alpha_0 = 0$). We initialize b to 100, b_{limit} to 10^4, α_{al} to 1.1 and λ_0 to 0. The algorithm converges in 90 iterations. The obtained orientation is given in figure 3.17. We observe that the constraint $C(\alpha) \leq 30$ is verified by the final orientation (see figure 3.18).

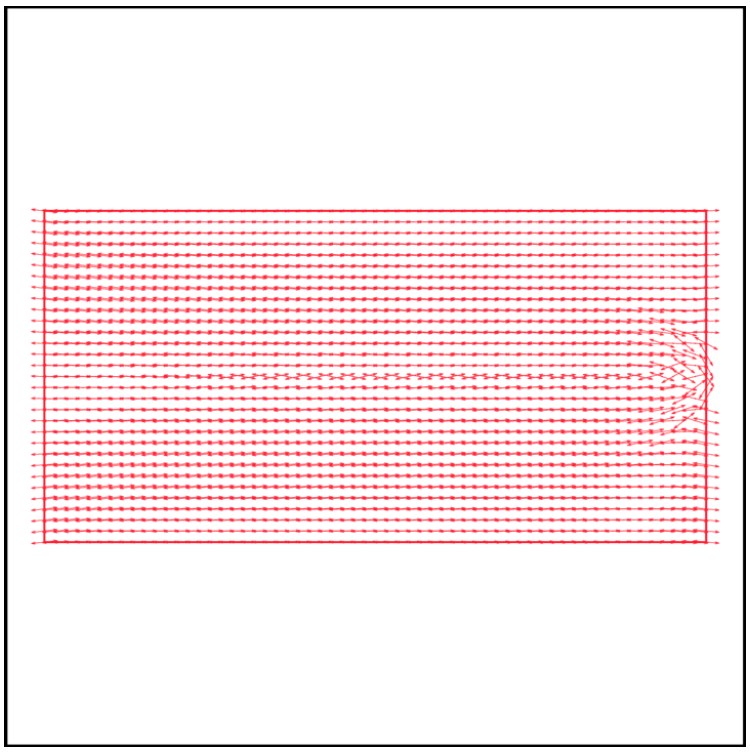

Figure 3.21: Optimized stiffest direction orientation under a constraint on the angle partial gradient with respect to y

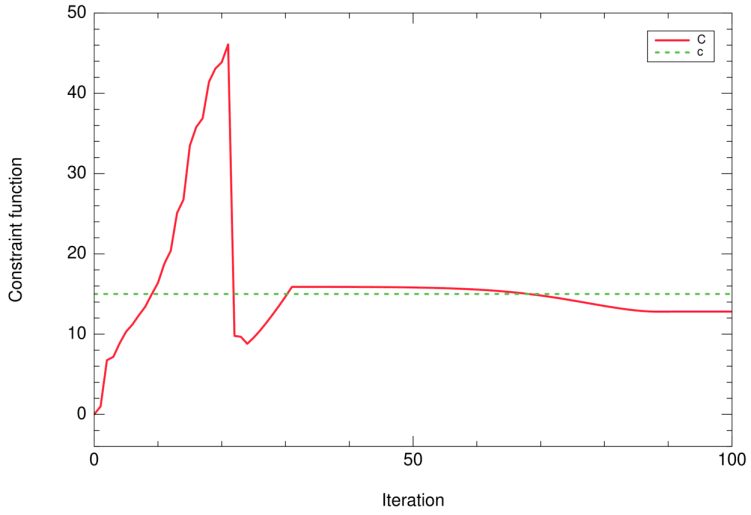

Figure 3.22: Evolution of the constraint function $C(\alpha)$ in the orientation optimization under a constraint on the angle partial gradient with respect to y

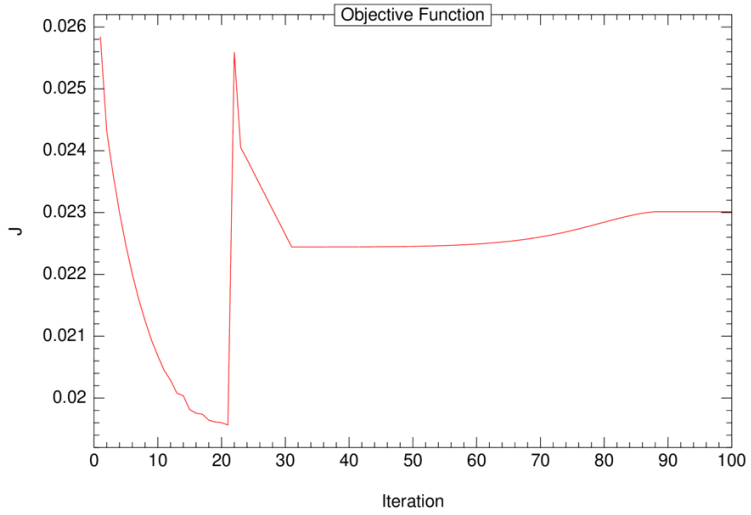

Figure 3.23: Evolution of the compliance in the orientation optimization under a constraint on the angle partial gradient with respect to y

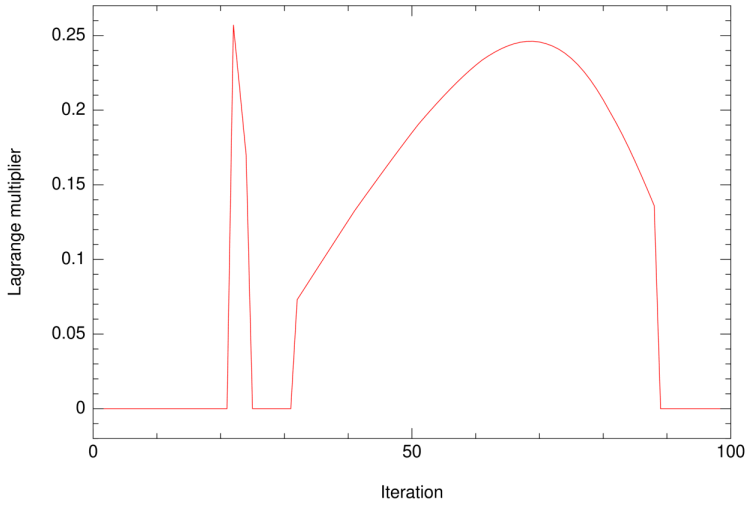

Figure 3.24: Evolution of the Lagrange multiplier in the orientation optimization under a constraint on the angle partial gradient with respect to y

3.6.4.3 2D constrained orientation optimization: constraint 3

Example 1

In this example, we apply the gradient descent orientation optimization algorithm under an upper bound constraint on the $L2$-norm of the difference of the angle α and a fixed angle value $\alpha_f = 0$ (see section 3.5.3.3 for more details on the approach). The initial orientation is set horizontally ($\alpha_0 = 0$). We initialize b to 10, b_{limit} to 10^4, α_{al} to 1.1, c to 0.1 and λ_0 to 0. The algorithm converges in 70 iterations. The obtained orientation is given in figure 3.25. We observe that the constraint $C(\alpha) \leq 0.1$ is verified by the final orientation (see figure 3.26). Accordingly, we also observe that the final orientation is symmetric and well regularized in the domain Ω.

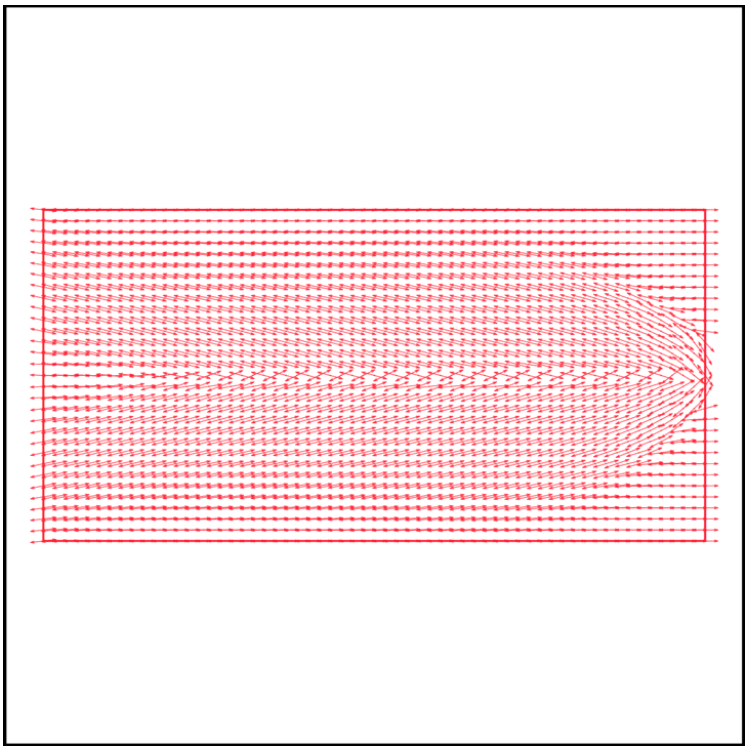

Figure 3.25: Optimized stiffest direction orientation under a constraint of orientation angle difference to a fixed angle (Example 1)

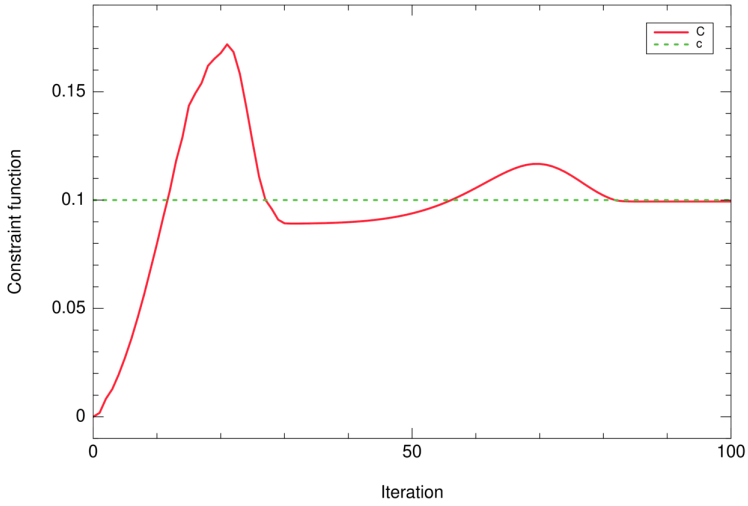

Figure 3.26: Evolution of the constraint function $C(\alpha)$ in the orientation optimization under a constraint of orientation angle difference to a fixed angle (Example 1)

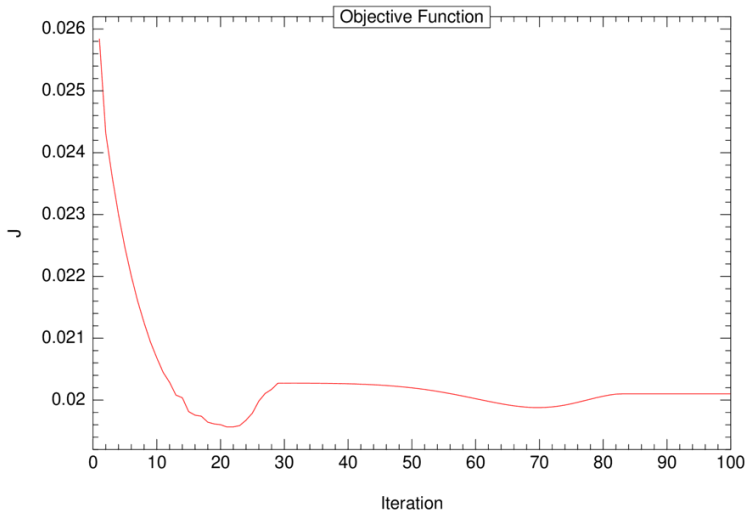

Figure 3.27: Evolution of the compliance in the orientation optimization under a constraint of orientation angle difference to a fixed angle (Example 1)

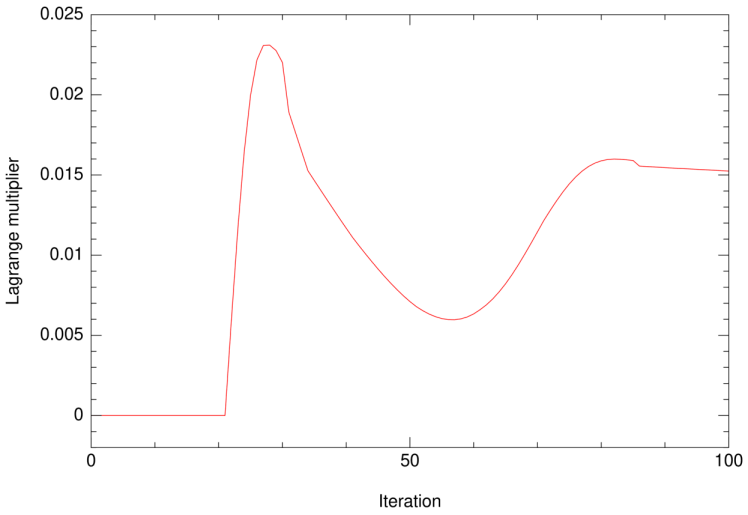

Figure 3.28: Evolution of the Lagrange multiplier in the orientation optimization a constraint of orientation angle difference to a fixed angle (Example 1)

Example 2

We apply an upper bound constraint on the L^2-norm of the difference of the angle α and a fixed angle value α_f that correspond to the orientation of figure 3.29. We set the initial orientation to the orientation of figure 3.29. We set b to 0.001, b_{limit} to 10, α_{al} to 1.3, c to 0.15 and λ_0 to 0. The algorithm converges in 70 iterations. The obtained orientation is given in figure 3.30. We observe that the constraint $C(\alpha) \leq 0.15$ is verified by the final orientation (see figure 3.31).

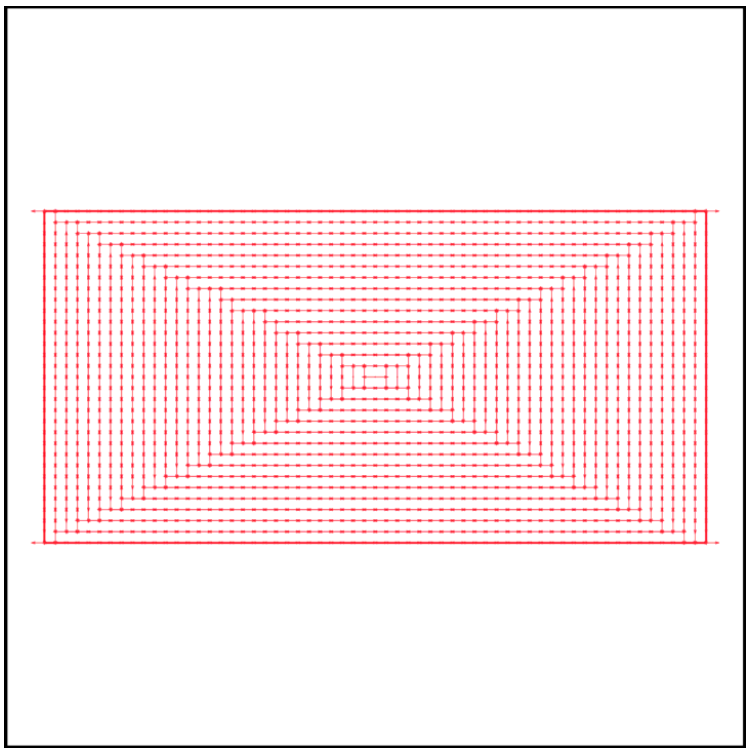

Figure 3.29: Initial stiffest direction orientation for the optimization under a constraint of orientation angle difference to a fixed angle (Example 2)

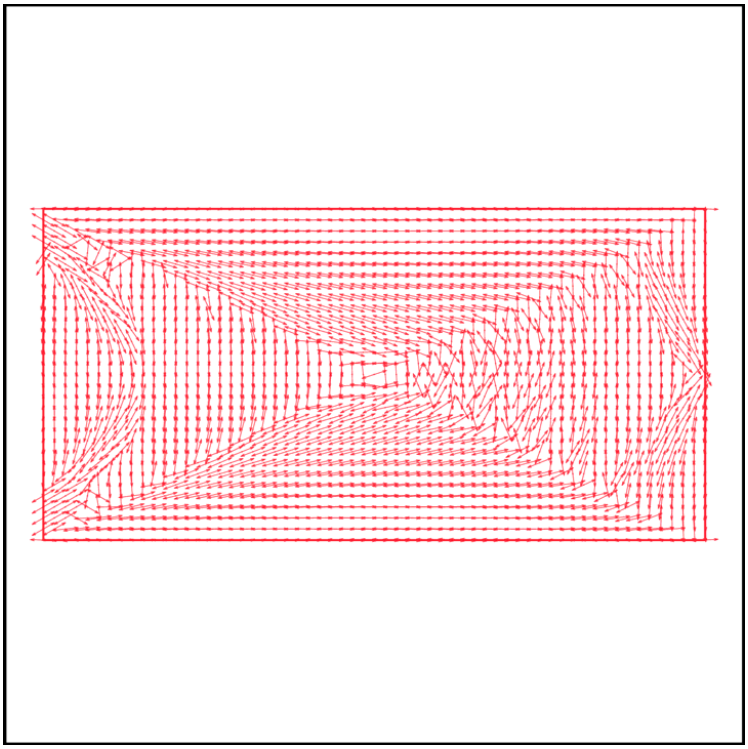

Figure 3.30: Optimized stiffest direction orientation under a constraint of orientation angle difference to a fixed angle (Example 2)

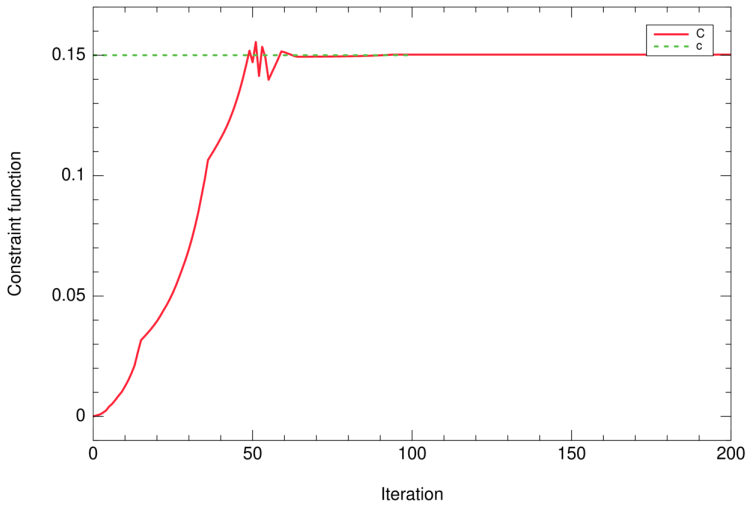

Figure 3.31: Evolution of the constraint function $C(\alpha)$ in the orientation optimization under a constraint of orientation angle difference to a fixed angle (Example 2)

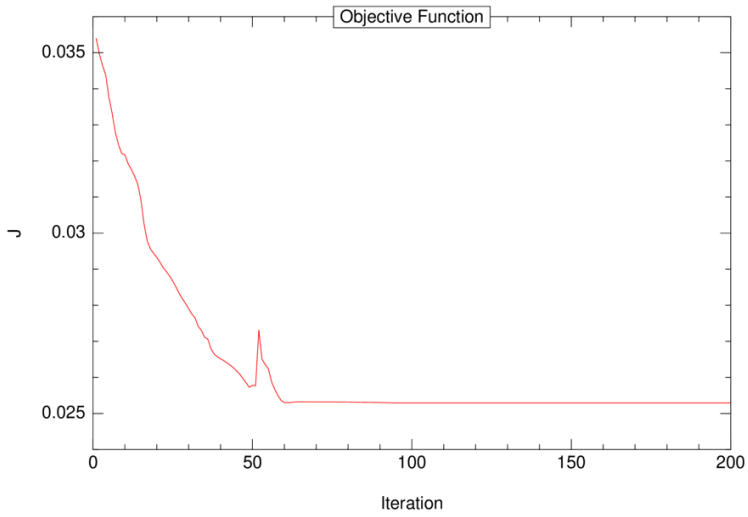

Figure 3.32: Evolution of the compliance in the orientation optimization under a constraint of orientation angle difference to a fixed angle (Example 2)

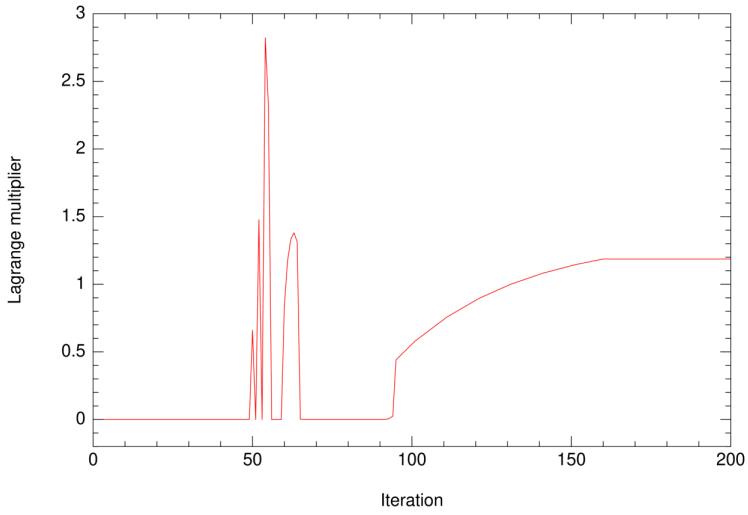

Figure 3.33: Evolution of the Lagrange multiplier in the orientation optimization a constraint of orientation angle difference to a fixed angle (Example 2)

Example 3

We apply an upper bound constraint on the L^2-norm of the difference of the angle α and a fixed angle value α_f that correspond to the orientation of figure 3.34 (see section 3.5.3.3 for more details on the approach). We set the initial orientation to the orientation of figure 3.34. We initialize b to 0.1, b_{limit} to 10^4, α_{al} to 1.3, c to 0.5 and λ_0 to 0. The algorithm converges in 70 iterations. The obtained orientation is given in figure 3.35. We observe that the constraint $C(\alpha) \leq 0.5$ is verified by the final orientation (see figure 3.36).

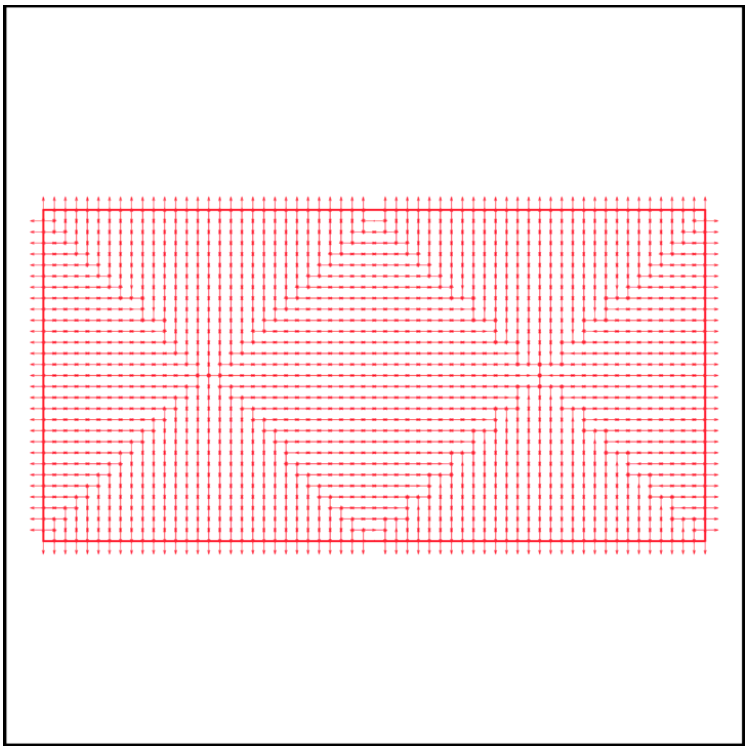

Figure 3.34: Initial stiffest direction orientation for the optimization under a constraint of orientation angle difference to a fixed angle (Example 3)

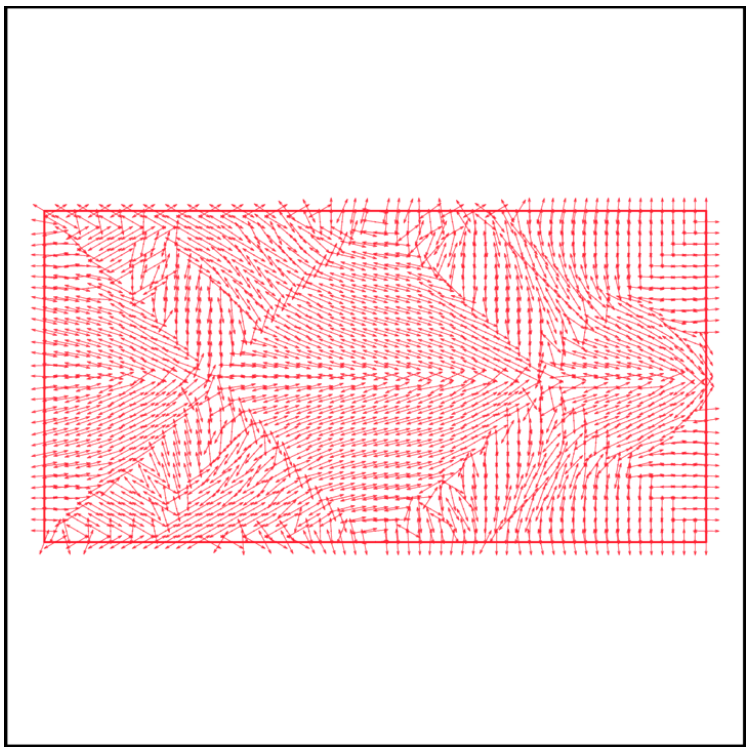

Figure 3.35: Optimized stiffest direction orientation under a constraint of orientation angle difference to a fixed angle (Example 3)

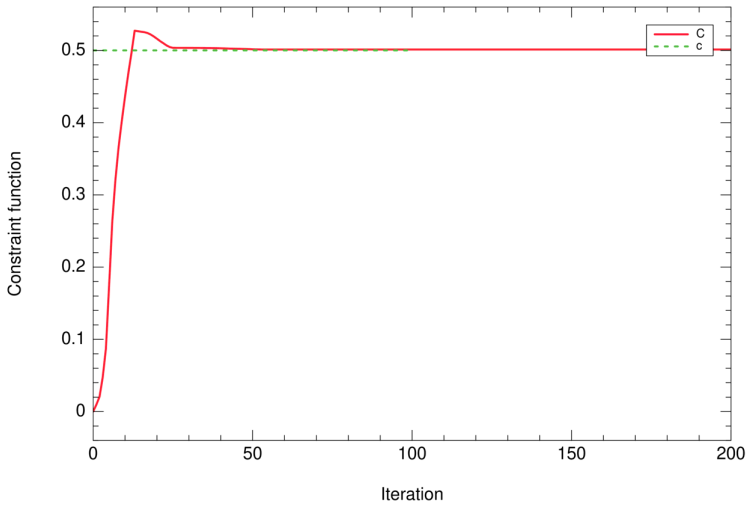

Figure 3.36: Evolution of the constraint function $C(\alpha)$ in the orientation optimization under a constraint of orientation angle difference to a fixed angle (Example 3)

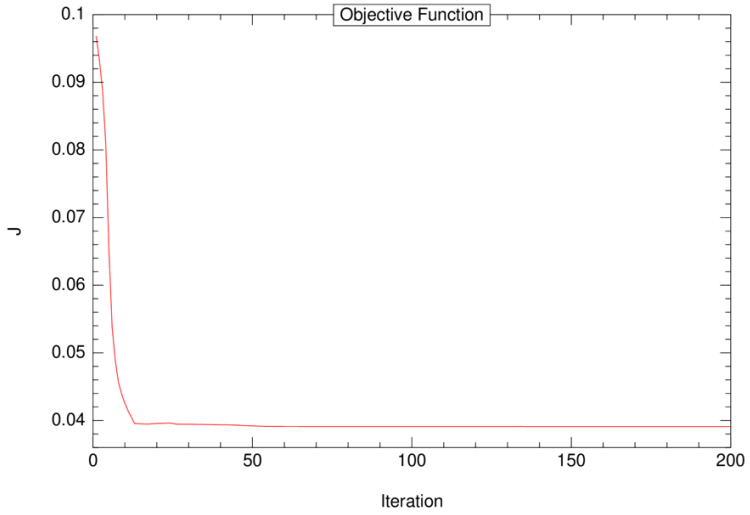

Figure 3.37: Evolution of the compliance in the orientation optimization under a constraint of orientation angle difference to a fixed angle (Example 3)

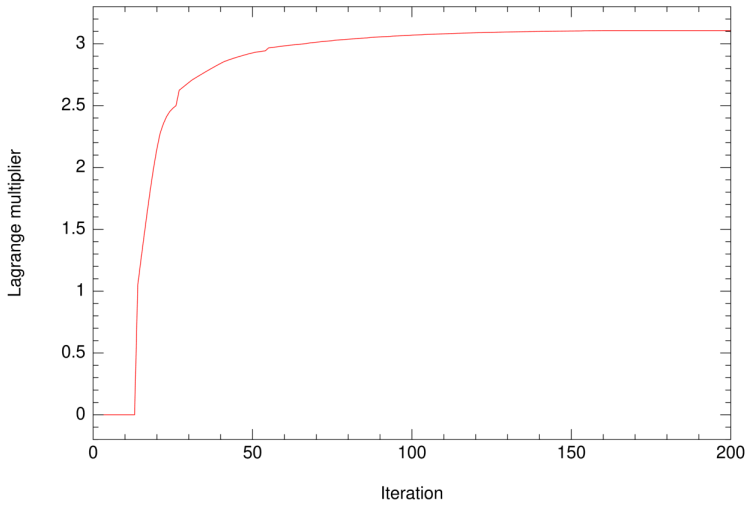

Figure 3.38: Evolution of the Lagrange multiplier in the orientation optimization a constraint of orientation angle difference to a fixed angle (Example 3)

Chapter 4

3D orientation optimization

4.1 Optimal direction using an optimality criterion

We consider a structure in a 3D problem with a fixed shape Ω filled by a linearly elastic anisotropic material with the Hooke's law fourth order elasticity tensor $A^*(\boldsymbol{\alpha})$. Here $\boldsymbol{\alpha}$ is a vector in $\mathbb{R}^N$ ($N = 2$ or 3, depending on the material type) that has the Euler angles, which define the orientation of the material in 3D, as components. The anisotropic material can be a general orthotropic material where we have $\boldsymbol{\alpha} = (\alpha_1, \alpha_2, \alpha_3) \in \mathbb{R}^3$ and the fixed Hooke's law A is written as (2.3), or a transverse isotropic material where we have $\boldsymbol{\alpha} = (\alpha_1, \alpha_2) \in \mathbb{R}^2$ and where A is written as (2.6). In the case of a general orthotropic material, A is defined by the following elasticity moduli: three Young's moduli E_1, E_2 and E_3, six Poisson's ratios ν_{12}, ν_{13}, ν_{23}, ν_{21}, ν_{31} and ν_{32}, related with the three relations $\nu_{21} = \nu_{12}\frac{E_2}{E_1}$, $\nu_{31} = \nu_{13}\frac{E_3}{E_1}$ and $\nu_{32} = \nu_{23}\frac{E_3}{E_2}$, and the three shear moduli G_{23}, G_{13} and G_{12}. We suppose that $E_1 \geq E_2 \geq E_3$. In the second case of transverse isotropic material, A is defined by the following elasticity moduli: two Young's moduli E_1 and E_p, three Poisson's ratios ν_{1p}, ν_{p1} and ν_p, with the relation $\nu_{p1} = \nu_{1p}\frac{E_p}{E_1}$, and one shear modulus G_{1p}. We suppose that $E_1 \geq E_p$.

The elasticity model that we study is the same as (1.1) (only the number of material parameters has changed). We want to find the material local anisotropy orientation everywhere in the domain Ω, that minimizes the compliance of this structure. The compliance objective function is then written as:

$$J(\boldsymbol{\alpha}) = \int_\Omega f u \,\mathrm{dx} + \int_{\Gamma_N} g u \,\mathrm{dx} = \int_\Omega A^*(\boldsymbol{\alpha}) e(u) \cdot e(u) \,\mathrm{dx}\,.$$

The orientation is modeled by the Euler angles vector $\boldsymbol{\alpha}$. Consequently, the set of admissible designs is defined by:

$$\mathcal{U}_{ad} = \left\{ \boldsymbol{\alpha} \in (L^2(\Omega))^N, N = 2 \text{ or } 3 \right\}, \tag{4.1}$$

where N is equal to 2 when the material is transversely isotropic and to 3 for the case of a general orthotropic material.

The optimization problem is then written as:

$$\inf_{\boldsymbol{\alpha} \in \mathcal{U}_{ad}} J(\boldsymbol{\alpha}) \tag{4.2}$$

The approach of optimality criterion in 3D is the same as in 2D, the only difference is that now we have two parameters α_1 and α_2 or three parameters α_1, α_2 and α_3 that should be optimized instead of only one parameter α in 2D.

Using the theorem of complementary energy (see section 2.22 in [2]) that gives:

$$\begin{aligned} \int_\Omega f u \,\mathrm{dx} + \int_{\Gamma_N} g u \,\mathrm{ds} = \quad & \min_{\sigma \in L^2(\Omega; \mathcal{M}_s)} \int_\Omega (A^*(\boldsymbol{\alpha}))^{-1} \sigma \cdot \sigma \,\mathrm{dx}, \\ & \begin{cases} -\operatorname{div} \sigma = f \text{ in } \Omega \\ \sigma n = g \text{ on } \Gamma_N \\ \sigma n = 0 \text{ on } \partial\Omega \setminus (\Gamma_D \cup \Gamma_N) \end{cases} \end{aligned} \tag{4.3}$$

where σ is a statically admissible stress tensor and $\mathcal{M}_s$ is the space of symmetric matrices. We can rewrite the optimization problem (4.2) as a double minimization, one for the orientation (i.e. $\boldsymbol{\alpha}$) and the other one for the admissible stress:

$$\begin{aligned} \inf_{\boldsymbol{\alpha} \in \mathcal{U}_{ad}} \quad & \min_{\sigma \in L^2(\Omega; \mathcal{M}_s)} \int_\Omega (A^*(\boldsymbol{\alpha}))^{-1} \sigma \cdot \sigma \,\mathrm{dx}, \\ & \begin{cases} -\operatorname{div} \sigma = f \text{ in } \Omega \\ \sigma n = g \text{ on } \Gamma_N \\ \sigma n = 0 \text{ on } \partial\Omega \setminus (\Gamma_D \cup \Gamma_N) \end{cases} \end{aligned} \tag{4.4}$$

The order of the two minimizations is unimportant: they can be exchanged or

combined in a single minimization on the pair $(\boldsymbol{\alpha}, \sigma)$. We write (4.4) in the form:

$$\inf_{\boldsymbol{\alpha}\in\mathcal{U}_{ad}} \min_{\sigma\in H_3} \int_\Omega (A^*(\boldsymbol{\alpha}))^{-1}\sigma\cdot\sigma \,\mathrm{dx}, \tag{4.5}$$

where H_3 is given by:

$$\begin{aligned} H_3 = \{\, \sigma \in L^2(\Omega; \mathcal{M}_s), \quad & -\operatorname{div}\sigma = f \text{ in } \Omega, \\ & \sigma n = g \text{ on } \Gamma_N, \quad \sigma n = 0 \text{ on } \partial\Omega \setminus (\Gamma_D \cup \Gamma_N)\} \end{aligned} \tag{4.6}$$

We note that $\mathcal{U}_{ad} \times H_3$ is a non-empty convex closed set. The interest of (4.5) is to exchange the two minimizations, which does not change the problem, and to optimize one and then the other. Note also that we have the same remark 1 in this 3D case.

By exchanging the two minimizations in (4.5), we obtain,

$$\inf_{\sigma\in H_3} \min_{\boldsymbol{\alpha}\in\mathcal{U}_{ad}} \int_\Omega (A^*(\boldsymbol{\alpha}))^{-1}\sigma\cdot\sigma \,\mathrm{dx},$$

It turns out that at fixed σ, it is easy to perform the minimization in the orientation angles vector $\boldsymbol{\alpha}$ in $\mathcal{U}_{ad}$.

Consequently, we have found optimality conditions for the optimization problem (4.2) which are:

1. if we know the optimal σ, then the optimal $\boldsymbol{\alpha}$ is given by solving:

$$\min_{\boldsymbol{\alpha}\in\mathcal{U}_{ad}} \int_\Omega (A^*(\boldsymbol{\alpha}))^{-1}\sigma\cdot\sigma \,\mathrm{dx} \tag{4.7}$$

   Optimizing the integral of (4.7) is equivalent to optimize $(A^*(\boldsymbol{\alpha}))^{-1}\sigma\cdot\sigma$ at every point $x \in \Omega$.

2. if we know the optimal $\boldsymbol{\alpha}$, then the optimal σ is the unique point of minimum of (4.3) (obtained by solving a simple partial differential equation).

4.1.1 Pointwise optimality criterion approach

Same as in 2D, the approach of a pointwise optimality criterion consists of reducing the global minimization problem (4.7) to a local pointwise mechanic

one (in the scale of a node or a finite element). To make such approach possible we suppose that the stress field σ is constant.

The problem of compliance minimization then becomes:

$$\min_{\boldsymbol{\alpha}} j(\boldsymbol{\alpha}) = (A^*)^{-1}(\boldsymbol{\alpha})\sigma \cdot \sigma,$$

which is possible only if

$$\frac{\partial j(\alpha_i)}{\partial \alpha_i} = 0 \text{ for } i \text{ in } 1, 2, 3.$$

One then has to search for the values of α_i that nullify $\frac{\partial j(\alpha_i)}{\partial \alpha_i}$ and then compare the values of the compliance $j(\boldsymbol{\alpha})$ that one get with each combination of the obtained zeros to determine the global minimum, which is the zero triplet that have the lowest compliance value.

4.1.2 Result of the orientation optimality criterion approach

The analysis of this problem is presented in [88, 77]. The optimal orientations are aligned with the directions of principal stresses [77] under certain conditions on the anisotropic material characteristics, that we assume satisfied in this work.

4.1.3 Principal stresses in 3D

To get the optimal orientation of the local anisotropic material one needs to determine the eigenvalues of σ by solving $\det(\sigma - \mathfrak{z} I_d) = 0$ where I_d is the identity matrix. Which gives the cubic characteristic equation:

$$\mathfrak{z}^3 - I_1 \mathfrak{z}^2 + I_2 \mathfrak{z} - I_3 = 0, \tag{4.8}$$

where I_1, I_2 and I_3 are the invariants of the stress tensor that have the expressions:

$$\begin{aligned} I_1 &= \operatorname{tr}(\boldsymbol{\sigma}), \\ I_2 &= \frac{1}{2}\left((\operatorname{tr}(\sigma))^2 - \operatorname{tr}\left(\sigma^2\right)\right), \\ I_3 &= \det(\boldsymbol{\sigma}), \end{aligned}$$

which gives:

$$
\begin{aligned}
I_1 &= \sigma_{11} + \sigma_{22} + \sigma_{33}, \\
I_2 &= \sigma_{11}\sigma_{22} + \sigma_{22}\sigma_{33} + \sigma_{33}\sigma_{11} - \sigma_{12}^2 - \sigma_{13}^2 - \sigma_{23}^2, \\
I_3 &= \sigma_{11}\sigma_{22}\sigma_{33} - \sigma_{11}\sigma_{23}^2 - \sigma_{22}\sigma_{13}^2 - \sigma_{33}\sigma_{12}^2 + 2\sigma_{12}\sigma_{13}\sigma_{23}.
\end{aligned}
$$

Since σ is symmetric, all of its eigenvalues have real values. The real roots of (4.8) are written [105, 113, 70] as:

$$
\begin{aligned}
\mathfrak{z}_1 &= 2\sqrt{-\mathcal{Q}}\cos\left(\frac{\theta}{3}\right) + \frac{1}{3}I_1, \\
\mathfrak{z}_2 &= 2\sqrt{-\mathcal{Q}}\cos\left(\frac{\theta + 2\pi}{3}\right) + \frac{1}{3}I_1, \\
\mathfrak{z}_3 &= 2\sqrt{-\mathcal{Q}}\cos\left(\frac{\theta + 4\pi}{3}\right) + \frac{1}{3}I_1,
\end{aligned}
$$

where θ and $\mathcal{Q}$ are intermediate variables defined by:

$$
\theta = \cos^{-1}\left(\frac{\mathfrak{R}}{\sqrt{-\mathcal{Q}^3}}\right), \quad \mathcal{Q} = \frac{3I_2 - I_1^2}{9},
$$

such that the intermediate variable $\mathfrak{R}$ is written:

$$
\mathfrak{R} = \frac{2I_1^3 - 9I_1I_2 + 27I_3}{54}.
$$

We then order the principal stresses from the greatest to the smallest absolute value and determine their associated eigenvectors e^I, e^{II} and e^{III}, which are also the principal stresses directions. We also choose e^I,e^{II} and e^{III} in a way that makes it an orthonormal basis.

4.1.4 Optimal orthotropic orientation

Suppose that the material is a general orthotropic material defined by (2.3). Let $e^{x_1}e^{y_1}e^{z_1}$, $e^{x_2}e^{y_2}e^{z_2}$ and $e^{x_3}e^{y_3}e^{z_3}$ be respectively the vector bases of the three frames $x^1y^1z^1$, $x^2y^2z^2$ and $x^3y^3z^3$ obtained by the three Euler elementary rotations (figure 4.3).

Let xyz be the canonical fixed frame and $e^Ie^{II}e^{III}$ the direct basis of principal stresses vectors. Recall that a 3D orthonormal basis orientation is determined by 3 elementary rotations using 3 Euler angles. We want to determine those 3

Euler angles for the basis $e^I e^{II} e^{III}$ geometrically ($e^I e^{II} e^{III}$=$e^{x_3} e^{y_3} e^{z_3}$ in this case).

The vector e^{III} is touched only by the second elementary rotation, thus α_2 is deduced by direct trigonometry to obtain:

$$\alpha_2^{opt} = \arccos(e_z^{III}). \tag{4.9}$$

In formula (4.9) α_2 is defined in the range $[0, \pi]$, modulo π.

Denote by OH the projection of e^{III} on the plane xy. The vector e^{x_1} is obtained by rotating the vector e^x of xyz by the angle α_1 in the plane xy. If $e_x^{III} > 0$, the angle α_1 is counterclockwise (or positive). The vector OH is orthogonal to e^{x_1} because e^{x_1} and e^{III} are orthogonal ($e^{x_1} = e^{x_2}$ and $e^{III} = e^{z_2}$). Thus OH make a counterclockwise angle α_1 with the direction of $-e_y$. As a result, we obtain that $\cos\alpha_1 = \frac{-OH_y}{|OH|}$. We also have $|OH| = \sin\alpha_2$ and $OH_y = e_y^{III}$, then the angle α_1 is determined by $\cos\alpha_1 = \frac{-e_y^{III}}{\sin\alpha_2} = \frac{-e_y^{III}}{\sqrt{1-(e_z^{III})^2}}$. If $e_x^{III} < 0$, the angle α_1 is clockwise (or negative), then we have $\cos(-\alpha_1) = \frac{-e_y^{III}}{\sqrt{1-(e_z^{III})^2}}$. If $e_x^{III} = 0$, only two possibilities for OH exist; either in the direction of e^y, where $\alpha_1 = \pi$, or of $-e^y$, where $\alpha_1 = 0$. This analysis leads to the following formula of α_1:

$$\alpha_1^{opt} = \begin{cases} \arccos(\frac{-e_y^{III}}{\sqrt{1-(e_z^{III})^2}}) & \text{if } e_x^{III} > 0 \\ -\arccos(\frac{-e_y^{III}}{\sqrt{1-(e_z^{III})^2}}) & \text{if } e_x^{III} < 0 \\ \pi & \text{if } e_x^{III} = 0 \text{ and } e_y^{III} > 0 \\ 0 & \text{otherwise} \end{cases} \tag{4.10}$$

Denote by OM the projection of e^{II} on the plane zx_1. The vectors e^{II}, e_z and e_{z_2} are in the same plane. If $e^{II} e^{x_1} < 0$, the vector e^{II} make a counterclockwise angle α_3 with the vector e_2 about e_{z_2}. The vectors e^{II}, e_z and e_{z_2} are in the same plane. Thus OM also make a counterclockwise angle α_3 with e_z in the plane zx_1. We obtain then that $\cos\alpha_3 = \frac{OM_z}{|OM|}$. We also have $|OM| = \cos(\pi/2 - \alpha_2) = \sin\alpha_2$ and $OM_z = e_z^{II}$, then the angle α_3 is determined by $\cos\alpha_3 = \frac{e_z^{II}}{\sin\alpha_2} = \frac{e_z^{II}}{\sqrt{1-(e_z^{III})^2}}$. If $e^{II} e^{x_1} > 0$, the angle α_1 is clockwise, then we have $\cos(-\alpha_1) = \frac{e_z^{II}}{\sqrt{1-(e_z^{III})^2}}$. If $e^{II} e^{x1} = 0$, only two possibilities for OM exist; either in the direction of e^z, where $\alpha_3 = 0$, or of $-e^z$, where $\alpha_3 = \pi$. This analysis leads to the following formula of α_3:

$$\alpha_3^{opt} = \begin{cases} \arccos \frac{e_z^{II}}{\sqrt{1-(e_z^{III})^2}} & \text{if } e^{II}e^{x_1} < 0 \\ -\arccos \frac{e_z^{II}}{\sqrt{1-(e_z^{III})^2}} & \text{if } e^{II}e^{x_1} > 0 \\ 0 & \text{if } e^{II}e^{x_1} = 0 \text{ and } e_z^{II} > 0 \\ \pi & \text{otherwise} \end{cases} \tag{4.11}$$

note that we also have:

$$e^{II}e^{x_1} = e_x^{II}\cos(\alpha_1^{opt}) + e_y^{II}\sin(\alpha_1^{opt})$$

In the singular case of $e_z^{III} = \pm 1$, the vector e_x^I stays in the plan xy. Consequently, the third elementary rotation that has the job of pulling out e_x^I from the plane xy is nonexistent, thus:

$$\alpha_3^{opt} = 0, \tag{4.12}$$

and α_1 is obtained by direct trigonometry; if $e_y^I > 0$, the angle α_1 is counterclockwise, then $\alpha_1 = \arccos(e_x^I)$. if $e_y^I < 0$, the angle α_1 is clockwise, then $\alpha_1 = -\arccos(e_x^I)$, and if $e_y^I = 0$, the vector e^I can be either the same as e^x or as -e^x (resp. $\alpha_1 = 0$ or $\alpha_1 = \pi$), which leads to:

$$\alpha_1^{opt} = \begin{cases} \arccos(e_x^I) & \text{if } e_y^I > 0 \\ -\arccos(e_x^I) & \text{if } e_y^I < 0 \\ 0 & \text{if } e_y^I = 0 \text{ and } e_x^I > 0 \\ \pi & \text{otherwise} \end{cases} \tag{4.13}$$

In formulas (4.10) and (4.13), α_1 is defined in the range $[-\pi, \pi]$, modulo 2π. We checked that passing from one regime to another, the result for α_1 is continuous at least modulo 2π. In formulas (4.11) and (4.12), α_3 is defined in the range $[-\pi, \pi]$, modulo 2π. We checked that passing from one regime to another, the result for α_2 is continuous at least modulo 2π.

4.1.5 Optimal transverse isotropic orientation

Suppose that the material is a transverse isotropic material defined by (2.6) Let $e^{x_1}e^{y_1}e^{z_1}$ and $e^{x_2}e^{y_2}e^{z_2}$ be respectively the vector bases of the two frames $x^1y^1z^1$ and $x^2y^2z^2$ obtained by the two Euler elementary rotations (figure 4.3).

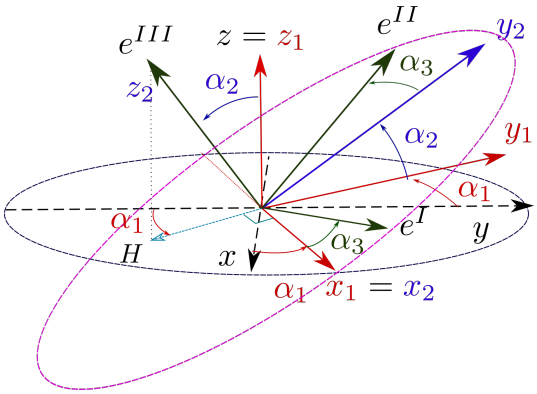

Figure 4.1: Projection of e^{III} on xy

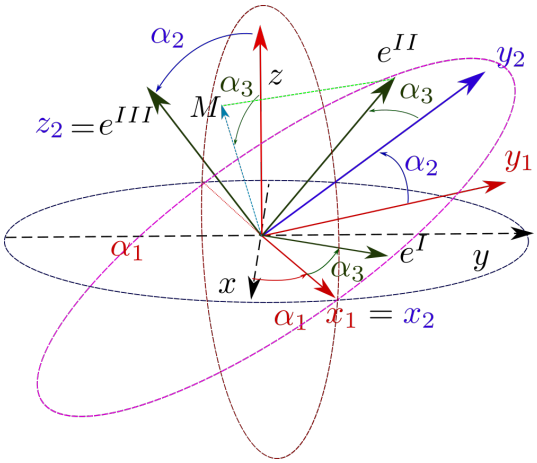

Figure 4.2: Projection of e^{II} on zx_1

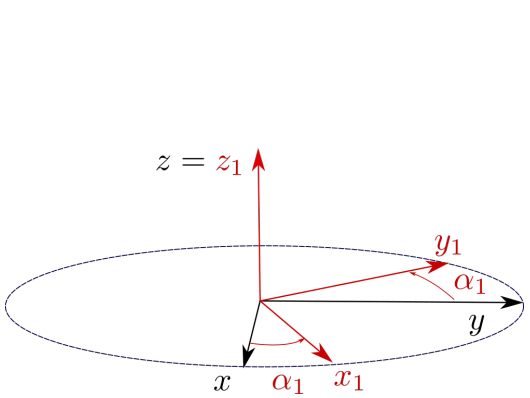

(a) Rotation by the first Euler angle about z'

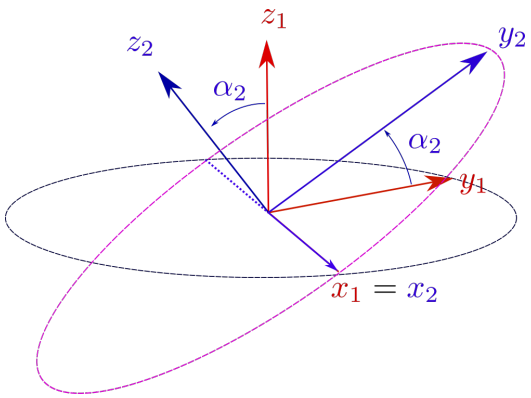

(b) Rotation by the second Euler angle about x_1

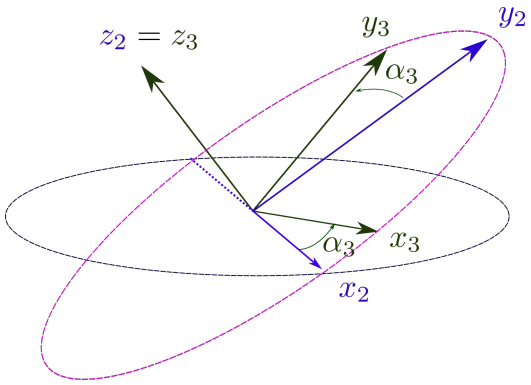

(c) Rotation by the third Euler angle about z_2

Figure 4.3: Rotation of the material frame using Euler angles, $x_3y_3z_3$ takes the orientation of $x'y'z'$

Let xyz be the canonical fixed frame and $e^I e^{II} e^{III}$ the direct basis of principal stresses vectors. In the case of $E_1 \geq E_p$, We orient the rigid material orientation $e^{x'} = e^{x^2}$ in the direction of the vector e^I. We determine the two Euler angles α_1 and α_2 that gives this orientation geometrically.

The vector projection of e^I on the z axis gives $e^I_z = -\sin(\alpha_2)$, thus α_2 is deduced directly by:

$$\alpha_2 = -\arcsin(e^I_z). \tag{4.14}$$

In formula (4.14) α_2 is defined in the range $[0, \pi]$, modulo π.

Denote by OH the projection of e^I on the plane xy. The vector e^{x_1} is obtained by rotating the vector e^x of xyz by the angle α_1 in the plane xy. If $e^I_y \geq 0$, the angle α_1 is counterclockwise (or positive), we also have $|OH| = \cos\alpha_2$ and $OH_x = e^I_x$, then the angle α_1 is determined by $\cos\alpha_1 = \frac{e^I_x}{\cos\alpha_2}$. If $e^I_y < 0$, the angle α_1 is clockwise (or negative), we then obtain $\cos\alpha_1 = \frac{-e^I_x}{\cos\alpha_2}$

$$\alpha_1 = \begin{cases} \arccos(\frac{e_x}{\cos(\alpha_2)}) & \text{if } e_y \geq 0 \\ -\arccos(\frac{e_x}{\cos(\alpha_2)}) & e_y < 0 \end{cases} \tag{4.15}$$

In formula (4.15), α_1 is defined in the range $[0, \pi]$, modulo π. We checked that passing from one regime to another, the result for α_1 is continuous modulo π.

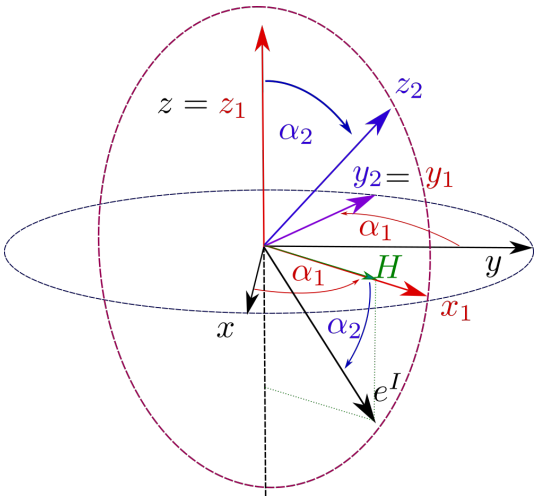

Figure 4.4: Projection of e^I on xy

4.1.6 Optimization algorithm

We deduce an alternate directions minimization algorithm for (4.2), which consists in minimizing successively and alternately in $\boldsymbol{\alpha}$ and in σ.

The alternate directions algorithm is described in algorithm 7.

Algorithm 7: 3D orientation optimization using the optimality criterion

1 Initialize the angles vector $\boldsymbol{\alpha}$.
2 **for** $n = 1, ..,$ *until convergence* **do**
3 Compute the state σ_n, unique solution of:

$$\min_{\sigma \in H} \quad \int_\Omega (A^*(\boldsymbol{\alpha}^n))^{-1}\sigma \cdot \sigma \, \mathrm{dx}, \tag{4.16}$$

4 Update the angles vector $\boldsymbol{\alpha}^n$ to $\boldsymbol{\alpha}^{n+1}$; the angles vector corresponding to the principal stresses directions obtained using the optimality formulas (4.9), (4.10), (4.13), (4.11) and (4.12) in case of a general orthotropic material, and the optimality formulas (4.14) and (4.15) in case of transverse isotropic material.
5 **end**

Note that minimizing (4.16) is equivalent to solving the elasticity equation (1.1) to get the displacement u_n and to determining σ_n by

$$\sigma_n = A^*(\boldsymbol{\alpha}^n)e(u_n)$$

This algorithm is interpreted as an alternating minimization in σ then in the orientation angles vector $\boldsymbol{\alpha}$ of the functional (4.5). In particular, we deduce that the objective function always decreases during the iterations

$$\begin{aligned} J\left(\boldsymbol{\alpha}^{n+1}\right) &= \int_\Omega A^*(\boldsymbol{\alpha}^{n+1})^{-1}\sigma_{n+1} \cdot \sigma_{n+1} dx \\ &\leq \int_\Omega A^*(\boldsymbol{\alpha}^{n+1})^{-1}\sigma_n \cdot \sigma_n dx \\ &\leq \int_\Omega A^*(\boldsymbol{\alpha}^n)^{-1}\sigma_n \cdot \sigma_n dx = J\left(\boldsymbol{\alpha}^n\right) \end{aligned}$$

4.2 Optimal direction using a gradient descent method

We study the model of elasticity (1.1) with the set of admissible designs (4.1), which means that the material that compose Ω can be either a general orthotropic material with the orientation angles vector $\boldsymbol{\alpha} = (\alpha_1, \alpha_2, \alpha_3) \in \mathbb{R}^3$, or a transverse isotropic material with the orientation angles vector $\boldsymbol{\alpha} = (\alpha_1, \alpha_3) \in \mathbb{R}^2$. We suppose a general objective function $J(\boldsymbol{\alpha})$ that is the sum of the integral of the function j defined on Ω and of the integral of the function l defined on Γ_J, where Γ_J do not intersect the Dirichlet boundary Γ_D (see figure 3.1).

$$J(\boldsymbol{\alpha}) = \int_\Omega j(u)\mathrm{d}x + \int_{\Gamma_J} l(u)\mathrm{d}s. \tag{4.17}$$

The orientation optimization problem is then written as:

$$\inf_{\boldsymbol{\alpha}\in\mathcal{U}_{ad}} J(\boldsymbol{\alpha}) \tag{4.18}$$

As with 2D orientation optimization, we notice that the orientation optimization problem is expressed in the same way of a parametrical shape optimization problem. Consequently, we use the theorem 1.1.1 to get the expression of the gradient of the objective function with respect to each angle α_i, which gives:

$$\frac{\partial J(\boldsymbol{\alpha})}{\partial \alpha_i} = -\frac{\partial A^*(\boldsymbol{\alpha})}{\partial \alpha_i} e(u) \cdot e(p), \tag{4.19}$$

where p is the adjoint displacement obtained by solving the adjoint problem (1.9).

If we write (4.19) using the Kelvin notation, replacing the expression of the derivative $\frac{\partial \hat{A}^*(\boldsymbol{\alpha})}{\partial \alpha_i}$ by the expression of (3.17) (which is also applicable in the 3D case, for each Euler orientation angle α_i) gives:

$$\frac{\partial J(\boldsymbol{\alpha})}{\partial \alpha_i} = -\Big\{e(u)\Big\}\Big(P_{\alpha_i}\hat{A}^*(\boldsymbol{\alpha}) + \hat{A}^*(\boldsymbol{\alpha})P_{\alpha_i}^t\Big)\Big\{e(p)\Big\}, \tag{4.20}$$

where $\Big\{e(u)\Big\}$ and $\Big\{e(p)\Big\}$ are respectively the two Kelvin notation strain vectors

for the strain tensor $e(u)$ and the adjoint strain tensor $e(p) = \frac{1}{2}(\nabla p + (\nabla p)^t)$, and where P_{α_i} is the constant matrix of (3.16) for each Euler angle α_i.

4.2.1 Algorithm

Algorithm 8: 3D orientation optimization using the gradient descent

Initialize the angles vector $\boldsymbol{\alpha}^0$.
Compute the displacement u_0 by solving the elasticity problem.
Compute the objective function $J(\boldsymbol{\alpha}^0)$.
for $n = 1, ..,$ *until convergence* **do**
  for $i = 1..N$ *(*$N = 2$ *or* 3*)* **do**
    Compute the gradient $\frac{\partial J(\boldsymbol{\alpha})}{\partial \alpha_i}$ using (4.20).
    $\alpha_i^n = \alpha_i^{n-1} - t_n \frac{\partial J(\boldsymbol{\alpha}^n)}{\partial \alpha_i^n}$, where t is a small descent step.
    compute u_n.
  end
  Compute the objective function $J(\boldsymbol{\alpha}^n)$.
  if $J(\boldsymbol{\alpha}^n) < J(\boldsymbol{\alpha}^{n-1})$ **then**
    $t_{n+1} = 1.2t_n$ and continue to the next iteration.
  else
    $t_{n+1} = t_n/2$ and return to step 5.
  end
end

4.3 Regularization of orientation

4.3.1 Regularization of a given orientation field

The problem of regularization of the Euler angles in 3D is that we do not only want to regularize the three orientation directions, but that we also want to keep the three directions of the material orthogonal. For the regularization of a given orientation field [50, 49] this can be achieved by regularizing a symmetric matrix M that has $Q(\boldsymbol{\alpha})$, the rotation matrix associated to the Euler angles α_1, α_2 and α_3, as a transformation matrix to a basis where M becomes diagonal and all the algebraic multiplicities of its eigenvalues are equal to one. The

diagonal matrix denoted D is chosen arbitrary as :

$$D = \begin{pmatrix} 1 & 0 & 0 \\ 0 & -1 & 0 \\ 0 & 0 & 0 \end{pmatrix},$$

The matrix M is then expressed as:

$$M(\boldsymbol{\alpha}) = Q(\boldsymbol{\alpha}) \begin{pmatrix} 1 & 0 & 0 \\ 0 & -1 & 0 \\ 0 & 0 & 0 \end{pmatrix} Q(\boldsymbol{\alpha})^T.$$

The regularized objective function thus is written:

$$J_{reg}(\boldsymbol{\alpha}) = \int_\Omega \left(A(\alpha)^{-1}\sigma \cdot \sigma + \eta^2 \|\nabla M(\boldsymbol{\alpha})\|^2 \right) \mathrm{dx}. \tag{4.21}$$

Where $\|\cdot\|$ denotes the Frobenius norm and η the regularization parameter (or the penalty coefficient).

The method of regularization that we used is developed and explained in [50] (and in [49] in section 7.4.3), it briefly consist of finding numerically the closest directions to the unregularized material directions that minimize $J_{reg}(\boldsymbol{\alpha})$.

4.4 Constrained orientation optimization

The aim of this section is to present two constrained optimization methods for different types of constraints. The first method is a projected gradient method that we developed for transverse isotropic materials. The latter method is an augmented Lagrangian method that deals with inequality constraints and that handles both transverse isotropic and general orthotropic materials.

4.4.1 Projected gradient descent

We suppose that we work with a transverse isotropic material that has a Hooke's tensor $A(\boldsymbol{\alpha})^*$ (defined in section 2.2.2.2) with the following mechanical moduli; two Young's moduli E_1 and E_p, three Poisson's ratios ν_{1p}, ν_{p1} and ν_p, with the relation $\nu_{p1} = \nu_{1p}\frac{E_p}{E_1}$, and one shear modulus G_{1p}. The Euler angles vector $\boldsymbol{\alpha} = (\alpha_1, \alpha_2) \in L^2(\Omega)$ defines the orientation of the material frame $x'y'z'$ through two elementary rotations (see section 2.2.3.2).

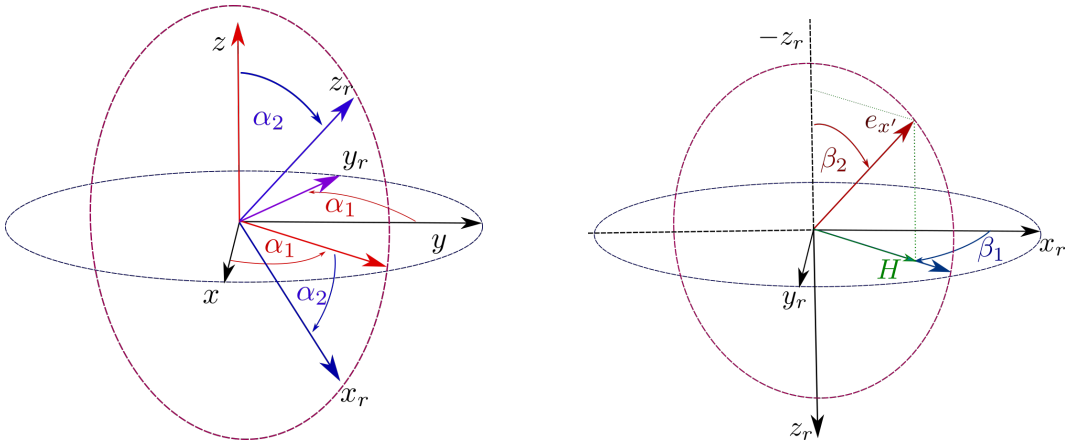

(a) Orientation of the frame $x_r y_r y_r$ with respect to xyz

(b) Orientation of the vector $e_{x'}$ with respect to the frame $x_r y_r y_r$

Figure 4.5: Frames of a 3D orientation projection for a transverse isotropic material

The projected gradient descent in 3D consists of projecting the orientation into a set of admissible orientations after each update of the angles vector during a gradient descent optimization loop. We define the set of admissible orientations as the set of orientations that make an angle, that we denote β_2, with a fixed axis a_r, and where the angles β_2 belong to a fixed interval $[\beta_2^{\min}, \beta_2^{\max}]$. The set of admissible designs is then expressed as:

$$\mathcal{U}_{ad} = \{\boldsymbol{\alpha} \in L^2(\Omega) \quad \text{s.t} \quad \beta_2(\boldsymbol{\alpha}) \in [\beta_2^{\min}, \beta_2^{\max}]\}.$$

Applying the Euler angles approach, we define a frame $\mathcal{R}_r = x_r y_r z_r$ that is fixed, and that is obtained as a result of two elementary rotations of the frame $\mathcal{R}_G = xyz$, using two Euler angles: first α_1^r about z, then α_2^r about y_r (see figure 4.5). We set the axis z_r as the axis a_r, and we define the angle β_2 from the vector $-e^z$, that we denote e^{a_r}, to the vector $e^{x'}$ (see figure 4.5b).

The value of β_2 is obtained directly using trigonometric geometry:

$$\beta_2 = -\arccos e_{z_r}^{x'}, \tag{4.22}$$

where $e_{z_r}^{x'}$, obtained by projecting $e^{x'}$ on axis z_r, is the third component of $e^{x'}$ in the frame $\mathcal{R}_r$.

Thus we obtain the projection $\bar{\beta}_2^n$, for $n \in \mathbb{N}$ by:

$$\bar{\beta}_2^n = \max(\min(\beta_2^n, \beta_2^{\max}), \beta_2^{\min}).$$

We also introduce another angle β_1 from e^x to the vector OH, which is the projection of the vector $e^{x'}$ in the plane $e^{x_r}e^{y_r}$ (see figure 4.5b).

The role of β_1 and β_2 is to orient the direction vector $e^{x'}$ with respect to the frame $\mathcal{R}_r$. Once written in $\mathcal{R}_r$, the direction vector can be expressed in R_G using the Euler rotations approach to determine the angle vector $\boldsymbol{\alpha}$ after the projection.

To determine β_1, we use the projection vector OH, which is obtained by:

$$OH = e^{x'} - e^{x'}_{z_r} e^{z_r}.$$

If $|OH| = 0$, the value β_1 can be anything, thus we set β_1 to zero. If $|OH| \neq 0$, then two cases are possible; the first is when the second component of $e^{x'}$ on the frame $\mathcal{R}_r$, denoted $e^{x'}_{y_r}$, is positive. In this case, β_2 is obtained by $\arccos(\frac{e^{x'}_{x_r}}{|OH|})$. The second case is when $e^{x'}_{y_r}$ is strictly negative, where β_2 becomes therefore equal to $-\arccos(\frac{e^{x'}_{x_r}}{|OH|})$. In a broad sense, when $|OH| \neq 0$, the angle β_1 is obtained by:

$$\beta_1 = \begin{cases} \arccos(\frac{e^{x'}_{x_r}}{|OH|}) & e^{x'}_{y_r} \geq 0 \\ -\arccos(\frac{e^{x'}_{x_r}}{|OH|}) & e^{x'}_{y_r} < 0. \end{cases} \tag{4.23}$$

Note that β_1 is defined in the range $[-\frac{\pi}{2}, \frac{\pi}{2}]$ modulo π and that passing from one regime to another, the result (4.23) for β_1 is continuous modulo π. The angle β_2 is defined in the range $[0, \pi]$ modulo π. Note also that for (4.22) and (4.23), the pair (β_1, β_2) is supposed in the interval $[0, \pi], [-\frac{\pi}{2} \times \frac{\pi}{2}]$. If $e^{x'} < 0$, and before computing (4.22) and (4.23) we flip the vector $e^{x'}$ to get the angles (β_1, β_2) in the interval $[0, \pi] \times [-\frac{\pi}{2}, \frac{\pi}{2}]$. Finally, we compute the material orientation vectors $e^{x'}e^{y'}e^{z'}$ in the reference $\mathcal{R}_r$ and we deduce the angles vector $\boldsymbol{\alpha}$ similarly to deducing it from the directions of principal stresses (in sections 4.1.4 and 4.1.5).

4.4.2 Augmented Lagrangian for inequality constraint

Similarly to the case of 2D orientation optimization in Section 3.5.2, and quite often, one has to include some inequality constraints to the 3D orientation of an orthotropic material. Consider a general orthotropic material oriented by three Euler angles or a transverse isotropic material oriented by two Euler angles. Let $\boldsymbol{\alpha} \in (L^2(\Omega))^N$ be the Euler angles vector, where $N = 2$ for the transverse isotropic material case and $N = 3$ for the general orthotropic material case. Suppose that we have one inequality constraint of the form $C(\boldsymbol{\alpha}) \leq c$, where $c \in \mathbb{R}$ is a given limit value. The optimization problem is then written:

$$\inf_{\alpha \in \mathcal{U}_{ad}} J(\alpha), \tag{4.24}$$

with the set of admissible variables:

$$\mathcal{U}_{ad} = \left\{ \boldsymbol{\alpha} \in (L^2(\Omega))^N, \quad C(\boldsymbol{\alpha}) \leq c \right\}.$$

To transform the problem (4.24) into an unconstrained problem, we use the first method of augmented Lagrangian that we introduced in (3.26) [76]. For the iteration $n \in \mathbb{N}$, the new objective function of the augmented Lagrangian is written:

$$\mathcal{L}_{al}(\boldsymbol{\alpha}, \lambda) = J(\boldsymbol{\alpha}) - \lambda(c - C(\boldsymbol{\alpha})) - \frac{b}{2} \left(\lambda - \lambda_{n-1}\right)^2, \tag{4.25}$$

where $\lambda \in \mathbb{R}_+$ is the Lagrange multiplier, λ_{n-1} is the previous estimate of the Lagrange multiplier obtained from the previous iteration and $b \in \mathbb{R}_+^*$ is a penalty parameter of the quadratic penalization in (4.25). Consequently, the constrained problem (4.24) changes into the following unconstrained problem:

$$\min_{\boldsymbol{\alpha} \in (L^2(\Omega))^N} \max_{\lambda \in \mathbb{R}_+} \mathcal{L}_{al}(\boldsymbol{\alpha}, \lambda). \tag{4.26}$$

For an iteration $n \in \mathbb{N}$, the augmented Lagrangian algorithm proceeds by alternating the resolution of (3.20) for fixed values of the parameters λ_n and b_n, and the update of the latter according to:

$$\lambda_{n+1} = \begin{cases} \lambda_n - \frac{1}{b_n} \left(c - C\left(\boldsymbol{\alpha}_n\right)\right) & \text{if} \quad \lambda_n - \frac{1}{b_n} \left(c - C\left(\boldsymbol{\alpha}_n\right)\right) \geq 0 \\ 0 & \text{otherwise,} \end{cases}$$

and:

$$b_{n+1} = \begin{cases} \alpha_{al} b_n & \text{if } b_n < b_{\text{target}} \\ b_n & \text{otherwise,} \end{cases}$$

for $\alpha_{al} > 1$. Note that it is unnecessary to make b_n tend to infinity to satisfy the Lagrange multiplier move constraint. Thus we gradually increase the value of b until it reaches the targeted value that is initially defined.

To obtain a smooth variation of the angles vector $\boldsymbol{\alpha}$, we chose to work with $\boldsymbol{\alpha}$ defined in $H^1(\Omega)$ instead of $L^2(\Omega)$, with the inner product:

$$a(u, v) = \int_\Omega \nabla u \nabla v \, \mathrm{d}x + \int_\Omega uv \, \mathrm{d}x,$$

instead of $\int_\Omega uv \, \mathrm{d}x$. Hence (4.26) becomes:

$$\min_{\boldsymbol{\alpha} \in (H^1(\Omega))^N} \max_{\lambda \in \mathbb{R}_+} \mathcal{L}_{al}(\boldsymbol{\alpha}, \lambda).$$

The inequality constraint augmented Lagrangian gradient descent algorithm works by replacing the partial gradient $\frac{\partial \mathcal{L}(\boldsymbol{\alpha}, \boldsymbol{p})}{\partial \alpha_i}$ with respect to each angle α_i in algorithm 8, for $0 \leq i \leq N$, by the expression:

$$\frac{\partial \mathcal{L}(\boldsymbol{\alpha}, p, \lambda)}{\partial \alpha_i} = -\frac{\partial A^*(\boldsymbol{\alpha})}{\partial \alpha_i} e(u) \cdot e(p) + \lambda \frac{\partial C(\boldsymbol{\alpha})}{\partial \alpha_i},$$

which is also obtained by applying the theorem 1.1.1, where p is the adjoint displacement that is obtained by solving some adjoint problem.

4.4.3 Examples using an augmented Lagrangian for inequality

In this section, we give some examples of constraints that we have applied to the orientation angle vector $\boldsymbol{\alpha}$ during the 3D optimization using the inequality constraint augmented Lagrangian. The examples are the same examples as the one studied in 2D case, but adapted to the 3D case.

4.4.3.1 Constraint on the angle's gradient

This example consists of optimizing the orientation angle vector $\boldsymbol{\alpha}$ under a constraint $C(\boldsymbol{\alpha}) \leq c$, where $C(\boldsymbol{\alpha})$ is given by the sum of the L^2-norms of the

geometrical gradients of each Euler angle:

$$C(\boldsymbol{\alpha}) = \int_\Omega \sum_{i=1}^{N} |\nabla \alpha_i|^2 \mathrm{dx}.$$

The optimization problem is then equivalent to (4.24) but with the set of admissible designs:

$$\mathcal{U}_{ad} = \left\{ \boldsymbol{\alpha} \in (H^1(\Omega))^N, \quad C(\boldsymbol{\alpha}) \leq c \right\}.$$

The augmented objective function is then defined as:

$$\mathcal{L}_{al}(\boldsymbol{\alpha}, \lambda) = J(\alpha) - \lambda \left(c - \int_\Omega \sum_{i=1}^{N} |\nabla \alpha_i|^2 \mathrm{dx} \right) - \frac{1}{2b} \left(\lambda - \lambda_{n-1} \right)^2.$$

To obtain the augmented Lagrangian function derivative with respect to each Euler angle α_i, for $0 \leq i \leq N$, we need to calculate $\frac{\partial C(\boldsymbol{\alpha})}{\partial \alpha_i}$, which can be obtained using a directional derivative. Thus, $\forall \beta \in H^1(\Omega)$:

$$< \frac{\partial C(\boldsymbol{\alpha})}{\partial \alpha_i}, \beta >= \int_\Omega \nabla \frac{\partial C(\boldsymbol{\alpha})}{\partial \alpha_i} \nabla \beta + \frac{\partial C(\boldsymbol{\alpha})}{\partial \alpha_i} \beta \mathrm{dx} = 2 \int_\Omega \nabla \alpha_i \nabla \beta \mathrm{dx}.$$

Consequently, $\frac{\partial C(\boldsymbol{\alpha})}{\partial \alpha_i}$ is obtained by solving the variational problem:

find $\frac{\partial C(\boldsymbol{\alpha})}{\partial \alpha_i}$, such that $\forall \beta \in H^1(\Omega)$,

$$\int_\Omega \nabla \frac{\partial C(\boldsymbol{\alpha})}{\partial \alpha_i} \nabla \beta + \frac{\partial C(\boldsymbol{\alpha})}{\partial \alpha_i} \beta \mathrm{dx} = 2 \int_\Omega \nabla \alpha_i \nabla \beta \mathrm{dx}.$$

Note that remark 3 page 72 done in the 2D context, still holds in 3D, which means that if we had worked with each Euler angle α_i defined in the space $L^2(\Omega)$ instead of $H^1(\Omega)$, we would have:

$$\int_\Omega \frac{\partial C(\boldsymbol{\alpha})}{\partial \alpha_i} \beta \ \mathrm{dx} = 2 \int_\Omega \nabla \alpha_i \nabla \beta \ \mathrm{dx}, \tag{4.27}$$

for each α_i.

4.4.3.2 Constraint on the angle's partial gradient

In this example, we apply an inequality constraint of the type $C(\boldsymbol{\alpha}) \leq c$ on the sum of the $L2$-norms of the geometrical partial derivatives of each angle $\boldsymbol{\alpha_i}$ with respect to a chosen coordinate, let's say, for example, the coordinate y (with $\mathrm{dx} = (x, y, z)$). The value $c \in \mathbb{R}$ is a fixed upper bound and $C(\boldsymbol{\alpha})$ is given in this case by:

$$C(\boldsymbol{\alpha}) = \int_\Omega \sum_{i=1}^{N} \left| \frac{\partial \alpha_i}{\partial y} \right|^2 \mathrm{dx}.$$

For $\boldsymbol{\alpha} \in (H^1(\Omega))^N$, using the same method described in Section 4.4.3.1, the gradient of $C(\boldsymbol{\alpha})$ with respect to each angle α_i is obtained by solving the following variational problem:

find $\frac{\partial C(\boldsymbol{\alpha})}{\partial \alpha_i}$, such that $\forall \beta \in H^1(\Omega)$,

$$\int_\Omega \nabla \frac{\partial C(\boldsymbol{\alpha})}{\partial \alpha_i} \nabla \beta + \frac{\partial C(\boldsymbol{\alpha})}{\partial \alpha_i} \beta \mathrm{dx} = 2 \int_\Omega \frac{\partial \alpha_i}{\partial y} \frac{\partial \beta}{\partial y} \mathrm{dx}.$$

4.4.3.3 Constraint on the orientation difference to a mean fixed orientation

In this example, we add an inequality constraint of the type $C(\boldsymbol{\alpha}) \leq c$ on the L^2-norm of the angle that the orientation $e^{x'}$ makes with some fixed orientation e^f, or in another words, the scalar product of those two orientations. Where the value $c \in \mathbb{R}$ is a fixed upper bound and $C(\boldsymbol{\alpha})$ is given in this case by:

$$C(\boldsymbol{\alpha}) = \int_\Omega |1 - e^{x'}(\alpha) e^f|^2 \mathrm{dx}.$$

For $\boldsymbol{\alpha} \in (H^1(\Omega))^N$ and by using the same reasoning of section 4.4.3.1, the partial gradient of $\boldsymbol{\alpha}$ with respect to one Euler angle α_i is obtained by solving the following variational problem:

find $\frac{\partial C(\boldsymbol{\alpha})}{\partial \alpha_i}$, such that $\forall \beta \in H^1(\Omega)$,

$$\int_\Omega \nabla \frac{\partial C(\boldsymbol{\alpha})}{\partial \alpha_i} \nabla \beta + \frac{\partial C(\boldsymbol{\alpha})}{\partial \alpha_i} \beta \mathrm{dx} = -2 \int_\Omega \frac{\partial e^{x'}(\boldsymbol{\alpha}) e^f}{\partial \alpha_i} e^{x'}(\boldsymbol{\alpha}) e^f \beta \mathrm{dx}.$$

4.5 Numerical results

4.5.1 3D constrained orientation optimization

In all the examples of this section , we study a 3D cantilever of dimensions $2 \times 1 \times 1$ that have the same applied load and boundary conditions as section 5.2.4. We consider a tetrahedral mesh of 960 nodes. The cantilever structure is filled with a transverse isotropic material whose mechanical moduli are given in table 4.1 (the Poisson's ratio ν_{p1} is given by $\nu_{p1} = \nu_{1p}\frac{E_p}{E_1}$). The material is also parameterized by two Euler orientation angles that are modeled by the vector $\boldsymbol{\alpha}$. We apply the gradient descent orientation optimization algorithm 8 under a generalized constraint that is written $C(\boldsymbol{\alpha}) \leq c$, where $C(\alpha)$ is the constraint function and c is a real constant that we fix before the optimization (see section 4.4.2 for details on the inequality constraint method).

Example: case 1

E_1	E_p	G_{1p}	ν_{1p}	ν_p
10	1	1	0.3	0.3

Table 4.1: Material characteristics for 3D augmented Lagrangian orientation optimization for an inequality constraint

In this example, we apply an upper bound constraint on the L^2-norm of geometrical gradient of the angle vector $\boldsymbol{\alpha}$, for $c = 30$ (see section 4.4.3.1). We set the initial orientation horizontally along the x-axis. We initialize b to 10^3, b_{limit} to 10^7, α_{al} to 1.2 and λ_0 to 0. The algorithm converges in 120 iterations. The obtained orientation is given in the figure 4.6. We observe that the constraint $C(\boldsymbol{\alpha}) \leq 30$ is verified by the final orientation (see figure 4.7). Accordingly, we also observe that the final orientation is well regularized in the domain Ω.

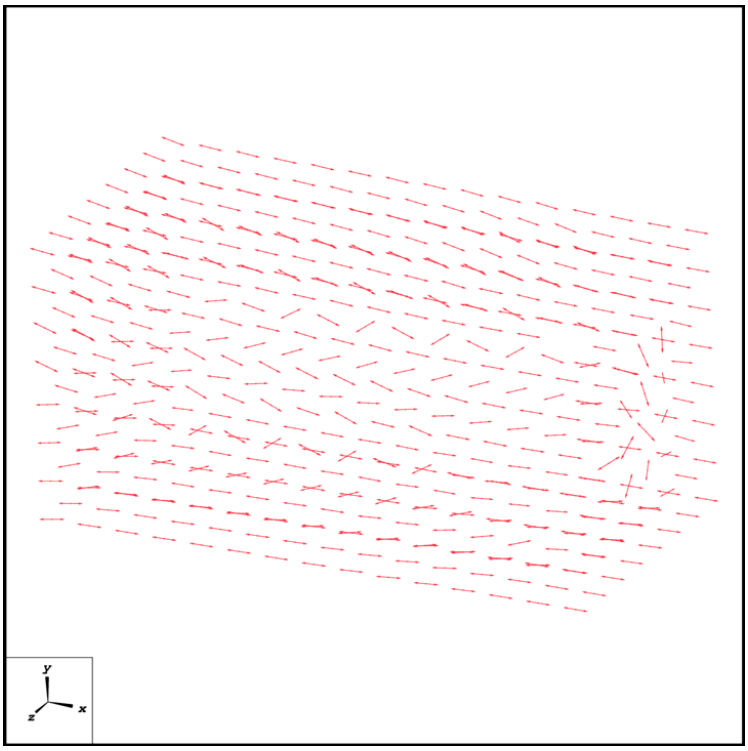

Figure 4.6: Optimized orientation in 3D under a constraint on the angles vector geometrical gradient

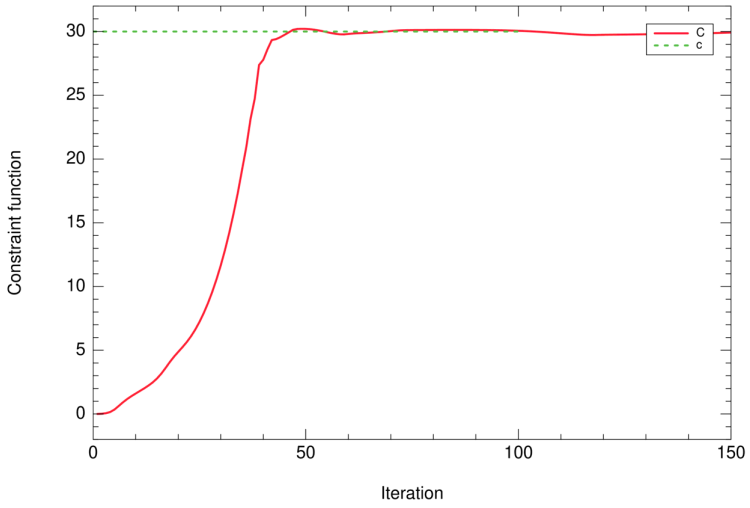

Figure 4.7: Evolution of the constraint function $C(\alpha)$ in the 3D orientation optimization under a constraint on the angles vector geometrical gradient

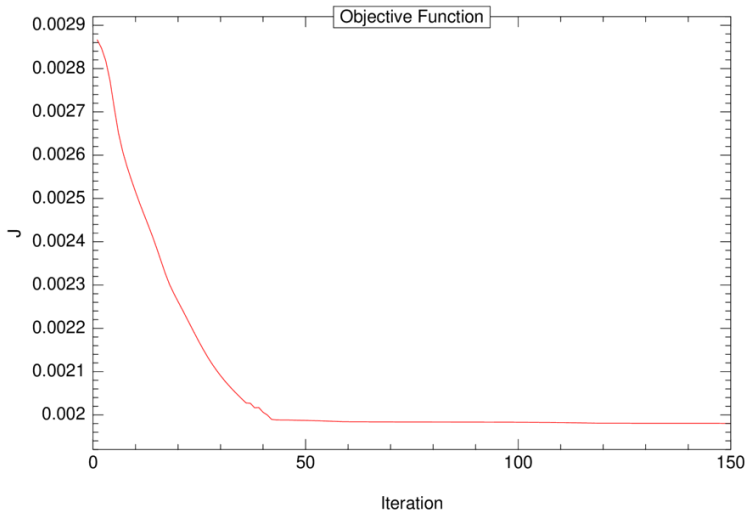

Figure 4.8: Evolution of the compliance in the 3D orientation optimization under a constraint on the angles vector geometrical gradient

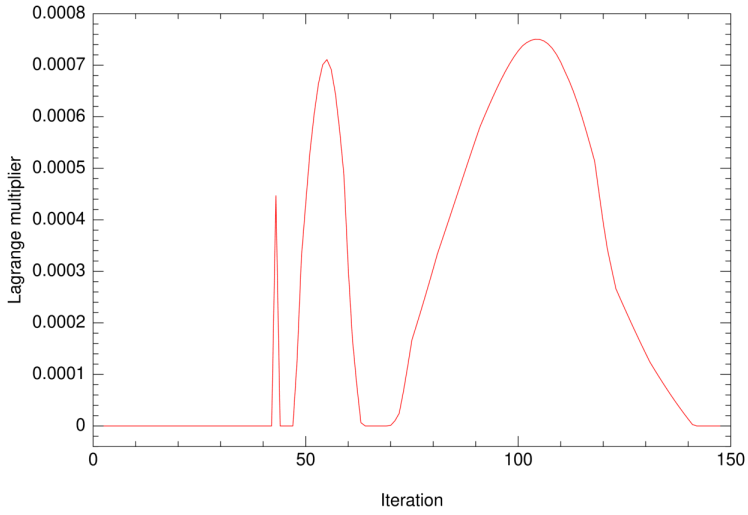

Figure 4.9: Evolution of the Lagrange multiplier in the 3D orientation optimization under a constraint on the angles vector geometrical gradient

Example: case 2

In this example, we apply an upper bound constraint on the $L2$-norm of geometrical partial gradient of the angle vector $\boldsymbol{\alpha}$ with respect of y, for $c = 15$ (see section 4.4.3.2). We set the initial orientation horizontally along the x-axis. We initialize b to 10^3, b_{limit} to 10^7, α_{al} to 1.2 and λ_0 to 0. The algorithm converges in 80 iterations. The obtained orientation is given in the figure 4.6. We observe that the constraint $C(\boldsymbol{\alpha}) \leq 15$ is verified by the final orientation (see figure 4.7).

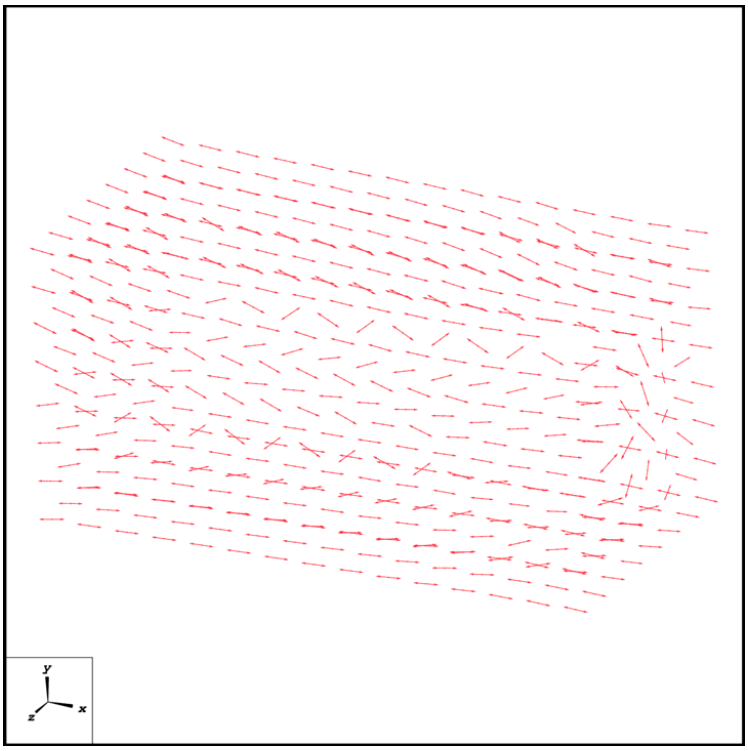

Figure 4.10: Optimized orientation in 3D under a constraint on the angle partial gradient along y

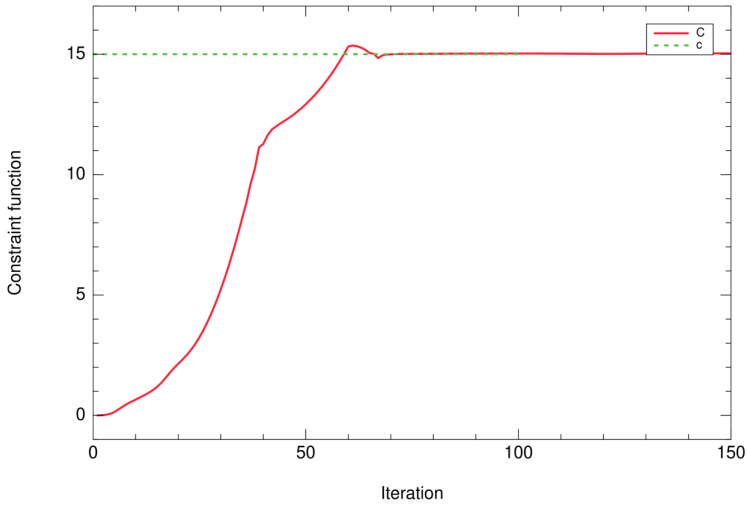

Figure 4.11: Evolution of the constraint function $C(\alpha)$ in the 3D orientation optimization under a constraint on the angle partial gradient along y

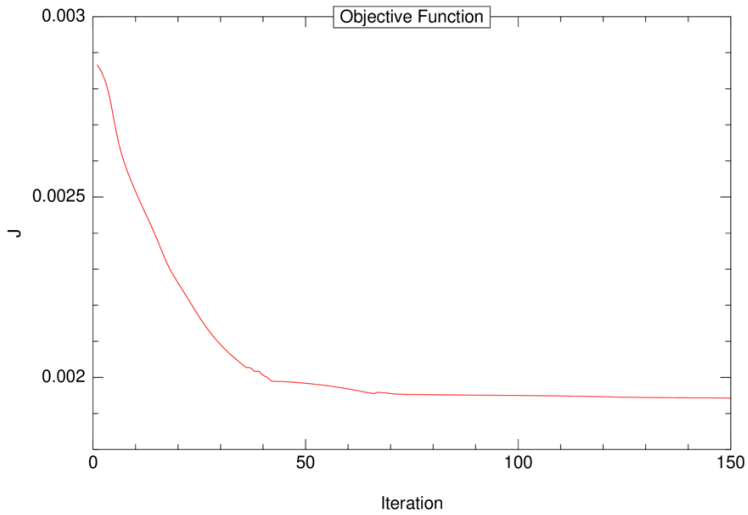

Figure 4.12: Evolution of the compliance in the 3D orientation optimization under a constraint on the angle partial gradient along y

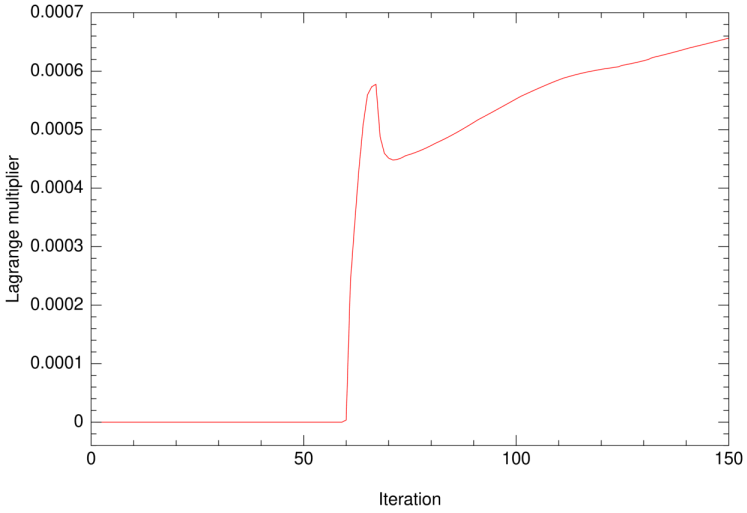

Figure 4.13: Evolution of the Lagrange multiplier in the 3D orientation optimization under a constraint on the angle partial gradient along y

Chapter 5

Coupled optimization of topology and orientation

5.1 Coupled optimization of topology and orientation in 2D

5.1.1 Optimization problem

Consider a structure in a 2D problem (hypothesis of plane stress or plane strain) with a shape Ω composed by a linearly elastic orthotropic material and defined inside a design domain D. The orthotropic material has the Hooke's law fourth order elasticity tensor $A^*(\alpha)$, where $\alpha \in L^2(D)$ is the angle from the x-axis of the initial frame of reference xy to the x'-axis of a material fixed frame $x'y'$ where the orthotropic elasticity Hooke's law is known, constant and denoted A. The tensor A is defined by the following elasticity moduli; two Young's moduli E_1 and E_2, with $E_1 > E_2$, one Poisson's ratio ν_{12} and one shear modulus G_{12}. The relation between A in Kelvin formalism and the elasticity moduli is given by (2.7).

We also suppose that the boundary of Ω is divided into three disjoints borders

$$\partial\Omega = \Gamma \cup \Gamma_N \cup \Gamma_D,$$

where Γ is the variable part of the boundary, Γ_D is a fixed part of the design boundary on which the mechanical displacement is not allowed (Dirichlet boundary condition), and Γ_N is also a fixed part of the design boundary on

which the force g is applied (Neumann boundary condition). It is assumed that the variable part Γ of the border is free of any effort.

The model of elasticity that is studied is then written: Find u in $(H^1(\Omega))^2$ such that:

$$\begin{cases} -\operatorname{div}(A^*(\alpha)e(u)) = f & \text{in } \Omega \\ u = 0 & \text{on } \Gamma_D \\ A^*(\alpha)e(u)n = g & \text{on } \Gamma_N \\ A^*(\alpha)e(u)n = 0 & \text{on } \Gamma. \end{cases} \tag{5.1}$$

The aim of the coupled optimization in this section is to find a structure shape Ω and an orientation angle α that optimize an objective function $J(\Omega, \alpha)$ which in the other hand represents some physical characteristic of the design.

We suppose a general objective function $J(\Omega, \alpha)$ that is the sum of the integral of the function j defined on Ω and of the integral of the function l defined on $\Gamma_J \subset \partial\Omega$, where Γ_J does not intersect the Dirichlet boundary Γ_D;

$$J(\Omega, \alpha) = \int_\Omega j(u)\mathrm{dx} + \int_{\Gamma_J} l(u)\mathrm{d}s. \tag{5.2}$$

The optimization problem is then written:

$$\inf_{\substack{\Omega \in \mathcal{U}_{ad}^\Omega \\ \alpha \in \mathcal{U}_{ad}^\alpha}} J(\Omega, \alpha), \tag{5.3}$$

where we have two sets of admissible designs:

$$\mathcal{U}_{ad}^\Omega = \left\{ \Omega \subset D \text{ s.t. } \int_\Omega dx = V_T \right\}, \tag{5.4}$$

and

$$\mathcal{U}_{ad}^\alpha = \left\{ \alpha \in L^2(\Omega) \right\}. \tag{5.5}$$

Note that the structure Ω is optimized under a volume constraint $\int_\Omega dx = V_T$, where $V_T \in \mathbb{R}_+^*$ is a fixed target volume for the structure.

In this work, we have implemented two methods of coupled optimization. While both methods use the level set approach to optimize the topology, they differ on the approach of orientation optimization. The first one consists of using the optimality criterion, while the latter method consists of using the gradient descent. The method that one has to use depends on the type of the

optimization problem.

5.1.2 Topology optimization coupled with an optimality criteria orientation optimization method

Suppose that we want to optimize the compliance of the structure Ω, or more precisely, the work of all the applied forces under a single loading case, the objective function (5.2) in this case is written:

$$J(\Omega, \alpha) = \int_{\Omega} fu\mathrm{dx} + \int_{\Gamma_N} gu\mathrm{ds} = \int_{\Omega} A^*(\alpha)e(u) \cdot e(u)\mathrm{dx}. \tag{5.6}$$

To take into account the volume constraint in (5.5), we write a Lagrangian $\mathcal{L}(\Omega, \alpha, \lambda)$ as the sum of the objective function $J(\Omega, \alpha)$ and the constraint function $C(\Omega) = \int_{\Omega} dx - V_T$ multiplied by a Lagrange multiplier $\lambda \in \mathbb{R}$:

$$\begin{aligned} \mathcal{L}(\Omega, \alpha, \lambda) &= J(\Omega, \alpha) + \lambda(\int_{\Omega} dx - V_T) \\ &= \int_{\Omega} A^*(\alpha)e(u) \cdot e(u)\mathrm{dx} + \lambda(\int_{\Omega} dx - V_T). \end{aligned} \tag{5.7}$$

The coupled optimization problem (5.3) becomes:

$$\min_{\substack{\Omega \in D \\ \alpha \in \mathcal{U}_{ad}^{\alpha}}} \max_{\lambda \in \mathbb{R}_+} \mathcal{L}(\Omega, \alpha, \lambda). \tag{5.8}$$

In practice, we perform an alternate minimization with respect to the angle α and to the shape Ω. Therefore, the angle is fixed when the shape is updated. However, in this case, the structure shape Ω^{n+1} will contain some regions where the angle is not defined if some boundary parts move outward from the domain Ω^n. To avoid this problem we use an ersatz material approximation (see section 1.3.1) and the orientation angle in this case is defined and optimized on the whole domain D (including the void).

Finally, the algorithm (Algorithm 9) of topology optimization coupled with optimality criterion method for the orientation consists of a topology optimization loop where after each update of the shape Ω_n to Ω_{n+1}, the orientation angle α_n, at each iteration n, is updated to align the stiffest axis of the material with the direction of the major principal stress. For this latter purpose, we compute the stress $\sigma^n_{\Omega_{n+1}}$ unique solution of:

$$\min_{\sigma \in H} \int_{\Omega_{n+1}} \left(A^*\left(\alpha_n\right)\right)^{-1} \sigma \cdot \sigma dx, \tag{5.9}$$

where the set H is given by (3.5). Then, we compute the angle α_{n+1} using the optimality formula (3.10). Note that the update of the angle using an optimality criterion corresponds to an alternate update (or alternate minimization) of the stress and the orientation (see section 3.1 for more details about this and about why we solve (5.9)). After each update on the angle, we regularize the orientation using the regularization algorithm 6. We repeat this whole procedure until the objective function is converged. In practice, the topology converge to a stable shape, mostly because the descent step of the shape is small. The final orientation that are obtained when the shape function is converged are usually optimal. If it is not the case, one could add some more iteration until the orientations also get into an optimal state.

Algorithm 9: 2D topology optimization coupled with the optimality criterion method for orientation

Initialize the anisotropy angle α_0 and the shape level set function ϕ_0
for $n = 0, ..,$ *until convergence* **do**
  Solve the elasticity problem (5.1) to get $u^n_{\Omega_n}$.
  Compute the shape sensitivity $\theta \mapsto \frac{\partial \mathcal{L}(\Omega_n, \alpha_n, \lambda_n)}{\partial \Omega}(\theta)$ using (1.21).
  Update the level set function ϕ_n (and the shape Ω_n) such that $\mathcal{L}\left(\Omega_{n+1}, \alpha_n, \lambda_n\right) < \mathcal{L}\left(\Omega_n, \alpha_n, \lambda_n\right)$ (see Algorithm 2)
  Update the Lagrange multiplier λ_n to λ_{n+1} using (1.24).
  Compute the stress $\sigma^n_{\Omega_{n+1}}$, unique solution of:

$$\min_{\sigma \in H} \quad \int_{\Omega_{n+1}} (A^*(\alpha_n))^{-1} \sigma \cdot \sigma \, \mathrm{dx}, \tag{5.10}$$

  by solving the elasticity problem (by deducing $\sigma^n_{\Omega_{n+1}}$ from $u^n_{\Omega_{n+1}}$).
  Update the angle α_n to α_{n+1}; the angle corresponding to the major principal stress obtained using the optimality criterion formula (3.10).
  Regularize the orientation using Algorithm 6.
end

Note that in each iteration $n \in \mathbb{N}$, we solve the elasticity problem twice to obtain two different displacements. The first time is before computing the shape sensitivity before updating the shape from Ω_n. We denote the obtained displacement by $u^n_{\Omega_n}$. The second time that we solve the elasticity problem is after the update of the shape to Ω_{n+1}, before updating the angle. We denote the displacement and the stress that are obtained from

this later resolution of elasticity $u^n_{\Omega_{n+1}}$ and $\sigma^n_{\Omega_{n+1}}$. Note also that, when λ is converged, the algorithm 9 is interpreted as an alternate minimization in the shape Ω then in the stress σ then in the angle α of the function $\mathcal{L}(\Omega, \alpha, \lambda)$.

5.1.3 Numerical results

Cantilever example

We study a classical example of a cantilever Ω in elasticity which is a subset of a rectangular domain D of dimension 2×1. The left side of D is fixed (Dirichlet boundary condition) and a vertical force $g = -e^y$ is applied on a small boundary subset Γ_N centered on the right side of the cantilever and that has a length size of 0.1(see figure 5.1). The structure is filled with an orthotropic material that is defined by the mechanical moduli of table 5.1 (the Poisson's ratio ν_{21} is given by $\nu_{21} = \nu_{12}\frac{E_2}{E_1}$). We optimize the compliance:

$$J(\Omega, \alpha) = \int_{\Gamma_N} gu\mathrm{ds}, \tag{5.11}$$

under a constraint of a target volume V_T which is equal to 40% of the volume of D. The Lagrangian of this problem is defined by:

$$\mathcal{L}(\Omega, \alpha, \lambda) = \int_{\Gamma_N} gu\mathrm{ds} + \lambda \left(\int_\Omega dx - V_T \right), \tag{5.12}$$

and the two set of admissible designs are defined by (5.4) and (5.5).

E_{11}	E_{22}	G_{12}	ν_{12}	α_0
10	5	2	0.3	0

Table 5.1: Material characteristics for the cantilever and the L-beam examples

We initialize the optimization with an horizontal orientation of the stiffer direction of the material ($\alpha_0 = 0$) and with the shape of figure 5.1. Then we apply the coupled topology and optimality criterion orientation optimization algorithm (algorithm 9). Note that we use a mesh of 11626 triangular elements.

The coupled shape and topology optimization algorithm converges after 70

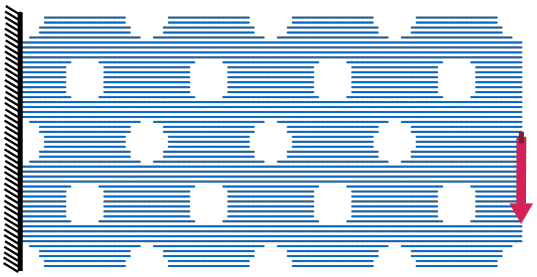

Figure 5.1: Initialization of the cantilever: plot of stiffest direction of the local anisotropy

iterations. When the optimization algorithm is converged, we obtain the optimized structure of figure 5.2. We observe that the stiffer material direction for the optimized orientation is uniformly parallel to the direction of the bars of the optimal shape. We also observe that the orientation is well regularized in the whole structure domain, except in the central zone, in the joint of the four bars that form an X-shape. The small irregularity of this region is caused by random local orientations that are obtained by the optimality criterion. This randomness is due to the stress being hydrostatic in this region. Another cause of irregularity is that we use a relatively small regularization radius (see subsection 3.4.1), because we do not want to lose the parallelism of the optimized orientation with the bars of the optimized shape. We also observe that the orientation is well symmetric in the whole domain, except the same irregular region. This is also another consequence of the stress being hydrostatic in this region.

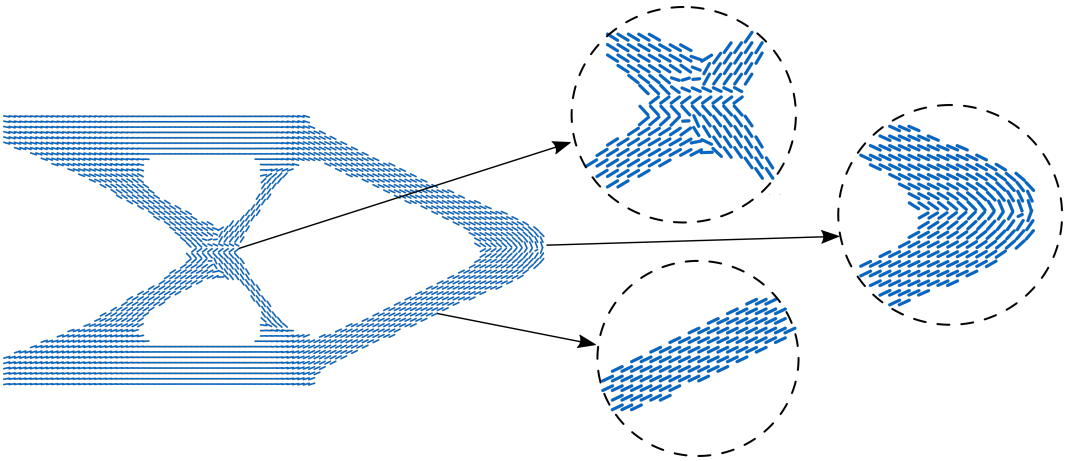

Figure 5.2: Optimized cantilever: plot of stiffest direction of the local anisotropy

Cantilever example: comparison of different strategies

In the following, we consider the same previous model problem of cantilever with the initial shape of figure 5.3 and with an horizontal orientation initialization ($\alpha_0 = 0$). We also consider the material characteristics of table 5.2 and a structured triangular mesh of 5151 nodes. In this study, we apply different strategies of coupled optimizations of shape and orientation using an optimality criterion: the first strategy consists of optimizing the orientation and the shape simultaneously during each iteration. This means that the orientation is updated after each update of the shape. The second strategy is the same as the first strategy but we begin updating the orientation at iteration $n = 25$. The third strategy is to optimize the orientation after each 50 updates of the shape and the last strategy is to optimize the orientation only after when shape and topology optimization is finished. The figures 5.4 to 5.7 give the obtained structures with each optimization strategy. The objective function, Lagrangian function and the volume evolution for each strategy are presented in the figures 5.8, 5.9 and 5.10.

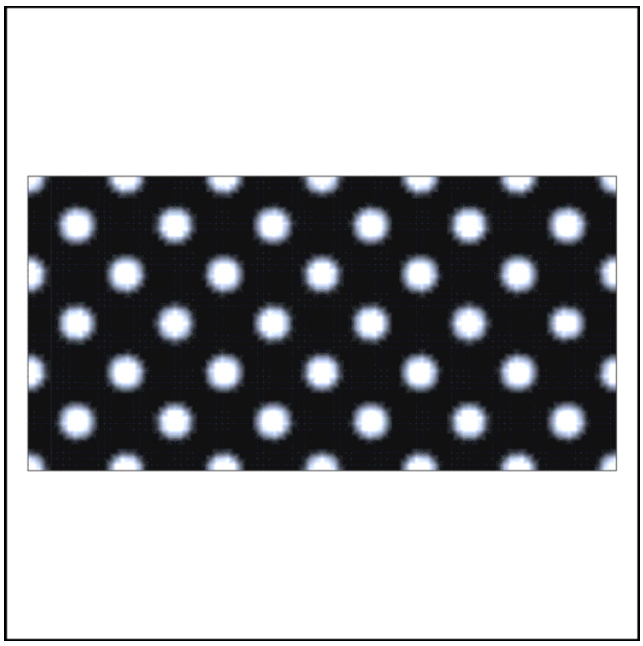

Figure 5.3: Initial shape of the cantilever

E_{11}	E_{22}	G_{12}	ν_{12}	α_0
10	1	1	0.3	0

E_{11}	E_{22}	G_{12}	ν_{12}	α_0

Table 5.2: Material characteristics for the cantilever

We observe that the four optimizations converge approximately after 65 iterations and that the obtained results are different from each other. The best compliance are obtained in the case of the simultaneous optimizations of the shape and orientation (strategy 1 and 2). We also observe that the structure that is obtained by the first strategy is not symmetric. This is because the starting topology contains many bar joints regions, which means regions of hydrostatic stress. This leads to some random values of local orientations on those regions when one starts the optimization of orientation from the beginning. Lastly, the strategy of optimizing the orientation after the optimization of the shape gave the worst final compliance of all four strategies. This latter obtained structure has the same topology as the results of strategy 3 and 5 but a different shape.

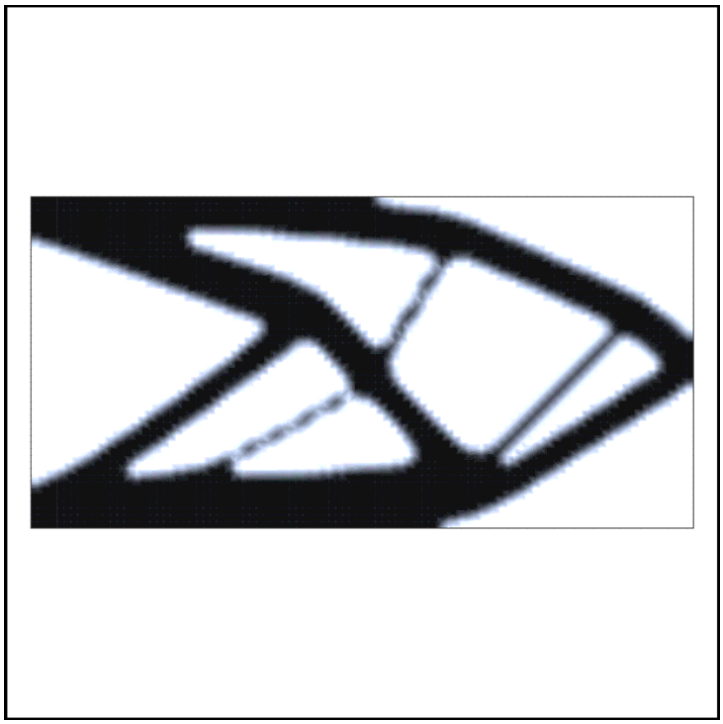

(a) Optimized cantilever: obtained shape

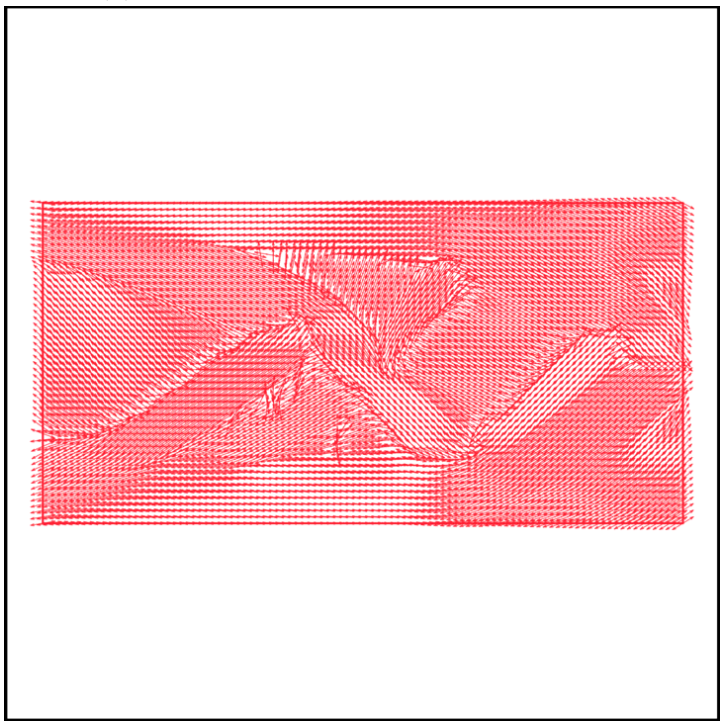

(b) Optimized cantilever: plot of stiffest direction of the local anisotropy

Figure 5.4: Optimized cantilever using strategy 1: simultaneous optimization of shape and orientation using the optimality criterion

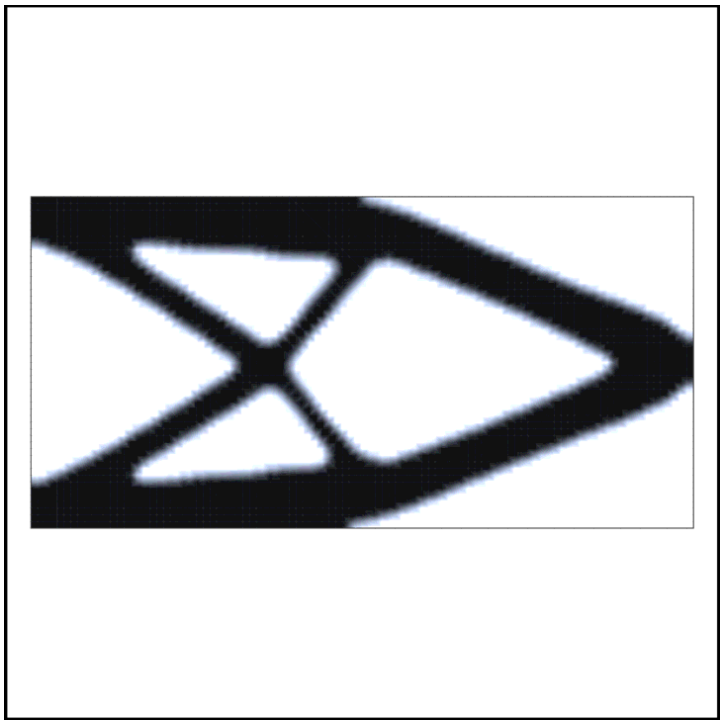

(a) Optimized cantilever: obtained shape

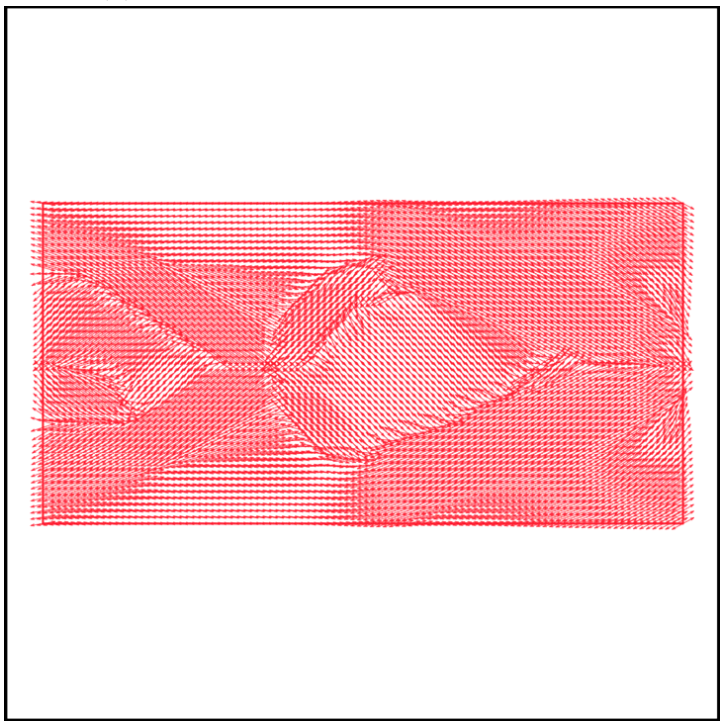

(b) Optimized cantilever: plot of stiffest direction of the local anisotropy

Figure 5.5: Optimized cantilever using strategy 2: simultaneous optimization of shape and orientation using the optimality criterion for $n \geq 25$

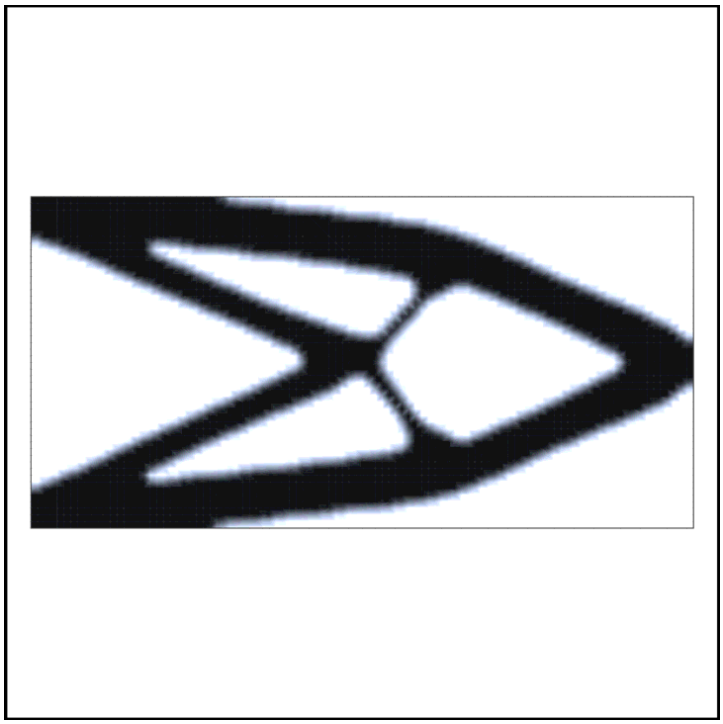

(a) Optimized cantilever: obtained shape

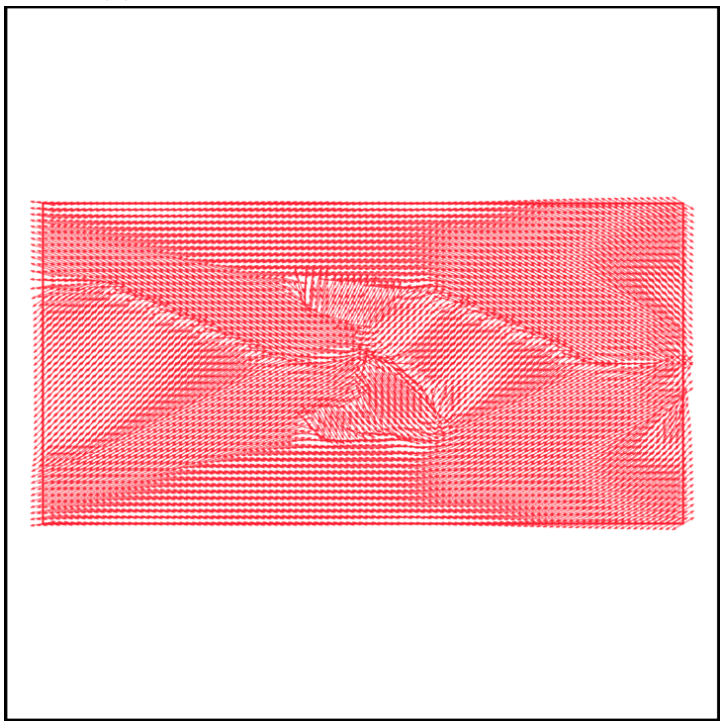

(b) Optimized cantilever: plot of stiffest direction of the local anisotropy

Figure 5.6: Optimized cantilever using strategy 3: optimization of orientation each 50 iterations of shape optimization using the optimality criterion

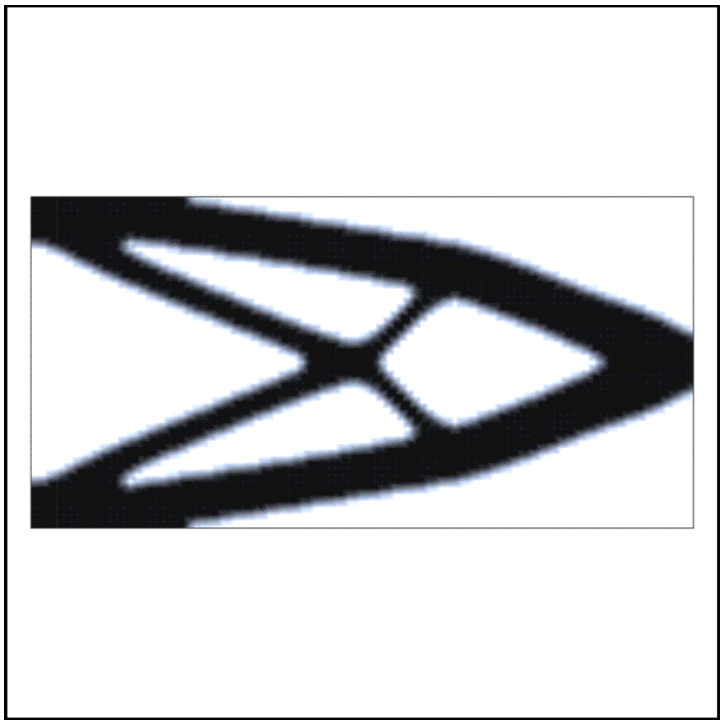

(a) Optimized cantilever: obtained shape

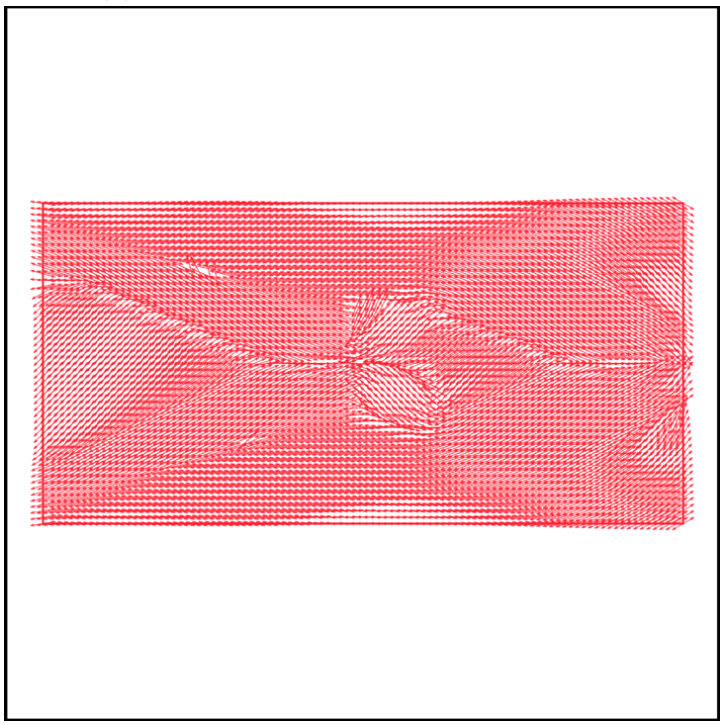

(b) Optimized cantilever: plot of stiffest direction of the local anisotropy

Figure 5.7: Optimized cantilever using strategy 4: optimization of shape then optimization of orientation using the optimality criterion

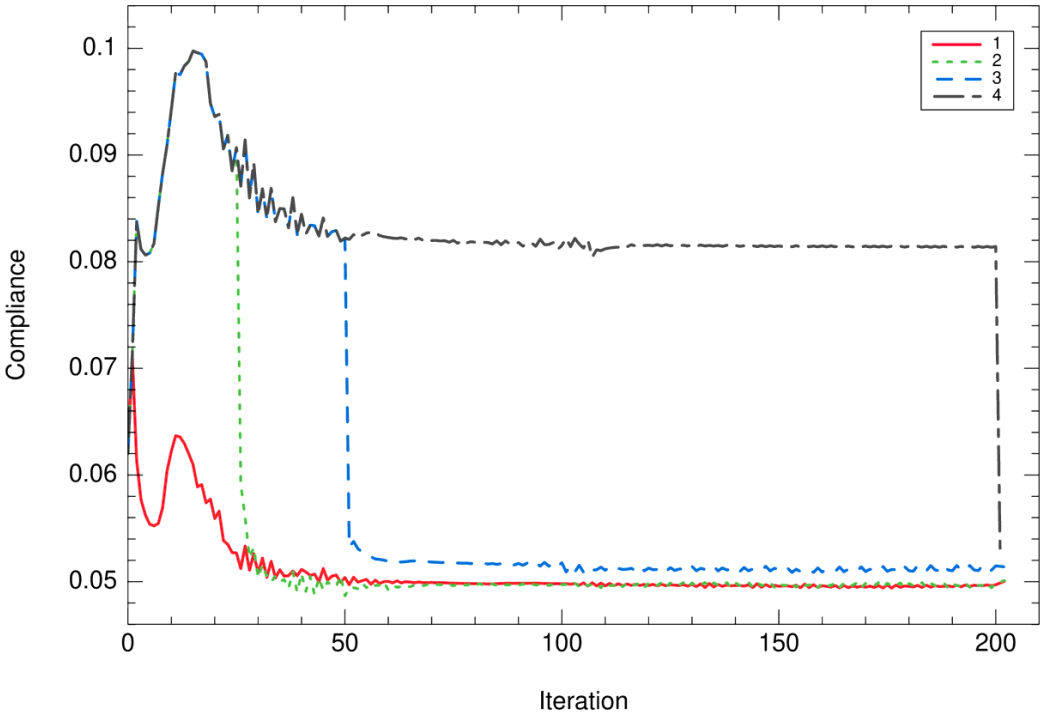

Figure 5.8: Compliance evolution for each strategy of the coupled shape and orientation optimization using an optimality criterion for the 2D cantilever example

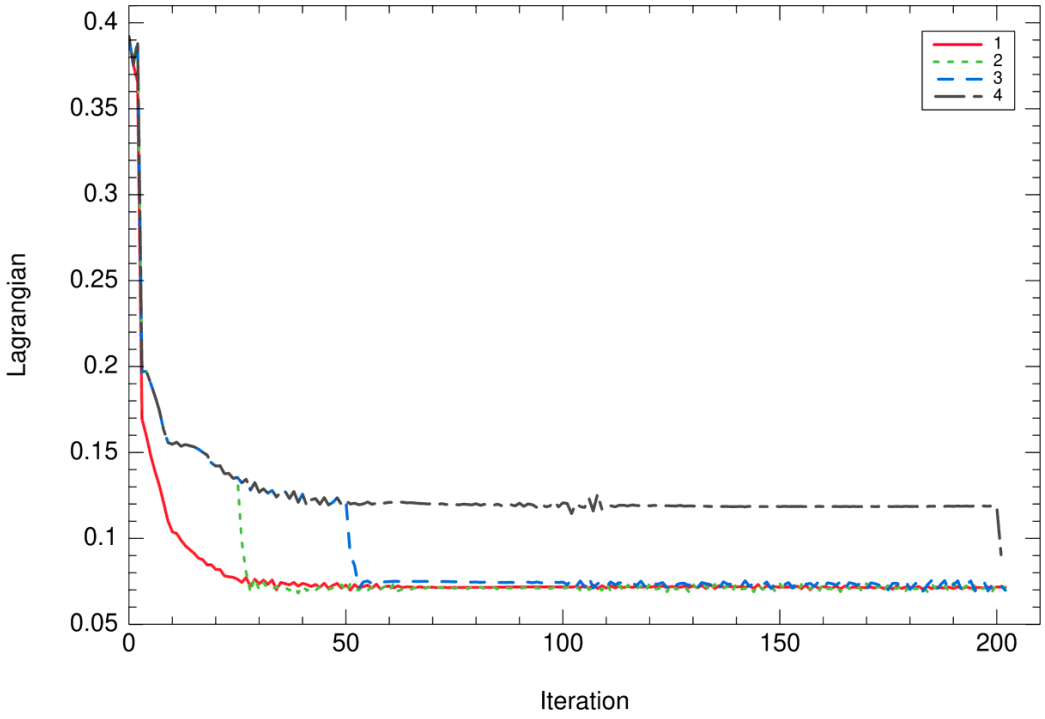

Figure 5.9: Lagrangian evolution for each strategy of the coupled shape and orientation optimization using an optimality criterion for the 2D cantilever example

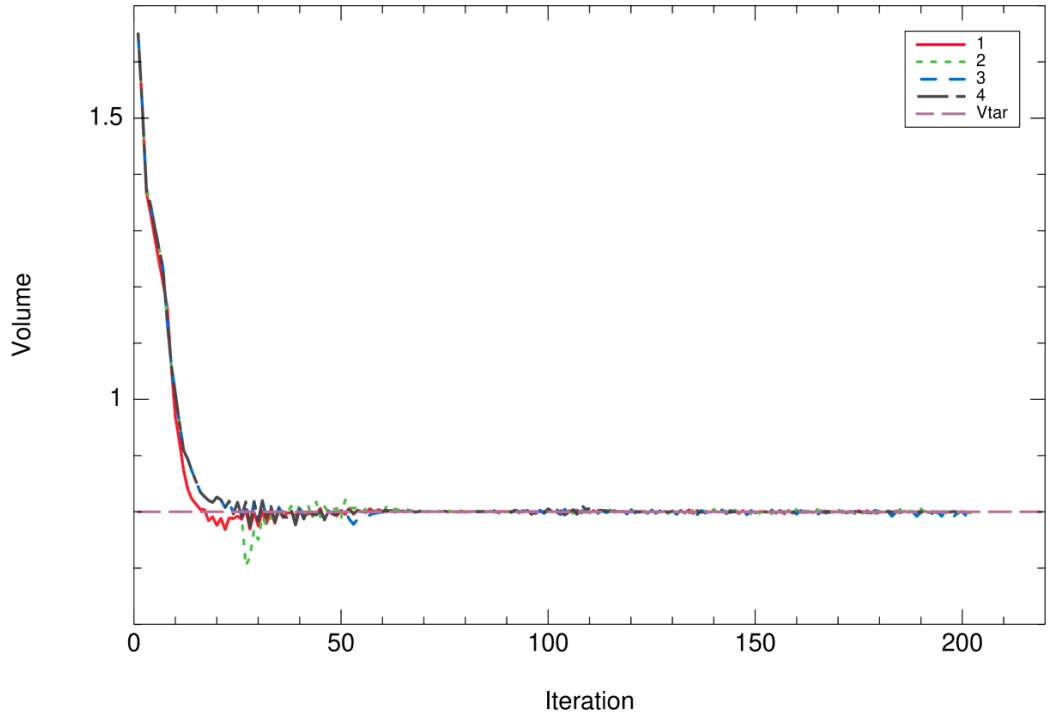

Figure 5.10: Volume evolution for each strategy of the coupled shape and orientation optimization using an optimality criterion for the 2D cantilever example

L-beam example

We study an example of an L-beam Ω in elasticity which belongs to the L-domain D of dimensions $L = H = 2$ and $l = h = 1$ shown on figure 5.11. The upper side of D is fixed (Dirichlet boundary condition) and a vertical force $g = -e^y$ is applied on a small boundary subset Γ_N located on the extreme left side and that have a length size of 0.1 (see figure 5.11). The structure is filled with an orthotropic material with the mechanical moduli of table 5.1 (the Poisson's ratio ν_{21} is given by $\nu_{21} = \nu_{12}\frac{E_2}{E_1}$). We optimize the compliance expressed by (5.11) under a volume constraint of 40% of the domain D. The Lagrangian of this problem is defined by (5.12) and the two sets of admissible designs are defined by (5.4) and (5.5). We initialize the optimization with the shape of figure 5.12 and an horizontal orientation of the stiffer direction of the material ($\alpha_0 = 0$). We use a mesh of 17468 triangular elements for the domain D. Finally, we perform the coupled optimization by applying the coupled topology and optimality criterion orientation optimization algorithm (algorithm 9).

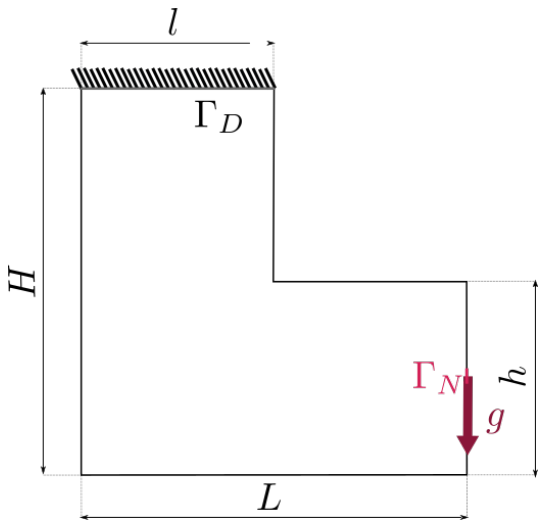

Figure 5.11: 2D L-beam load and boundary condition

The coupled shape and topology optimization algorithm converges after 60 iterations. When the optimization algorithm has converged, we obtain the optimized structure of figure 5.13. We observe that the stiffer material direction for the optimized orientation is uniformly parallel to the direction of the bars of the obtained optimal shape. We also observe that the orientation is well regularized on the whole structure, even in the structure joints.

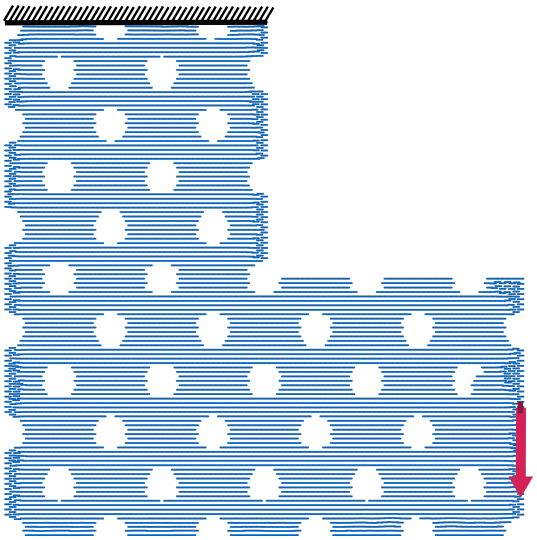

Figure 5.12: Initialization of the L-beam: plot of stiffest direction of the local anisotropy

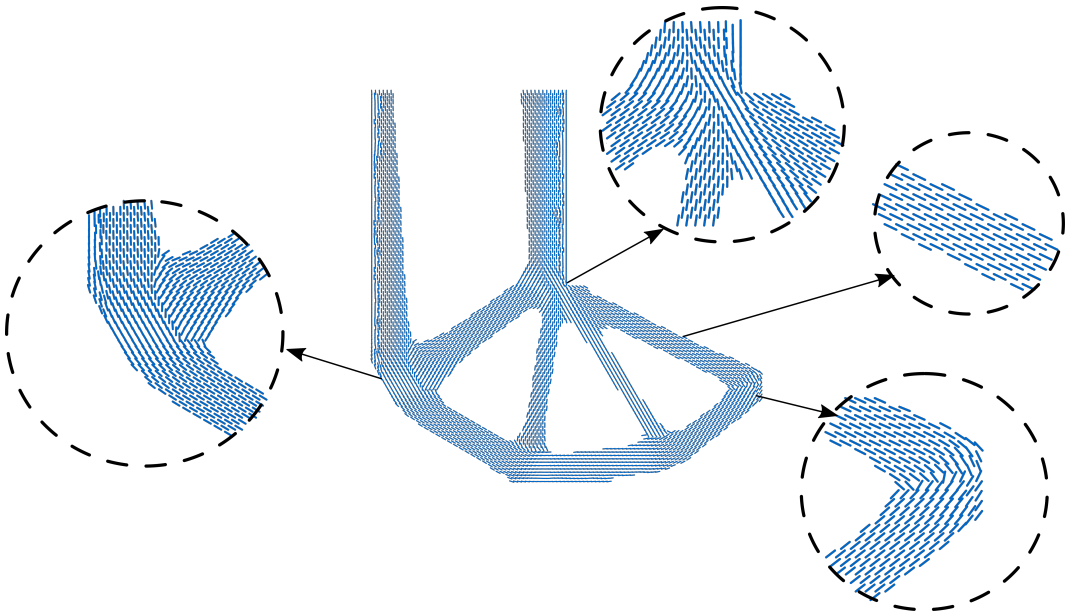

Figure 5.13: Optimized L-beam: plot of stiffest direction of the local anisotropy

5.1.4 Topology optimization coupled with a gradient descent orientation optimization method.

Because the optimization of the orientation with an optimality criterion is very limited to the self-adjoint problem of single load compliance optimization, one has to turn to the gradient descent method for the orientation optimization. It is rather interesting when one wants to consider a further industrial problem such as a multi-load optimization problem, a constrained orientation problem or a non self-adjoint problem such as the target displacement or stress optimization problem. For this reason. we present in this section the coupled optimization of the topology with the orientation of the anisotropy using a gradient descent method in 2D. We suppose a general objective function $J(\Omega, \alpha)$ written as (5.2), where Γ_J does not intersect the Dirichlet boundary Γ_D (see figure 3.1). The Lagrangian function, defined to take into account the volume constraint (5.5), is written:

$$\mathcal{L}(\Omega, \alpha, \lambda) = J(\Omega, \alpha) + \lambda \left(\int_\Omega dx - V_T \right), \tag{5.13}$$

where $\lambda \in \mathbb{R}$ is the Lagrange multiplier. The coupled optimization problem (5.3) is then written:

$$\min_{\substack{\Omega \in D \\ \alpha \in \mathcal{U}_{ad}^{\alpha}}} \max_{\lambda \in \mathbb{R}} \mathcal{L}(\Omega, \alpha, \lambda). \tag{5.14}$$

While one has to use the sensitivity of the Lagrangian with respect to the shape during the optimization, the optimization in the orientation is indifferent to the constraint $C(\Omega)$ thus the sensitivity of the Lagrangian with respect to the orientation angle is equivalent to the sensitivity of the objective function also with respect to the orientation angle. Besides, in practice, we suppose that the angle is fixed when the shape is updated. We use an ersatz material approximation (see section 1.3.1) to avoid having regions in the shape Ω_{n+1} that do not have an orientation when some boundaries parts move outward from the domain Ω^n. As a result, the orientation angle in this case is defined and optimized on the whole domain D (including the void).

The algorithm (Algorithm 10) of coupled optimization consists of a topology optimization loop, where at each iteration $n \in \mathbb{N}$, one adds a fixed number $M \in \mathbb{N}$ of updates of the orientation angle using the gradient descent. Note

that the update of the orientation is accepted only when:

$$J(\Omega_n, \alpha_{n,m+1}) < J(\Omega_n, \alpha_{n,m}). \tag{5.15}$$

In the other case, the step is repeatedly decreased until the condition (5.15) is verified. The whole steps on an iteration n are repeated until the objective function is converged. In practice, we observe that the sequence of shapes Ω_n converges. In other words, the algorithm stops when the shape is converged. The orientations that are obtained in the end are usually optimal. If it is not the case, one could add some more iterations of orientation optimization by repeating only the steps 9 to 17 in algorithm 10 until the orientation converge to an optimal state.

Note that, when λ is converged, this algorithm is interpreted as an alternate minimization in the shape Ω and in the angle α of the function $\mathcal{L}(\Omega, \alpha, \lambda)$.

Cantilever example: comparison of different strategies

In the following, we consider the same compliance optimization problem of cantilever as in section 5.1.3 with the initial shape of figure 5.3 and with an horizontal orientation initialization ($\alpha_0 = 0$). We also consider the material characteristics of table 5.2 and a triangular mesh of 5151 nodes. Recall also that we have a constraint of a target volume V_T which is equal to 40% of the volume of D. In this study, we apply different strategies of coupled optimizations of shape and orientation using the gradient descent method and without applying the orientation regularization: the first strategy consists of optimizing the orientation and the shape simultaneously during each iteration. This means that the orientation is updated after each update of the iteration. The second strategy is the same as the first strategy but we begin updating the orientation at iteration $n = 20$. The third strategy is also the same as the first strategy but we begin updating the orientation at iteration $n = 50$. The fourth strategy is to apply 60 iterations of gradient descent of the orientation optimization after each 20 updates of the shape optimization. The fifth strategy is to apply 60 iterations of gradient descent of the orientation optimization after each 50 updates of the shape optimization. Lastly, the sixth strategy is to optimize the orientation only after when the shape optimization loop has finished. The figures 5.14 to 5.19 give the obtained structures with each optimization strategy. The objective function, Lagrangian function and the volume evolution for each strategy are presented in the figures 5.20, 5.21 and 5.22.

The shape converges approximately in 70 iterations, for all the six optimizations. For the simultaneous optimization strategies (strategy 1 to 3). The obtained

Algorithm 10: 2D topology optimization coupled with the gradient descent method for orientation

Initialize the anisotropy angle α_0 and the shape level set function ϕ_0
for $n = 1, .., $ *until convergence* **do**
  Solve the elasticity problem, then solve the adjoint problem (in case of a non self-adjoint problem).
  Compute the shape sensitivity.
  Update the level set function ϕ_n and the shape Ω
  Update the Lagrange multiplier λ_n to λ_{n+1} using (1.24)
  if $(n \geq n_{or})$ *and* $(n \mod n_{per} = 0)$ **then**
    for $m = 1, .., M$ **do**
      Solve the elasticity problem, then solve the adjoint problem (in case of a non self-adjoint problem).
      Compute the gradient $\frac{\partial J(\Omega_n, \alpha_{n,m})}{\partial \alpha_{n,m}}$ using (3.18).
      Regularize the gradient $\frac{\partial J(\Omega_n, \alpha_{n,m})}{\partial \alpha_{n,m}}$.
      $\alpha_{n,m+1} = \alpha_{n,m} - t_{n,m} \frac{\partial J(\Omega_n, \alpha_{n,m})}{\partial \alpha_{n,m}}$, where $t_{n,m}$ is a small descent step.
      if $J(\Omega_n, \alpha_{n,m}) < J(\Omega_n, \alpha_{n,m-1})$ **then**
        $t_{n,m+1} = 1.2 t_{n,m}$ and continue to the next iteration.
      else
        $t_{n,m+1} = t_{n,m}/2$ and return to the step 9.
      end
    end
    $\alpha_{n+1} = \alpha_{n,M}$.
  end
end

shapes are different from each others even if both the shapes and orientations are symmetric in the three obtained structures. The best compliance is obtained for the second strategy, namely when we started optimizing the orientation at iteration 20. This shows that starting the optimization of orientation from the first shape optimization iteration is not a good strategy. This is because in the beginning of the optimization the shape has a bad topology that would influence the orientation result, which in turn will influence the result of the final shape. However when we start from the orientation optimization after 20 iterations, which means after the first changes of topology. The orientation would start converging according to a better shape (parallel to the bars). On the other hand, starting optimizing the orientation optimization latter did not make the final compliance any better from the first strategy. This is because the shape in this case missed the influence of the orientation optimization before the 50 iterations which lead it to converge to a worse shape than that of the second strategy. The fourth strategy which consists of optimizing the orientation each 20 iterations gave the same result as the simultaneous optimization starting from iteration 20, with the same final compliance. Also the fifth strategy which consists of optimizing the orientation each 50 iterations gave the same result as the simultaneous optimization starting from iteration 50, with the same final compliance. Lastly, the strategy of optimizing the orientation after the optimization of the shape gave the worst final compliance of all six strategies. The obtained structure have the same topology as the results of strategy 3 and 5 but a different shape.

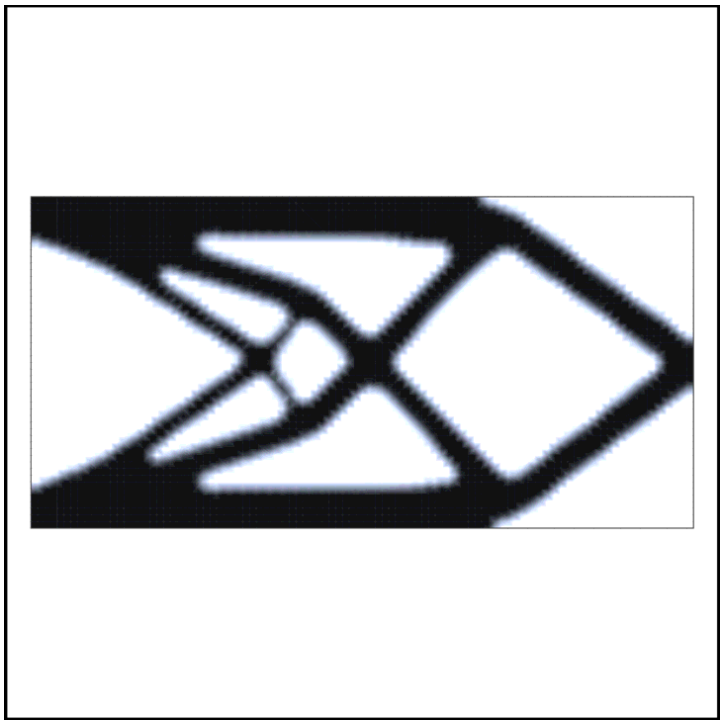

(a) Optimized cantilever: obtained shape

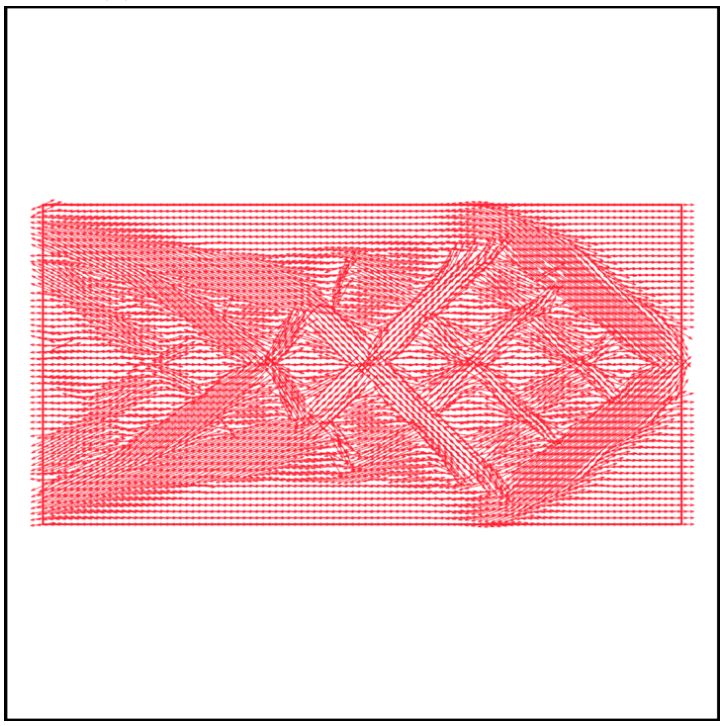

(b) Optimized cantilever: plot of stiffest direction of the local anisotropy

Figure 5.14: Optimized cantilever using strategy 1: simultaneous optimization of shape and orientation using the gradient descent method

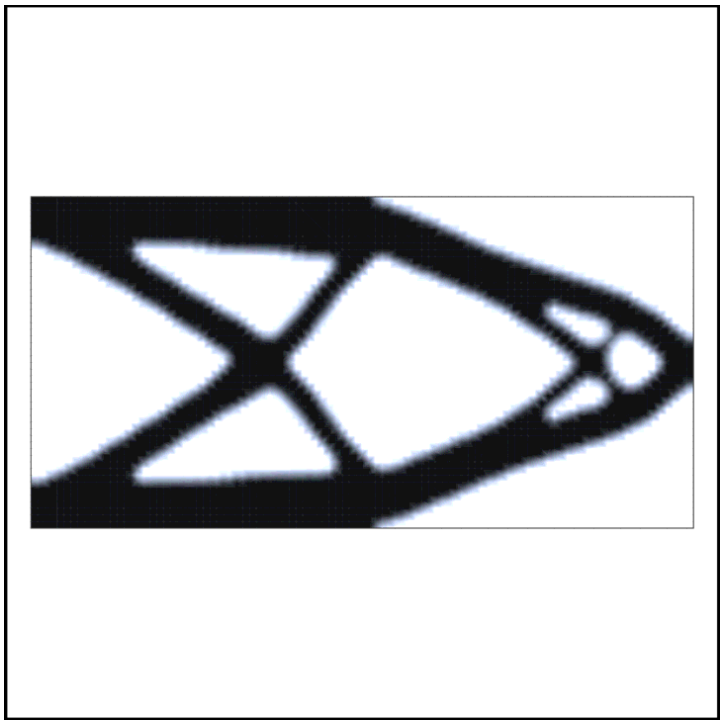

(a) Optimized cantilever: obtained shape

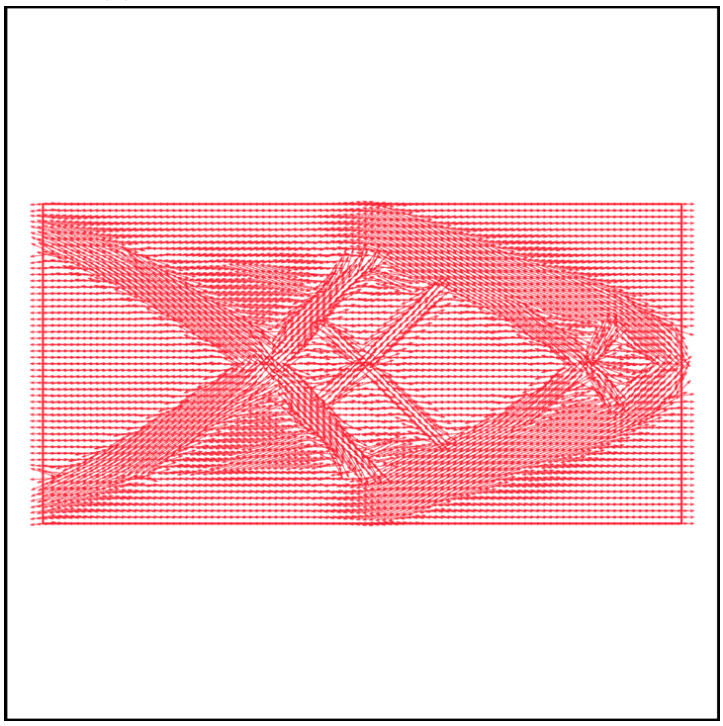

(b) Optimized cantilever: plot of stiffest direction of the local anisotropy

Figure 5.15: Optimized cantilever using strategy 2: simultaneous optimization of shape and orientation using the gradient descent method for $n \geq 20$

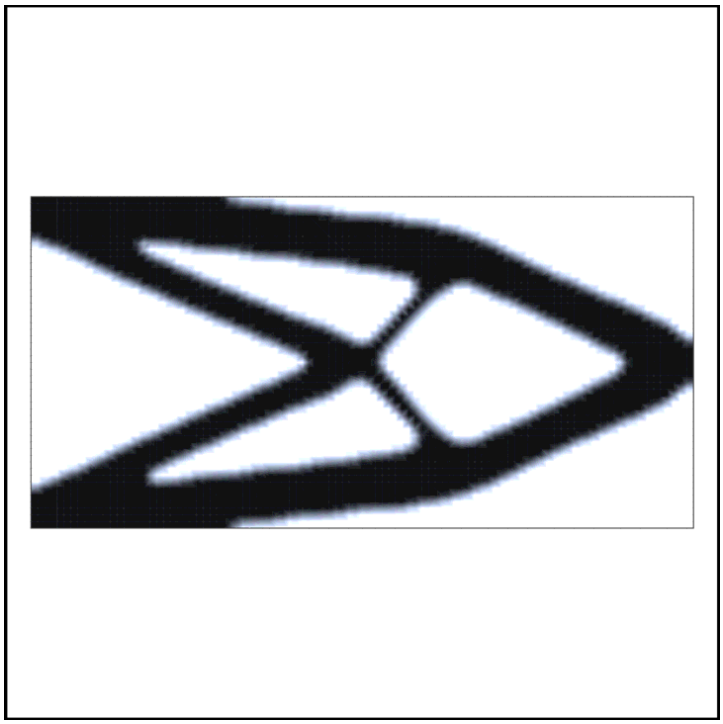

(a) Optimized cantilever: obtained shape

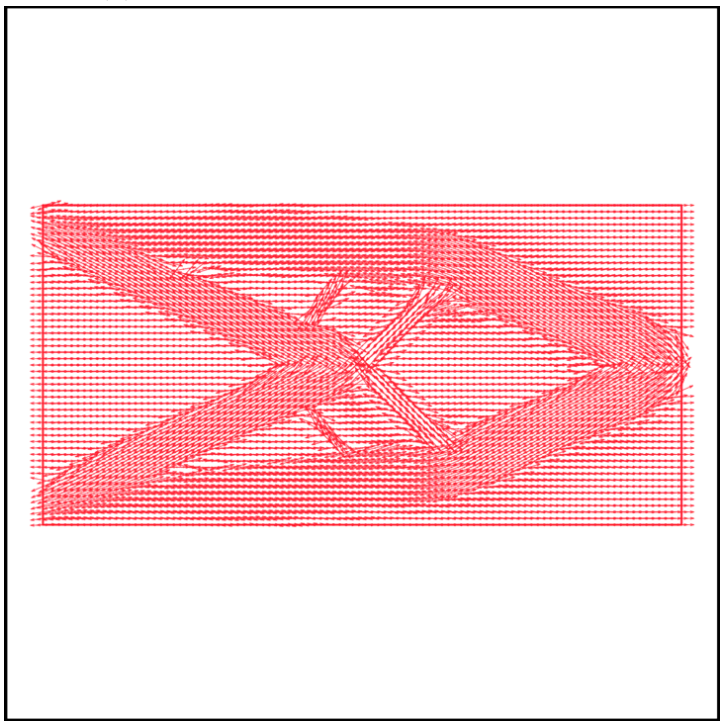

(b) Optimized cantilever: plot of stiffest direction of the local anisotropy

Figure 5.16: Optimized cantilever using strategy 3: simultaneous optimization of shape and orientation using the gradient descent method for $n \geq 50$

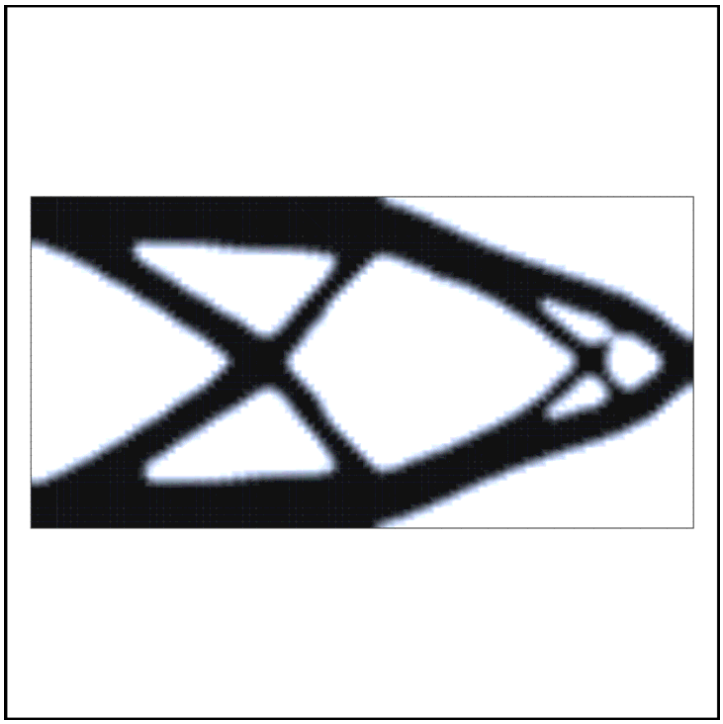

(a) Optimized cantilever: obtained shape

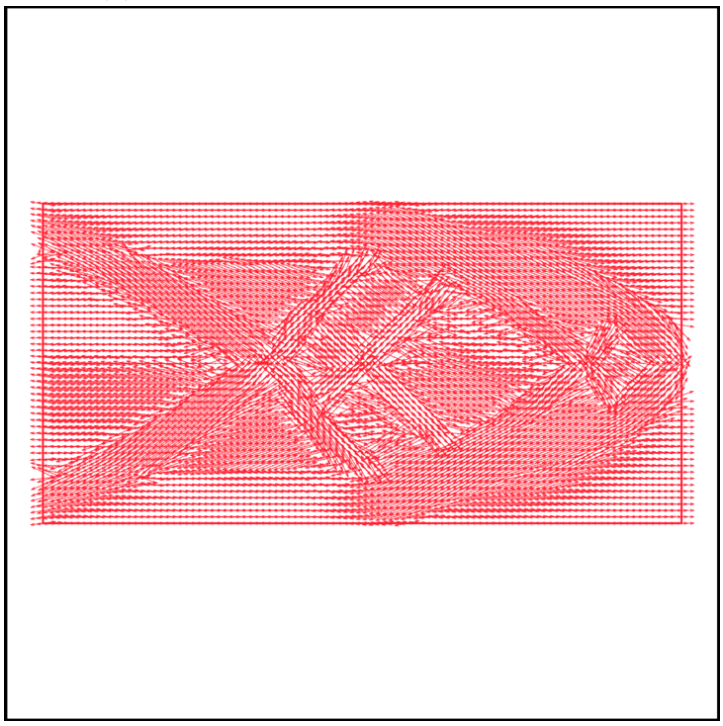

(b) Optimized cantilever: plot of stiffest direction of the local anisotropy

Figure 5.17: Optimized cantilever using strategy 4: optimization of orientation the gradient descent method after each 20 iterations of shape optimization

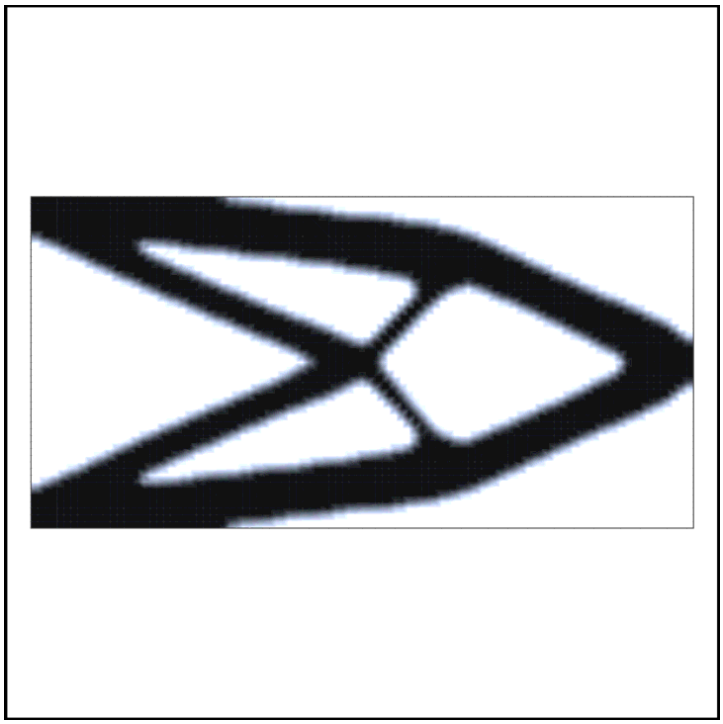

(a) Optimized cantilever: obtained shape

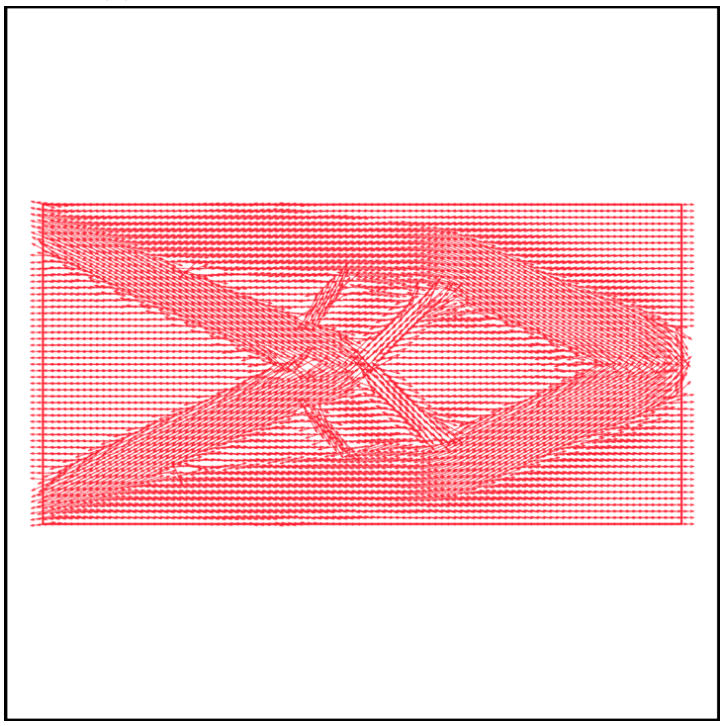

(b) Optimized cantilever: plot of stiffest direction of the local anisotropy

Figure 5.18: Optimized cantilever using strategy 5: optimization of orientation using the gradient descent method after each 50 iterations of shape optimization

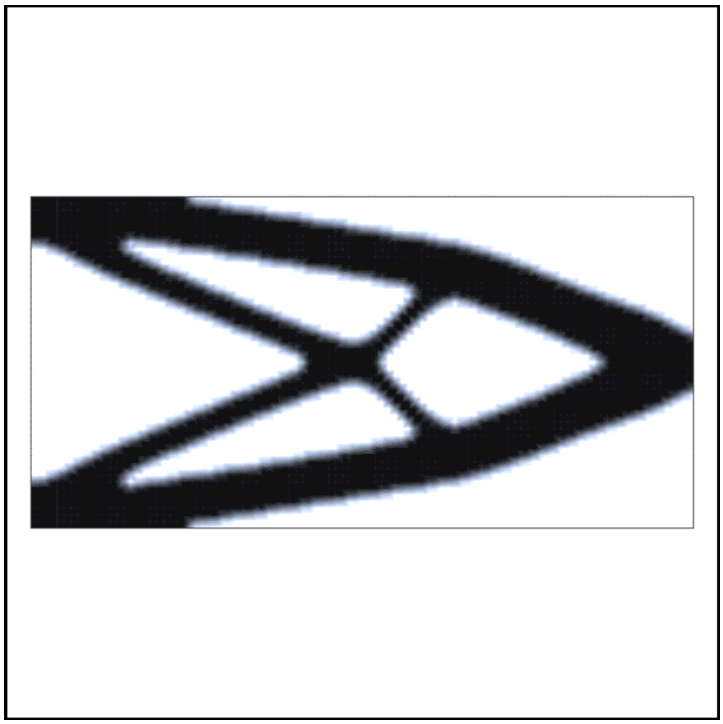

(a) Optimized cantilever: obtained shape

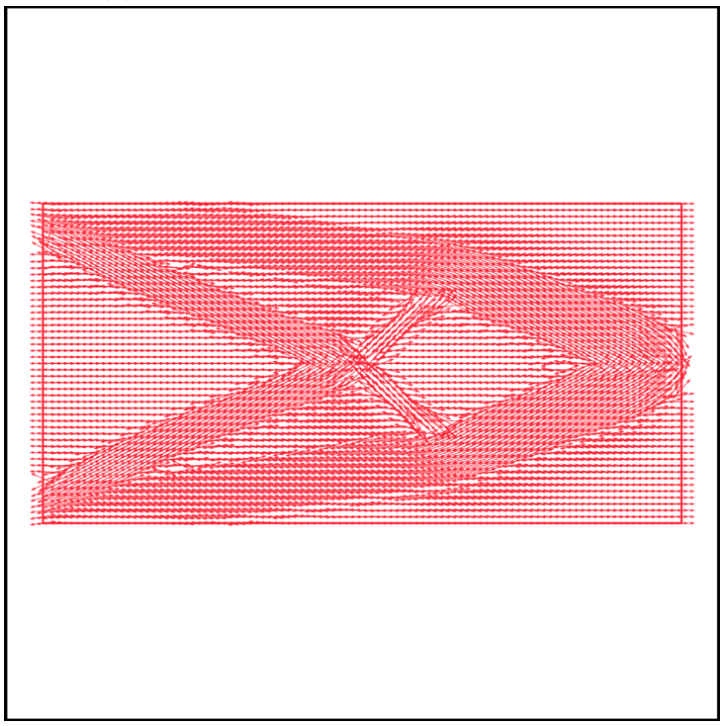

(b) Optimized cantilever: plot of stiffest direction of the local anisotropy

Figure 5.19: Optimized cantilever using strategy 6: optimization of shape then optimization of orientation using the gradient descent method

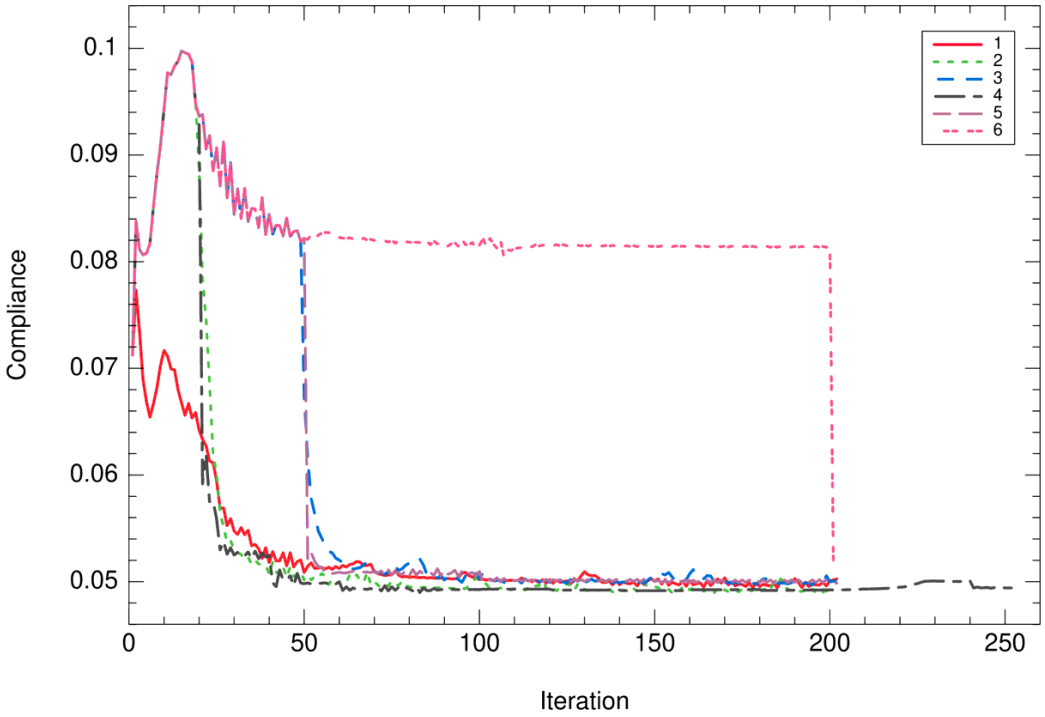

Figure 5.20: Compliance evolution for each strategy of the coupled shape and orientation optimization using the gradient descent method for the 2D cantilever example

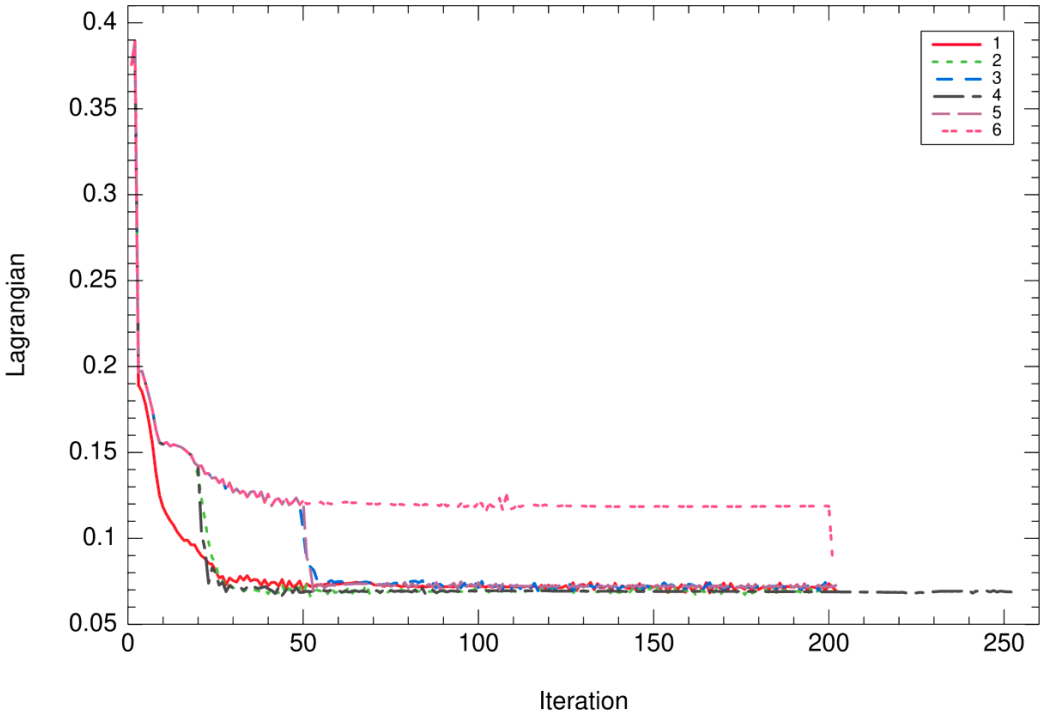

Figure 5.21: Lagrangian evolution for each strategy of the coupled shape and orientation optimization using the gradient descent method for the 2D cantilever example

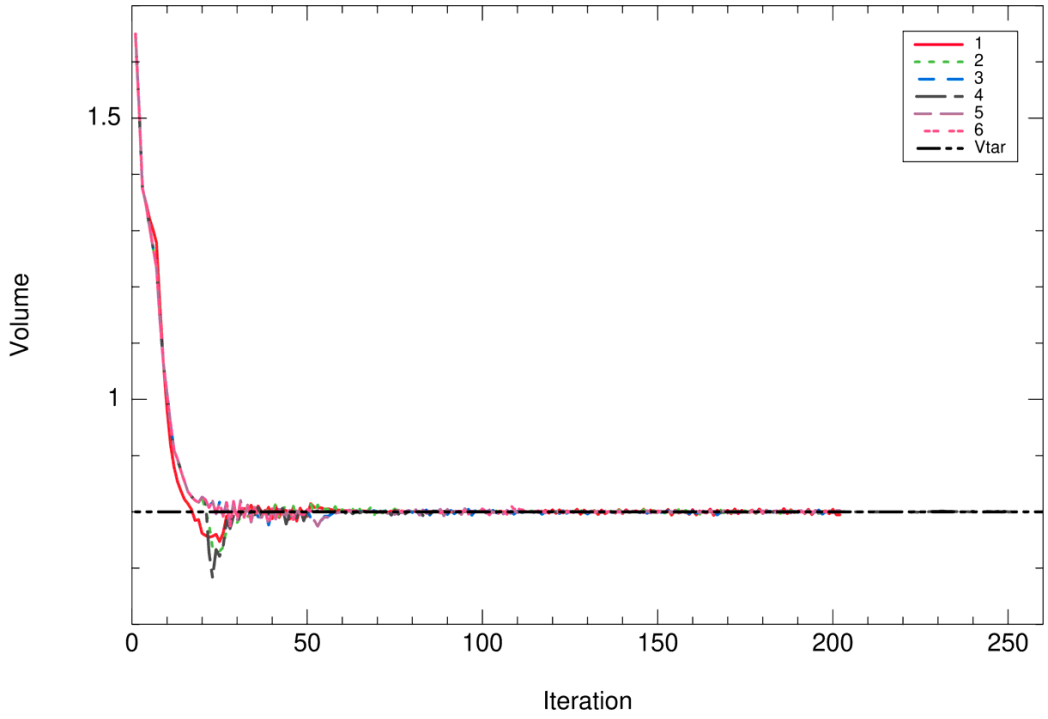

Figure 5.22: Volume evolution for each strategy of the coupled shape and orientation optimization using the gradient descent method for the 2D cantilever example

Displacement inverter example

We study an example of a displacement inverter Ω in elasticity which belongs to a square domain D of dimensions 1×1. It is fixed on two small boundary subsets Γ_D, of a length size 0.04, located on the left side of D and a force $g = -e^x$ is applied on a centered boundary subset Γ_N, of a length size 0.1, located on the left side of D (see figure 5.23a). The structure is filled with an orthotropic material where the values of its mechanical moduli are given in table 5.3 (the Poisson's ratio ν_{21} is given by $\nu_{21} = \nu_{12}\frac{E_2}{E_1}$). The material is also parameterized by an orientation angle α. A displacement inverter function is to move the subset Γ_0, of a length size 0.1, to the opposite direction of the pulling force g, applied on the subset Γ_N that is also of the length size 0.1. This means that the x component of the displacement u on Γ_0 should be positive. Therefore, the objective function of this problem, which is minimized, consists of the squared error between a target displacement u_0 and the structure displacement on the surface Γ_0:

$$J(\Omega, \alpha) = \int_{\Gamma_0} \frac{1}{2}|u - u_0|^2 \mathrm{d}x. \tag{5.16}$$

We do not want the left surface of the mesh to move dramatically when we pull it, thus we add a null target displacement condition on the surface Γ_N. The objective function becomes:

$$J(\Omega, \alpha) = \int_{\Gamma_0} \frac{1}{2}\left|u - u_0\right|^2 \mathrm{ds} + \int_{\Gamma_N} \frac{1}{2}|u|^2 \mathrm{ds}. \tag{5.17}$$

We also have a constraint of a target volume that makes 40% of the whole domain D. We define the Lagrangian of this problem by:

$$\mathcal{L}(\Omega, \alpha, \lambda) = \int_{\Gamma_0} \frac{1}{2}|u - u_0|^2 \mathrm{d}x + \int_{\Gamma_N} \frac{1}{2}|u|^2 \mathrm{ds} + \lambda \left(\int_{\Omega} dx - V_T \right), \tag{5.18}$$

and the two sets of admissible designs are defined by (5.4) and (5.5). Wee also added a constraint of symmetry of the material orientation about the axis of the applied force, this constraint is taken into account by applying a symmetrization of the orientation angle α whenever it is updated using the angle gradient.

We initialize the optimization with an horizontal orientation of the stiffer direction of the material ($\alpha_0 = 0$) and with the shape of figure 5.23b. We set

the target displacement to $u_0 = e^x$. Then we apply the coupled topology and gradient descent orientation optimization algorithm (algorithm 10) without the orientation regularization step 11 for $M = 60$, $n_{or} = 50$ and $n_{per} = 50$. Note that we use a mesh of 20000 triangular elements and that, before the optimization, we have $u_x = -0.05630157$ at the midpoint of Γ_0. Note also that because the optimization problem of this example is non self-adjoint, we have to solve an adjoint problem and compute an adjoint state p before computing either the shape or the orientation gradient, at each iteration n. The adjoint problem is given by:
Find $p \in (H^1(\Omega))^2$, such that:

$$\begin{cases} -\operatorname{div}(A^*(\alpha)e(p)) = 0 & \text{in } \Omega \\ p = 0 & \text{on } \Gamma_D \\ A^*(\alpha)e(p)n = u_0 & \text{on } \Gamma_0 \\ A^*(\alpha)e(p)n = 0 & \text{on } \Gamma. \end{cases}$$

E_{11}	E_{22}	G_{12}	ν_{12}	α_0
10	1	1	0.3	0

Table 5.3: Material characteristics for the displacement inverter example

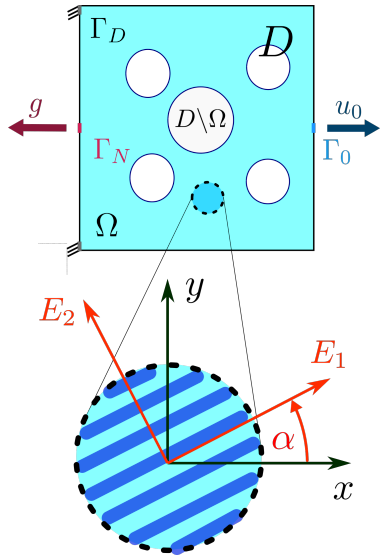

(a) Model and boundary conditions of the displacement inverter

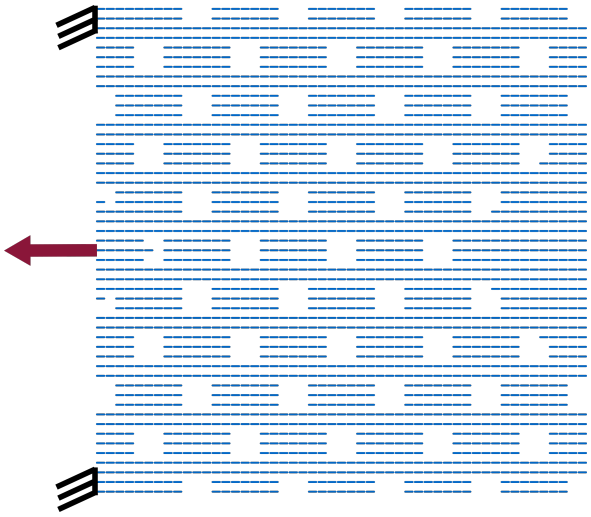

(b) Initialization of the displacement inverter: plot of stiffest direction of the local anisotropy

Figure 5.23: Displacement inverter optimization problem

Figure 5.24 presents the structure that was generated by the coupled optimization algorithm 10. We observe that the optimization of the shape has removed a significant amount of material from the central region of the structure to create a compliant mechanism. The obtained compliant mechanism works in a way that, when the force g is applied, the upper and bottom sides of the structure are closed together to make the two bars, that are on the right, push the surface Γ_0 in the direction of e^x. We also observe that the obtained optimal orientation of the stiffer material direction is globally parallel to the bars of the shape and that the obtained orientation is symmetric and well regularized, even at the level of the joints of the bars. The value of the displacement in the direction of e^x at the midpoint of Γ_0 gives $u_x = 0.302197$. This value verifies that the surface Γ_0 is moving in the opposite direction of the applied force g.

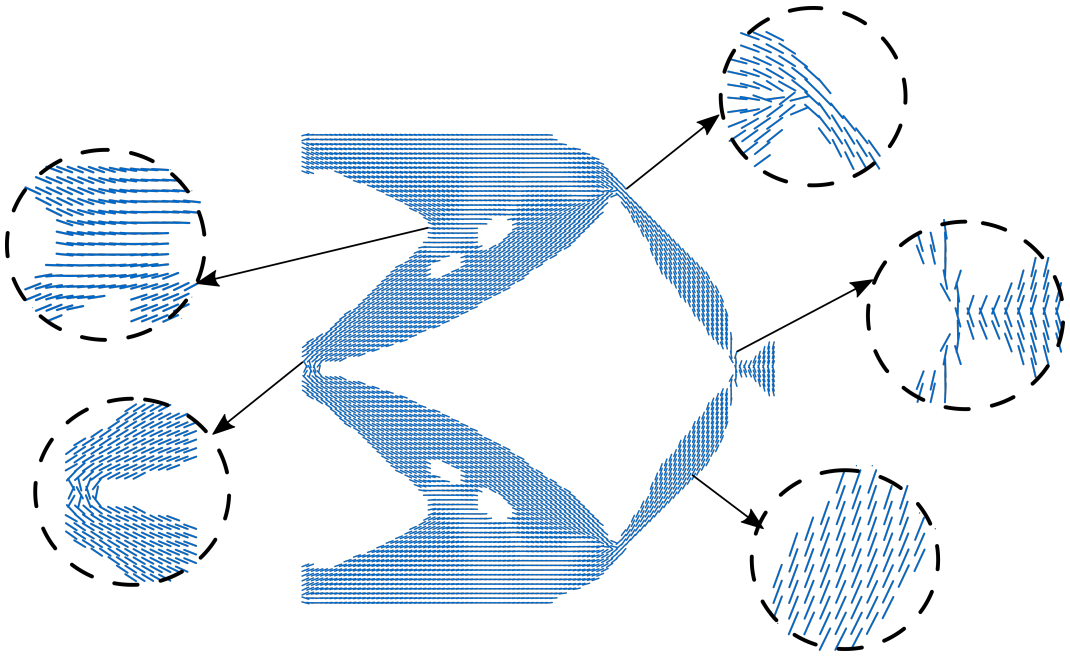

Figure 5.24: Optimized displacement inverter: plot of stiffest direction of the local anisotropy

Results: Comparison of the inverter results

In the following, we consider the same previous problem of inverter optimization with the same initial shape of figure 5.23b. We also consider the same material characteristics of table 5.3 and the same mesh. We apply two different strategies of coupled optimizations of shape and orientation using the gradient descent method without applying the orientation regularization: the first strategy consists of applying 60 iterations of gradient descent optimization orientation after each 50 iteration of shape optimization and the second strategy is to optimize the orientation only after applying the topology optimization. The figure 5.25 gives the results that are obtained with each optimization strategy for two different initialization of the orientation; horizontally and vertically.

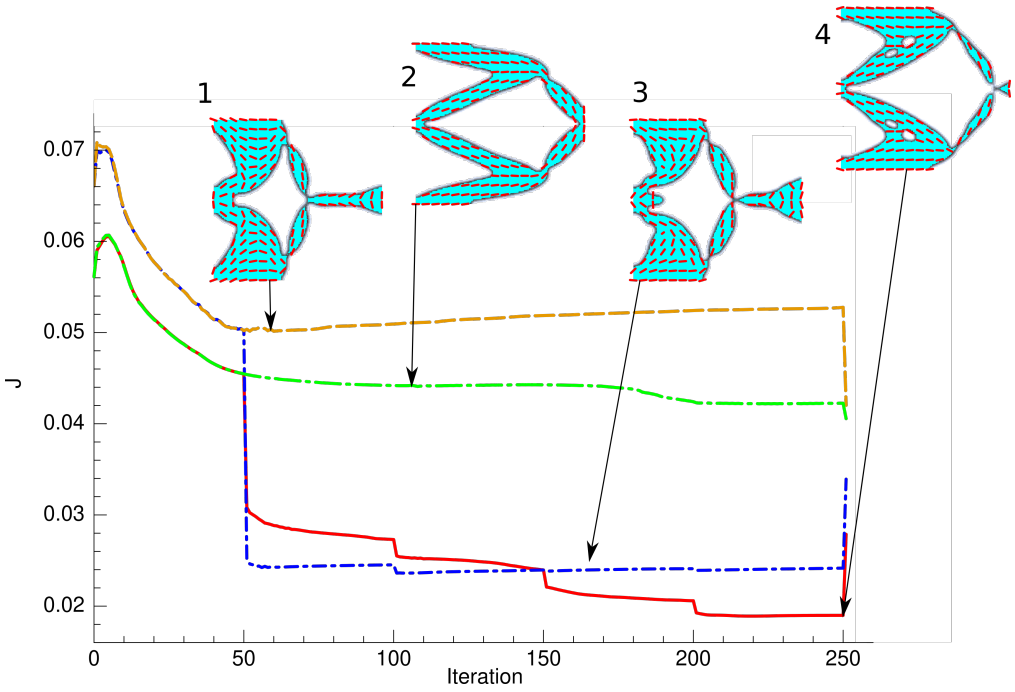

Figure 5.25: Obtained structures and objective functions for the two optimization strategies and the two initializations of the inverter example. Optimization 1: orientation optimized only in the end with $\alpha_0 = \pi/2$. Optimization 2: orientation optimized only in the end with $\alpha_0 = 0$. Optimization 3: concurrent optimization with $\alpha_0 = \pi/2$. Optimization 4: concurrent optimization with $\alpha_0 = 0$

The shape converges approximately after 70 iterations for the example 1. For the remaining three examples, the convergence of the shape is after 210

iterations. We observe that four obtained results are different from each other. The examples 3 and 4 results, where one optimized the shape and the orientation concurrently, gave a lower objective function than the ones where we have optimized the orientation only at the end. Also the optimizations where we have initialized the orientations horizontally gave a lower objective function than when they were initialized vertically. The best result, of objective function and consequently of displacement on the surface Γ_0 (see table 5.4), is obtained when we optimized the orientation concurrently with the shape (optimization number 4). Note that in the last iteration of each optimization, the value of each objective function increases because of the regularization of orientation that we do at the end.

Optimization	1	2	3	4
u_x	$u_x = 0.10011$	$u_x = 0.12936$	$u_x = 0.20876$	$u_x = 0.30220$

Table 5.4: The inverter example obtained displacement along e^x, in the midpoint of the subset Γ_0 of each optimization

Results: 2D Bridge

We study a 2D bridge in elasticity, which is a subset of a rectangular domain D of dimension 4×1, under three vertical loading cases with the three forces g_1, g_2 and g_3, applied respectively on the three surface boundaries Γ_{N_1}, Γ_{N_2} and Γ_{N_3} (see Fig. 5.39a). During each loading case i is applied a force g_i and generated is a displacement field u_i. The applied forces can be interpreted as a vehicle that crosses the bridge and that changes its position, to a position x_i associated to the force g_i. The mesh D is fixed from the tips of its right bottom corners. We fix the movement of the tip of its left bottom corner along the y-axis while we let it moves freely along the direction of the x- axis. The structure is filled with an orthotropic material where the values of its mechanical moduli are given in table 5.3 (The Poisson's ratio ν_{21} is given by $\nu_{21} = \nu_{12}\frac{E_2}{E_1}$). The objective function of this problem is written as the sum of compliance of each loading case i:

$$J(\Omega, \alpha) = \sum_{i=1}^{3} \int_{\Gamma_{N_i}} g_i u_i \mathrm{d}x. \tag{5.19}$$

We also have a constraint of a target volume that makes 30% of the whole

volume of D. We define the Lagrangian then by:

$$\mathcal{L}(\Omega, \alpha), \lambda) = \sum_{i=1}^{3} \int_{\Gamma_{N_i}} g_i u_i \mathrm{d}x + \lambda \left(\int_{\Omega} dx - V_T \right), \tag{5.20}$$

and the two sets of admissible designs by (5.4) and (5.5).

We choose a structured and symmetric triangular mesh that is constituted by 6601 nodes. We run the coupled optimization using two strategies without applying the orientation regularization; the first strategy consists of applying 60 iterations of gradient descent orientation optimization each 50 iterations of the shape optimization. The second strategy consists of optimizing the orientation using the gradient descent method when the shape optimization loop is finished. We proceed with the two strategies using the initial shape of figure 5.27 and using two different initializations of the orientation one horizontally and the other vertically. In the end, the obtained structures are presented in the figures 5.28 to 5.30. The objective function, Lagrangian function and the volume evolution for each strategy are presented in the figures 5.31, 5.32 and 5.33.

Note that in this problem we have three displacement. This means that one needs to solve the elasticity problem three times, once for each displacement, whenever we want to compute a shape gradient or an Euler angle partial gradient in the two used algorithms. At the end of the optimization, we obtain the structure in the figure 5.40.

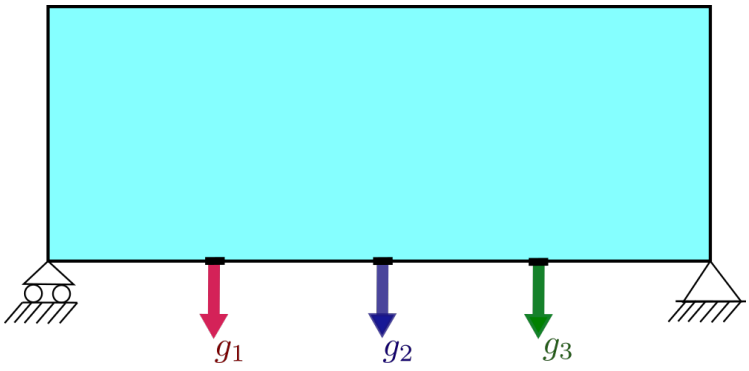

Figure 5.26: 2D bridge loads and boundary conditions

We observe that obtained results are different from each other. The coupled shape optimization where one optimize the shape and the orientation gave a lower global compliance than the ones where the orientation is fixed. Also the optimizations where we have initialized the orientations horizontally gave a lower global compliance than when we they were initialized vertically. The best result,

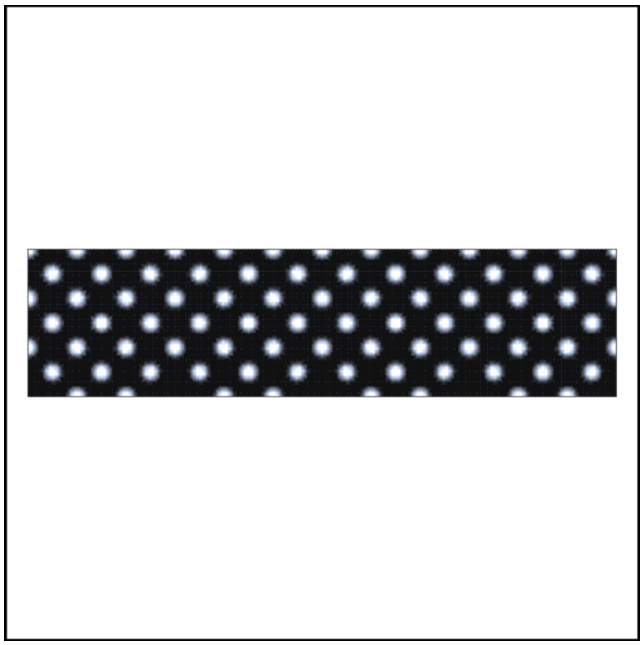

Figure 5.27: Initial 2D bridge shape

of global compliance is obtained when we optimized the orientation concurrently with the shape starting with an horizontal orientation. The convergence of the algorithm while the orientation is fixed horizontally (140 iterations) was faster than the concurrent orientation. However, the convergence was the slowest of the four optimizations when the orientation was fixed vertically (230 iterations). In the other side, the concurrent optimization iterations was not influenced by the initialization of orientation (160 iterations until convergence for both initializations).

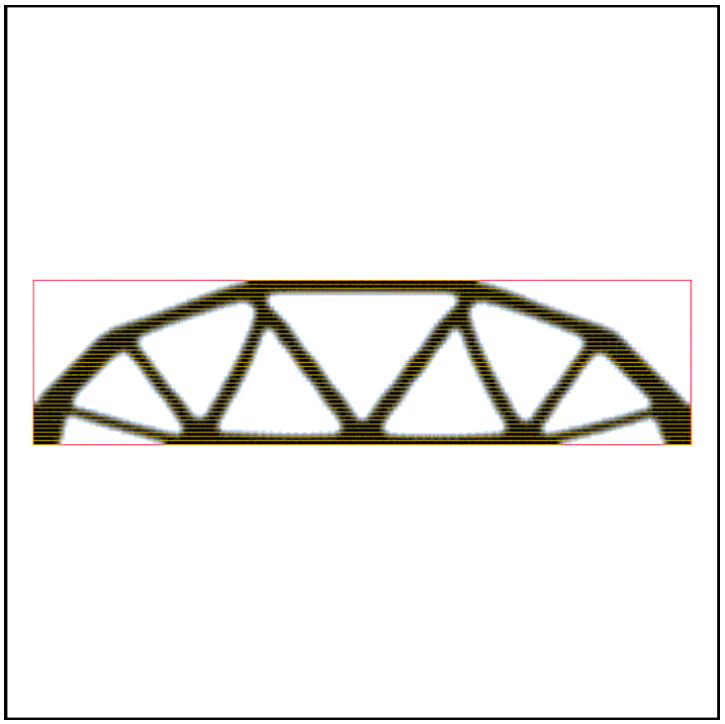

(a) Optimized shape for the case of horizontal stiff orientation ($\alpha = 0$)

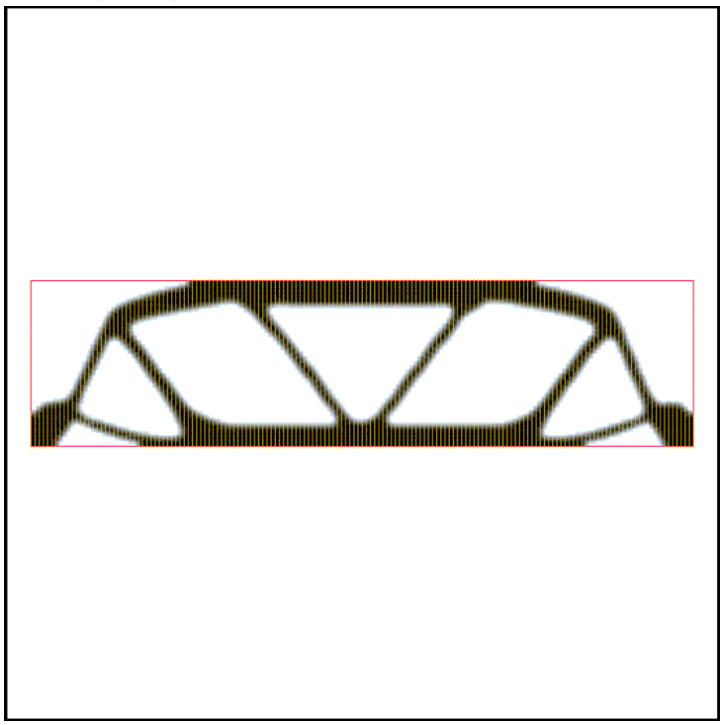

(b) Optimized shape for the case of vertical stiff orientation ($\alpha = \frac{\pi}{2}$)

Figure 5.28: Shape optimized anisotropic bridge with a fixed orientation

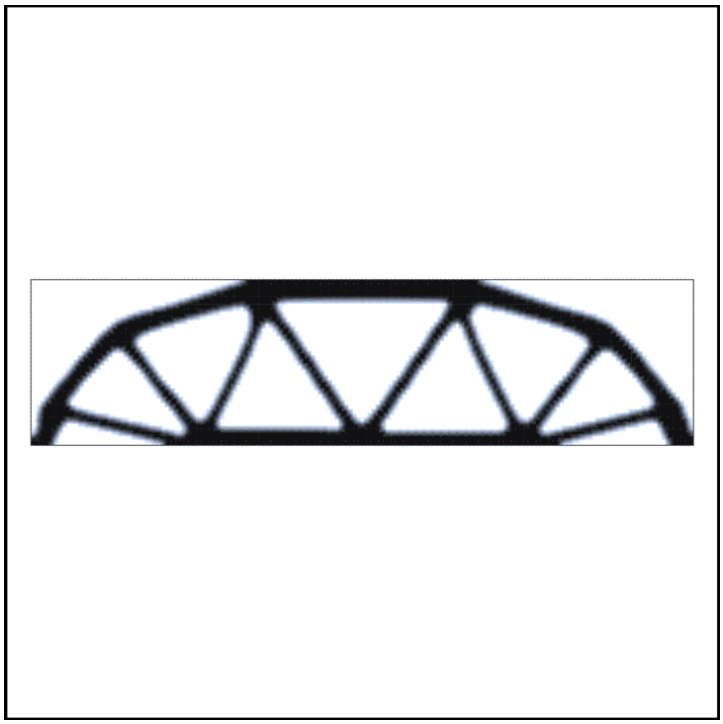

(a) Optimized bridge: obtained shape

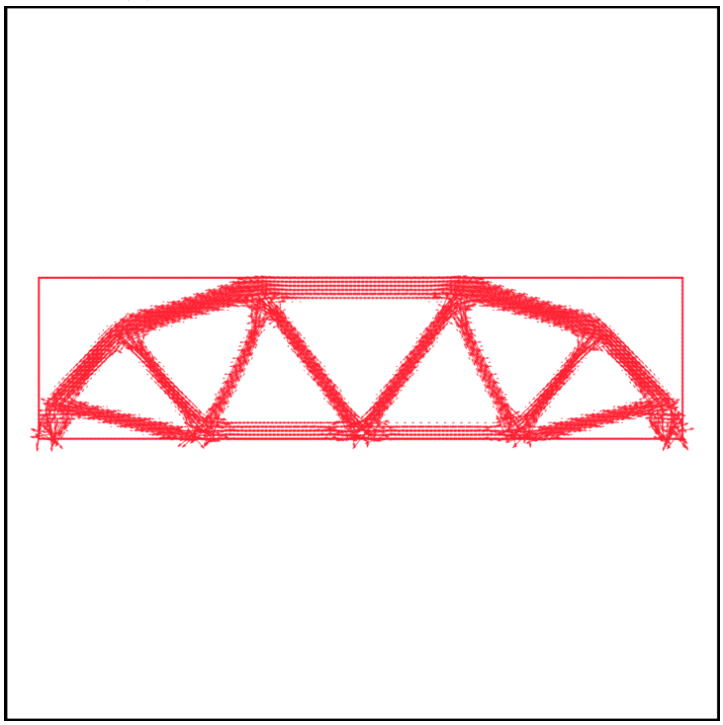

(b) Optimized bridge: plot of stiffest direction of the local anisotropy

Figure 5.29: Optimized bridge using horizontal orientations initialization and the strategy of optimizing the orientation using the gradient descent method after each 50 iterations of shape optimization

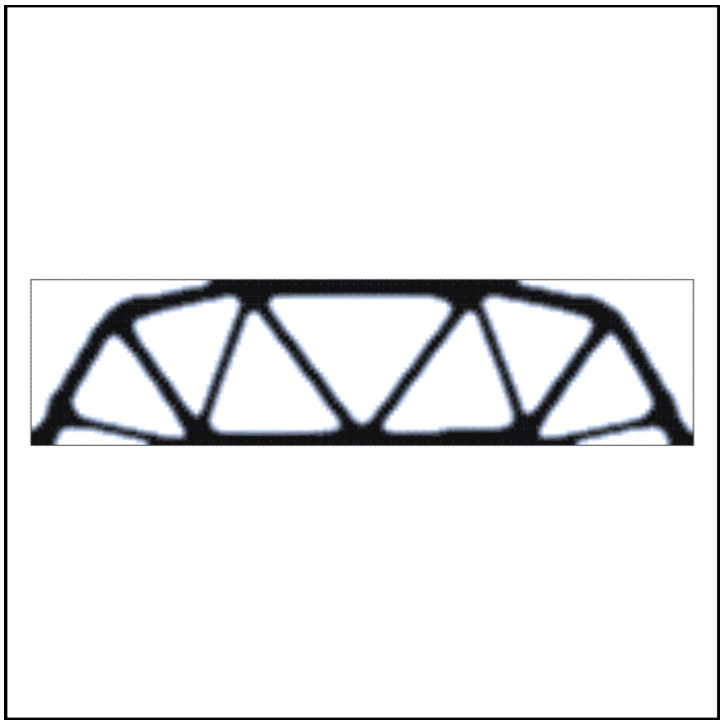

(a) Optimized bridge: obtained shape

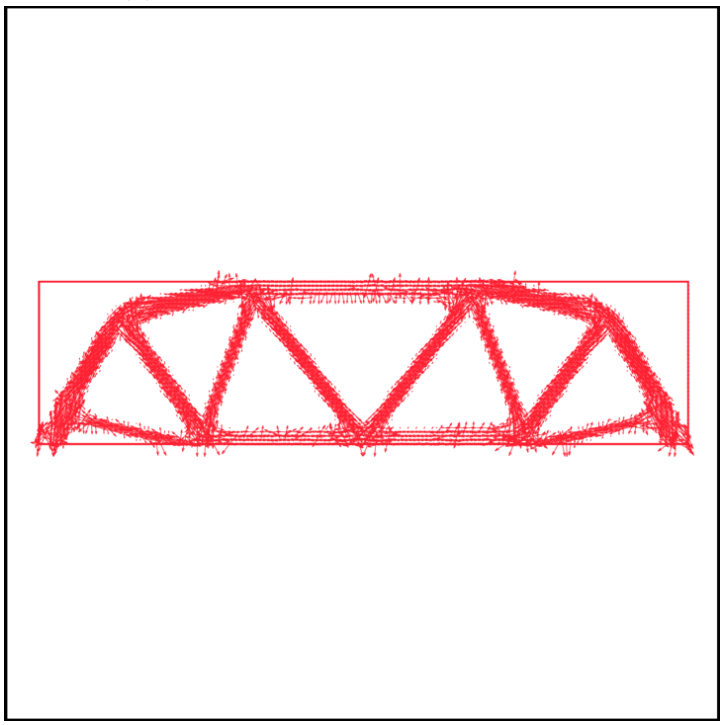

(b) Optimized bridge: plot of stiffest direction of the local anisotropy

Figure 5.30: Optimized bridge using vertical orientations initialization and the strategy of optimizing the orientation using the gradient descent method after each 50 iterations of shape optimization

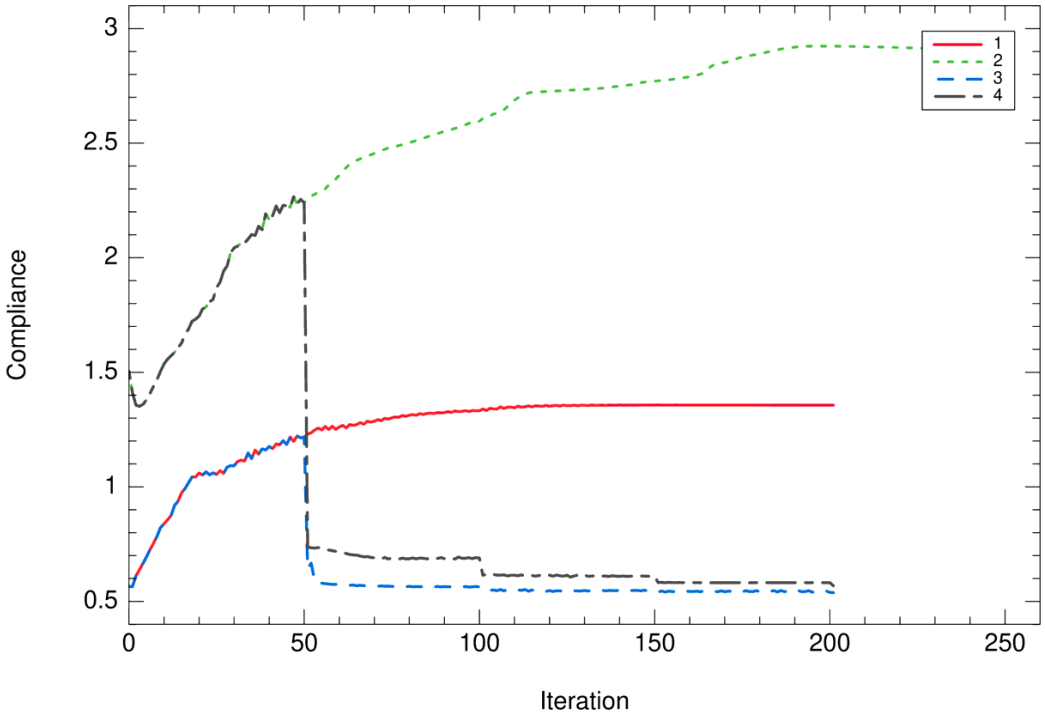

Figure 5.31: Compliance evolution for each optimization of the coupled shape and orientation optimization using the gradient descent method for the 2D bridge example

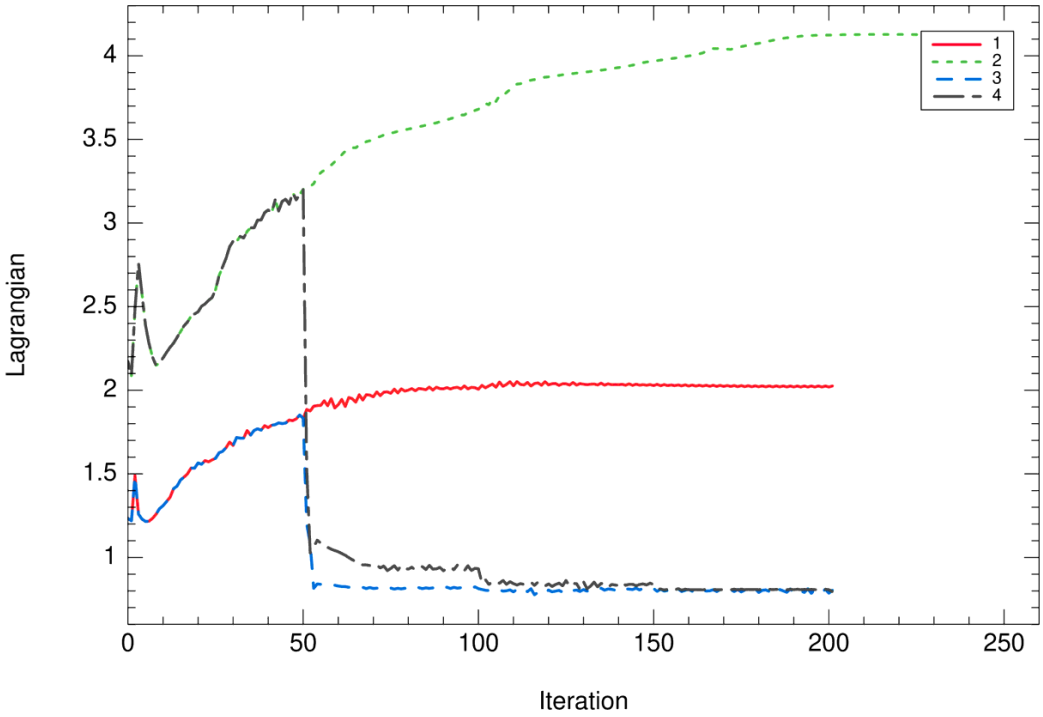

Figure 5.32: Lagrangian evolution for each optimization of the coupled shape and orientation optimization using the gradient descent method for the 2D bridge example

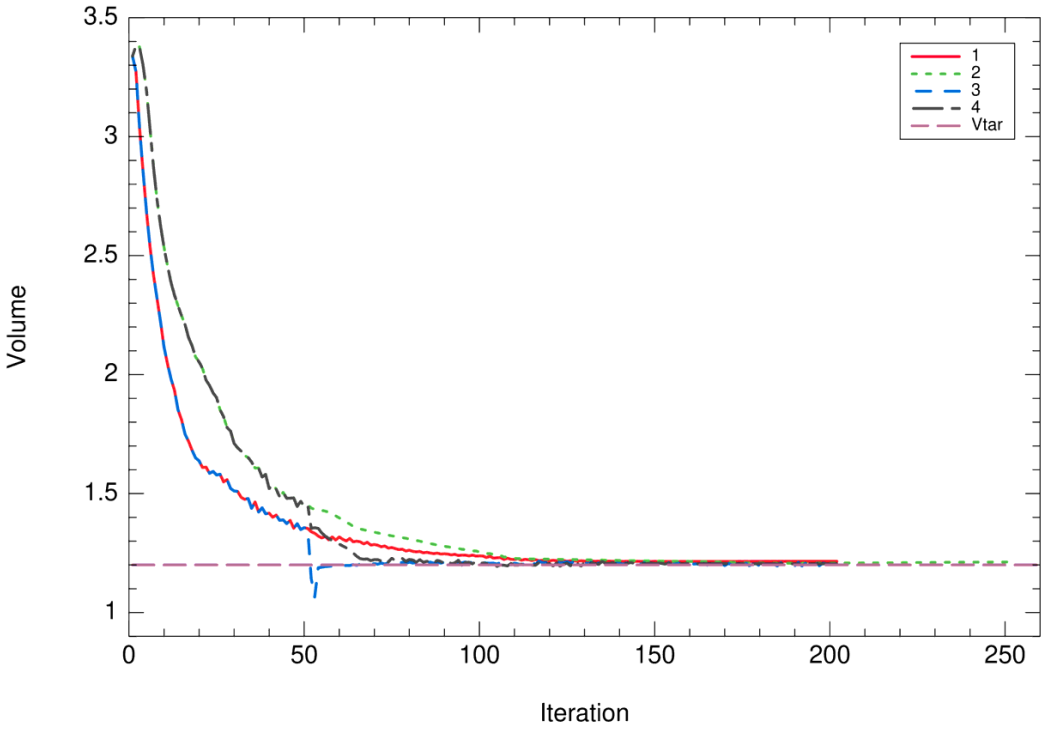

Figure 5.33: Volume evolution for each optimization of the coupled shape and orientation optimization using the gradient descent method for the 2D bridge example

5.2 Coupled optimization of topology and orientation in 3D

5.2.1 Optimization problem

Consider a structure in 3D with a shape Ω composed by a linearly elastic orthotropic material and defined inside a design domain D. The orthotropic material has the Hooke's law fourth order elasticity tensor $A^*(\boldsymbol{\alpha})$, where $\alpha \in (L^2(D))^N$ is the Euler angles vector that orient the material fixed frame $x'y'z'$ with respect to the initial frame of reference xyz, where $N = 2$ in the case of a transverse isotropic material and $N = 3$ in the case of a general orthotropic material. In the material frame $x'y'z'$, the orthotropic elasticity Hooke's law is known, constant and denoted A. In the case of transverse isotropic material, the tensor A is defined by the following elasticity moduli; two Young's moduli E_1 and E_p, three Poisson's ratios ν_{1p}, ν_{p1} and ν_p, with the relation $\nu_{p1} = \nu_{1p}\frac{E_p}{E_1}$, and one shear modulus G_{1p}. We suppose that $E_1 \geq E_p$. In the case of a general orthotropic material, A is defined by the following elasticity moduli; three Young's moduli E_1, E_2 and E_3, six Poisson's ratios $\nu_{12}, \nu_{13}, \nu_{23}, \nu_{21}, \nu_{31}$ and ν_{32}, related with the three relations $\nu_{21} = \nu_{12}\frac{E_2}{E_1}, \nu_{31} = \nu_{13}\frac{E_3}{E_1}$ and $\nu_{32} = \nu_{23}\frac{E_3}{E_2}$, and the three shear moduli G_{23}, G_{13} and G_{12}. We suppose that $E_1 \geq E_2 \geq E_3$. The relation between A in Kelvin formalism and the elasticity moduli, in the two cases, is given respectively by the formulas (2.6) and (2.3). We also suppose that the boundary of Ω is divided into three disjoints borders

$$\partial\Omega = \Gamma \cup \Gamma_N \cup \Gamma_D,$$

where Γ is the variable part of the boundary, Γ_D is a fixed part of the design boundary on which the mechanical displacement is fixed (Dirichlet boundary condition), and Γ_N is also a fixed part of the design boundary on which the force g is applied (Neumann boundary condition). It is assumed that the variable part Γ of the border is free of any effort.

The model of elasticity that is studied is then written: Find u in $(H^1(\Omega))^3$ such that:

$$\begin{cases} -\operatorname{div}(A^*(\boldsymbol{\alpha})e(u)) = f & \text{in } \Omega \\ u = 0 & \text{on } \Gamma_D \\ A^*(\boldsymbol{\alpha})e(u)n = g & \text{on } \Gamma_N \\ A^*(\boldsymbol{\alpha})e(u)n = 0 & \text{on } \Gamma. \end{cases}$$

The aim of the coupled optimization in this section is to find a structure shape Ω

and an orientation angles vector $\boldsymbol{\alpha}$ that optimize an objective function $J(\Omega, \boldsymbol{\alpha})$ which in the other hand represents some physical characteristic of the design.

We suppose a general objective function $J(\Omega, \boldsymbol{\alpha})$ that is the sum of the integral of the function j defined on Ω and of the integral of the function l defined on Γ_J, where Γ_J does not intersect the

$$J(\Omega, \boldsymbol{\alpha}) = \int_\Omega j(u)\mathrm{dx} + \int_{\Gamma_J} l(u)\mathrm{d}s. \tag{5.21}$$

The optimization problem is then written:

$$\inf_{\substack{\Omega \in \mathcal{U}_{ad}^{\Omega} \\ \alpha \in \mathcal{U}_{ad}^{\boldsymbol{\alpha}}}} J(\Omega, \boldsymbol{\alpha}), \tag{5.22}$$

where we have two sets of admissible designs:

$$\mathcal{U}_{ad}^{\Omega} = \left\{ \Omega \subset D \text{ s.t. } \int_\Omega dx = V_T \right\}, \tag{5.23}$$

and

$$\mathcal{U}_{ad}^{\boldsymbol{\alpha}} = \left\{ \boldsymbol{\alpha} \in (L^2(\Omega))^N \right\}. \tag{5.24}$$

Note that the structure Ω is optimized under a volume constraint $\int_\Omega dx = V_T$, where $V_T \in \mathbb{R}_+^*$ is a fixed target volume for the structure.

5.2.2 Topology optimization coupled with an optimality criterion orientation optimization method

Similarly to 2D, this method in 3D is limited to the optimization problem of a single load compliance minimization. The objective function, which is now parameterized by the shape Ω and the angles vector $\boldsymbol{\alpha}$ is written:

$$J(\Omega, \boldsymbol{\alpha}) = \int_\Omega fu\mathrm{dx} + \int_{\Gamma_N} gu\mathrm{ds} = \int_\Omega A^*(\Omega, \boldsymbol{\alpha}) e(u) \cdot e(u)\mathrm{dx}. \tag{5.25}$$

The Lagrangian function that contains the volume constraint (5.23) is written,

for $\lambda \in \mathbb{R}$

$$\mathcal{L}(\Omega, \boldsymbol{\alpha}, \lambda) = \int_{\Omega} A^*(\Omega, \boldsymbol{\alpha}) e(u) \cdot e(u) \mathrm{dx} + \lambda \left(\int_{\Omega} dx - V_T \right).$$

The coupled optimization problem (5.22) becomes written:

$$\min_{\substack{\Omega \in D \\ \boldsymbol{\alpha} \in \mathcal{U}_{ad}^{\boldsymbol{\alpha}}}} \max_{\lambda \in \mathbb{R}} \mathcal{L}(\Omega, \boldsymbol{\alpha}, \lambda). \tag{5.26}$$

In practice, we suppose that the angle is fixed when the shape is updated. We use an ersatz material approximation (see ersatz material approximation in section 1.3.1) to avoid having regions in the shape Ω^{n+1} that do not have an orientation when some boundaries parts move outward from the domain Ω^n. As a result, the orientation angle in this case is defined and optimized on the whole domain D (including the void).

The algorithm (Algorithm 11) of topology optimization coupled with optimality criterion method for the orientation consists of a topology optimization loop where after each update of the shape Ω^n to Ω^{n+1}, the 3D anisotropy orientation, at each iteration n, is updated to make the axis of the material coincide with directions the principal stress. For this latter purpose, we compute the stress $\sigma^n_{\Omega_{n+1}}$ unique solution of:

$$\min_{\sigma \in H_3} \int_{\Omega^{n+1}} \left(A^*\left(\boldsymbol{\alpha}^n\right)\right)^{-1} \sigma \cdot \sigma dx, \tag{5.27}$$

where the set H_3 is given by (4.6). Note that in this section, the top right index of an algorithm variable (e.g. $\boldsymbol{\alpha^n}$) indicates the iteration number and not a power exponent. The usual iteration index spot is taken by the angles vector component number. After computing $\sigma^n_{\Omega_{n+1}}$, we update the Euler angles vector $\boldsymbol{\alpha}^n$ using the optimality formulas (4.9), (4.10), (4.13), (4.11) and (4.12) in case of a general orthotropic material, and the optimality formulas (4.14) and (4.15) in case of transverse isotropic material. We repeat this whole procedure until the objective function is converged. Practically, because the descent step of the shape is small. The final orientation that are obtained when the objective function is converged are usually optimal. If it is not the case, one could add some more iterations until the orientations also get into an optimal state. In the end, we regularize the obtained orientation using the method of section 4.3.1.

Note that, when λ is converged, this algorithm is interpreted as an alternate

Algorithm 11: 3D topology optimization coupled with the optimality criterion method for orientation

Initialize the anisotropy angles vector $\boldsymbol{\alpha}^0$ and the shape level set function ϕ^0

for $n = 0, ..,$ *until convergence* **do**

  Solve the elasticity problem (5.1) to get $u^n_{\Omega_n}$.

  Compute the shape sensitivity $\theta \mapsto \frac{\partial \mathcal{L}(\Omega^n, \boldsymbol{\alpha}^n, \lambda^n)}{\partial \Omega}(\theta)$ using (1.21).

  Update the level set function ϕ^n (and the shape Ω^n) such that

  $\mathcal{L}\left(\Omega^{n+1}, \alpha^n, \lambda^n\right) < \mathcal{L}\left(\Omega^n, \alpha^n, \lambda^n\right)$ (see Algorithm 2)

  Update the Lagrange multiplier λ^n to λ^{n+1} using (1.24)

  Compute the stress $\sigma^n_{\Omega_{n+1}}$, unique solution of:

$$\min_{\sigma \in H_3} \quad \int_{\Omega^{n+1}} (A^*(\boldsymbol{\alpha}^n))^{-1} \sigma \cdot \sigma \, \mathrm{dx}, \tag{5.28}$$

  by solving the elasticity problem (by deducing $\sigma^n_{\Omega_{n+1}}$ from $u^n_{\Omega_{n+1}}$).

  Update the angles vector $\boldsymbol{\alpha}^n$ to $\boldsymbol{\alpha}^{n+1}$; the angles vector corresponding to the principal stresses directions obtained using the optimality formulas (4.9), (4.10), (4.13), (4.11) and (4.12) in case of a general orthotropic material, and the optimality formulas (4.14) and (4.15) in case of transverse isotropic material.

end

Regularize the orientation by optimizing the regularization objective function (4.21).

minimization in the shape Ω then in the angles vector $\boldsymbol{\alpha}$ of the function $\mathcal{L}(\Omega, \boldsymbol{\alpha}, \lambda)$.

5.2.3 Topology optimization coupled with a gradient descent orientation optimization method

For the resolution of industrial optimization problem such as a multi-load optimization problem, a constrained orientation problem or a non self-adjoint problem such as the target displacement or stress optimization problem. One has to use a gradient descent method for the orientation optimization of an anisotropic material instead of the optimality criterion method. In the same way as the 3D case. In this section, we update the algorithm of coupled optimization of the topology with the orientation of the anisotropy using a gradient descent method in 2D to the 3D case. We consider a general objective function $J(\Omega, \boldsymbol{\alpha})$ written as (5.21), where Γ_J does not intersect the Dirichlet boundary Γ_D (see figure 3.1). The Lagrangian function, defined to take account of the volume constraint (5.23), is written:

$$\mathcal{L}(\Omega, \boldsymbol{\alpha}, \lambda) = J(\Omega, \boldsymbol{\alpha}) + \lambda \left(\int_\Omega dx - V_T \right) \tag{5.29}$$

where $\lambda \in \mathbb{R}$ is the Lagrange multiplier. The coupled optimization problem (5.22) is then written:

$$\min_{\substack{\Omega \in D \\ \boldsymbol{\alpha} \in \mathcal{U}_{ad}^{\boldsymbol{\alpha}}}} \max_{\lambda \in \mathbb{R}} \mathcal{L}(\Omega, \boldsymbol{\alpha}, \lambda) \tag{5.30}$$

While one has to use the sensitivity of the Lagrangian with respect to the shape during the optimization, the optimization in the orientation is indifferent to the constraint $C(\Omega)$ thus the sensitivity of the Lagrangian with respect to each orientation angle is equivalent to the sensitivity of the objective function also with respect to each the orientation angle. Besides, In practice, we suppose that the angle vector $\boldsymbol{\alpha}$ is fixed when the shape is updated. We use an ersatz material approximation (see ersatz material approximation in section 1.3.1) to avoid having regions in the shape Ω_{n+1} that do not have an orientation when some boundaries parts move outward from the domain Ω^n. As a result, the orientation angles vector in this case is defined and optimized on the whole domain D (including the void).

The algorithm (Algorithm 12) of coupled optimization problem consists of a

topology optimization loop, where at each iteration $n \in \mathbb{N}$, one adds a fixed number $M \in \mathbb{N}$ of updates of the orientation angle using the gradient descent. Note that the update of the orientation is accepted only when:

$$J\left(\Omega^n, \boldsymbol{\alpha}^{n,m+1}\right) < J\left(\Omega^n, \boldsymbol{\alpha}^{n,m}\right). \tag{5.31}$$

In the other case, the step is repeatedly decreased until the condition (5.31) is verified (also note that in this section, the top right index of an algorithm variable, e.g. $\boldsymbol{\alpha^n}$, indicates the iteration number and not a power exponent. The usual iteration index spot is taken by the angles vector component number). The whole steps on an iteration n are repeated until the objective function is converged. Consequently, we observe that the topology converges to a stable shape. The algorithm end when the shape is converged. The orientations that are obtained in the end should be optimal. If it is not the case, one could add some more iterations of orientation optimization by repeating only the steps 9 to 21 in algorithm 12 until the orientation converge to an optimal state. Note that, when λ is converged, this algorithm is interpreted as an alternate minimization in the shape Ω then in the angle vector $\boldsymbol{\alpha}$ of the function $\mathcal{L}(\Omega, \boldsymbol{\alpha}, \lambda)$.

Algorithm 12: 3D topology optimization coupled with the gradient descent method for orientation

1 Initialize the angles vector $\boldsymbol{\alpha}^0$ and the shape level set function ϕ^0.
2 **for** $n = 1, ..,$ *until convergence* **do**
3 Solve the elasticity problem, then solve the adjoint problem (in case of a non self-adjoint problem).
4 Compute the shape sensitivity.
5 Update the level set function ϕ^n and the shape Ω.
6 Update the Lagrange multiplier λ^n to λ^{n+1} using (1.24).
7 **if** $(n \geq n_{or})$ *and* $(n \bmod n_p = 0)$ **then**
8 **for** $m = 2, .., M$ **do**
9 **for** $i = 1..N$ *(*$N = 2$ *or* 3*)* **do**
10 Solve the elasticity problem, then solve the adjoint problem (in case of a non self-adjoint problem).
11 Compute the gradient $\frac{\partial J(\boldsymbol{\alpha})}{\partial \alpha_i}$ using (4.20).
12 Regularize the gradient $\frac{\partial J(\boldsymbol{\alpha})}{\partial \alpha_i}$.
13 $\alpha_i^n = \alpha_i^{n-1} - t_n \frac{\partial J(\boldsymbol{\alpha}^n)}{\partial \alpha_i^n}$, where $t_{n,m}$ is a small descent step.
14 **end**
15 Solve the elasticity problem, then solve the adjoint problem (in case of a non self-adjoint problem).
16 Compute the objective function $J(\boldsymbol{\alpha}^n)$.
17 **if** $J(\boldsymbol{\alpha}^n) < J(\boldsymbol{\alpha}^{n-1})$ **then**
18 $t^{n,m+1} = 1.2t^{n,m}$ and continue to the next iteration.
19 **else**
20 $t^{n,m+1} = t^{n,m}/2$ and return to step 9.
21 **end**
22 **end**
23 $\boldsymbol{\alpha}_{n+1} = \boldsymbol{\alpha}_{n,M}$.
24 **end**
25 **end**

5.2.4 Numerical results

3D displacement inverter example

We study a 3D displacement inverter in elasticity which belongs to a cubic domain D of dimensions $1 \times 1 \times 1$ (see figure 5.34a). It is fixed on four small surfaces Γ_D in the corners of the left side of D, of size 0.02×0.02. A force $g = -e^x$ is applied on a small surface Γ_N, of size 0.1×0.1, in the middle of the left side of D. The structure is filled with a transverse isotropic material where the values of its mechanical moduli are given in table 5.5 (the Poisson's ratio ν_{p1} is given by $\nu_{p1} = \nu_{1p}\frac{E_p}{E_1}$). The material is also parameterized by two Euler orientation angles that are modeled by the vector $\boldsymbol{\alpha} \in (L^2(\Omega))^2$. Similarly to the 2D displacement inverter example, a 3D displacement inverter function is to move the surface Γ_0 (the blue surface of figure 5.34a), of size 0.1×0.1, to the opposite direction of the pulling force g applied on the surface Γ_N. This means that ue^x on Γ_0 has to be positive. Therefore, we choose an objective function, for a minimization optimization problem, that consists of the squared error between a target displacement $u_0 = e^x$ and the structure displacement on the surface Γ_0 :

$$J(\Omega, \boldsymbol{\alpha}) = \int_{\Gamma_0} \frac{1}{2}|u - u_0|^2 \mathrm{d}x. \tag{5.32}$$

We do not want the surface Γ_N of the mesh to move dramatically when we pull it: thus we add a null target displacement condition on Γ_N. The objective function becomes:

$$J(\Omega, \boldsymbol{\alpha}) = \int_{\Gamma_0} \frac{1}{2}\left|u - u_0\right|^2 \mathrm{d}s + \int_{\Gamma_N} \frac{1}{2}|u|^2 \mathrm{d}s. \tag{5.33}$$

We also have a constraint of a target volume that make 15% of the whole volume of D. We define the Lagrangian of this problem by:

$$\mathcal{L}(\Omega, \boldsymbol{\alpha}, \lambda) = \int_{\Gamma_0} \frac{1}{2}|u - u_0|^2 \mathrm{d}x + \int_{\Gamma_N} \frac{1}{2}|u|^2 \mathrm{d}s + \lambda \left(\int_{\Omega} \mathrm{d}x - V_T \right), \tag{5.34}$$

and the two sets of admissible designs by (5.23) and (5.24).

We initialize the optimization with an horizontal orientation of the stiffer direction of the material, that are parallel to the x-axis, and with the shape of figure 5.34b. The domain D is meshed by a structured and symmetric tetrahedral mesh which has 30000 nodes. We optimize the shape using the

level set topology optimization algorithm (algorithm 2) then we optimize the orientation of the anisotropy while the shape Ω is fixed using the gradient descent algorithm (algorithm 8), without regularizing the orientation. Note that because the optimization problem of this example is not self-adjoint, we have to solve an adjoint problem and compute an adjoint state p before computing either the shape or the orientation gradient, at each iteration n. The topology optimization algorithm converges in 55 iterations and the orientation optimization algorithm converges in 100 iterations.

The resulting optimized structure is shown in figure 5.35.

E_1	E_p	G_{1p}	ν_{1p}	ν_p
10	1	1	0.3	0.3

Table 5.5: Material characteristics for the 3D displacement inverter example

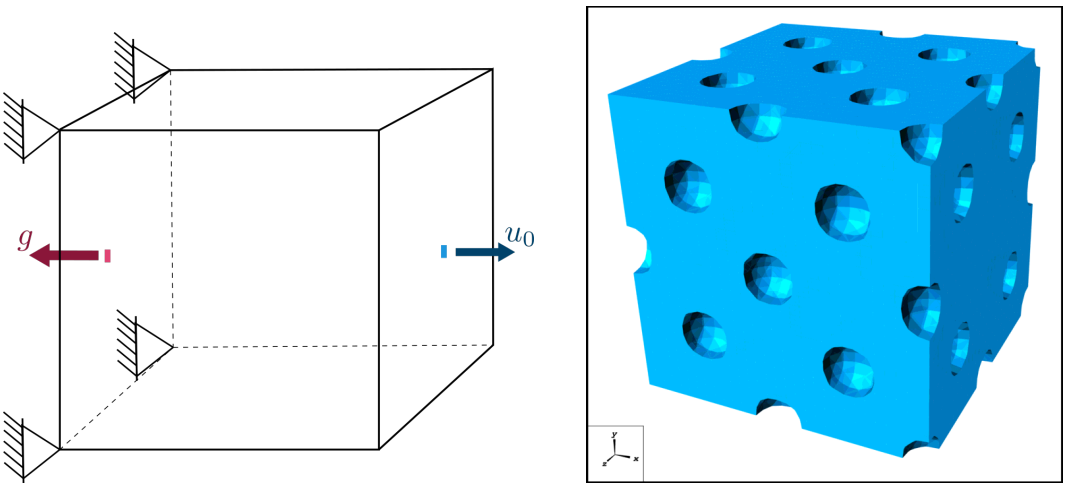

(a) Loads and boundary conditions of the displacement inverter

(b) Initial shape of the displacement inverter

Figure 5.34: 3D displacement inverter problem model

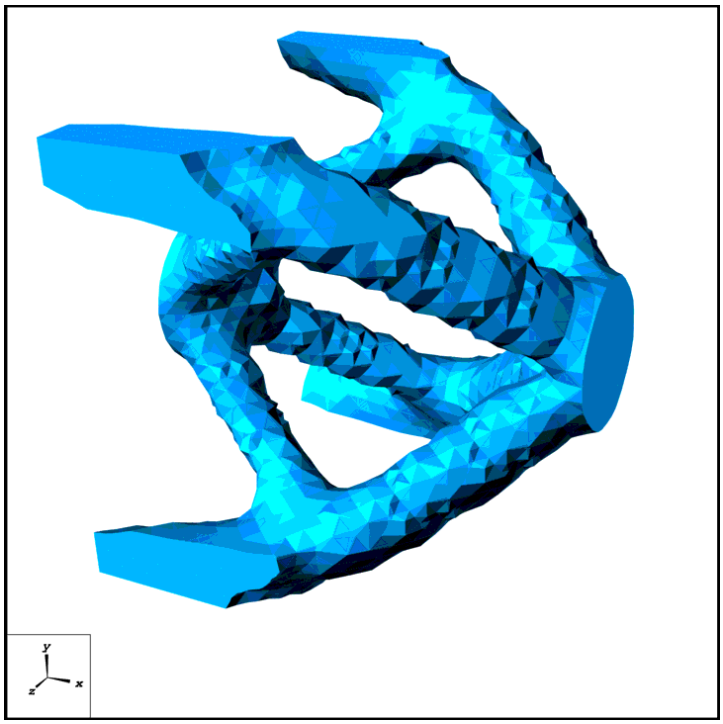

(a) Optimized displacement inverter: obtained shape

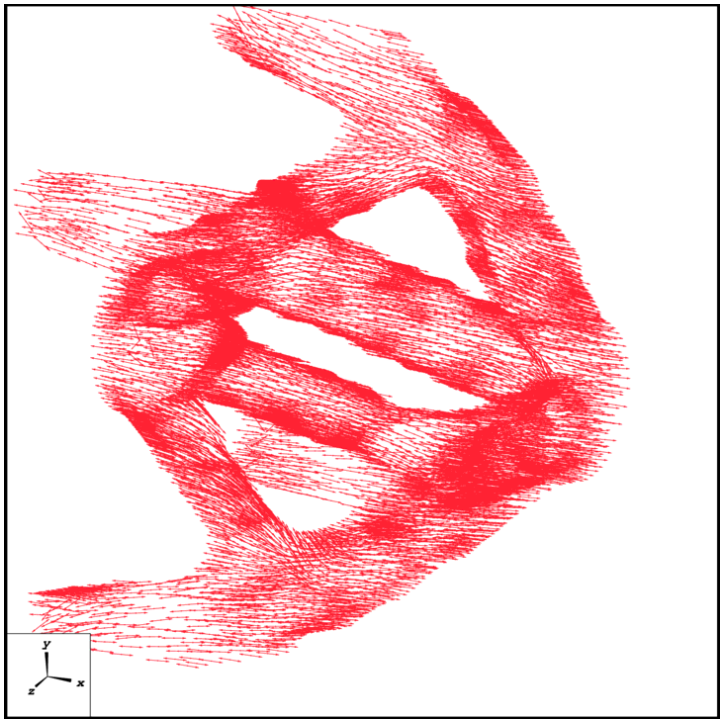

(b) Optimized displacement inverter: plot of stiffest direction of the local anisotropy

Figure 5.35: Optimized displacement inverter

3D cantilever example

We study a 3D cantilever of dimensions $2 \times 1 \times 1.1$ in elasticity that has a fixed boundary (left surface of figure 5.36a) and an applied force $g = -e^y$ on a small surface on the opposite surface boundary Γ_N (the red surface of figure 5.36a), of size 0.1×0.1. The structure is filled with a transverse isotropic material where the values of its mechanical moduli are given in table 5.5 (The Poisson's ratio ν_{p1} is given by $\nu_{p1} = \nu_{1p}\frac{E_p}{E_1}$). The material is also parameterized by two Euler orientation angles that are modeled by the vector $\boldsymbol{\alpha} \in (L^2(\Omega))^2$. We want minimize the compliance of the shape Ω, which is expressed as the work of the applied force:

$$J(\Omega, \boldsymbol{\alpha}) = \int_{\Gamma_N} gu\mathrm{d}x. \tag{5.35}$$

We also have a constraint of a target volume that makes 40% of the whole mesh volume. We define the Lagrangian of this problem by:

$$\mathcal{L}(\Omega, \boldsymbol{\alpha}), \lambda) = \int_{\Gamma_N} gu\mathrm{d}x + \lambda \left(\int_{\Omega} dx - V_T \right), \tag{5.36}$$

and the two sets of admissible designs by (5.23) and (5.24).

We initialize with two different orientations of the anisotropy: one with an horizontal orientation of the stiffer direction of the material, that are parallel to the x-axis. and the other with a vertical orientation of the stiffer direction of the material, that are parallel to the y-axis. The initial shape for the two different problem is the same (figure 5.36b). We choose a structured and symmetric tetrahedral mesh of 29613 nodes. We optimize the shape using the level set topology optimization algorithm (algorithm 2) then we optimize the orientation of the anisotropy while the shape Ω is fixed using the gradient descent algorithm (algorithm 8), without regularizing the orientation. Note that the Lagrange multiplier λ is always fixed to a value of 0.006 during the optimizations. Both shape and orientation converge, for the two initialization, approximately in 55 iterations. In the end of the two optimizations, we obtain the structures of the figures 5.38 and 5.37.

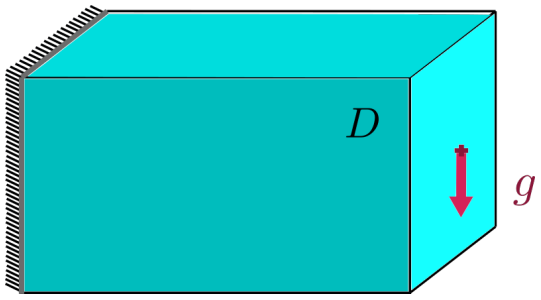

(a) Model and boundary conditions of the cantilever

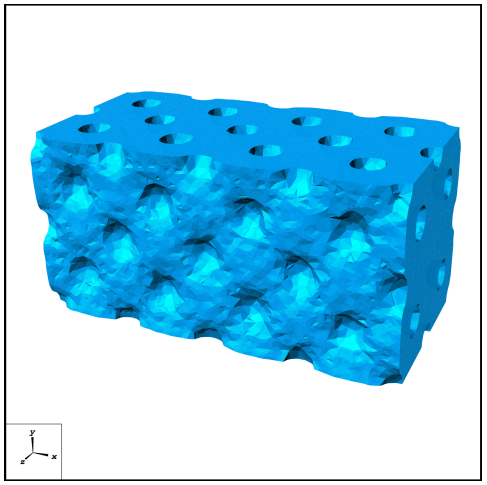

(b) 3D cantilever shape initialization

Figure 5.36: 3D cantilever problem model

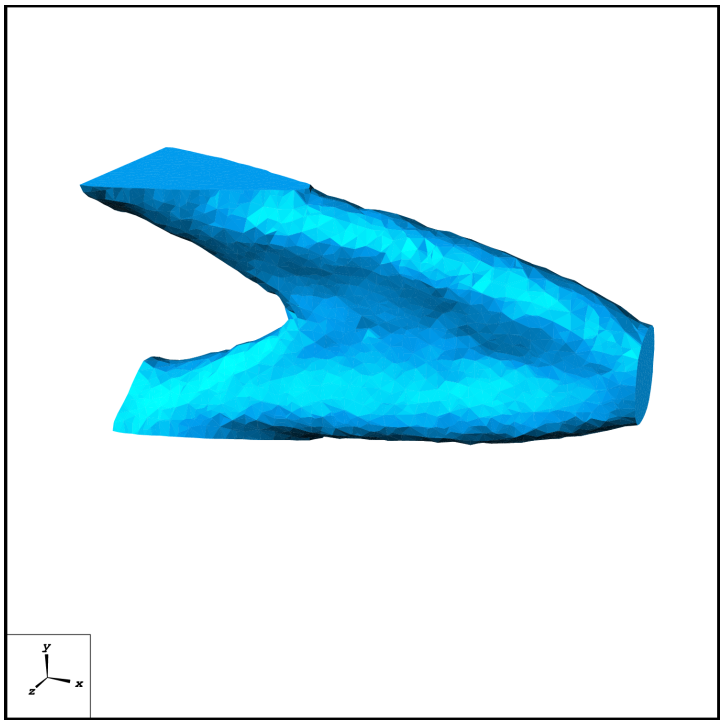

(a) Optimized cantilever: obtained shape

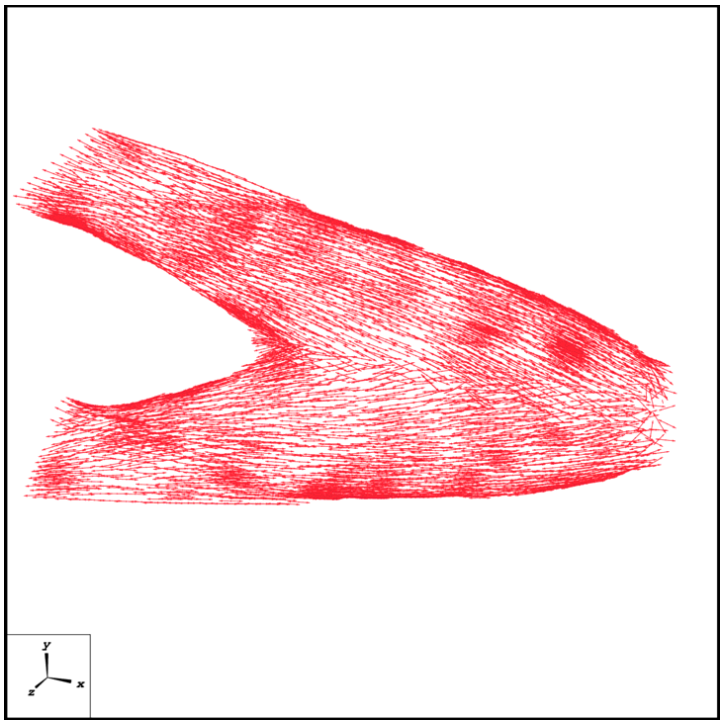

(b) Optimized cantilever: plot of stiffest direction of the local anisotropy

Figure 5.37: Optimized 3D cantilever structure for initialization using horizontal orientation case

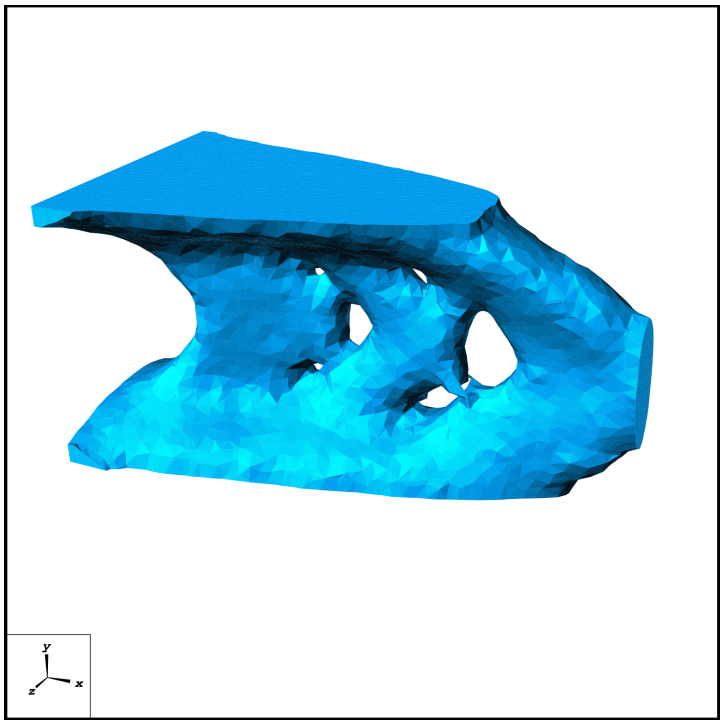

(a) Optimized cantilever: obtained shape

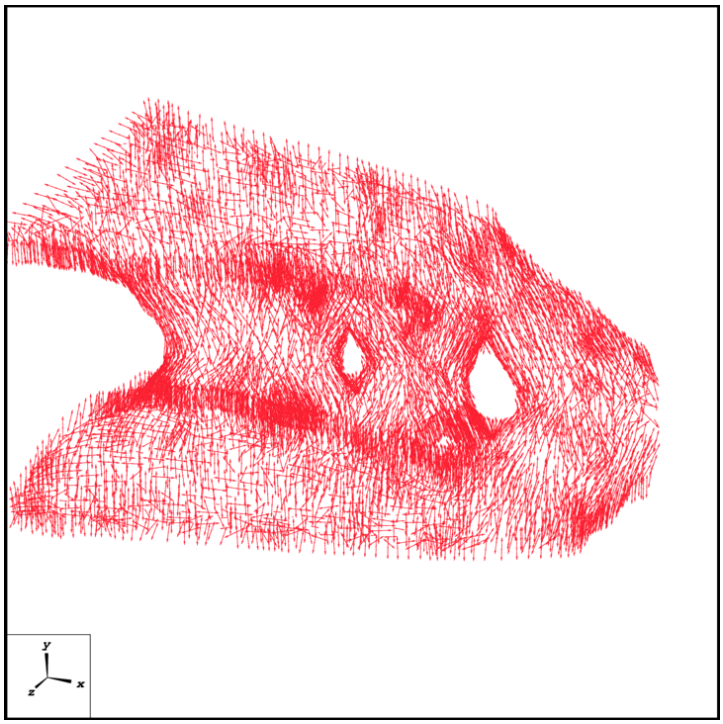

(b) Optimized cantilever: plot of stiffest direction of the local anisotropy

Figure 5.38: Optimized 3D cantilever structure for initialization using vertical orientation case

Multiple load 3D bridge example

We study a 3D bridge in elasticity, that have side plates of dimensions $4.5 \times 1.2 \times 0.1$, under three vertical loading cases g_1, g_2 and g_3, applied respectively on the three surface boundaries Γ_{N_1}, Γ_{N_2} and Γ_{N_3} (see Fig. 5.39a) of sizes 0.2×1. Each loading case i generates a displacement field u_i. The applied forces can be interpreted as a vehicle that crosses the bridge and that changes its position, to a position i associated to the load case i. The gray region that models a road then is not optimized in this problem, it have the dimensions of $4.5 \times 0.1 \times 0.8$.

The mesh D is fixed from the tips of its right bottom corners on surfaces of sizes 0.1×0.1. We fix the movement of the tips of its left bottom corners along the y-axis and the z-axis while we let them move freely along the direction of the x- axis, on another surfaces of sizes 0.1×0.1. The structure is filled with a transverse isotropic material where the values of its mechanical moduli are given in table 5.5 (The Poisson's ratio ν_{p1} is given by $\nu_{p1} = \nu_{1p}\frac{E_p}{E_1}$). The material is also parameterized by two Euler orientation angles that are modeled by the vector $\boldsymbol{\alpha} \in (L^2(\Omega))^2$. The objective function written as the sum of compliance of each loading case i:

$$J(\Omega, \boldsymbol{\alpha}) = \sum_{i=1}^{3} \int_{\Gamma_{N_i}} g_i u_i \mathrm{d}x. \tag{5.37}$$

We also have a constraint of a target volume that make 30% of the whole mesh volume. We define the Lagrangian of this problem by:

$$\mathcal{L}(\Omega, \boldsymbol{\alpha}), \lambda) = \sum_{i=1}^{3} \int_{\Gamma_{N_i}} g_i u_i \mathrm{d}x + \lambda \left(\int_{\Omega} dx - V_T \right), \tag{5.38}$$

and the two sets of admissible designs by (5.23) and (5.24). We initialize the optimization with an horizontal orientation of the stiffer direction of the material, that are parallel to the x-axis, and with the shape of figure 5.39b. We choose a structured and symmetric tetrahedral mesh that is constituted by 40000 nodes. We optimize the shape using the level set topology optimization algorithm (algorithm 2) then we optimize the orientation of the anisotropy while the shape Ω is fixed using the gradient descent algorithm (algorithm 8), without regularizing the orientation. Note that in this problem we have three displacement. This means that one needs to solve the elasticity problem three times, once for each displacement, whenever he wants to compute a shape gradient or an Euler angle partial gradient in the two used algorithms. The

shape optimization algorithm converges in 108 iterations and the orientation optimization algorithm converges in 55 iterations. In the end of the two optimizations, we obtain the structure in the figure 5.40.

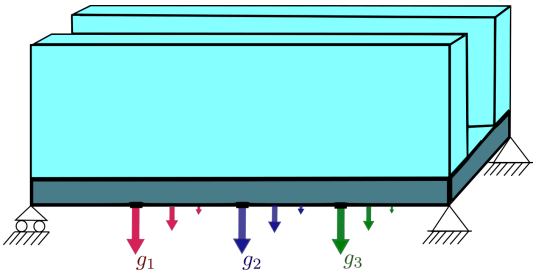

(a) Model and boundary conditions of the bridge

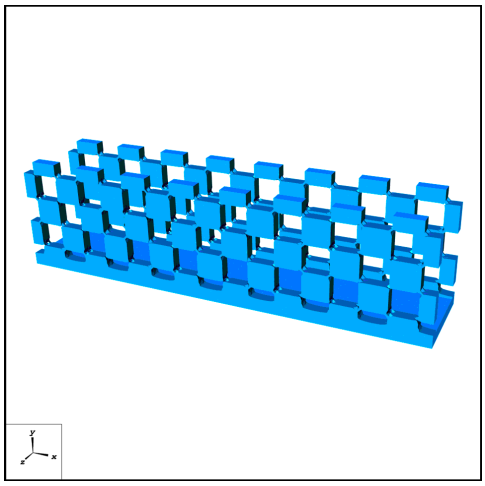

(b) Initial shape of the bridge

Figure 5.39: 3D bridge optimization problem model

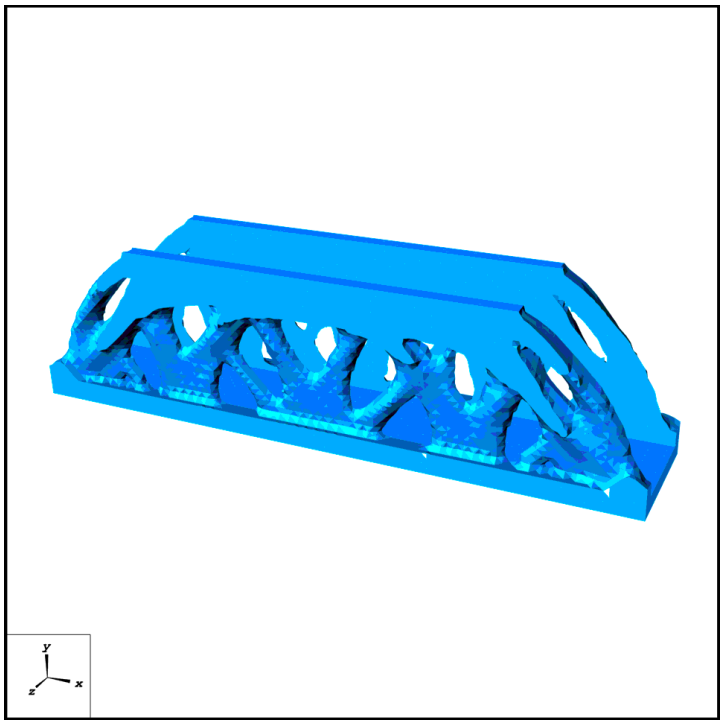

(a) Optimized 3D bridge: obtained shape

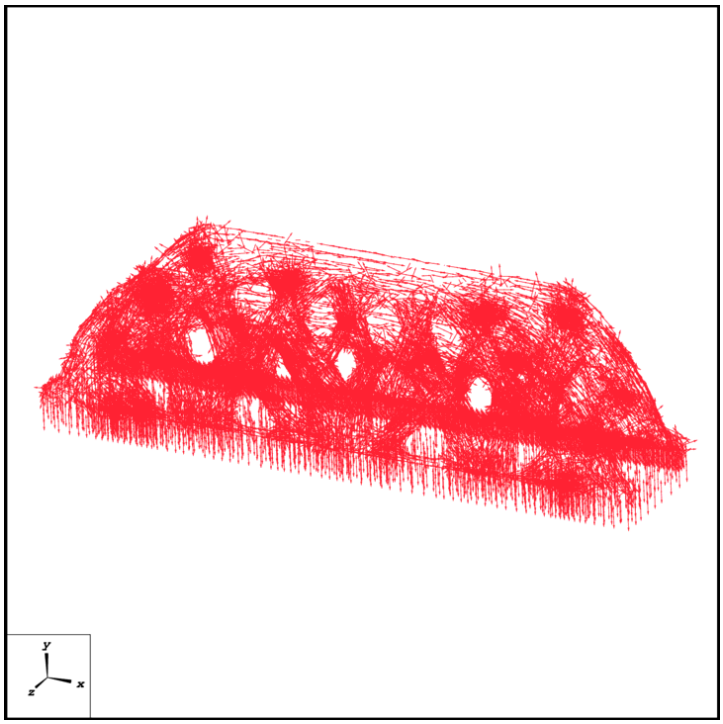

(b) Optimized 3D bridge: plot of stiffest direction of the local anisotropy

Figure 5.40: Optimized 3D multi-loaded bridge structure

Conclusion

In this work, we presented the coupled topology and orthotropic anisotropy orientation optimization methods, which are based on the level set topology optimization and can be applied numerically to additive manufacturing technologies. The optimization of the orientation is based on two methods for different types of problems. For single-load compliance problems, we used the Pedersen optimality criterion. On the other hand, for other types of problems such as multiple-loads and non self-adjoint problems, we used a gradient descent method. We treated various examples, from a cantilever and an L-beam to a displacement inverter and a multi-loaded bridge, in 2D and 3D. The variety of the treated examples demonstrates the robustness of the algorithms that we have implemented.

By observing the results that we have obtained, we conclude that the level set method topology optimization works properly when coupled with the optimization of the anisotropy orientation. We also conclude that the optimal topology of a structure is heavily influenced by the anisotropy of the material and that, in general, the stiffest direction of the material is parallel to the direction of the bars of an optimized structure. Finally, we conclude that optimizing the local orientation is very important in the case of an anisotropic material as it further optimizes the objective function, but also improves the quality of the topology that is obtained by the topology optimization algorithm.

After completion of this phd thesis, further research is still needed to improve the applicability of coupled shape and orientation optimization. Considering an orthotropic material that is not transversely isotropic is a work that has to be done. In this case, the orientation is modelled using 3 Euler angles. Also, we still need to adapt the Ginzburg-Landau approach of orientation optimization to 3D. Including 3D printing manufacturing technological constraints to the coupled optimization of shape and orientation, such as overhangs, supports and residual stresses, also including a regularization scheme for the coupled 3D problem and treating other types of physical problems such as stress minimization, fatigue,

plasticity and damage minimization, thermic, fluids and thermo-elasticity, are all problems which could be addressed in the future.

Another obvious possible work is to build the geometries that were obtained using an additive manufacturing technology and to test their qualities experimentally.

Bibliography

[1] Grégoire Allaire. *Shape optimization by the homogenization method*, volume 146. Springer Science & Business Media, 2002.

[2] Grégoire Allaire. *Conception optimale de structures*, volume 58 of *Mathématiques & Applications (Berlin) [Mathematics & Applications]*. Springer-Verlag, Berlin, 2007. With the collaboration of Marc Schoenauer (INRIA) in the writing of Chapter 8.

[3] Grégoire Allaire, Eric Bonnetier, Gilles Francfort, and François Jouve. Shape optimization by the homogenization method. *Numerische Mathematik*, 76(1):27–68, 1997.

[4] Grégoire Allaire and Charles Dapogny. A deterministic approximation method in shape optimization under random uncertainties. *SMAI Journal of computational mathematics*, 1:83–143, 2015.

[5] Grégoire Allaire, Charles Dapogny, Gabriel Delgado, and Georgios Michailidis. Multi-phase structural optimization via a level set method. *ESAIM: Control, Optimisation and Calculus of Variations*, 20(2):576–611, 2014.

[6] Grégoire Allaire, Charles Dapogny, and Pascal Frey. Shape optimization with a level set based mesh evolution method. *Computer Methods in Applied Mechanics and Engineering*, 282:22–53, 2014.

[7] Grégoire Allaire, Frédéric de Gournay, François Jouve, and Anca-Maria Toader. Structural optimization using topological and shape sensitivity via a level set method. *Control and Cybernetics*, 34(1):59, 2005.

[8] Grégoire Allaire, Perle Geoffroy-Donders, and Olivier Pantz. Topology optimization of modulated and oriented periodic microstructures by the homogenization method. *Computers & Mathematics with Applications*, 78(7):2197–2229, 2019.

[9] Grégoire Allaire and François Jouve. A level-set method for vibration

and multiple loads structural optimization. *Computer methods in applied mechanics and engineering*, 194(30-33):3269–3290, 2005.

[10] Grégoire Allaire and François Jouve. Minimum stress optimal design with the level set method. *Engineering analysis with boundary elements*, 32(11):909–918, 2008.

[11] Grégoire Allaire, François Jouve, and Georgios Michailidis. Thickness control in structural optimization via a level set method. *Structural and Multidisciplinary Optimization*, 53(6):1349–1382, 2016.

[12] Grégoire Allaire, François Jouve, and Anca-Maria Toader. A level-set method for shape optimization. *Comptes Rendus Mathematique*, 334(12):1125–1130, 2002.

[13] Grégoire Allaire, François Jouve, and Anca-Maria Toader. Structural optimization using sensitivity analysis and a level-set method. *Journal of computational physics*, 194(1):363–393, 2004.

[14] Grégoire Allaire, François Jouve, and Nicolas Van Goethem. Damage and fracture evolution in brittle materials by shape optimization methods. *J. Comp. Phys.*, 230:5010–5044, 2011.

[15] Grégoire Allaire, Anton Karrman, and Georgios Michailidis. `A 2-d level set code for shape and topology optimization`, available at: `http://www.cmap.polytechnique.fr/~allaire/levelset_en.html`, 2009.

[16] Grégoire Allaire and Olivier Pantz. Structural Optimization with FreeFem++. *Structural and Multidisciplinary Optimization*, 32:173–181, 2006.

[17] Grégoire Allaire and Olivier Pantz. Structural optimization with `FreeFem++`. *Structural and Multidisciplinary Optimization*, 32(3):173–181, 2006.

[18] Grégoire Allaire, Charles Dapogny, and François Jouve. Shape and topology optimization. Handbook of numerical analysis. Elsevier, 2020.

[19] Grégoire Allaire, François Jouve, and Anca-Maria Toader. A level-set method for shape optimization. *Comptes Rendus Mathematique*, 334(12):1125–1130, jan 2002.

[20] Samuel Amstutz and Peter Gangl. Topological derivative for the nonlinear magnetostatic problem. *ETNA, Electron. Trans. Numer. Anal.*, 51:169–218, 2019.

[21] Samuel Amstutz and Antonio A. Novotny. Topological optimization of structures subject to von Mises stress constraints. *Struct. Multidiscip. Optim.*, 41(3):407–420, 2010.

[22] Samuel Amstutz, Antonio A. Novotny, and Eduardo Alberto De Souza Neto. Topological derivative-based topology optimization of structures subject to Drucker-Prager stress constraints. *Comput. Methods Appl. Mech. Eng.*, 233-236:123–136, 2012.

[23] Douglas N. Arnold and Richard S. Falk. Well-posedness of the fundamental boundary value problems for constrained anisotropic elastic materials. *Archive for rational mechanics and analysis*, 98(2):143–165, Jun 1987.

[24] Long Bai, Cheng Gong, Wei Chen, Yuanxi Sun, Yiyi Zhang, Yidong Cai, Zhaoyu Zhu, and Xie Chen. Additive manufacturing of customized metallic orthopedic implants: Materials, structures, and surface modifications. *Metals*, 9:1004, 09 2019.

[25] Timothy J Barth and James A Sethian. Numerical schemes for the hamilton–jacobi and level set equations on triangulated domains. *Journal of Computational Physics*, 145(1):1–40, 1998.

[26] Martin P Bendsøe and Ole Sigmund. Material interpolation schemes in topology optimization. *Archive of applied mechanics*, 69(9):635–654, 1999.

[27] Martin Philip Bendsøe and Noboru Kikuchi. Generating optimal topologies in structural design using a homogenization method. *Computer methods in applied mechanics and engineering*, 71(2):197–224, 1988.

[28] Martin Philip Bendsøe and Ole Sigmund. *Topology optimization: theory, methods, and applications*. Springer Science & Business Media, 2013.

[29] Fabrice Bethuel, Haïm Brezis, Frédéric Hélein, et al. *Ginzburg-landau vortices*, volume 13. Springer, 1994.

[30] Martin Bihr, Grégoire Allaire, Xavier Betbeder-Lauque, Beniamin Bogosel, Felipe Bordeu, and Julie Querois. Part and supports optimization in metal powder bed additive manufacturing using simplified process simulation. *Comput. Methods Appl. Mech. Eng.*, 395:30, 2022. Id/No 114975.

[31] C Bui, C Dapogny, and P Frey. An accurate anisotropic adaptation method for solving the level set advection equation. *International Journal for Numerical Methods in Fluids*, 70(7):899–922, 2012.

[32] Pierre Carpentier and Guy Cohen. *Décomposition-coordination en optimisation déterministe et stochastique*, volume 81 of *Mathématiques et Applications*. Springer Berlin Heidelberg, 2017.

[33] Beth E Carroll, Todd A Palmer, and Allison M Beese. Anisotropic tensile behavior of ti–6al–4v components fabricated with directed energy deposition additive manufacturing. *Acta Materialia*, 87:309–320, 2015.

[34] Vivien J. Challis and James K. Guest. Level set topology optimization of fluids in Stokes flow. *Int. J. Numer. Methods Eng.*, 79(10):1284–1308, 2009.

[35] Zhen Chen, Shenggui Chen, Zhengying Wei, Lijuan Zhang, Wei Pei, Bingheng Lu, Shuzhe Zhang, and Yu Xiang. Anisotropy of nickel-based superalloy k418 fabricated by selective laser melting. *Progress in Natural Science: Materials International*, 28, 08 2018.

[36] H. C. Cheng, N. Kikuchi, and Z. D. Ma. An improved approach for determining the optimal orientation of orthotropic material. *Structural Optimization*, 8(2-3):101–112, oct 1994.

[37] Charles Dapogny, Alexis Faure, Georgios Michailidis, Grégoire Allaire, Agnes Couvelas, and Rafael Estevez. Geometric constraints for shape and topology optimization in architectural design. *Computational Mechanics*, 59(6):933–965, 2017.

[38] Charles Dapogny and Pascal Frey. Computation of the signed distance function to a discrete contour on adapted triangulation. *Calcolo*, 49(3):193–219, 2012.

[39] Frédéric de Gournay. Velocity extension for the level-set method and multiple eigenvalues in shape optimization. *SIAM journal on control and optimization*, 45(1):343–367, 2006.

[40] Frédéric de Gournay, Grégoire Allaire, and François Jouve. Shape and topology optimization of the robust compliance via the level set method. *ESAIM: Control, Optimisation and Calculus of Variations*, 14(1):43–70, 2008.

[41] Jeet Desai, Grégoire Allaire, and François Jouve. Topology optimization of structures undergoing brittle fracture. *J. Comput. Phys.*, 458:35, 2022. Id/No 111048.

[42] Jeet Desai, Grégoire Allaire, François Jouve, and Chetra Mang. Topology optimization in quasi-static plasticity with hardening using a level-set

method. *Structural and Multidisciplinary Optimization*, 64(5):3163–3191, 2021.

[43] Ugur M Dilberoglu, Bahar Gharehpapagh, Ulas Yaman, and Melik Dolen. The role of additive manufacturing in the era of industry 4.0. *Procedia Manufacturing*, 11:545–554, 2017.

[44] F. Feppon, G. Allaire, F. Bordeu, J. Cortial, and C. Dapogny. Shape optimization of a coupled thermal fluid-structure problem in a level set mesh evolution framework. *S$\vec{e}$MA J.*, 76(3):413–458, 2019.

[45] Florian Feppon, Grégoire Allaire, Felipe Bordeu, Julien Cortial, and Charles Dapogny. Shape optimization of a coupled thermal fluid–structure problem in a level set mesh evolution framework. *SeMA Journal*, 76(3):413–458, 2019.

[46] William E Frazier. Metal additive manufacturing: a review. *Journal of Materials Engineering and performance*, 23(6):1917–1928, 2014.

[47] Peter Gangl. Sensitivity-based topology and shape optimization with application to electric motors. In *Frontiers in PDE-constrained optimization. Selected papers based on the presentations at the workshop, Minneapolis, MN, USA, June 6–10, 2016*, pages 317–340. New York, NY: Springer, 2018.

[48] H.C. Gea and J.H. Luo. On the stress-based and strain-based methods for predicting optimal orientation of orthotropic materials. *Structural and Multidisciplinary Optimization*, 26(3-4):229–234, feb 2004.

[49] Perle Geoffroy-Donders. *Homogenization method for topology optimization of structures built with lattice materials*. Theses, Ecole Polytechnique, December 2018.

[50] Perle Geoffroy-Donders, Grégoire Allaire, and Olivier Pantz. 3-d topology optimization of modulated and oriented periodic microstructures by the homogenization method. *Journal of Computational Physics*, 401:108994, 2020.

[51] Hamid Ghasemi, Harold S. Park, and Timon Rabczuk. A level-set based IGA formulation for topology optimization of flexoelectric materials. *Comput. Methods Appl. Mech. Eng.*, 313:239–258, 2017.

[52] Ian Gibson, David W Rosen, Brent Stucker, Mahyar Khorasani, David Rosen, Brent Stucker, and Mahyar Khorasani. *Additive manufacturing technologies*, volume 17. Springer, 2021.

[53] Phillip L. Gould. *Introduction to Linear Elasticity*. Springer, 2013.

[54] J. Groen and O. Sigmund. Homogenization-based topology optimization for high-resolution manufacturable microstructures. *Internat. J. Numer. Methods Engrg.*, 113(8):1148–1163, 2018.

[55] Nannan Guo and Ming C Leu. Additive manufacturing: technology, applications and research needs. *Frontiers of mechanical engineering*, 8(3):215–243, 2013.

[56] Nadim S Hmeidat, Robert C Pack, Samantha J Talley, Robert B Moore, and Brett G Compton. Mechanical anisotropy in polymer composites produced by material extrusion additive manufacturing. *Additive Manufacturing*, 34:101385, 2020.

[57] Samuel H Huang, Peng Liu, Abhiram Mokasdar, and Liang Hou. Additive manufacturing and its societal impact: a literature review. *The International Journal of Advanced Manufacturing Technology*, 67(5):1191–1203, 2013.

[58] François Jouve and Houari Mechkour. Level set based method for design of compliant mechanisms. *European Journal of Computational Mechanics/Revue Européenne de Mécanique Numérique*, 17(5-7):957–968, 2008.

[59] T. Kellner. 3d-printed 'bionic' parts could revolutionize aerospace design. *General Electric Reports: Boston, MA, USA*, 2017.

[60] Ron Kimmel and James A Sethian. Computing geodesic paths on manifolds. *Proceedings of the national academy of Sciences*, 95(15):8431–8435, 1998.

[61] Yihong Kok, Xi Peng Tan, P Wang, MLS Nai, Ngiap Hiang Loh, Erjia Liu, and Shu Beng Tor. Anisotropy and heterogeneity of microstructure and mechanical properties in metal additive manufacturing: A critical review. *Materials & Design*, 139:565–586, 2018.

[62] Jean-Pierre Kruth, Ludo Froyen, Jonas Van Vaerenbergh, Peter Mercelis, Marleen Rombouts, and Bert Lauwers. Selective laser melting of iron-based powder. *Journal of materials processing technology*, 149(1-3):616–622, 2004.

[63] William Thomson L. Kelvin. *Elements of a Mathematical Theory of Elasticity*. Royal Society of Edinburgh, 1856.

[64] Emmanuel Laporte and Patrick Le Tallec. *Numerical methods in sen-*

sitivity analysis and shape optimization. With CD-ROM. Model. Simul. Sci. Eng. Technol. Boston, MA: Birkhäuser, 2003.

[65] Karl-Heinz Leitz, P. Singer, Arno Plankensteiner, B. Tabernig, Heinrich Kestler, and Lorenz Sigl. 2016.

[66] Malin Lervåg, Camilla Sørensen, Andreas Robertstad, Bård Brønstad, Bård Nyhus, Magnus Eriksson, Ragnhild Aune, Xiaobo Ren, Odd Akselsen, and Ivan Bunaziv. Additive manufacturing with superduplex stainless steel wire by cmt process. *Metals - Open Access Metallurgy Journal*, 10:272, 02 2020.

[67] J. Luo and Hae Chang Gea. Optimal orientation of orthotropic materials using an energy based method. *Structural Optimization*, 15:230–236, 06 1998.

[68] Zhen Luo, Liyong Tong, Michael Yu Wang, and Shengyin Wang. Shape and topology optimization of compliant mechanisms using a parameterization level set method. *J. Comput. Phys.*, 227(1):680–705, 2007.

[69] Jean Mandel. Généralisation de la théorie de plasticité de wt koiter. *International Journal of Solids and structures*, 1(3):273–295, 1965.

[70] Bob McGinty. Principal stresses & invariants. https://www.continuummechanics.org/principalstress.html.

[71] Morteza M. Mehrabadi and Stephen C. Cowin. Eigentensors of linear anisotropic elastic materials. *The Quarterly Journal of Mechanics and Applied Mathematics*, 43, 02 1990.

[72] Morteza M. Mehrabadi, Stephen C. Cowin, and Jovo Jaric. Six-dimensional orthogonal tensor representation of the rotation about an axis in three dimensions. *International Journal of Solids and Structures*, 32(3):439–449, 1995.

[73] Yulin Mei and Xiaoming Wang. A level set method for structural topology optimization and its applications. *Adv. Eng. Softw.*, 35(7):415–441, 2004.

[74] Barry Merriman, James Kenyard Bence, and Stanley Osher. *Diffusion generated motion by mean curvature.* Department of Mathematics, University of California, Los Angeles, 1992.

[75] Bijan Mohammadi and Olivier Pironneau. *Applied shape optimization for fluids.* Numer. Math. Sci. Comput. Oxford: Oxford University Press, 2nd ed. edition, 2009.

[76] Jorge Nocedal and Stephen J. Wright. *Numerical Optimization*. Springer New York, 2006.

[77] A. N. Norris. Optimal orientation of anisotropic solids. *The Quarterly Journal of Mechanics and Applied Mathematics*, 59(1):29–53, feb 2006.

[78] Stanley Osher and Ronald Fedkiw. *Level set methods and dynamic implicit surfaces*, volume 153. Springer Science & Business Media, 2006.

[79] Stanley Osher and James A Sethian. Fronts propagating with curvature-dependent speed: algorithms based on hamilton-jacobi formulations. *Journal of computational physics*, 79(1):12–49, 1988.

[80] Stanley Osher and Chi-Wang Shu. High-order essentially nonoscillatory schemes for hamilton–jacobi equations. *SIAM Journal on numerical analysis*, 28(4):907–922, 1991.

[81] Stanley J Osher and Fadil Santosa. Level set methods for optimization problems involving geometry and constraints: I. frequencies of a two-density inhomogeneous drum. *Journal of Computational Physics*, 171(1):272–288, 2001.

[82] P. Pedersen. On optimal orientation of orthotropic materials. *Structural Optimization*, 1(2):101–106, jun 1989.

[83] P. Pedersen. Bounds on elastic energy in solids of orthotropic materials. *Structural Optimization*, 2(1):55–63, mar 1990.

[84] Olivier Pironneau. Optimal shape design for elliptic systems. Springer Series in Computational Physics. New York etc.: Springer-Verlag. XII, (1984)., 1984.

[85] VA Popovich, EV Borisov, AA Popovich, V Sh Sufiiarov, DV Masaylo, and Laurie Alzina. Functionally graded inconel 718 processed by additive manufacturing: Crystallographic texture, anisotropy of microstructure and mechanical properties. *Materials & Design*, 114:441–449, 2017.

[86] Lalaina Rakotondrainibe, Jeet Desai, Patrick Orval, and Grégoire Allaire. Coupled topology optimization of structure and connections for bolted mechanical systems. *Eur. J. Mech., A, Solids*, 93:19, 2022. Id/No 104499.

[87] Ali Rezaei, Ahmad Rezaeian, Ahmad Kermanpur, M. Badrossamay, Ehsan Foroozmehr, Seyed Mahdi Marashi, Ali Foroozmehr, and Jeongho Han. Microstructural and mechanical anisotropy of selective laser melted in718 superalloy at room and high temperatures using small punch test. *Materials Characterization*, 162:110200, 02 2020.

[88] Marco Rovati and Alberto Taliercio. Stationarity of the strain energy density for some classes of anisotropic solids. *International Journal of Solids and Structures*, 40(22):6043–6075, nov 2003.

[89] Alexander A. Safonov. 3D topology optimization of continuous fiber-reinforced structures via natural evolution method. *Composite structures*, 215:289–297, may 2019.

[90] Robert Saye and James A Sethian. A review of level set methods to model interfaces moving under complex physics: Recent challenges and advances. In *Geometric Partial Differential Equations, Part 1, Handbook of Numerical Analysis, 21*, pages 509–554. Elsevier, 2020.

[91] Martin-Pierre Schmidt, Laura Couret, Christian Gout, and Claus B. W. Pedersen. Structural topology optimization with smoothly varying fiber orientations. *Structural and Multidisciplinary Optimization*, jul 2020.

[92] James A Sethian. Fast marching methods. *SIAM review*, 41(2):199–235, 1999.

[93] James A Sethian. *Level set methods and fast marching methods: evolving interfaces in computational geometry, fluid mechanics, computer vision, and materials science*, volume 3. Cambridge university press, 1999.

[94] James A Sethian and Andreas Wiegmann. Structural boundary design via level set and immersed interface methods. *Journal of computational physics*, 163(2):489–528, 2000.

[95] Corey Shemelya, Angel De La Rosa, Angel R Torrado, Kevin Yu, Jennifer Domanowski, Peter J Bonacuse, Richard E Martin, Michael Juhasz, Frances Hurwitz, Ryan B Wicker, et al. Anisotropy of thermal conductivity in 3d printed polymer matrix composites for space based cube satellites. *Additive Manufacturing*, 16:186–196, 2017.

[96] Ole Sigmund. A 99 line topology optimization code written in matlab. *Structural and multidisciplinary optimization*, 21(2):120–127, 2001.

[97] Martin Spoerk, Chethan Savandaiah, Florian Arbeiter, Gerhard Traxler, Ludwig Cardon, Clemens Holzer, and Janak Sapkota. Anisotropic properties of oriented short carbon fibre filled polypropylene parts fabricated by extrusion-based additive manufacturing. *Composites Part A: Applied Science and Manufacturing*, 113:95–104, 2018.

[98] Austin T Sutton, Caitlin S Kriewall, Ming C Leu, and Joseph W Newkirk. Powder characterisation techniques and effects of powder characteristics

on part properties in powder-bed fusion processes. *Virtual and physical prototyping*, 12(1):3–29, 2017.

[99] Ana Vafadar, Ferdinando Guzzomi, Alexander Rassau, and Kevin Hayward. Advances in metal additive manufacturing: A review of common processes, industrial applications, and current challenges. *Applied Sciences*, 11:1213, 01 2021.

[100] Paolo Vannucci. *Anisotropic Elasticity*, volume 85. Springer, 2018.

[101] Silvia Vock, Burghardt Klöden, Alexander Kirchner, Thomas Weißgärber, and Bernd Kieback. Powders for powder bed fusion: a review. *Progress in Additive Manufacturing*, 4(4):383–397, 2019.

[102] Woldemar Voigt. *Textbook on crystal physics:(excluding crystal optics)*, volume 34. BG Teubner, 1910.

[103] Michael Yu Wang and Xiaoming Wang. "Color" level sets: A multi-phase method for structural topology optimization with multiple materials. *Comput. Methods Appl. Mech. Eng.*, 193(6-8):469–496, 2004.

[104] Yiqiang Wang, Zhen Luo, Zhan Kang, and Nong Zhang. A multi-material level set-based topology and shape optimization method. *Comput. Methods Appl. Mech. Eng.*, 283:1570–1586, 2015.

[105] Eric W Weisstein. Cubic formula. *https://mathworld. wolfram. com/*, 2002.

[106] Kaufui V Wong and Aldo Hernandez. A review of additive manufacturing. *International scholarly research notices*, 2012.

[107] I Yadroitsev, Ph Bertrand, and I Smurov. Parametric analysis of the selective laser melting process. *Applied surface science*, 253(19):8064–8069, 2007.

[108] Chor Yen Yap, Chee Kai Chua, Zhi Li Dong, Zhong Hong Liu, Dan Qing Zhang, Loong Ee Loh, and Swee Leong Sing. Review of selective laser melting: Materials and applications. *Applied physics reviews*, 2(4):041101, 2015.

[109] Kewei Zhang. On universal coercivity in linear elasticity. *SIAM Journal on Mathematical Analysis*, 42(1):298–322, Jan 2010.

[110] Xing Zhang, Christopher J. Yocom, Bo Mao, and Yiliang Liao. Microstructure evolution during selective laser melting of metallic materials: A review. *Journal of Laser Applications*, 31(3):031201, 2019.

[111] Hong-Kai Zhao, Stanley Osher, and Ronald Fedkiw. Fast surface reconstruction using the level set method. In *Variational and Level Set Methods in Computer Vision, 2001. Proceedings. IEEE Workshop on*, pages 194–201. IEEE, 2001.

[112] Shiwei Zhou and Qing Li. A variational level set method for the topology optimization of steady-state Navier-Stokes flow. *J. Comput. Phys.*, 227(24):10178–10195, 2008.

[113] Dan Zwillinger. *CRC standard mathematical tables and formulas*. chapman and hall/CRC, 2018.

Table of contents

Introduction (en français) **1**

Introduction (in english) **9**

1 Shape optimization **19**
1.1 Parametric shape optimization 20
1.1.1 Setting of the problem 20
1.1.2 Existence and uniqueness of solution of the elasticity problem 22
1.1.3 Objective function and the Lagrangian 22
1.1.4 Derivation with respect to the optimization parameters . 24
1.2 Geometric shape optimization 26
1.2.1 Model problem 26
1.2.2 Derivation with respect to the shape 28
1.2.3 Shape gradient in linear elasticity 30
1.3 Topology optimization with the level set method 31
1.3.1 Regularization of the shape derivative 33
1.3.2 Adding a constraint to topology optimization 34
1.3.3 Topology optimization algorithm 37
1.3.4 Industrial applications with the level set topology optimization method 38

2 Mechanical problem and model **41**
2.1 Additive manufacturing 41
2.2 Elastic anisotropy 44
2.2.1 Hooke's law for anisotropic bodies 44
2.2.2 Examples of constitutive matrices 46
2.2.3 Orientation of an anisotropic material model in elasticity 49

3 2D orientation optimization **55**
3.1 Optimal direction using an optimality criterion 55

3.1.1 Pointwise optimality criterion approach 57
3.1.2 Optimal orientation 58
3.1.3 Numerical algorithm 59
3.2 Optimal direction using a gradient descent method 60
3.3 Optimal direction using a Ginzburg-Landau based gradient descent method 63
3.4 Regularization of orientation 65
3.4.1 Regularization of a given orientation field 66
3.4.2 Regularization while optimizing the orientation 67
3.5 Constrained orientation optimization 68
3.5.1 Projected gradient descent 68
3.5.2 Augmented Lagrangian for inequality constraints 68
3.5.3 Examples using an augmented Lagrangian for inequality constraint 71
3.6 Numerical Results 73
3.6.1 2D orientation optimization using the optimality criterion 73
3.6.2 2D orientation optimization using the gradient descent method 78
3.6.3 2D orientation optimization using the Ginzburg-Landau approach 85
3.6.4 2D constrained orientation optimization 90

4 3D orientation optimization 105
4.1 Optimal direction using an optimality criterion 105
4.1.1 Pointwise optimality criterion approach 107
4.1.2 Result of the orientation optimality criterion approach . 108
4.1.3 Principal stresses in 3D 108
4.1.4 Optimal orthotropic orientation 109
4.1.5 Optimal transverse isotropic orientation 111
4.1.6 Optimization algorithm 115
4.2 Optimal direction using a gradient descent method 116
4.2.1 Algorithm 117
4.3 Regularization of orientation 117
4.3.1 Regularization of a given orientation field 117
4.4 Constrained orientation optimization 118
4.4.1 Projected gradient descent 118
4.4.2 Augmented Lagrangian for inequality constraint 121
4.4.3 Examples using an augmented Lagrangian for inequality 122
4.5 Numerical results 125
4.5.1 3D constrained orientation optimization 125

5 Coupled optimization of topology and orientation 131
5.1 Coupled optimization of topology and orientation in 2D 131
5.1.1 Optimization problem 131
5.1.2 Topology optimization coupled with an optimality criteria orientation optimization method 133
5.1.3 Numerical results 135
5.1.4 Topology optimization coupled with a gradient descent orientation optimization method. 148
5.2 Coupled optimization of topology and orientation in 3D 175
5.2.1 Optimization problem 175
5.2.2 Topology optimization coupled with an optimality criterion orientation optimization method 176
5.2.3 Topology optimization coupled with a gradient descent orientation optimization method 179
5.2.4 Numerical results 182

Conclusion 193

Bibliography 195

Table of contents 206